The Middle Miocene Climate Transition in the Central Mediterranean

Anja Mourik

GEOLOGICA ULTRAIECTINA
Mededelingen van de Faculteit Geowetenschappen - Universiteit Utrecht - No. 326

Members of the dissertation committee:

Dr. Ann Holbourn
Institute for Geosciences
University of Kiel
Germany

Prof. dr. Wolfgang Kuhnt
Institute for Geosciences
University of Kiel
Germany

Dr. Caroline Lear
School of Earth and Ocean Sciences
Cardiff University
United Kindom

Prof. dr. Dick Kroon
School of Geosciences
University of Edinburgh
United Kindom

Prof. dr. Jack Middelburg
Faculty of Geosciences
Utrecht University
The Netherlands

Prof. dr. Andy Lotter
Institute of Environmental Biology
Utrecht University
The Netherlands

The research presented in this thesis was funded by the Darwin Center for Biogeosciences and the University of Utrecht.

Research was carried out at the Stratigraphy/Paleontology Group, Department of Earth Sciences, Utrecht University, Budapestlaan 4, 3584 CD, Utrecht, The Netherlands.

ISBN/EAN: 978-90-5744-188-2

Cover and graphic design: Anja Mourik

The Middle Miocene Climate Transition in the Central Mediterranean

De Midden Miocene Klimaattransitie in het centrale Middellandse Zeegebied

(met een samenvatting in het Nederlands)

Proefschrift

ter verkrijging van de graad van doctor aan de Universiteit Utrecht
op gezag van de rector magnificus, prof. dr. J.C. Stoof, ingevolge het besluit van het college voor promoties in het openbaar te verdedigen op maandag 10 mei 2010 des middags te 2.30 uur

door

Anja Ariëtta Mourik

geboren op 22 september 1981 te Haarlem

Promotor: Prof. dr. G. J. van der Zwaan

Co-promotoren: Dr. F. J. Hilgen
Dr. T. J. Kouwenhoven

voor Marjon

.... en voor Demis

That is just the way it was
Nothing could be better
And nothing ever was

Coldplay

Glass Of Water

Contents

Introduction and Summary 11

Chapter 1

Astronomical tuning of the La Vedova High Cliff Section (Ancona, Italy) – Implications of the Middle Miocene Climate Transition for Mediterranean sapropel formation 19

A. A. Mourik, J. F. Bijkerk, A. Cascella, S.K. Hüsing, F.J. Hilgen, L. J. Lourens, and E. Turco.

Chapter 2

Onset of orbitally induced dry-wet climate oscillations in the Mediterranean during the Middle Miocene Climate Transition

A.A. Mourik, S. K. Hüsing, F.J. Hilgen, G. J. Reichart, and T.J. Kouwenhoven 39

Chapter 3

Improved astronomical age constraints for the Middle Miocene Climate Transition based on high-resolution stable isotope records from the Central Mediterranean (Maltese Islands)

A. A. Mourik, H. A. Abels, F. J. Hilgen, A. di Stefano and W.J. Zachariasse 55

Chapter 4

Benthic foraminiferal response to environmental changes during the Middle Miocene Climate Transition in the Central Mediterranean (Maltese Islands)

A. A. Mourik, J. Sprong, T. J. Kouwenhoven and G.J. van der Zwaan. 81

Chapter 5

Synthesis: Environmental changes in the Mediterranean area across the MMCT – perspectives from the marine and terrestrial realms

A. A. Mourik 101

References 112

Introductie en Samenvatting in het Nederlands 122

Acknowledgements 128

Curriculum Vitae 133

Introduction and Summary

1. Introduction

Understanding the complex Earth system, with its continuously transforming landscape, its incredible variety of life forms and its ever changing climate, is of crucial importance to be able to predict the Earth's future. The increasing greenhouse conditions we observe today are a major issue for our densely populated world. Climate models are essential to predict our future, but their robustness also depends on what we learn from climate changes of the past. It is therefore of crucial importance to study the major climate transitions of the past and most noticeably the timing and time involved in these transitions. In addition, we would like to increase our knowledge on feedback mechanisms, which may potentially speed up or slow down climate change.

Climatic changes in the past have been inferred from, amongst others, studies on plant and animal fossils, fossil soils, lake deposits and sea floor sediments. Since the start of the Deep Sea Drilling Programme (DSDP) in 1968, later followed by the Ocean Drilling Program (ODP) and now International Ocean Drilling Program (IODP), extensive studies have been conducted on Mesozoic and Cenozoic sediments from the Atlantic, Pacific and Indian Ocean and the Mediterranean.

Important tools in climate reconstructions from deep sea sediments are foraminifera, single celled organisms often building a test of calcium carbonate. Most species of foraminifera live on the sea floor and are known as benthic foraminifera. Planktic foraminifera have a pelagic life style and inhabit the surficial water masses.

The chemical composition of foraminiferal tests is widely used in paleo-studies since it may contain information on sea water temperature, ice volume, salinity, productivity, the global carbonate pump and ocean circulation patterns (Raymo and Ruddiman, 1992; Ruddiman, 2000). In addition, foraminifera are studied for their ecological preferences. The fossil assemblages may reflect the paleo-environmental conditions in which they were living.

During the Cenozoic, starting 65 million years ago (Ma), three major cooling steps took place, which turned the world from a greenhouse- into the icehouse state of today. The major transitions occurred during the Eocene/Oligocene transition, during the middle Miocene and during the middle Pliocene (Shackleton and Kennett, 1975; Miller et al., 1987; Lear et al., 2000; Zachos et al., 2001a). Large continental ice sheets started to evolve on Antarctica from ~34 Ma onwards whereas major Northern Hemisphere glaciation is more refined to the later Neogene (e.g. Zachos et al., 2001a; 2008). However, glaciers and small isolated ice caps were probably present on the Northern Hemisphere throughout much of the Cenozoic, especially during favorable orbital periods (DeConto et al., 2008).

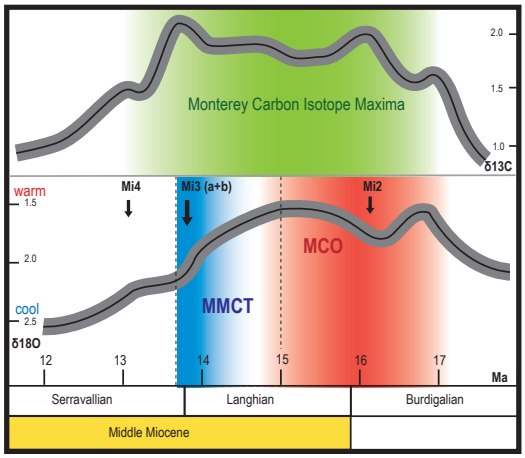

Figure 1. Simplified scheme of the $\delta^{18}O$ and $\delta^{13}C$ isotope stack after Zachos et al., 2001a. The high $\delta^{13}C$ values are associated with the Monterey Carbon Event, in which six Carbon Maxima (CM-events) have been distinguished (Woodruff and Savin, 1991). Benthic $\delta^{18}O$ records show depleted values between ~17 and 15 Ma, related to warm global climate and small ice caps. After the Miocene Climatic Optimum (MCO), a long lasting cooling trend commenced. The Middle Miocene Climate Transition is here defined as the first cooling phase after the MCO. The MMCT is characterized by a ~ 1 Myr gradual cooling phase, starting at the end of the MCO, and a second more rapid phase, associated with the major expansion of the East Antarctic Ice Sheet at ~13.8 Ma. The oxygen isotope excursion related to this step is the Mi3(b)-event (Miller et al., 1991;1996).

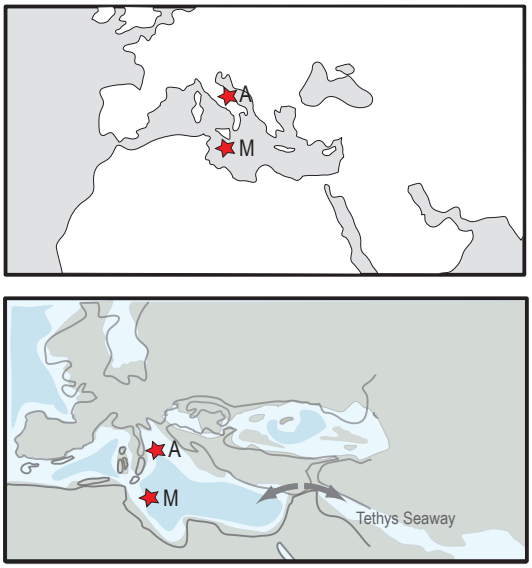

Figure 2. Upper panel shows the present day Mediterranean Sea with the localities studied in this thesis: A: along the Adriatic coast near Ancona (Italy), and M: Maltese Islands (Malta and Gozo). Lower panel is a paleogeographic map for the studied time interval (~15-13 Ma), modified after Rögl, 1999 and Harzhauser and Piller, 2007. The eastern portal of the Tethys Seaway, which connected the Mediterranean to the Indian Ocean, closed somewhere between the late Oligocene and middle Miocene.

1.1 The Middle Miocene Climate Transition

The focus of this thesis is the Middle Miocene Climate Transition (MMCT) which terminated the Miocene Climatic Optimum (MCO), the warmest phase of the Neogene. A major expansion of the East Antarctic Ice Sheet caused the transition to cooler climates and changes in ocean circulation patterns (e.g. Kennett, 1975; Miller et al., 1987; Flower and Kennett, 1994; Zachos et al., 2001a; Shevenell and Kennett, 2004). A detailed review on the Middle Miocene Climate Transition is given by Flower and Kennett (1994).

The time-slice encompassing the MMCT varies between authors, and may be in the range of ~17-11 Ma, depending on whether the focus is on all oxygen isotope enrichments during the middle Miocene, or only on the major shift at ~13.8 Ma (Miller et al., 1991; 1996; Woodruff and Savin, 1991; Flower and Kennett, 1994; Shevenell and Kennett, 2004). Presently, it is not exactly clear when the Miocene Climatic Optimum ended. Despite the fact that the end of the MCO is not very well defined, in this thesis the last representative warm phase will be considered at ~15 Ma. The MMCT will therefore be defined as the phase between the end of the Miocene Climatic Optimum (MCO; ~15 Ma) and the end of the rapid cooling step at ~13.7 Ma (Fig. 1).

Important factors for long-term trends in climate change are variations in atmospheric CO_2, linked to the global carbon cycle, opening and closure of oceanic gateways, and uplift of mountain ranges (e.g. Hay et al., 2002). The Middle Miocene Climate Transition has been associated with all of these factors, but up to date no clear consensus on the exact cause exists.

Like other major Cenozoic climate shifts, the timing of the major cooling step is supposedly controlled by long-period orbital forcing (Abels et al., 2005; Holbourn et al., 2005; 2007). Minima in the amplitude variation of Earth's tilt (obliquity) and minima in the ellipsoidal shape of the Earth's orbit around the sun (eccentricity), which modulates the amplitude of climatic precession (the rotational movement of the Earth's axis relative to the elliptical orbit), might have suppressed summer insolation maxima for a prolonged interval of time, thereby favoring ice sheet growth. However, orbital forcing alone can not explain the long-term cooling trend from the MCO onwards.

A long-lasting positive carbon-isotope excursion between ~17 and 13.5 Ma (the "Monterey Excursion" of Vincent and Berger, 1985), is a prominent feature in oceanic stable isotope records (Woodruff and Savin, 1991). Together with the deposition of large amounts of organic rich sediments along the circum-Pacific margins this gave support to the hypothesis that increased burial of organic carbon drove atmospheric CO_2 drawdown, thereby reducing the greenhouse effect (Vincent and Berger, 1985; Woodruff and Savin, 1991; Flower and Kennett, 1994). Another sink for CO_2 is increased silicate weathering. The middle Miocene cooling has, among others, been related to the uplift of the Tibetan Plateau (e.g. Raymo and Ruddiman, 1992), thereby increasing silicate weathering, but recent work by Wan et al. (2009) suggests that warm and humid conditions during the MCO caused a global increase in erosion. Current hypotheses suggest that the increase in $\delta^{13}C$ in the marine realm is caused primarily by increased organic carbon sequestration on the continents which would be in agreement with coeval lignite deposits worldwide (Diester-Haass et al., 2009).

Changes in ocean circulation patterns have been mentioned as another important long-term factor in cooling the Antarctic region. Several authors proposed that the closure of the Tethys seaway, linking the Atlantic and the Indian Ocean through the proto-Mediterranean (Fig. 2), could have decreased meridional heat transport to high southern latitudes allowing cooling of Antarctic surface waters and expansion of the EAIS (e.g. Woodruff and Savin, 1989; Flower and Kennett, 1995; Ramsay et al., 1998). However, a direct relationship between the Middle Miocene Climate Transition and the closure of the Tethys seaway has so far never been proven (e.g. Hüsing et al. 2008; Smart et al., 2007). Many attempts have been made to date the closure more accurately, but the lack of properly datable sediments, and complex processes involved in the convergence of the Eurasian- and African-Arabian plates complicate reconstructions of the closure. The timing of the closure of the Tethys seaway is thus still elusive and estimates range from late Oligocene to late middle Miocene. Mammal migrations from ~18 Ma onwards (e.g Rögl, 1999; Wessels, 2009) suggest that the connection was nearly, if not completely, closed well before the onset of the MMCT.

1.2 The Middle Miocene Climate Transition in the Mediterranean

The climatic history of the semi-enclosed Mediterranean started after the disconnection to the Indian Ocean, most probably before the onset of the Miocene Climatic Optimum. Water exchange was only with the Atlantic and, depending on the fresh water budget, an anti-estuarine or an estuarine circulation would have developed (Fig. 3; Karami et al., 2009). With the near landlocked physiography the Mediterranean's buffering capacity reduced, which increased the basin's sensitivity to climatic change (Gladstone et al., 2007; Rohling et al., 2009; Karami et al., 2009). Moreover, the geographical position of the Mediterranean, located on the boundary between the subtropical/monsoon regime of Africa and the temperate westerlies of Europe, means that the basin is influenced by changes in both these systems (Rohling et al., 2009). This makes the Mediterranean an excellent site to study past changes in climate.

The frequent occurrence of dark organic-rich layers (sapropels) in Mediterranean sediments has been related to intensified monsoon activity and westerly moisture flow during periods of maximum summer insolation correlated to variations in the eccentricity, obliquity and precession (Rossignol-Strick, 1983; 1985; Hilgen, 1991a, b; Hilgen et al., 1995; Lourens et al., 1996). The deposition of sapropels reflects most likely an increase in marine productivity and a restriction in ventilation, caused by increased supply of freshwater into the Mediterranean basin (for reviews on sapropels see Rohling et al., 1994; Cramp and O'Sullivan, 1999; Rohling et al., 2009).

Rhythmic sedimentary alternations in marine successions potentially allow astronomical tuning, which increases the age control of important environmental changes. Despite extensive studies on late Neogene sedimentary sequences (e.g. Hilgen et al., 2000; Wehausen and Brumsack, 2000; Turco et al., 2001; Hüsing et al., 2009), less work has been done on the Mediterranean middle Miocene. This is partly the consequence of DSDP regulations which did not allow drilling through the Messinian evaporites. Marine outcrops on land are therefore currently the only place to study the early history of the semi-enclosed Mediterranean.

Sediments from the Adriatic coast near Ancona (Italy) and from the Maltese Islands (Malta and Gozo) (Fig. 2) are the subject of this thesis as they record the Middle Miocene Climate Transition in the Mediterranean. This thesis aims to relate global climate change to observed environmental changes in the Central Mediterranean and to improve the age models for this enigmatic time interval.

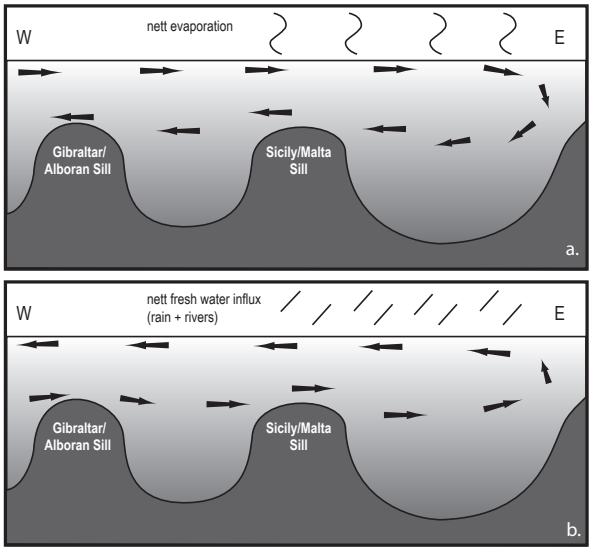

Figure 3. Simplified view of the general circulation patterns in the Mediterranean across an East-West transect. Today, a negative fresh water budget causes an anti-estuarine circulation (a) with Atlantic surface water inflow and deeper outflow of Mediterranean water (see Rohling et al., 2009; Karami et al., 2009). If the fresh water budget is positive, an estuarine circulation will develop (b).

2. Summary

Initially, this research started with the sections on Malta and Gozo, but the construction of an astronomically tuned age model for the older part of the section was complicated by the lack of good magnetostratigraphy and a not very straightforward cyclostratigraphy. With the recent tuning of the La Vedova beach section in Italy (Hüsing et al., 2010) and its upward extension high in the cliffs, an astronomically tuned age model for the MMCT in the Italien sections could be constructed. The new information could potentially help to solve the problems encountered on Malta.

Therefore, **Chapter 1** starts with the astronomical tuning of the newly discovered La Vedova High Cliff section. This section is one of the few Mediterranean sections covering the critical time interval of the MMCT. A robust astronomical tuning was constructed for the interval between 14.2 and 13.5 Ma, using geochemical element data and time series analysis. Bulk carbonate isotope records show a shift in $\delta^{18}O$ between ~13.92 and 13.78 Ma which can be related to the Mi3b oxygen isotope event. The onset of the $\delta^{13}C$ CM6 carbon excursion is dated at ~13.86 Ma. The results confirm the proposition that these events coincide with a ~405-kyr minimum in eccentricity and a node in obliquity amplitudes related to the ~1.2 Myr cycle. From 13.8 Ma onwards, distinct quadruplet cycles containing sapropelitic sediments are observed, suggesting a causal connection between the main middle Miocene cooling step and sedimentation and circulation in the Mediterranean.

Combining the La Vedova Beach and La Vedova High Cliff sections, a composite section was established, covering the interval between ~15.3 and 13.5 Ma. In **Chapter 2**, a high-resolution geochemical dataset is used to study the long-term development of insolation-controlled sedimentary cycles. Low bottom-water oxygen levels are inferred for the interval of the last phase of the Miocene Climatic Optimum where high sedimentation rates are related to high fluvial runoff and high organic fluxes. Regular enrichments in Ti/Al and Zr/Al suggest that eolian dust input becomes more significant from ~14.5 Ma onwards, which may evidence early aridification of northern Africa in the middle Miocene. Geochemically inferred dry-wet oscillations become especially pronounced after the major global cooling step at 13.8 Ma when Ti/Al and Zr/Al rich marls increase in thickness. The occurrence of sapropelitic layers in a basic cycle with a characteristic quadruplet structure points to periodically decreased bottom water ventilation. The increasing differentiation between sedimentary phases related to predominantly dry- and predominantly wet conditions, suggest that seasonal contrast increased after the MMCT. Especially high freshwater influx during summer insolation maxima may have triggered the onset of rhythmic sapropel formation after 13.8 Ma.

In **Chapter 3**, an astronomically tuned age model for the Upper Member of the Globigerina Limestone Formation (Maltese Islands) is presented, which has been constructed using high resolution stable isotope records. In addition, a revision of the tuning of the basal part of the Blue Clay Formation was made using new ages for bioevents from Chapter 1. The Upper Member of the Globigerina Limestone is now dated between ~14.95 and 13.76 Ma (± 0.02), although the possibility of a hiatus between 13.95 and 13.76 Ma could not be excluded. This could have implications for the Serravallian GSSP (Global Stratotype Section and Point), which is currently defined in this section. Benthic and planktic carbon isotope records show ~405 kyr maxima in $\delta^{13}C$, associated with the Monterey Carbon Excursion. The global middle Miocene cooling is reflected in the benthic oxygen isotope record, showing a ~0.6‰ increase (Mi3b) between ~13.95 and 13.76 Ma. Increased run-off after the climate transition probably caused a decrease in ventilation thereby inducing a divergence between the planktic and benthic isotope signals.

In **Chapter 4** benthic foraminiferal assemblages from the Maltese Islands have been studied to gain more insight in the effects of the Middle Miocene Climate Transition on Mediterranean paleoenvironments. In addition, geochemical- and isotope records have been used to trace environmental changes. Between ~14.95 and 13.9, benthic assemblages point to a mesotrophic and well-ventilated environment. The rapid increase in clay influx at the base of the Blue Clay Formation (~13.76 Ma) causes carbonate content to drop by more than 50%. Increased river run-off caused an increase in food availability and lower bottom water oxygen levels to which the benthic assemblage responded by an increase in infaunal taxa. Ongoing environmental changes related to restriction in circulation are inferred from the successional increase in infaunal species after the MMCT and the occurrence of the first sapropelitic sediments at 13.24 Ma.

Chapter 5 is a synthesis based on results from Chapters 1-4. In addition, an impression of the climate- and environmental changes in and around the Mediterranean before, during and after the MMCT is presented. Comparing the Central Mediterranean sites an increase in terrestrial influx is observed in the Adriatic (La Vedova) and on the Malta-Hyblean Plateau (Maltese Islands), which can possibly be related to the Middle Miocene Climate Transition. Precession controlled alternation between sediments enriched in eolian dust and the occurrence of sapropelitic sediments suggest that the African monsoon system was already operative in the middle Miocene. With the expansion of the East Antarctic Ice Sheet, climate belts possibly contracted and more modern climate conditions for the Mediterranean were established.

Chapter 1

Astronomical tuning of the La Vedova High Cliff Section (Ancona, Italy) – Implications of the Middle Miocene Climate Transition for Mediterranean sapropel formation

A. A. Mourik, J. F. Bijkerk, A. Cascella, S.K. Hüsing, F.J. Hilgen, L. J. Lourens and E. Turco

Submitted to Earth and Planetary Science Letters, in review

Abstract
Continuous marine successions covering the Middle Miocene Climate Transition (MMCT; ~15-13.7 Ma) are scarce and the lack of a high-resolution magnetobiostratigraphic framework hampers the construction of astronomically tuned age models for this time interval. The La Vedova High Cliff section, exposed along the coast of the Cònero Riviera near Ancona (Italy), is one of the few Mediterranean sections covering the critical time interval of the MMCT. Starting from an initial magnetobiostratigraphic age model, a robust astronomical tuning was constructed for the interval between 14.2 and 13.5 Ma, using geochemical element data and time series analysis. A shift in $\delta^{18}O$ of bulk sediment occurs between ~13.92 and 13.78 Ma and can be related to the Mi3b oxygen isotope event, reflecting the rapid expansion of the East Antarctic Ice Sheet in the Middle Miocene. The onset of the $\delta^{13}C$ CM6 carbon excursion is dated at ~13.86 Ma. Our results confirm the proposition that these events coincide with a 405-kyr minimum in eccentricity and a node in obliquity related to the ~1.2 Myr cycle. From 13.8 Ma onwards, distinct quadruplet cycles containing sapropelitic sediments are observed, suggesting a causal connection between the main Middle Miocene cooling step and sedimentation and circulation in the Mediterranean.

1. Introduction

One of the major Cenozoic cooling steps is the rapid expansion of the East Antarctic Ice Sheet (EAIS) in the Middle Miocene, referred to as the Mi3b isotope shift or event (Miller et al., 1991; 1996). This is reflected in several benthic oxygen isotope records, showing a shift of ~1‰ between ~13.9 and 13.8 Ma (Abels et al., 2005; Holbourn et al., 2005; 2007; Miller et al., 1991; 1996; Woodruff and Savin, 1991; Zachos et al., 2001a). The timing of this major isotope shift is supposedly controlled by long period orbital forcing (Abels et al., 2005; Holbourn et al., 2005; 2007). More specifically, the long-period node in obliquity related to the 1.2-Myr cycle, in close harmony with low eccentricity values related to the 405-kyr cycle (Abels, 2008), suppressed peak summers for a prolonged interval of time, favoring ice sheet growth (e.g. Billups et al., 2004; Coxall et al., 2005; Pälike et al., 2006; Zachos et al., 2001b). However, similar orbital configurations preceding the shift at ~13.8 Ma did not cause major growth of the EAIS, which suggests that the step occurred superimposed on a long-term cooling trend.

The notion of a causal connection between the orbital configuration and the Mi3b ice growth event is derived from the orbital tuning of cyclic marine successions (e.g. Abels et al., 2005; Holbourn et al., 2005). However, the existing tuned age models are still uncertain to some extent due to 1) the - potential - presence of hiatuses or condensed intervals as a result of major changes in ocean circulation and carbonate dissolution, and 2) the lack of sufficient magnetobiostratigraphic tiepoints to constrain the tuning (Holbourn et al., 2007).

Evidently, well-tuned sections with high-resolution isotope records are needed to further test the orbital forcing scenario for the major EAIS expansion in the middle Miocene. Recent work on the marine La Vedova beach section, located along the Adriatic coast in northern Italy, revealed a high potential for integrated magnetobiostratigraphic studies and astronomical dating for the interval between 15.3-14.1 Ma (Hüsing et al., 2010). In this chapter, we present an astronomical tuning for the upward extension of the La Vedova beach section, exposed in a new section situated high in the coastal cliffs and covering the interval from ~14.2 to ~13.5 Ma. Astronomical dating of this section, which incorporates the major step of EAIS expansion during the Middle Miocene Climate Transition (MMCT), is of crucial importance to further investigate the potential relation between orbital configurations and the onset of major ice growth events, and to reconstruct the influence of the Mi3b event on sedimentation and circulation in the Central Mediterranean. Unfortunately, a benthic isotope record can not be constructed due to the moderate to poor preservation of the foraminiferal carbonate. Instead, we established a bulk isotope record to detect the Mi3b isotope event and associated paleoenvironmental changes.

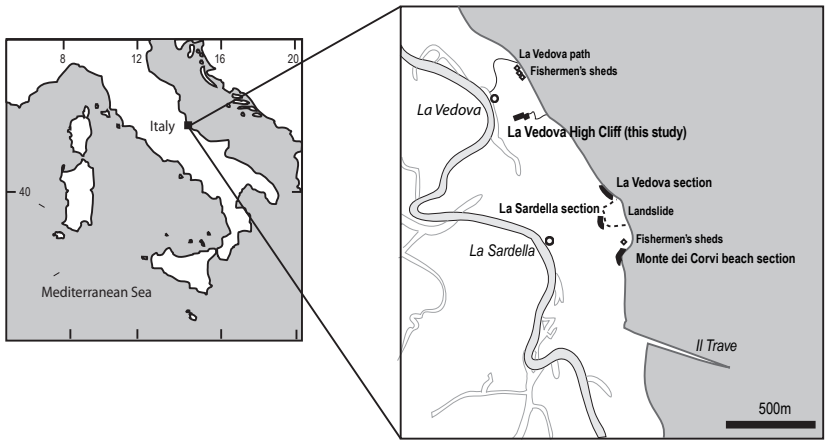

Figure 1: Location map of the La Vedova section (Hüsing et al., 2010) and La Vedova High Cliff section (this study) along the Adriatic coast in Italy.

2. Geological Setting and Section

One of the most complete Miocene marine successions in the Mediterranean is exposed along the Adriatic coast, between Ancona and the locality called Il Trave (Monte Cònero Riviera) (Fig. 1). The pelagic and hemipelagic carbonate succession is characterized by a rhythmic alternation of marly limestones and marls, while black organic-rich layers are found interbedded in the upper half of the succession (Montanari et al., 1997).

The middle - upper Miocene La Vedova and Monte dei Corvi beach sections have proven excellently suitable for integrated magnetobiostratigraphic studies, and radioisotopic and astronomical dating (Hüsing et al., 2007; 2010). The stratigraphic interval between the youngest levels of the La Vedova beach section and the base of the Monte dei Corvi section is covered by a landslide. This interval, which includes the Langhian/Serravallian boundary (Hilgen et al., 2009) and therefore the Mi3b isotope shift, is well exposed high in the cliffs directly below the village of La Vedova. Fieldwork on this poorly accessible location was carried out in May 2008, with the initial aim to recover the entire missing interval. Unfortunately, the upper part could not be reached as the outcrop becomes near-vertical.

The base of the recovered interval is the limestone bed that forms the top of the La Vedova beach section of Hüsing et al. (2010). The section ends ~2 m above the Cavolo sandstone bed. In total, 34.2 m has been logged and sampled in detail.

3. Lithology

The La Vedova High Cliff section (LVHC) consists of a rhythmic alternation of marls and limestones, varying in bed-thickness between 5 and 125 cm (Fig. 2). Based on field observations, two intervals, labeled A and B, have been distinguished of which the lower interval A (0-13.8 m) is divided in three subintervals. The first of these subintervals (0-4.5 m) is dominated by marls with thinly-bedded marly limestones. Limestones become more pronounced in the second subinterval (4.5-12 m), whereas the marls become thinner. These marls are mostly light grey, with the exception of some thicker darker colored marls at ~5.5, ~7.5 and ~12.5 m. Marls are hardly developed in the third subinterval (12-13.8 m).

Marls become significantly thicker from the base of interval B upwards. In addition, thin dark marl beds with a fresh greenish color start to appear often with a thin limestone bed below and a thicker well developed limestone bed on top. This strongly resembles the quadruplet structure of the basic precession-related cycles at Monte dei Corvi (Hilgen et al., 2003), where sapropels are intercalated in limestones. Because of their visual resemblance to sapropels, we will call these dark greenish layers 'sapropelitic'. The first distinct quadruplet cycle containing a sapropelitic layer is observed around 15 m. Finally, a turbiditic sandstone bed with a thickness of ~10 cm, known as the Cavolo bed (Montanari et al., 1997), is found at ~33 m.

4. Calcareous plankton biostratigraphy

4.1 Planktic foraminifera

Preservation of planktic foraminifera, being generally re-crystallized and often encrusted, varies from moderate to poor and is usually better in marls than in limestones. Moreover, washed residues mainly from limestone layers often consist of very abundant fragments of disaggregated sediment, resulting in a very scarce fossil content. Therefore, a semi-quantitative analysis of planktic foraminifer assemblages was performed on 79 samples only (out of 180), although a qualitative analysis was carried out on all samples. Counting was made on splits of the greater than 125 μm fraction of the washed residue, and is based on the number of a specific taxon in nine fields with a maximum of 30 specimens, using a rectangular picking tray of 45 fields. In case of abundant taxa, all the specimens present in the first field were counted even when they exceeded 30 individuals. The semi-quantitative analysis concentrated on 5 selected taxa, *Globigerinita glutinata*,

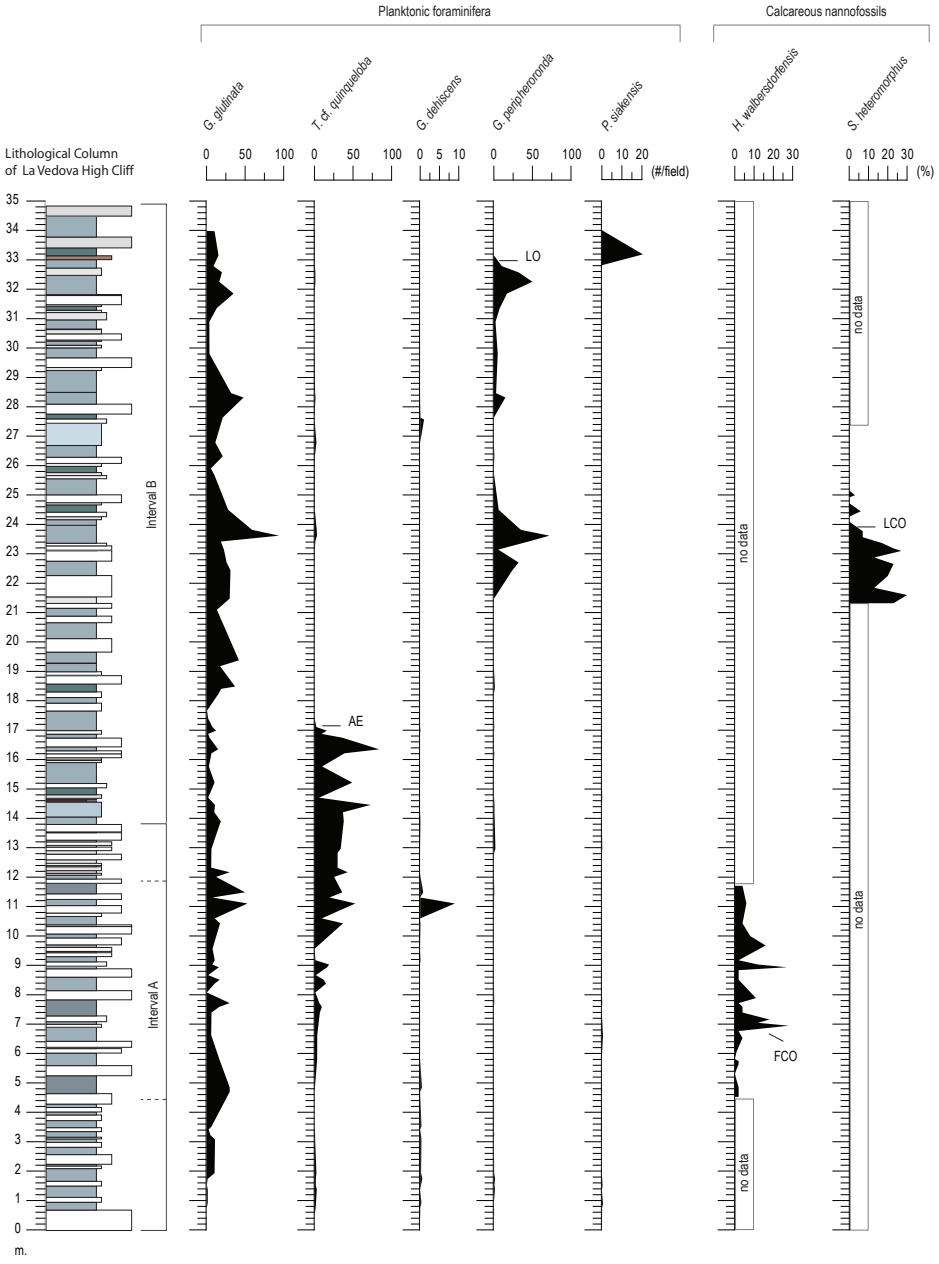

Figure 2: Lithological column of the La Vedova High Cliff section showing the alternations of grey marls and white limestones. The section has been subdivided in two intervals: Interval A (0-13.8 m) and Interval B (13.8-35 m). Interval A can be subdivided into three subintervals (see text for discussion). In Interval B characteristic quadruplets with dark sapropelitic sediments are observed at a level of 15, 18.5, 24-28 and 31-33.5 m. The Cavolo sandstone turbidite is found at 33 m. Next to the column, semi-quantitative abundance patterns are shown for the planktonic foraminiferal species *Globigerinita glutinata*, *Turborotalita* cf. *quinqueloba*, *Globoquadrina dehiscens*, *Globorotalia peripheroronda* and *Paragloborotalia siakensis,* and quantitative counts for the calcareous nannofossils *Sphenolithus heteromorphus* and *Helicosphaera walberdorfensis*.

Turborotalita cf. *quinqueloba*, *Globoquadrina dehiscens*, *Globorotalia peripheroronda* and *Paragloborotalia siakensis*, which show significant changes close to the Langhian/Serravallian boundary (Abels et al., 2005; Di Stefano et al., 2008; Hilgen et al., 2009). Distribution patterns of planktic foraminifera, expressed as number of specimens per field, are shown in Figure 2.

G. glutinata and *T.* cf. *quinqueloba* are present from the base of the section and show a turnover in abundance in the succession. *T.* cf. *quinqueloba* is characterized by a marked abundance decrease (indicated as Acme End) at 17.10 m; above this stratigraphic level *G. glutinata* shows an abundance increase, while *T.* cf. *quinqueloba* is rare and discontinuously present up the top of the section. *G. dehiscens* is nearly absent in the section except for an abundance peak at 11.1 m and second minor peak at 27.6 m. *Globorotalia peripheroronda* is scattered and rare from the base of the section up to about 22 m. Above this level it represents an important component of the assemblage and shows two intervals of increased abundance between ~22 and ~24 m, and ~31 and ~33 m. The last occurrence (LO) of this species is recorded at the top of the second abundance interval, at 32.99 m. *P. siakensis* is nearly absent in the entire succession except for an abundance peak at 33.17 m, just above the LO of *G. peripheroronda*.

The absence of *P. siakensis*, together with the occurrence of *Orbulina universa* (based on qualitative analysis), indicates that the base of La Vedova High Cliff section postdates the $Acme_b$ End of *P. siakensis*, dated at 14.234 (+/-0.005) Ma by Hüsing et al. (2010), and falls within the upper Langhian MMi5b Subzone of Di Stefano et al. (2008). The succession of planktic foraminiferal events in the La Vedova High Cliff section, i.e. the AE of *T.* cf. *quinqueloba*, the abundance peak of *G. dehiscens* , the LO of *G. peripheroronda* and the abundance peak of *P. siakensis*, is comparable with that recorded at Site 372 (DSDP Leg 42, Balearic basin) (Di Stefano et al., 2008), and in the San Nicola section on Tremiti Islands (Italy) and the Ras il Pellegrin section on Malta (Abels et al., 2005; Hilgen et al. 2009). At Ras il Pellegrin the AE of *T.* cf. *quinqueloba*, which falls within MMi5c Zone of Di Stefano et al. (2008), has been recorded just above the top of the oxygen isotopic shift Mi3b, which represents the guiding criterion for the Langhian/Serravallian boundary (Hilgen et al., 2009). Finally, the LO of *G. peripheroronda*, dated at 13.535 Ma (Hilgen et al., 2009), indicates that the topmost part of the section is referable to the lower Serravallian MMi6 Zone of Sprovieri et al.(2002)

4.2 Calcareous nannofossil biostratigraphy of the La Vedova High Cliff Section

A quantitative analysis of calcareous nannofossil assemblages was carried out to locate the stratigraphic position of the FCO (first common occurrence) of *Helicosphaera walbersdorfensis*, and the LCO (last common occurrence) and LO (last occurrence) of *Sphenolithus heteromorphus*. In total, 57 samples were studied for this purpose. Since the approximate position of the events was known, 34 samples were selected from the interval between 4.11 and 11.72 m, and 23 samples between 21.33 and 27.35 m. The analyses were performed with a polarized light microscope at 1250X magnification and on smear slides prepared following standard methodology (*Bown*, 1998).Quantitative data were collected using the methodology described by Di Stefano et al. (2008). A counting of 30 sphenoliths was performed to evaluate the abundance of *S. heteromorphus*, while 50 helicoliths were counted to quantify *Helicosphaera* species. The zonal assignment followed the scheme of Di Stefano et al. (2008) for the Langhian of the Mediterranean area. The quantitative patterns of selected taxa are shown in Figure 2.

Di Stefano et al. (2008) defined the FCO of *H. walbersdorfensis* at Site 372, as the level above which the taxon is continuously present with percentages higher than 10% of the total helicoliths. In the section we identified this event at 6.87 m, where the species reaches a percentage higher than 10% for the first time. The distribution pattern of *H. walbersdorfensis* above its FCO does not entirely satisfy the above definition. Nevertheless, our data are in good agreement with the data from a number of sections in the Northern Apennines (Fornaciari et al., 1996).

In the lower part of the interval between 21.33 and 27.35 m, the quantitative record of *S. heteromorphus* indicates percentages higher than 20% for this taxon. This high abundance suddenly drops to values lower than 10% at 23.45 m. Following Di Stefano et al. (2008) the LCO of *S. heteromorphus* should be placed at 23.53 m, about 2 m below its LO recorded at 25.11 m.

In terms of calcareous nannofossil biozones, the studied section encompasses the stratigraphic interval between the LCO of *H. waltrans* and the FCO of *Reticulofenestra pseudoumbilicus* corresponding to the MNN5b, MNN5c and MNN6a subzones of Di Stefano et al. (2008).

Summarizing, the La Vedova High Cliff section contains the upper Langhian to lower Serravallian, and the succession of calcareous plankton events and their relative position, i.e. the FCO of *H. walbersdorfensis*, the AE of *T.* cf. *quinqueloba*, the LCO of *S. heteromorphus*, the LO of *G. peripheroronda* and the abundance peak of *P. siakensis*, suggests a continuous deposition across the Langhian/Serravallian boundary.

5. Palaeomagnetic results

5.1 Methodology

Oriented hand-samples were taken for palaeomagnetic purpose at about every 10 to 20 cm (about 6 to 8 levels per cycle). The close vicinity to the Monte dei Corvi section (Hüsing et al., 2007) and the stratigraphic connection with the older La Vedova Beach section (Hüsing et al., 2010) makes it plausible that the sediments contain the same magnetic mineral assemblage. Therefore, we followed the same experimental protocol as (Hüsing et al., 2007; 2010). Magnetic property analysis was carried out through isothermal remanent magnetization (IRM) acquisition on a suit of eleven selected samples. For palaeomagnetic purpose, one oriented specimen per sample level was thermally demagnetized and the natural remanent magnetization (NRM) was measured. The 42º tilt (bedding orientation 110/42; strike/dip) helped to distinguish primary (pre-tilt) from secondary (post-tilt) components and to recognize the present-day field overprint.

5.2 IRM acquisition

Following (Hüsing et al., 2009), a total of four components were fitted to the IRM acquisition curves (Fig. 3). Component 1 with low $B_{1/2}$ values and a relatively small contribution is related to thermal activation (Egli, 2004a; b; Heslop et al., 2004), and is physically meaningless. Following (Hüsing et al., 2009), components 2 and 3 with the same $B_{1/2}$ values but with different distribution parameters (DP) correspond to two greigite populations: Component 2 with a wider grain size distribution represents authigenic greigite and component 3 with a narrow distribution represents fine-grained (biogenic) greigite (Roberts, 1995; Vasiliev et al., 2008). Component 4 is fitted to high $B_{1/2}$ values and has a large DP. This component is responsible for the non-saturation of IRM in all samples and is interpreted as goethite. The fine-grained (biogenic) greigite component 3 is considered to be the magnetic remanence carrier of the NRM.

5.3 Magnetostratigraphy

Initial NRM intensities are low, ranging between 0.0018 and 0.0255 mA/m. Nevertheless, a sufficient number of samples (45%) resulted in a good quality of demagnetization, so that the direction of the characteristic remanent magnetization (ChRM) could be interpreted (Fig. 3). Poor demagnetization quality is especially found in the upper 14 meters of the LVHC section (~80 %).

Generally, a randomly oriented viscous NRM component was removed during thermal demagnetization to 100ºC (Fig. 3). Further heating revealed in some samples the removal of a second component between 100 and 140/160ºC (Fig. 3). Before tectonic correction, this component progressively decays towards the origin and is therefore interpreted as secondary post-tilt overprint. Further heating reveals the removal of a third component between 160 and 280ºC or up to 360ºC. After tectonic correction, this component shows dual polarity and is considered as primary component. The complex NRM behaviour indicates two partially overlapping components and it proved difficult to isolate the primary component from the secondary overprint resulting in slight non-antipodality of the NRM directions when plotted on the equal area projection (Fig. 3).

Plotting the ChRM directions of the third component in stratigraphical order reveals a distinct polarity pattern with three normal polarity and two reversed polarity intervals (Fig. 4a). The long normal polarity interval in the mid-part of the section is much thicker than the lower and upper normal and reversed polarity intervals. This suggests that the

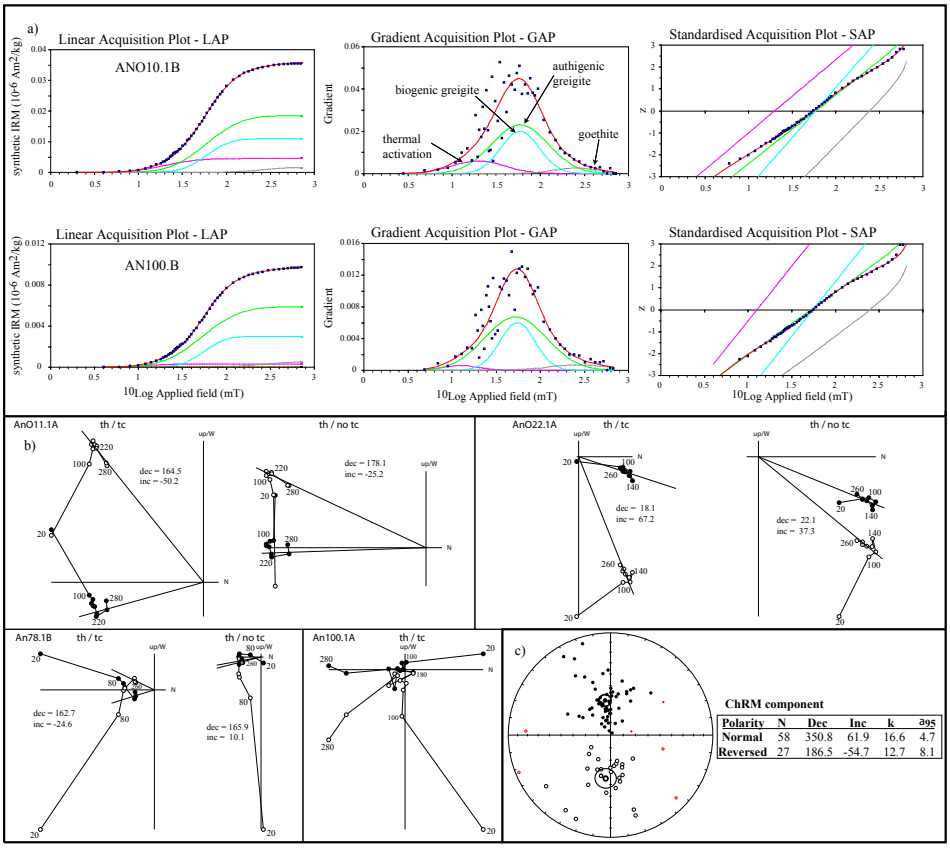

Figure 3. a) representative examples of isothermal remanent magnetization (IRM) acquisition curves and analysis of cumulative log-Gaussian (CLG) curves, which can be individually characterized by their saturation IRM (SIRM), remanent acquisition coercive force (B1/2), and dispersion parameter (DP) (Kruiver et al., 2001) ; b) representative thermal demagnetization diagrams of samples from the La Vedova High Cliff section; closed (open) points denote declination (inclination); numbers along demagnetization graphs denote temperature increments in degree Celsius (ºC); tc denotes tectonic correction, and; c) Plotted directions of the ChRM component on the stereonet showing a slight non-antipodality. Smaller (red) points indicate samples that were excluded using VanDamme cut-off. Mean declination and inclination directions are given in box, where N=number of samples, Dec=declination, Inc=inclination, k=Fisher's precision parameter, α95=radius of 95% confidence cone.

long normal interval is of significantly longer duration than the other polarity intervals. Since the LVHC section is the upward continuation of the La Vedova Beach section by Hüsing et al.(2010) which is correlated to the interval between C5Br and C5ACr of the Geomagnetic Polarity Time Scale (GPTS), the normal polarity interval at the base of the LVHC section can be unambiguously correlated to normal Chron C5ADn (Fig. 4a). Consequently, the long normal polarity interval correlates to C5ACn and the normal polarity interval at the top of the section to C5ABn. The LVHC section therefore ranges from the top of C5ADn to the approximate middle of C5ABn. This correlation is confirmed by the biostratigraphic constraints presented before.

An initial age model is based on the correlation of bio-events and magnetic reversals to the integrated magnetobiostratigraphic scale of ATNTS2004, showing that the section covers the interval between ~14.2 and 13.5 Ma (Fig. 4b). This age model reveals a slight reduction in sedimentation rate between 9 and 17 m and, in particular, a strong increase in sedimentation rate starting around 17 m. Average sedimentation rate in interval A is ~4 cm/kyr, whereas it is almost twice as high in Interval B.

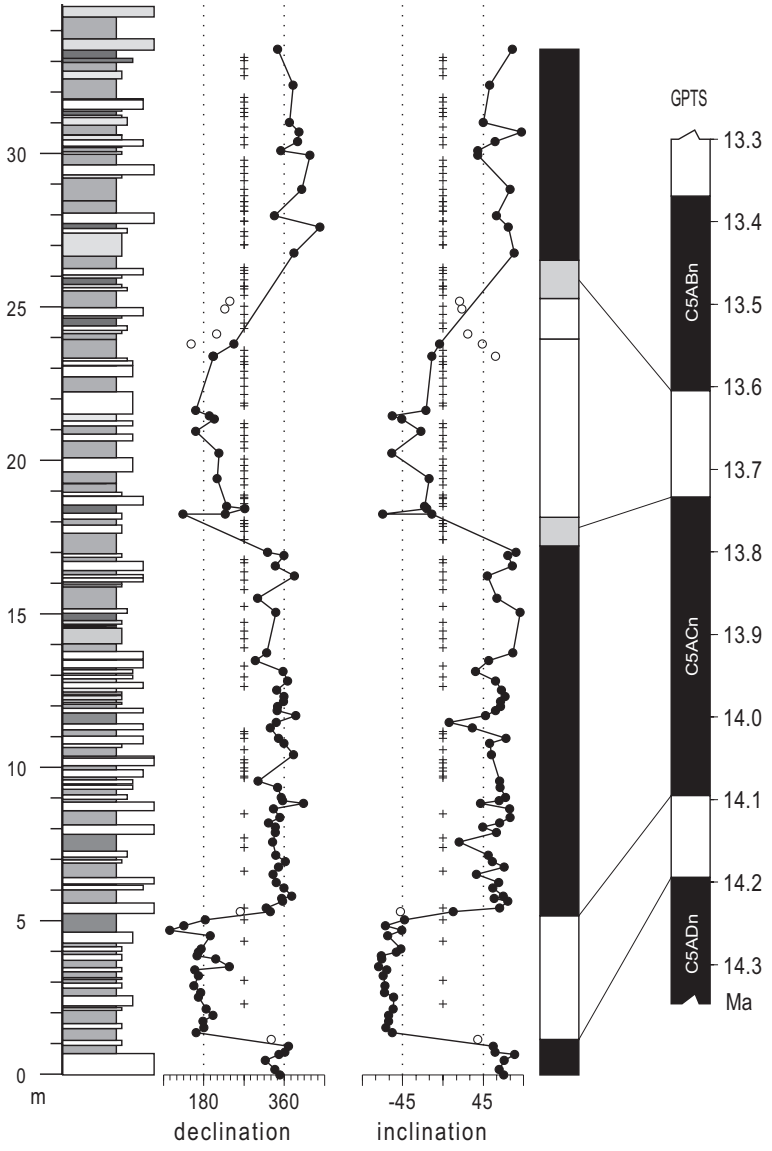

Figure 4: a) Magnetostratigraphy of the La Vedova High Cliff section and calibration to the polarity time scale of the ATNTS2004 [*Lourens et al.*, 2004]. Black (white) points denote reliable (uncertain) ChRM directions; crosses indicate unreliable ChRM directions, which have not been taken into account. In the polarity column, black (white) zones indicate normal (reversed) polarity intervals; grey zones are uncertain polarity intervals. The interval between 24 and 25m is characterized by poor quality thermal demagnetization but declination values are used to interpret normal polarity for this interval; b) Age-depth plot of the La Vedova High Cliff section. Black squares indicate the position of magnetic reversals and bioevents used for the initial age model. Magnetic reversals were initially correlated to the ATNTS2004 of Lourens et al. (2004). Crosses indicate tie-points used for the final tuning.

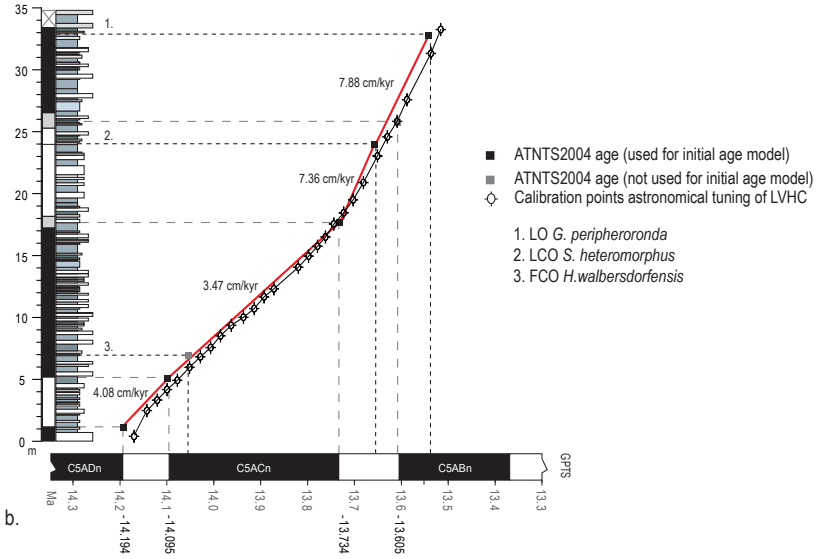

5.4 Magnetic susceptibility

Magnetic susceptibility (MS) reflects the abundance of magnetic minerals in the sediment and is a sensitive indicator of the marine sedimentary iron concentration (e.g. Ellwood et al., 2000; Hay, 1996; 1998). Fluctuations in MS can reveal variability in terrigenous sediment content since iron is mainly supplied from land (Jickells et al., 2005; Poulton and Raiswell, 2002).

Magnetic susceptibility of 340 samples was measured on a Kappabridge KLY-2. Measured susceptibility values were divided by the sample's weight, yielding the specific susceptibility, given in 10^{-8} m^3/kg. The specific magnetic susceptibility ranges from 0.30 to 5.97*10^{-8} m^3/kg, with an average of 2.63 *10^{-8} m^3/kg (Fig. 5a). Limestones are in general characterized by low values whereas the marls have relatively high values. More specifically, the highest values are attained in the darker marls and sapropelitic layers. Overall, the magnetic susceptibility is slightly higher in Interval A than in Interval B, despite the more marly character of the latter.

6. Geochemical proxies

6.1 Bulk Isotopes

Bulk isotope data were generated on 636 samples with an average sample distance of ~10 cm. Samples were oven-dried at 45 ºC for at least 48 h, and then powdered to homogenize, before they were measured on a SIRA-24 VG (vacuum generators) at Utrecht University. Results, in per mil (‰) relative to the Peedee Belemnite standard were corrected with international (IAEA-CO-1 and Utrecht in-house standard Naxos 45-125 µm, validated with NBS-18 and 19). Duplicate measurements of the Naxos standard every eight standards reveal an analytical error of less than 2%.

The most prominent feature of the bulk isotope curves is a distinct shift between ~9.5 and 18 m. Bulk $\delta^{18}O$ values gradually increase by ~0.7‰, while $\delta^{13}C$ shows a sharp step towards heavier values at ~12.7 m (Fig. 5a). From 13.8 m onwards, $\delta^{13}C$ and $\delta^{18}O$ values are relatively light in the sapropelitic layers, whereas the light-grey marls reveal heavier values. Limestones are generally characterized by relatively heavy $\delta^{13}C$ and $\delta^{18}O$ values compared to the marls. However, limestones in the quadruplets tend to be much lighter.

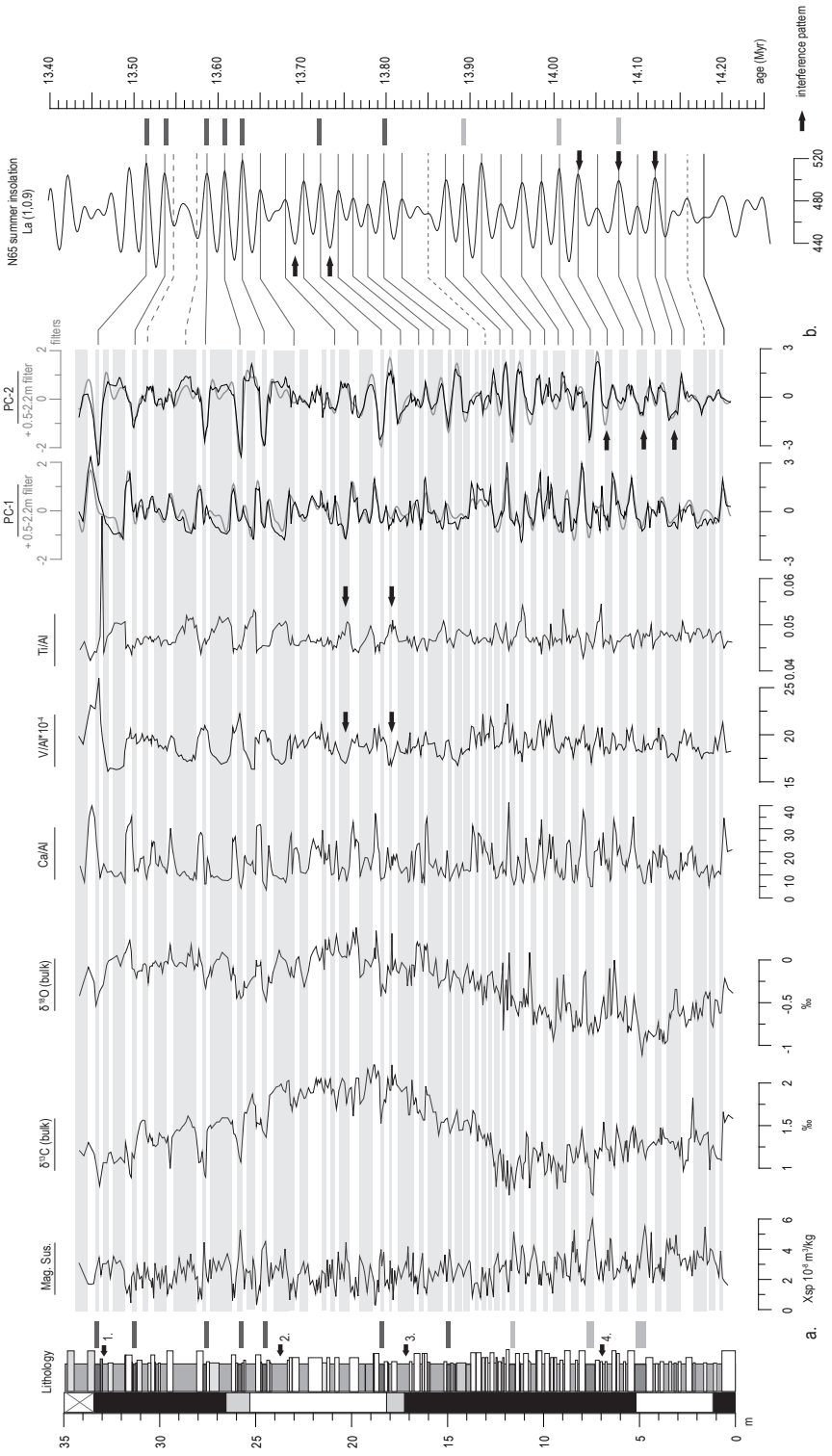
Lithology
Mag. Sus.
δ13C (bulk)
δ18O (bulk)
Ca/Al
V/Al*10-4
Ti/Al
PC-1
+ 0.5-2.2m filter
PC-2
+ 0.5-2.2m filter
filters
N65 summer insolation
La (1,0,9)
age (Myr)
interference pattern
a.
b.
m
Xsp 10-4 m3/kg
‰

«**Figure 5 :** a) Magnetic sucsceptibility, bulk isotopes, geochemical proxies and regression scores for the first two Principal Component Analysis axes. Dark marly layers and sapropelitic layers are indicated next to the lithological column as well as the positions of bioevents (1 = *G. peripheroronda* LO, 2 = *S. heteromorphus* LCO, 3 = *T.* cf. *quinqueloba* AE, 4 = *H. walbersdorfensis* FCO). Grey shading under proxy records corresponds to magnetic susceptibility maxima and Ca/Al minima. The filtered records (0.5-2.2m) of PC-1 and PC-2 are in grey. For discussion of PC-1 and PC-2 see text; b) Correlation of the La Vedova High Cliff section to the N65 summer insolation target curve of La2004(1,0.9). Astronomical tuning is based on cyclic patterns in Ca/Al, V/Al, Ti/Al and PC-2. Arrows indicate precession-obliquity interference pattern observed in the records and the isolation curve of La2004(1,0.9).

6.2 Geochemical element analysis (ICP-OES)

For geochemical element analysis, the same set of dried and powdered samples has been used as for the bulk isotope analysis. From each of the homogenized samples, ~125 mg was dissolved in 2.5 ml HF (40%) and 2.5 ml mixing acid (HNO_3 16.25% and $HClO_4$ 45.5%) and heated at 90 ºC in a closed vial for at least 8 hours. Samples were then dried by evaporating acids at 160 °C and subsequently dissolved in 25ml HNO_3 (4.5%). The resulting solutions were analyzed for a number of elements (Al, Ba, Ca, Co, Cr, Cu, Fe, K, Mg, Mn, Ni, P, S, Ti, V, and Zr) by a Perkin Elmer Optima 3000 ICP-OES at Utrecht University. Where needed the results were refined using in-house standards (ise-921). Relative precision and accuracy were established through duplicate analyses and standards and were better than 4% relatively for all elements except for Zr (<6%).

Cyclic patterns observed in the field are also prominent in several elemental records. The Ca/Al record will reflect the relative carbonate content with respect to the input of clay, assuming that most of the Ca present in the sediments is derived from calcium carbonate. Carbonate-rich intervals correspond to the limestone beds (Fig. 5a). Elemental/Al ratios show that V is relatively enriched in the limestone beds and sapropelitic layers, whereas Ti is relatively higher in the marls. This relationship is especially clear in the quadruplet-bearing interval between 24 and 28 m. The Cavolo sandstone turbidite at 33 m is low in carbonate but reveals extremely high values for Ti/Al.

6.3 Principal Component Analysis

Data reduction techniques like Principal Component Analysis (PCA) can be performed to present the most important aspects of a multivariate dataset in a small number of dimensions (Hammer and Harper, 2006). The components are orthogonal, linear combinations of the original variables that account for as much of the variance in the dataset as possible (see Hammer and Harper, 2006). The different components may be interpreted as environmental parameters that cause variability in the dataset, although in some cases this might be ambiguous.

In addition to the single elemental records, Principal Component Analysis (PCA) has been performed on the LVHC geochemical data. The sandstone turbidite at ~33 m has been excluded from analysis, to avoid extreme values not related to normal sedimentation patterns.

Results of the PCA are given in Table 1. The first axis explains 30.8% of the total variance and has high positive loadings for Ca/Al, Mn/Al, Ba/Al and V/Al. Negative loadings are found for Ti/Al and Zr/Al. Values close to zero contribute little to the axis. The pattern on this axis strongly resembles the Ca/Al record, which suggests that PC-1 reflects the marl-limestone alternation (Fig. 5a). The second axis explains 17.2% of the variance and is characterized by Zr/Al, P/Al, Ti/Al and Mg/Al on the positive side and Ni/Al and Co/Al, and in minor extent Cr/Al and V/Al, on the negative side. Enrichments in Ni/Al, Co/Al, Cr/Al and V/Al may point to reducing conditions and, in case of Ni/Al, the presence of organic matter (e.g. Tribovillard et al., 2006). The elements Ti and Zr are related to heavy minerals and are commonly used as proxy for eolian input.(e.g. Lourens et al., 2001; Wehausen and Brumsack, 2000). Clearly, the sapropelitic layers score high on the negative side of the axis, whereas the marls enriched in Ti and Zr are positive. The cyclic alternation of sediments associated with more arid periods marked by enhanced eolian input, and sediments associated with decreased bottom water ventilation are typical for deep marine successions in the Mediterranean Neogene (e.g. Nijenhuis et al., 1996; Schenau et al., 1999; Wehausen and Brumsack, 1999; 2000). The second PC-axis seems to reflect this characteristic signal well.

To reduce noise, a bandpass filter (0.5-2.2 m) has been applied to the PC records. Regular variations in PC-1 and PC-2 are now easy to detect, and show a more distinct cyclic pattern than the records of the individual elements. The width of the filter was selected after applying spectral analysis in the depth domain (results not shown).

Table 1: Component matrix for the first two axis of Principal Component Analysis

PC-1		PC-2	
Ca/Al	0.929	Zr/Al	0.602
Mn/Al	0.863	P/Al	0.564
Ba/Al	0.843	Ti/Al	0.489
V/Al	0.727	Mg/Al	0.474
P/Al	0.553	Ba/Al	0.231
Mg/Al	0.548	Ca/Al	0.206
Cu/Al	0.377	Fe/Al	0.145
Cr/Al	0.346	S/Al	0.090
Fe/Al	0.316	Mn/Al	0.086
Ni/Al	0.046	K/Al	0.077
Co/Al	-0.052	Cu/Al	-0.175
S/Al	-0.125	V/Al	-0.294
K/Al	-0.267	Cr/Al	-0.390
Zr/Al	-0.484	Co/Al	-0.660
Ti/Al	-0.695	Ni/Al	-0.774

7. Spectral analysis, orbital control and astronomical tuning

7.1 Spectral analysis in the time domain

To detect cyclic patterns in the elemental record, Blackman-Tukey spectral analysis of the AnalySeries program 1.2 (Paillard et al., 1996) was applied on the Ca/Al, PC-1 and PC-2 records in the time domain starting from our initial magnetobiostratigraphic age model with the magnetic reversal boundaries and the LCO of *S. heteromorphus* and LO of *G. peripheroronda* with their ATNTS2004 ages as tie points (Fig. 4b). All spectra reveal strong peaks in the precession band and somewhat weaker peaks in the obliquity band of the spectrum. In this respect, PC-2 provides the most convincing spectra with a clear precession component, and a well-defined peak at ~40 kyr (Fig. 6a). In addition, spectral analysis was carried out on the intervals A and B separately because of the different expression of the sedimentary cycles in these intervals. Precession-related peaks are dominant in both intervals whereas the obliquity-related peak is only clearly seen in the PC-2 spectrum of Interval A (Fig. 6a). Based on these results, we interpret the lithological- and proxy cycles recognized in the LVHC succession as driven by orbitally forced climate cycles. Considering the clear precession component in PC-2 we selected this record for the tuning.

7.2 Phase relations

Now that the orbital origin of the cyclic variations in the elemental proxy records is sufficiently proven, we can attempt to tune PC-2 to an astronomical target curve. To establish a detailed tuning, the phase relations between the elemental proxies and the selected astronomical target curve should be known. The 65°N summer insolation curve is widely used as tuning target in the Mediterranean Neogene (Hilgen et al., 1995; 2003; Laskar et al., 1993; Lourens et al., 1996; 2001; Lourens et al., 2004; Tuenter et al., 2003), because of the great similarities of this target curve with cycle patterns in both lithology and proxy records. The $La2004_{(1,0.9)}$ solution - with a present-day value of 1 for dynamical ellipticity and 0.9 for tidal dissipation (see Laskar et al., 1993) - was selected because of its excellent fit with the details of the cycle patterns. This was especially the case for patterns related to the interference of precession and obliquity in the older La Vedova Beach section (Hüsing et al., 2010). Characteristic for the upper sapropelitic layer-bearing interval B is the anti-phase relation between Ti/Al and V/Al,

with the sapropelitic layers being characterized by minima in Ti/Al and maxima in V/Al. These elemental patterns are similar to those normally found in the Mediterranean Neogene (e.g. Nijenhuis et al., 1996; Schenau et al., 1999; Wehausen and Brumsack, 1999; 2000). Therefore, a similar phase relation with Ti/Al maxima corresponding to insolation minima should be used for the tuning. Since the variability in V/Al and Ti/Al is well reflected in PC-2, PC-2 maxima will correspond to insolation minima as well.

7.3 Astronomical tuning

Starting point for the tuning is our initial age model based on the integrated magnetobiostratigraphy and the calibration of the magnetostratigraphy to the ATNTS2004 (Fig. 4b). The position of the LCO of *S. heteromorphus* is particularly helpful as it has been reliably astronomically dated at 13.654 Ma on Tremiti islands (Abels et al., 2005) where it is recorded below a group of three sapropels. This is similar to the position of the event below a distinct cluster of three sapropelitic layers (between 24 and 28 m) in our LVCH section. The interval with marked variations in Ti/Al, V/Al and thus PC-2, between 23 and 29 m can be correlated straightforwardly to the interval with high amplitude changes in the insolation curve associated with the 100-kyr eccentricity maxima around 13.6 Ma (Fig. 5b).

The next older interval between 17 and 21 m is characterized by relatively high amplitude variations and distinct cycles in elemental records and PC-2 and corresponds to the 100-kyr maximum at 13.7 Ma. The younger interval above, between 28 and 34 m, is characterized by thick marls, 6 limestone beds and 2 sapropelitic layers. Cycles in PC-2 are not very distinct except for two pronounced minima at 31.38 and 33.17 m, which correspond to the two sapropelitic layers. The LO of *G. peripheroronda* (32.99 m) has been dated at 13.535 Ma in the tuned San Nicola section on Tremiti islands (see Figures 7 and 8 in Abels et al., 2005), which suggests that the minima in PC-2 should be tuned to the 100-kyr maximum around 13.52 Ma. At La Vedova, at least two cycles can be detected in PC-2 between the LO of *G. peripheroronda* and the sapropelitic layer at ~27.8 m, while the lithology, Ca/Al and PC-1 suggest that three cycles are present. Starting from the reliable tuning of the sapropelitic layer at ~27.8 m, these cycles can thus be tuned in two different ways. Here we prefer to tune the two distinct PC-2 minima at 31.38 m and 33.17 m to the prominent insolation maxima at 13.54 and 13.52 Ma, respectively. However, an upward shift in the tuning by one precession-related cycle can not be excluded. The presence of the short *P. siakensis* peak at 33.17 m, i.e. directly above the *G. peripheroronda* LO, provides an additional check on the tuning as a similar peak has also been found in the San Nicola section (Abels et al., 2005).

Low variability in the elemental records and absence of distinct quadruplets between 16 and 17, 21 and 23 and 29 and 31 m are consequently related to the ~100-kyr eccentricity minima at 13.77, 13.67 and 13.56 Ma, respectively.

The single sapropelitic layer at ~15 m is correlated to the relatively pronounced insolation maximum at 13.80 Ma. Below follows a thinly-bedded limestone interval (12 to 13.8 m) in which individual cycles are difficult to distinguish in the lithology and geochemical records. As in the upper part of the LVHC section, the lack of well developed marls seems to be related to minima in the 100-kyr eccentricity cycle. Crucial in this problematic interval are the three distinct maxima in PC-2 between 11 and 13 m, which we tuned to the three insolation minima between 13.85 and 13.90 Ma. This is consistent with the pattern and tuning of minima in PC-1.

The minima in PC-2 between 11 and 2 m can be tuned to successively older insolation maxima. Obliquity-precession interference patterns observed in the insolation curve between 14 and 14.2 Ma are also evident in both PC-2 and magnetic susceptibility (Fig. 5a). This distinct pattern confirms the tuning of the cycles between 2 and 11 m. However, this fit critically depends on the selection of the astronomical solution and, in particular, on the values adopted for dynamical ellipticity and tidal dissipation in the solution. Like in the older La Vedova Beach section (Hüsing et al., 2009), the $La2004_{(1,0.9)}$ solution resulted in a very good to excellent fit with the detailed cycle patterns observed in the proxy records (Figure 5a). The limestone at the base of the section is the same bed as the uppermost limestone bed logged at La Vedova beach, and is tuned to the insolation minimum of 14.170 Ma (Hüsing et al., 2010).

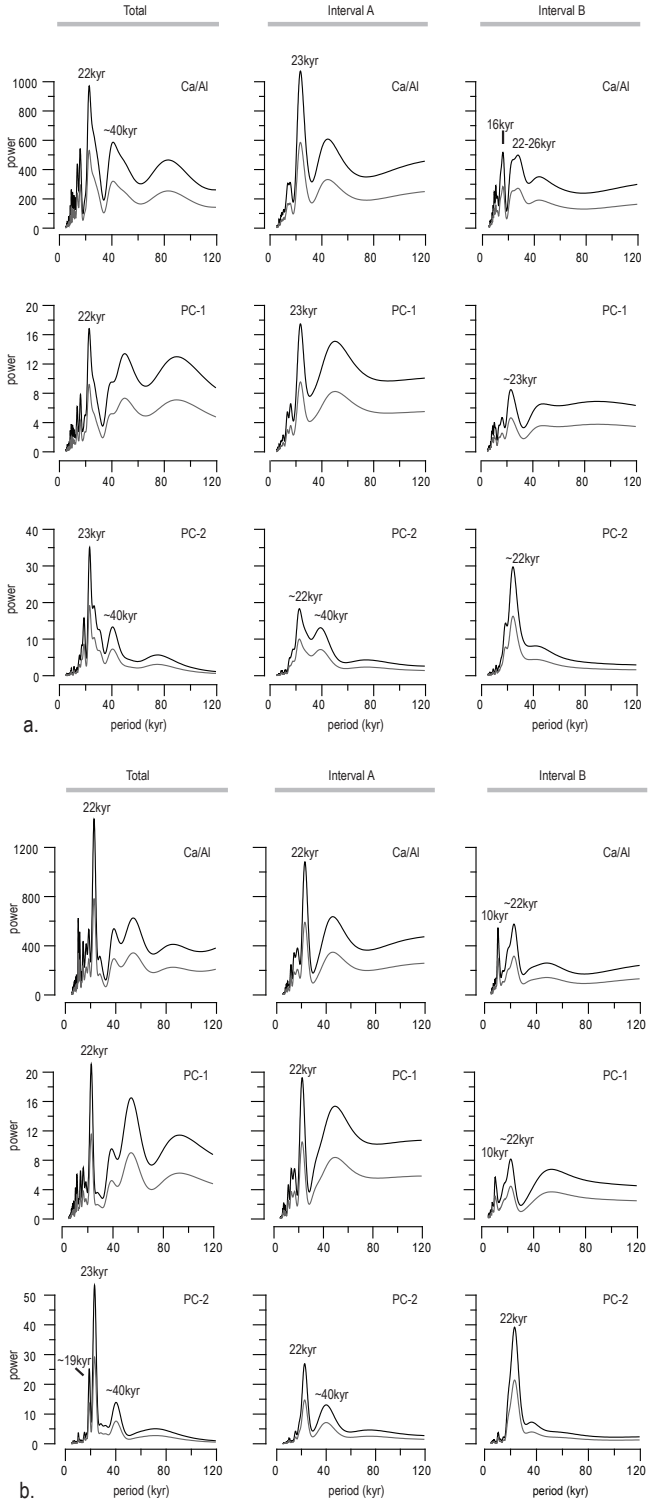

Figure 6: Blackman Tukey power spectra of Ca/Al, PC-1 and PC-2 calculated with the Analyseries Program (Paillard et al. 1996). Spectra are shown in the time domain, using the initial age model (a), and the tuned age model (b) to calculate the time series. For all series the figures on the left show the results for the entire section, whereas spectra for sub-interval A and B are presented in the middle and to the right. The lower 90% confidence limit for each spectrum is shown in grey.

7.4 Spectral and wavelet analysis

The tuning to the insolation target curve has resulted in a high-resolution age model for the entire LVHC section and can be used to calculate astronomical ages for the reversal boundaries and calcareous plankton events (Table 2). The age model is also used to generate new time series of the proxy records.

To test our astronomical tuning we run spectral analysis on the tuned time series. If the tuning is correct, then all spectral peaks should be well-defined (above the 90% confidence level) corresponding to the periods of orbital precession, obliquity and eccentricity. On the other hand, noise in the data should be significantly reduced. The time spectra indeed reveal the strong influence of precession. Obliquity is to somewhat lesser extent recorded and is only present in Interval A, most clearly so in the PC-2 spectrum (Fig. 6b) . The PC-1 spectrum of Interval B reveals an extra ~10 kyr peak that reflects the quadruplet structure of the precession-related basic cycles.

To track the spectral characteristics and frequency behavior in the time domain in more detail, we also applied wavelet analysis on the tuned PC-2 series. The wavelet plot reveals the dominance of the precession-related component, the bundling of this component in clusters related to amplitude modulation by the ~100-kyr eccentricity cycle (from ~14 Ma onwards), and the additional but admittedly weak presence of an obliquity-related component between 14.2 and 14.0 Ma (Fig. 7a). Besides, the wavelet of PC-2 in the depth domain is shown to demonstrate that the 100-kyr clustering of the precession-related is not an artifact of the tuning (Fig. 7b). The wavelet in depth reveals the clusters of the basic precession-related cycles as well as the increase in cycle thickness towards the top of the section as a consequence of the increased sedimentation rate.

In addition, we applied wavelet analysis on the tuned bulk isotope time series (Fig. 7c and d). The $\delta^{13}C$ wavelet plot reveals a weak obliquity related component between 14.2 and 14.0 Ma, a weak 100-kyr eccentricity related component between 14.0 and 13.5 Ma, and a strong precession related component around 13.62 Ma. The $\delta^{18}O$ wavelet plot does not provide much evidence for astronomical forcing, apart from a precession related signal around 13.62 Ma.

8. Discussion

8.1 Astronomical ages of magnetic reversals and bioevents

The tuning of the La Vedova High Cliff succession is an important step in closing the Middle Miocene gap in the astronomical calibration of cyclic proxy records with an integrated magnetobiostratigraphy. Based on this tuning, astronomical ages have been calculated for the magnetic reversals and calcareous plankton bio-events; they are compared with the ATNTS2004 ages in Table 2. The LVHC ages for C5ABr and C5ACN reversals are in very good agreement with the ATNTS2004 ages. The LO of *G. peripheroronda,* positioned just below the influx of *P. siakensis*, is ~17 kyr younger than in the ATNTS2004. This results from the tuning of the correlative cycles in the San Nicola section on Tremiti Islands one precession cycle younger, the different phase relation applied, and the use of the $La2004_{(1,1)}$ instead of $La2004_{(1,0.9)}$ (Figs. 7 and 8 in Abels et al., 2005) The ages of the two oldest reversals, C5ACn(o) and C5Dn(y), and the *H. walbersdorfensis* FCO are younger by ~25 kyr. These age differences may result from the fact that the ATNTS2004 reversal ages in this interval lack direct astronomical calibration being based on linear interpolation of seafloor-spreading rates (Lourens et al., 2004).

8.2 The Mi3b and CM6 events in bulk isotopes

The shift of ~ 0.7‰ towards heavier values in bulk $\delta^{18}O$ in the LVHC section is astronomically dated between 13.92 and 13.78 Ma (Fig. 8). This shift is interpreted as the expression of the major middle Miocene ice sheet expansion, referred to as the Mi3b event (Miller et al., 1991; 1996). In open ocean records from the Pacific and the Atlantic, the major shift in $\delta^{18}O$ is astronomically dated between 13.87 and 13.84 Ma (Holbourn et al., 2005; 2007, Raffi et al., 2006), which suggest a more rapid transition than in the Central Mediterranean. However, preservation of calcareous microfossils in La Vedova is poor and, in addition, bulk records are strongly influenced by the faunal composition. Therefore, a duration of 140 kyr for the isotope shift may not be representative.

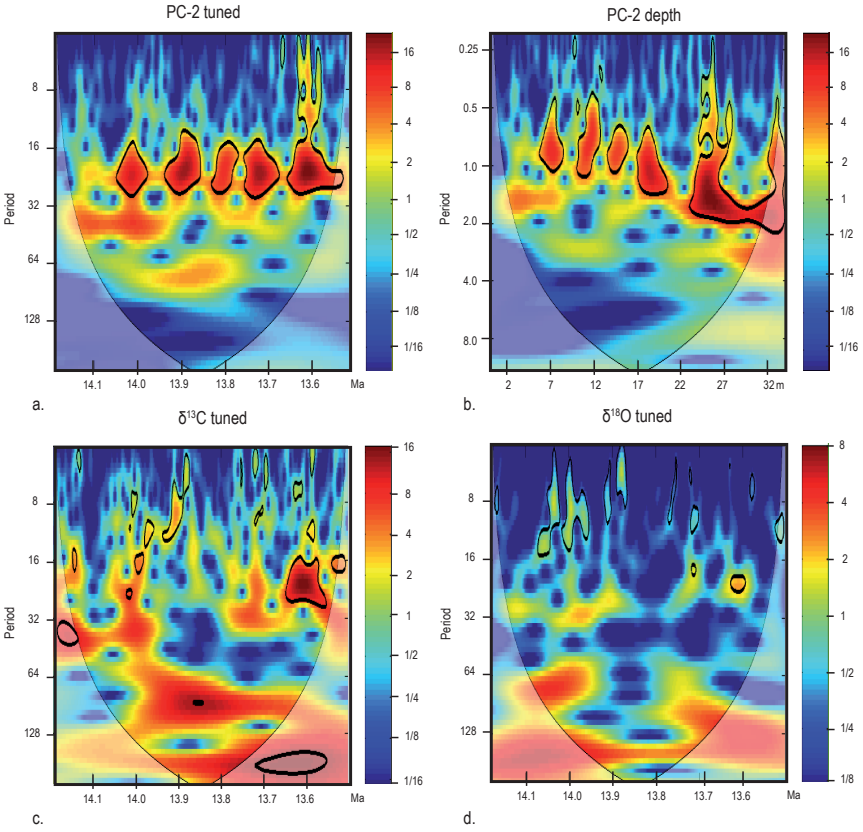

Figure 7: Wavelet spectra of a) PC-2 time series , b) PC-2 in depth, c) $\delta^{13}C$ time series, and d) $\delta^{18}O$ time series, calculated with the tuned age model. Spectrum of the tuned PC-2 shows a strong precession signal and obliquity in the older part (14.1-13.95 Ma); $\delta^{13}C$ reveals obliquity control and 100-kyr eccentricity. Around 13.65 Ma, precession is dominant and related to the presence of sapropelitic layers.

The pronounced step in bulk $\delta^{13}C$ at LVHC is astronomically dated at 13.86 Ma and can be linked to the onset of the CM6 carbon isotope maximum (Holbourn et al., 2007; Woodruff and Savin, 1991). The increase at 13.86 Ma is in good agreement with data from the Pacific and equatorial Atlantic (Ceara Rise, N.J. Shackleton, unpublished data; Holbourn et al., 2005; 2007)

Bulk isotope records from the Maltese Islands (Central Mediterranean) show the onset of CM6 simultaneous with the Mi3b shift (~0.6‰) at 13.82 Ma (Abels et al., 2005). The offset of ~40-kyr with respect to the open ocean records is probably due to uncertainties in the tuning of Malta (see discussion in Abels et al. 2005). A detailed comparison of middle Miocene isotope records and tunings will be made in a separate paper in which the benthic isotope records of Malta are presented.

The spectral characteristics of $\delta^{13}C$ in the time domain as revealed by wavelet analysis, with an obliquity control between 14.2 and 14.0 Ma and a precession-eccentricity control for the interval younger than 13.8 Ma (Fig. 7c), is different from that observed in the open ocean (e.g Holbourn et al., 2007), suggesting that it reflects a regional rather than a global signal. Shifts towards lighter $\delta^{13}C$ values in the sapropelitic layers in the LVHC section have been related to the dominantly precession-induced regional climate oscillations, and the fluvial input of continental-derived isotopically light carbon (Van der Zwaan and Gudjonsson, 1986). In fact, this may explain both the precession as well as the obliquity related signal in $\delta^{13}C$.

Table 2: Astronomical ages for magnetic reversals and bioevents between 14.17 and 13.50 Ma based on our astronomically tuned age model for the La Vedova High Cliff section.

Magnetic reversals	position (m)	±	age (Ma)	±	ATNTS2004	difference
C5ABn(o)	26.57	0.24	**13.608**	0.011	13.605	-0.003
C5ABr(y)	25.32	0.10				
C5ABr(o)	18.19	0.11	**13.739**	0.013	13.734	-0.005
C5ACn (y)	17.25	0.21				
C5ACn (o)	5.19	0.13	**14.070**	0.003	14.095	0.025
C5ADn (y)	1.16	0.23	**14.163**	0.004	14.194	0.031

Bio-events	position (m)	±	age (Ma)	±	ATNTS2004	difference
P. siakensis (short influx)	33.17	0.33	**13.516**	0.004		
G. peripheronda LO	32.99	0.19	**13.518**	0.002	13.535	0.017
S. heteromorphus LCO	23.53	0.10	**13.643**	0.001	13.655	0.012
T. cf *quinqueloba AE*	17.10	0.06	**13.751**	0.001		
H. walbersdorfensis	6.87	0.09	**14.026**	0.003	14.053	0.027

The tuning of LVHC confirms the relation between the major cooling step and the node in the 1.2 Myr obliquity cycle and a 400-kyr minimum in eccentricity (Fig. 8). Reduced amplitudes of obliquity and precession (i.e., at times of eccentricity minima) might prevent significant melting of the ice sheets during summer (e.g. Billups et al., 2004; Coxall et al., 2005; Pälike et al., 2006; Zachos et al., 2001b). A similar relation between oxygen isotope excursions, and nodes in the ~1.2 Myr obliquity cycle combined with minima in eccentricity has also been reported for the Mi1, Mi5 and Mi6 oxygen isotope events (Billups et al., 2004; Pälike et al., 2006; Turco et al., 2001; Zachos et al., 2001b). However, unraveling such relationships critically depends on the robustness of the astronomical tuning.

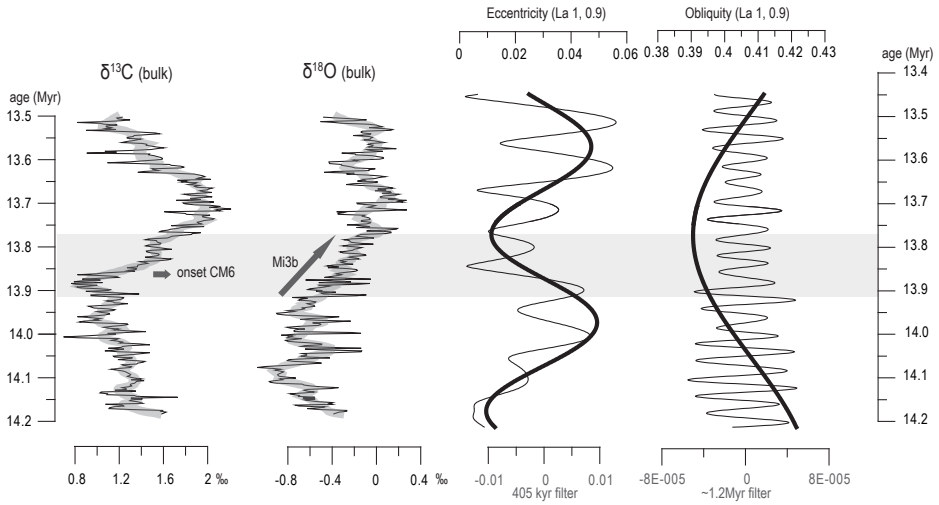

Figure 8: Bulk isotope records of the La Vedova High Cliff section in the time domain and correlation to eccentricity and long period obliquity. The positive shift in $\delta^{13}C$ at 13.86 Ma represents the onset of CM6 (Woodruff and Savin, 1991), which coincides with the positive shift of ~0.7‰ in $\delta^{18}O$, known as Mi3b (Miller et al., 1991;1996). The shift in $\delta^{18}O$ has its onset around 13.92 Ma and terminates at 13.78 Ma (grey band). Our age model confirms the relation of the major cooling step to a node in the 1.2 Myr obliquity cycle and a 400-kyr minimum in eccentricity.

8.3 Quadruplets and sapropelitic layers in LVHC

One of the most remarkable features in the lithology is the presence of quadruplets and sapropelitic layers in the upper part of the LVHC section. The oldest sapropelitic layer in a quadruplet is found at 15 m and has been astronomically dated at 13.80 Ma. It corresponds to the increase in sedimentation rate (Fig. 4b) and the onset of the strong and consistent anti-phase relationship between Ti/Al and V/Al. Moreover, it occurs directly at the top of the level that corresponds to the Mi3b isotope shift. Although precession induced changes in geochemical elements are also found at older levels, this close temporal relation indicates a possible causal connection between the Mi3b and the (first) occurrence of sapropelitic layers in quadruplets.

The oldest sapropelic layers in other Mediterranean sections postdate the level of the Mi3b as well. The oldest chondrites in the Ras il Pellegrin section on Malta, indicative of reduced bottom water oxygenation, occur at ~13.75 Ma, whereas the first sapropel with an astronomical age of ~13.23 Ma is much younger. On Tremiti Islands, the oldest reddish bed in the San Nicola section, considered to be the equivalent of a sapropel, is younger than the Mi3b event and has been dated 13.65 Ma (Abels et al., 2005). No such reddish layers are found on the nearby island of Cretaccio, where sediments older than 14.2 Ma are exposed (*Di* Stefano et al., 2008; Russo et al., 2007). The oldest sapropel in the classical Giammoia section on Sicily closely coincides with or slightly predates the LO of *S. heteromorphus* (See Figure 12 in De Visser, 1991), and thus directly postdates the Mi3b event as weAs long as no sapropels are recovered from sediments older than ~13.8 Ma, we suggest that the MMCT has been the trigger for the onset of sapropel formation in the Mediterranean. Apparently, the Mediterranean became more sensitive to record the dominantly precession induced climate oscillations since the growth of the East Antarctic Ice Sheet at ~13.9 Ma. Whether increased sensitivity of the Mediterranean basin is related to the glacio-eustatic sea-level fall of ~40-50 m associated with the rapid expansion of the East Antarctic Ice Sheet (e.g. John et al., 2004; Westerhold et al., 2005) or to climatic changes as a consequence of the cooling (e.g. John et al., 2003; Kender et al., 2009) is at present not clear.

9. Conclusions

An astronomical age model can be constructed for the La Vedova High Cliff section and used to assign astronomical ages to magnetic reversal boundaries and biostratigraphic events in the Mediterranean for the interval between ~14.2 and 13.5 Ma. In addition, this age model has been used to date major shifts in bulk carbonate $\delta^{18}O$ and $\delta^{13}C$ which correspond to the Mi3b and CM6 isotope events in the open ocean. Our results are consistent with previous findings that both isotopic events are related to a minimum in the 400 kyr cycle of eccentricity and a minimum in obliquity amplitudes related to the 1.2 Myr cycle. The middle Miocene cooling step is furthermore reflected in an increase in sedimentation rate and the occurrence of sapropelitic layers in basic precession-controlled quadruplet cycles typical of the Mediterranean late Neogene.

Acknowledgements

The authors thank Geert Ittmann, Helen de Waard, and Arnold van Dijk. Furthermore we acknowledge the Darwin Center for Biogeosciences for financial support.

Chapter 2

Onset of orbitally induced dry-wet climate oscillations in the Mediterranean during the Middle Miocene Climate Transition

A. A. Mourik, S. K. Hüsing, F. J. Hilgen, G. J. Reichart and T. J. Kouwenhoven

Abstract
Marine sediments, exposed along the coastal cliffs near Ancona (Italy), provide a unique middle Miocene sequence ranging from 15.3 to 13.5 Ma, thereby encompassing the Middle Miocene Climate Transition (~15-13.7 Ma). A high-resolution geochemical dataset is used to study the long-term development of insolation controlled sedimentary cycles. Bottom water dysoxia and occasional anoxia is inferred for the interval of the Miocene Climatic Optimum (17-15 Ma) where high sedimentation rates are related to high fluvial runoff and organic fluxes. At the onset of the Middle Miocene Climatic Transition (~15 Ma), sedimentation rates drop and the internal cycle structure becomes complex. Basin ventilation seems to ameliorate, since geochemical data do not suggest dysoxia. Regular enrichments in Ti/Al and Zr/Al point to more significant eolian dust input from ~14.5 Ma onwards, which may evidence early aridification of northern Africa in the middle Miocene. Geochemically inferred dry-wet oscillations become especially pronounced after the major global cooling step around 13.8 Ma, when Ti/Al and Zr/Al rich marls increase in thickness. The occurrence of sapropelitic layers in a basic cycle with a characteristic quadruplet structure points to decreased bottom water ventilation. The increasing differentiation between sedimentary phases related to predominantly dry- and predominantly wet conditions suggest that seasonal contrast increased after the MMCT. Especially high freshwater influx during insolation maxima may have triggered the onset of rhythmic sapropel formation from 13.8 Ma onwards.

1. Introduction

The middle Miocene is a key period in Cenozoic climate history, as Earth's climate changed from the warm Miocene Climate Optimum (17-15 Ma) to an interval of global climatic cooling between ~15 and 13.7 Ma. The rapid expansion of the East Antarctic Ice Sheet (EAIS), around 13.8 Ma, referred to as the Mi3b event in oxygen isotope records (Miller et al., 1991; 1996), is one of the major cooling steps in the Middle Miocene climate evolution (Abels et al., 2005; Flower and Kennett, 1994; Holbourn et al., 2005; 2007; Miller et al., 1991; Shackleton and Kennett, 1975; Shevenell et al., 2004; Woodruff and Savin, 1989; Zachos et al., 2001a). With the expansion of the EAIS, increased meridional temperature gradients and major environmental changes have been inferred from numerous Middle Miocene proxy records (e.g. Böhme, 2003; Flower and Kennett, 1994; Mosbrugger et al., 2005; Shevenell et al., 2008; Smart et al., 2007; Van der Meulen and Daams, 1992). Marine records recovered from the Mediterranean show changes in circulation patterns and sedimentation rates across the critical time interval of ice sheet expansion (Abels et al., 2005; Bellanca et al., 2002; Gebhardt, 1999; Jacobs et al., 1996; John et al., 2003; Mourik et al., in review).

In addition, the collision of the Arabian and Eurasian plates and the closure of the Tethys Seaway in the early to middle Miocene (Harzhauser et al., 2007; Harzhauser et al., 2002; Hsü and Bernoulli, 1978; Okay et al., 2010; Rögl, 1999) shaped the basin into its present day semi-enclosed configuration. This near landlocked physiography reduced the Mediterranean's buffering capacity, which increased the basin's sensitivity to climatic change (Gladstone et al., 2007; Rohling et al., 2009). Today, net evaporative loss and winter cooling result in a primarily salt-driven deep water ventilation of the Mediterranean (Rohling et al., 2009).

During the late Neogene, deep water formation was periodically reduced due to dominantly precession induced dry-wet climate oscillations resulting in the deposition of organic rich layers called sapropels (Cramp and O'Sullivan, 1999; Kidd et al., 1978). Remarkably, the first marl-limestone alterations with sapropelitic layers start to occur just after the Middle Miocene Climate Transition (Mourik et al., in review). One of the questions that remains to be answered is what exactly triggered the onset of sapropel formation in this critical interval of paleo-geographic and climatic reorganisations in the middle Miocene. To investigate this, we studied marine sediments, exposed along the coastal cliffs near Ancona (Italy), which provide a unique middle Miocene sequence. The astronomical dated La Vedova Beach (LV) and La Vedova High Cliff (LVHC) sections cover a continuous time interval from ~15.3 to 13.5 Ma, thereby encompassing the transition from the Miocene Climatic Optimum to the cooling step at ~13.8 Ma (Hüsing et al., 2010; Mourik et al., in review). Here, we combine two high-resolution geochemical datasets, previously used for astronomical tuning of the sections, to investigate long-term changes in the geochemical expression of insolation controlled cycles in this crucial interval. Comparing these cycles before, during and after the climate transition will provide insight in the evolution of the basic cycle and the onset of sapropel-type sedimentation.

2. Section & Methods

2.1 Section

Miocene marine sediments are well exposed along the coastal cliffs of the Cònero Riviera in Italy (Montanari et al., 1997). Two middle Miocene sections, the La Vedova section (Hüsing et al., 2010; Mader et al., 2004) and the La Vedova High Cliff section (Mourik et al., in review) were sampled and studied in detail near the village La Vedova (Figure 1). Integrated stratigraphy and astronomical tuning have been independently established for both sections. The older, La Vedova Beach section is exposed along the beach, covering part of the Langhian from ~15.28 to 14.17 Ma. The La Vedova High Cliff section is accessible high up in the cliffs and comprises the interval between 14.17 and 13.50 Ma, thereby covering the Langhian-Serravallian transition (Mourik et al., in review). The Cavolo sandstone turbidite, a recognizable marker bed along the cliffs (Montanari et al., 1997) is situated in the uppermost part of the High Cliff section. No direct overlap between these two sections has been sampled, but the cycles of the upper part of the

La Vedova (beach) section can easily be recognized high in the cliffs. This enabled us to combine the two sections to construct the La Vedova Beach High Cliff composite (LVBHC; Figure 2a).

The LVBHC succession consists of rhythmic alternations of homogeneous marls and indurated homogeneous marly limestones. After cleaning of the exposed surface, the fresh sediments can be visually distinguished into whitish, greyish or bluish limestones and greyish, brownish, bluish or greenish marls. Bed thickness of marls and limestones varies from a few centimeters to more than a meter.

Based on field observations and lithology, four intervals can be distinguished. The lowermost interval, from 0 - 9 m, is characterized by relatively thick grey to brownish marls and relatively thin whitish or bluish indurated limestones. In the second interval (9 - 22.5 m), the thickness of the marls is substantially reduced. Thinly-bedded whitish or bluish limestones dominate, especially between 9 - 12 m and 19 - 22.5 m. Prominent dark green marls occur in bundles of two or three at ~14 and ~17 m. A bluish dark marl is observed at the base of interval III (22.5-52 m), followed by more greenish marls around 24 m. In this interval an increase in the thickness of limestone and marl beds is observed. Thick and indurated limestones rhythmically alternate with thin and less indurated limestones, with grey to bluish marls intercalated regularly between limestone beds. Limestones become thinner again between 43 m and 52 m, but remain indurated. The upper interval (52-72 m) shows a prominent increase in the thickness of relatively light grey marls. Moreover, thin dark greenish marl beds start to appear between a thin limestone bed and an indurated thicker limestone bed. This strongly resembles the quadruplet structure of the basic precession-related cycles at Monte dei Corvi (Hilgen et al., 2003), where sapropels are intercalated in limestones. Therefore, the dark marls in interval IV will be referred to as sapropelitic layers (see Mourik et al., in review; Ch. 1).

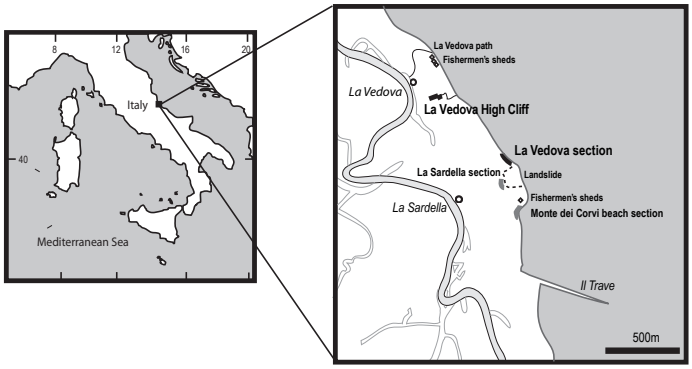

Figure 1 Location map of the La Vedova (Beach) section (Hüsing et al., 2010) and La Vedova High Cliff section (Mourik et al., in review; Chapter 1) along the Adriatic coast in Italy.

2.2 Geochemical element analysis

Selected samples (915) from the La Vedova and La Vedova High Cliff sections were dried and thoroughly ground in an agate mortar prior to dissolution. Of each sample 125 mg was dissolved in 2.5 mL HF (40%) and 2.5 mL pre-mixed acid (HNO_3 16.25% and $HClO_4$ 45.5%) and heated at 90°C in a closed Teflon reaction vessel for at least 8 hours. Samples were subsequently dried by evaporating acids at 160°C and re-dissolved in 25mL HNO_3 (4.5%). The resulting solutions were analyzed for the elements Al, Ba, Ca, Cr, Cu, Fe, K, Mg, Mn, Mo, Ni, Na, P, S, Sr, Ti, V, Y, and Zr with an ICP-OES (Perkin Elmer Optima 3000) at Utrecht University. Relative precision and accuracy were established through duplicate analyses and in-house standards (ISE-921 and CS) and were better than 5% relatively for all elements except Y and Zr (better than 8%).

2.3 Principal component analysis

To interpret the variance within the data set a principal component analysis (PCA) was performed. This data reduction method presents the most important aspects of a multivariate dataset in a small number of dimensions, the principal components. These components may be interpreted as reflecting "underlying variables" with a biological or environmental significance (Hammer and Harper, 2006). First, a PCA was performed on the complete elemental data set, but excluding outliers (values exceeding the mean ± three times the standard deviation). Second, elemental concentrations were normalized using aluminium as a common divisor to compensate for changes in the relative input of carbonates versus terrestrial sediment. These Element/Al ratios (indicated by *) were subsequently used as input for a second PCA. Outliers (defined as > 3x standard deviation) were again excluded from this analysis.

Since interval I has a very distinct lithology and geochemistry (Figure 2) an additional PCA was performed, excluding interval I samples, to verify whether the components extracted from intervals I-IV are representative for the entire section.

Based on the PCA results we decided to make slight adjustments in some tuning calibration points of the La Vedova section, which was initially tuned using calcium carbonate- and magnetic susceptibility records (Hüsing et al., 2010). In this way the tuning of the LVBHC composite becomes more consistent, since PCA has also been used for the tuning of the La Vedova High Cliff section (Mourik et al., in review).

2.4 Cross-spectral analysis

Blackman-Tukey cross-spectral analysis (using the Anayseries programme of Paillard et al., 1996) was run on a selection of elemental records to determine phase relations between the different elements and precession and obliquity induced variations in insolation. To trace changes in phase relations we applied cross-spectral analysis for the different intervals separately. Confidence levels were set at 80% and 95%.

3. Results

3.1. Elemental records

Figure 2a shows the LVBHC composite and the patterns of $CaCO_3$ (calculated from Ca, under the assumption that most, if not all, Ca is present as $CaCO_3$), Ti* and V* (for other element records we refer to the supplementary information). Carbonate content in the LVBHC ranges from 50-70% in the marls to 80-95% in the limestones. In intervals I (0-9 m) and II (9-22.5 m), a gradual increase in carbonate content is observed. Furthermore, interval I is characterized by high Ba*, S* and K* (Hüsing et al., 2010; supplementary information), which decrease rapidly at the transition to interval II. A second step in elemental patterns marks the base of interval III (22.5-51.7 m). The carbonate content recovers gradually, remaining more or less constant from 29m onwards. Distinct minima in $CaCO_3$ and V* in interval II and III are in most cases related to ash layers recognized in the field. Interval IV (51.7-72 m) is characterized by clear variability in V* and Ti*. Pronounced enrichments in various elements are observed in the Cavolo sandstone turbidite at ~71 m.

3.2. Principal component analysis

Principal component analysis of the non-normalized elemental data reveals one major component (eigenvalues level off after first component), explaining 69% of the variance. This component is characterized by a strong negative loading of Ca versus high positive loadings (>0.95) of terrestrial elements like K, Ti and Al (Table 1). Due to the closed sum effect, samples with high carbonate content have a relatively small proportion of terrestrial material, which causes the dominant anti-correlation between Ca and terrestrial elements and the dominance of component 1. Using normalized data (elemental/Al ratios) largely eliminates this closed sum effect.

The first three components of the PCA performed on the Al-normalized data are significant (eigenvalues level off after the third component), explaining 30.4%, 17.7% and 12.9% of the observed variability respectively. The first axis is characterized by high positive loadings (>0.7) of Ca*, Sr* and Mn* and intermediate loadings (0.4-0.7) of

Table 1. Component matrix for principal component analysis on non-normalized data.
Table 2. Component matrix for principal component analysis on Al-normalized data (interval I-IV).

Table 1

	PC-1
Ca	-0.927
Mn	-0.370
Sr	-0.141
Ba	0.527
S	0.551
P	0.595
Cu	0.846
Na	0.848
Ni	0.887
Zr	0.940
Y	0.942
Mg	0.949
Cr	0.959
Fe	0.963
V	0.969
Al	0.972
Ti	0.974
K	0.981

Table 2

PC-1		PC-2		PC-3	
Ti *	-0.112	Mn*	-0.380	Zr *	-0.701
Ni *	-0.062	Ca*	-0.324	Ti *	-0.560
Zr *	-0.056	Sr *	-0.288	P *	-0.498
K*	-0.030	P *	-0.034	Mg*	-0.237
S *	0.052	Y *	-0.020	Sr *	-0.150
Cu*	0.253	Cr*	-0.003	Ca*	-0.138
Cr*	0.438	V *	0.054	Mn*	-0.067
Na*	0.448	Fe*	0.222	Fe*	-0.008
Mg*	0.564	Ni *	0.259	K*	0.036
Fe*	0.583	Ba*	0.300	Y *	0.041
P *	0.611	Cu*	0.417	Na*	0.068
V *	0.613	Na*	0.448	Ba*	0.101
Ba*	0.653	Zr *	0.455	S *	0.135
Y *	0.771	Ti *	0.530	V *	0.368
Mn*	0.798	Mg*	0.567	Cr*	0.466
Ca*	0.907	S *	0.747	Cu*	0.544
Sr *	0.914	K*	0.765	Ni *	0.727

P*, V*, Fe*, Ba*, Mg* and Cr*. Except for Cu* all other elements have weak negative loadings, close to zero (Table 2, Figure 3a). The second PC axis is characterized by high positive loadings of K* and S*, intermediate loadings for Mg*, Ti*, Cu*, Zr* and Ba* whereas Mn*, Ca*, Sr* and P* show weak negative loadings (<0.3). The third PC axis is characterized by positive loadings of Ni* (>0.7), Cu* and Cr*, and negative loadings of Zr* (>-0.7), Ti* and P*. The regression scores of the samples with depth are shown in Figure 2b.

The additional PCA using Al-normalized data from intervals II-IV, excluding interval I, reveals a similar first PC axis, but a different second PC-axis, compared to the PCA on the entire section. The component plot of the first two axes of the PCA on interval II-IV is shown in Figure 3c and demonstrates that PC-2 is essentially the same as PC-3 of the PCA on all four intervals. In addition, there is no axis similar to the K* dominated PC-2 of all four intervals, suggesting that this component is entirely related to interval I.

4. Discussion

4.1 Principal Components

The interpretation of the principal components is based on the element loadings on each axis. In the original data set the first component is dominated by Ca and therefore reflects the relative contribution of calcium carbonate versus terrestrial input. The pattern of this axis is very similar to $CaCO_3$. In the next paragraphs only the PCA of the normalized data will be discussed.

Also in the PCA based on normalized data, the first axis represents the relative input of terrestrial versus carbonate input and the pattern is similar to the Ca/Al record (supplementary information). This implies that normalizing elemental concentrations to Al does not completely remove the effect of relative changes in the carbonate- and terrestrial fractions from the data set. The second PC axis is predominantly characterized by high K* and S* values during interval I, which reflects the different geochemical composition of this interval compared to intervals II-IV. Potassium (K) supply to marine sediments is usually in the form of K-rich clay minerals like illite. Fluctuations in K* may therefore reflect the relative contribution of a specific source area (Wehausen and Brumsack, 1998; Wehausen and Brumsack, 2000) and hence sedimentation rate. Sulphur (S) may be trapped within the sediment by reaction and precipitation with iron to form pyrite (FeS_2), or by incorporation into organic matter (Brüchert and Pratt, 1996). The ubiquitous presence of pyrite shows that S is present mainly in a reduced form.

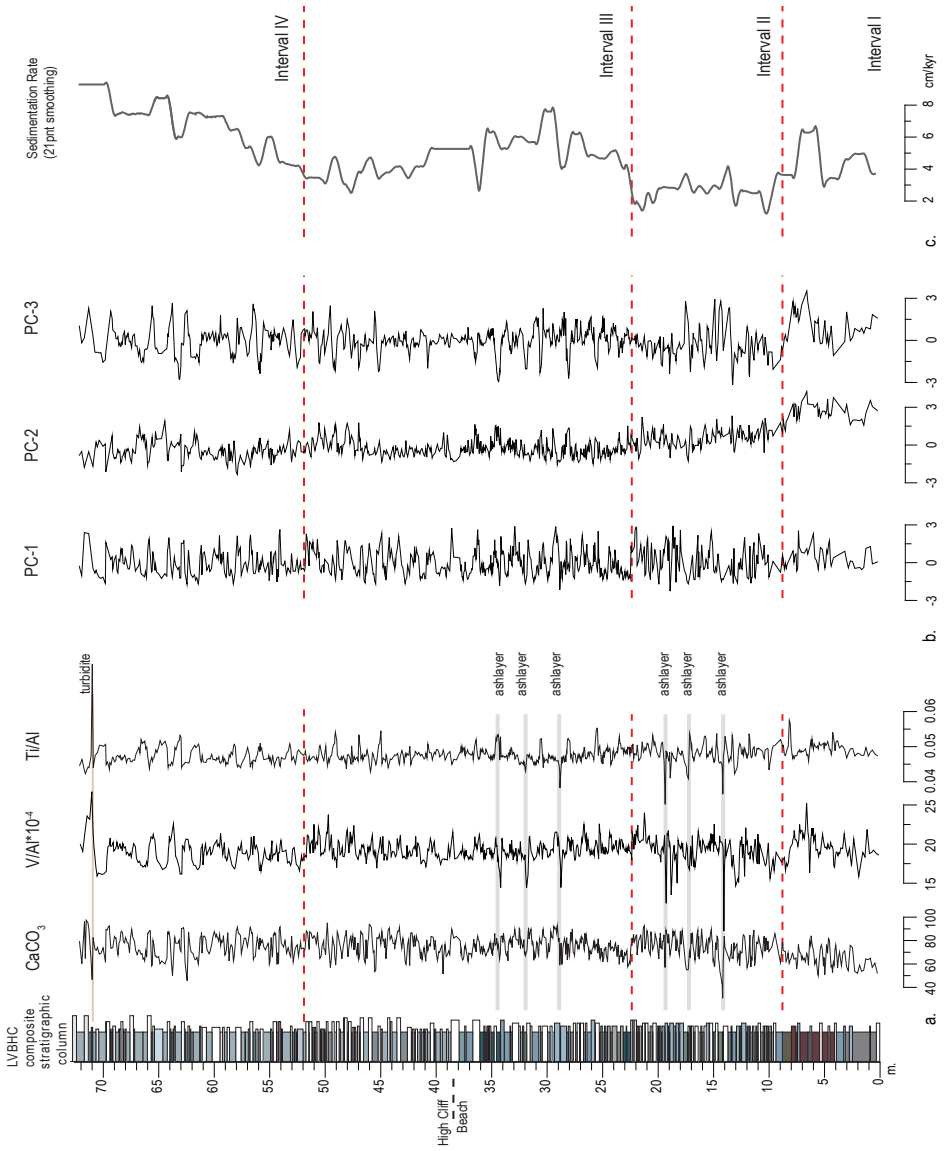

Figure 2. a) Lithological column of the La Vedova Beach – High Cliff composite (LVBHC) showing rhythmic alternations of homogeneous marls and indurated homogeneous limestones. Based on field observations and lithology four intervals are distinguished (dashed lines). The records of CaCO3, V* and Ti* are shown next to the column. Ash layers and the Cavolo sandstone turbidite are indicated by grey shading; b) Regression scores of the first 3 axes resulting from principal component analysis on the Al-normalized dataset (see text for discussion); c) Sedimentation rates (21 point smoothing).

Reduced conditions at or near the sediment water interface are confirmed by the high Mo concentrations (e.g. Tribovillard et al., 2006). Such conditions can be caused by high organic matter fluxes, reduced bottom water oxygenation and high sedimentation rates (Middelburg et al., 1993; Müller and Suess, 1979). High K* in association with high S* could point to the latter. However, K* does not seem to be related to sedimentation rate in interval II – IV. Therefore, the interpretation of this axis in terms of sedimentation rate and reduced conditions remains limited to interval I. This is in line with the fact that the second axis does not explain a significant amount of variance in the data when interval I is omitted from the analysis.

The third PC axis is characterized by variability in Ni*, Cu*, Cr* and V* versus Zr*, Ti* and P* (Table 2, Figure 3b). Positively loading elements are all redox-sensitive, which suggests that PC-3 is related to some extent to ventilation of the basin. In addition, Ni and Cu are delivered to the sediment in association with organic matter and may therefore be linked to paleoproductivity (Tribovillard et al., 2006). The negatively loading element ratios of Ti* , Zr* and P* suggest a relative enrichment in heavy minerals and could be associated with winnowing (Schnetger et al., 2000). Alternatively, Ti* and Zr* could be reflective of eolian dust input (e.g. Lourens et al., 2001; Wehausen and Brumsack, 1998; Wehausen and Brumsack, 2000). The component plot (Fig. 3c) shows a close relation between Ti* and Zr* and a more deviating position of P*, especially in interval II-IV. From this perspective, PC-3 is more likely to reflect the relative contribution of eolian input. Combining this with the interpretation of the positively loading redox-sensitive elements, PC-3 might reflect oxygenated environments with relatively increased dust input, versus oxygen depleted environments, possibly associated with high organic matter (OM) fluxes.

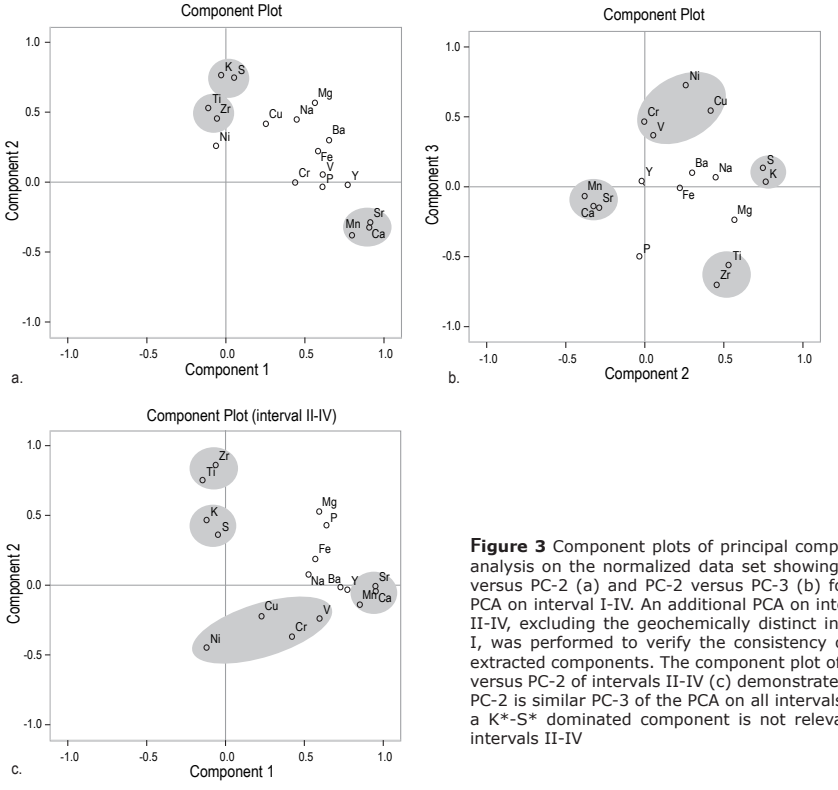

Figure 3 Component plots of principal component analysis on the normalized data set showing PC-1 versus PC-2 (a) and PC-2 versus PC-3 (b) for the PCA on interval I-IV. An additional PCA on intervals II-IV, excluding the geochemically distinct interval I, was performed to verify the consistency of the extracted components. The component plot of PC-1 versus PC-2 of intervals II-IV (c) demonstrates that PC-2 is similar PC-3 of the PCA on all intervals, and a K*-S* dominated component is not relevant to intervals II-IV

4.2 Insolation control on chemical cycles

The rhythmic alternation of sediments enriched in redox-sensitive elements and sediments enriched in Zr* and Ti* suggests that PC-3 reflects a characteristic climate signal for the Mediterranean. Oxygen depletion and accumulation of OM have been related to summer insolation maxima when increased river runoff decreases ventilation of deep waters by stratification (e.g. Hilgen, 1991a,b; Hilgen et al., 1995; Rossignol-Strick, 1983). By contrast, enrichments in Ti* and Zr*, reflecting predominantly dry periods, have been related to summer insolation minima (Lourens et al., 2001).

The relation between the precession controlled summer insolation pattern and PC-3 is especially clear in the quadruplet interval between 61 and 64 m where Ti* and Zr* rich marls, indicative of eolian dust input, alternate with Ni* and Cu* rich marls, elements usually enriched in sapropels (Nijenhuis et al., 1996; 1998; Nijenhuis and de Lange, 2000; Schenau et al., 1999; Wehausen and Brumsack, 2000). This remarkable variability has been used by Mourik et al. (in review) to construct an astronomical tuning for the La Vedova High Cliff. Since PC-3 is essentially the same as the PC-axis used for the tuning of La Vedova High Cliff, we decided to make the tuning of the LVBHC more consistent by adjusting the tuning calibration points, where needed, to PC-3 (Fig. 4).

4.3 Phase relation to insolation

Cross spectral analysis on the elemental ratios and N65 summer insolation (La 1,0.9) shows that element/Al records have most significant coherencies in the precessional band. For interval I-III an anti-phase relation of Ca* and Mg* to precession minima is observed (Fig. 5). In interval II-IV, Ni* and Cu* are in-phase with precession, whereas Ti* and Zr* show the opposite phase. In interval III a clear obliquity influence is present in all records. The phase-relation of Ca* seems to migrate from an in-phase relation with Ti*, Zr* and Mg* in interval II towards an almost anti-phase relation with Ti* and

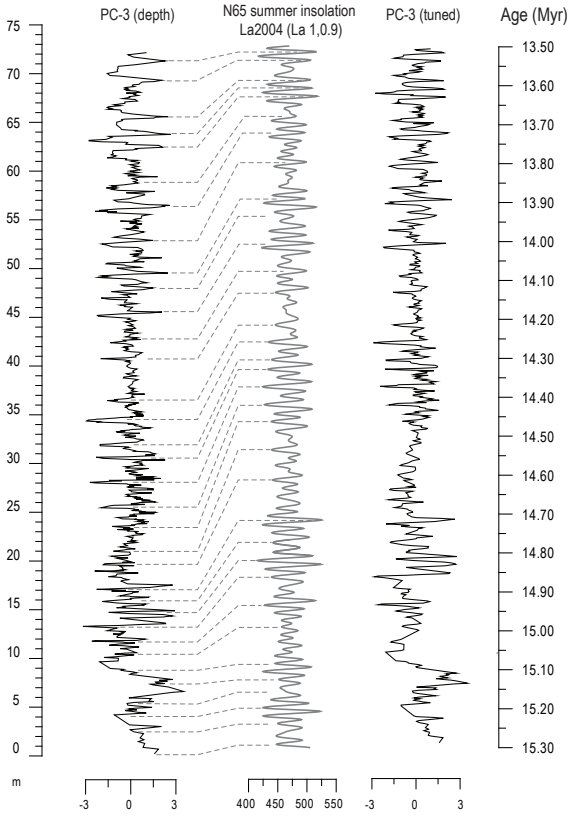

Figure 4. Regression scores of PC-3 in depth (a) and relation to the N65 summer insolation curve (La1,0.9) using the astronomically tuned age models by Hüsing et al., 2010 and Mourik et al., in review (Ch. 1). The tuning of La Vedova beach was initially based on calcium carbonate and magnetic susceptibility records, whereas the tuning of La Vedova High Cliff is based on a similar PC-axis. Calibration points of the La Vedova beach section have been slightly adjusted, where needed, to construct a more consistent tuning.

Zr* in interval IV. Also V* shifts from a anti-phase relation with Ni* towards an in-phase relation in interval IV. Considering the relation of PC-3, and thus insolation, to lithology, with minima and maxima in most cases related to marly deposits, it is not surprising that limestone deposition would be confined to the phase between minimum and maximum insolation. The apparent phase change is therefore possibly caused by relative changes in marl thickness (see section 4.5), with an increase of the Ti* and Zr* rich marls with respect to the Ni* and Cu* rich marls.

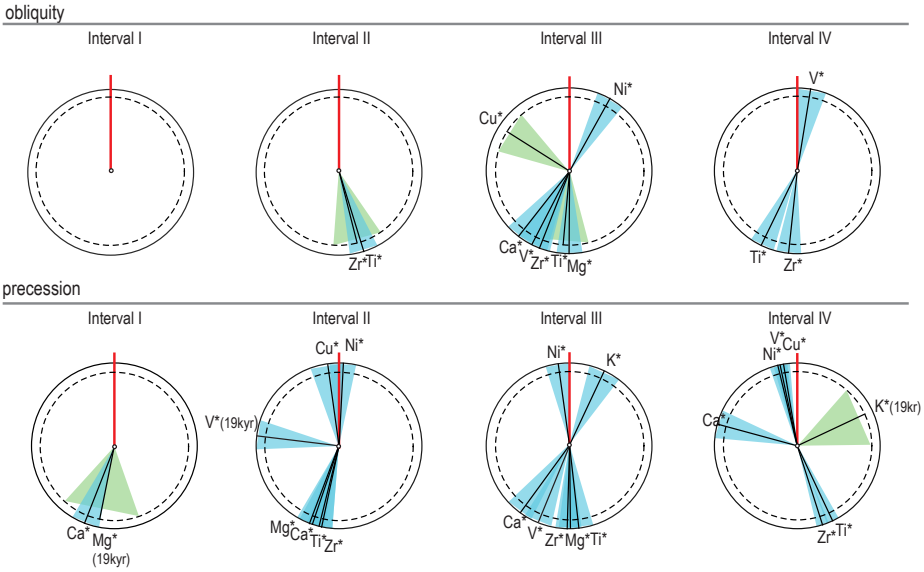

Figure 5. Phase wheels for element/Al ratios relative to precession and obliquity in the 65°Nlat summer insolation curve with significant coherencies at a 80% and 95% confidence level. Vector length represents coherence (dashed circle marks 80% and solid line circle marks 95%). The 12 o'clock position is the in-phase relation with maximum obliquity or minimum precession (maximum Northern Hemisphere summer insolation). Cross-spectral analysis was applied for intervals I-IV separately in order to trace changes in phase relationship. For explanation see text.

4.4. Cycle structure and elemental distribution

Sedimentary cycles in marine successions in the Mediterranean are generally related to orbitally forced climate variability (e.g. Abdul Aziz et al., 2008; Abels et al., 2005; Hilgen et al., 2000; 2003; Hüsing et al., 2009). Internal cycle structure in the younger Monte Dei Corvi section (13.4-6.2 Ma) ranges from duplet (marl-limestone or marl-sapropel), triplet (marl, sapropel, limestone) to quadruplet (marl, limestone, marl, limestone) (Hilgen et al., 2003; Hüsing et al., 2009). All forms are found intermingled across the entire LVBHC section except for interval I, which has only marl-limestone duplets. The relationship between cycle structure, insolation and a selection of element to Al ratios is given in Figure 6.

Interval I

The base of the LVBHC section (interval I, 15.29-15.06 Ma) is characterized by duplets of thick brownish marls and thin limestones. Calcium carbonate content in interval I is relatively low (Fig. 2a) and elemental patterns do not show a consistent relation to lithology (Fig. 6a). Nevertheless, generally high values of Ni*,Cu* (PC-2 and PC-3) , S* and Ba* (see Hüsing et al., 2010) reflect increased productivity and low bottom water oxygen levels, which is supported by the presence of Mo* peaks (Fig. 6a). However, sulfate-reducing conditions may have led to barite dissolution and Ba migration through pore waters which limits the use of Ba as paleoproductivity proxy here (e.g. Tribovillard et al., 1996 and references therein).

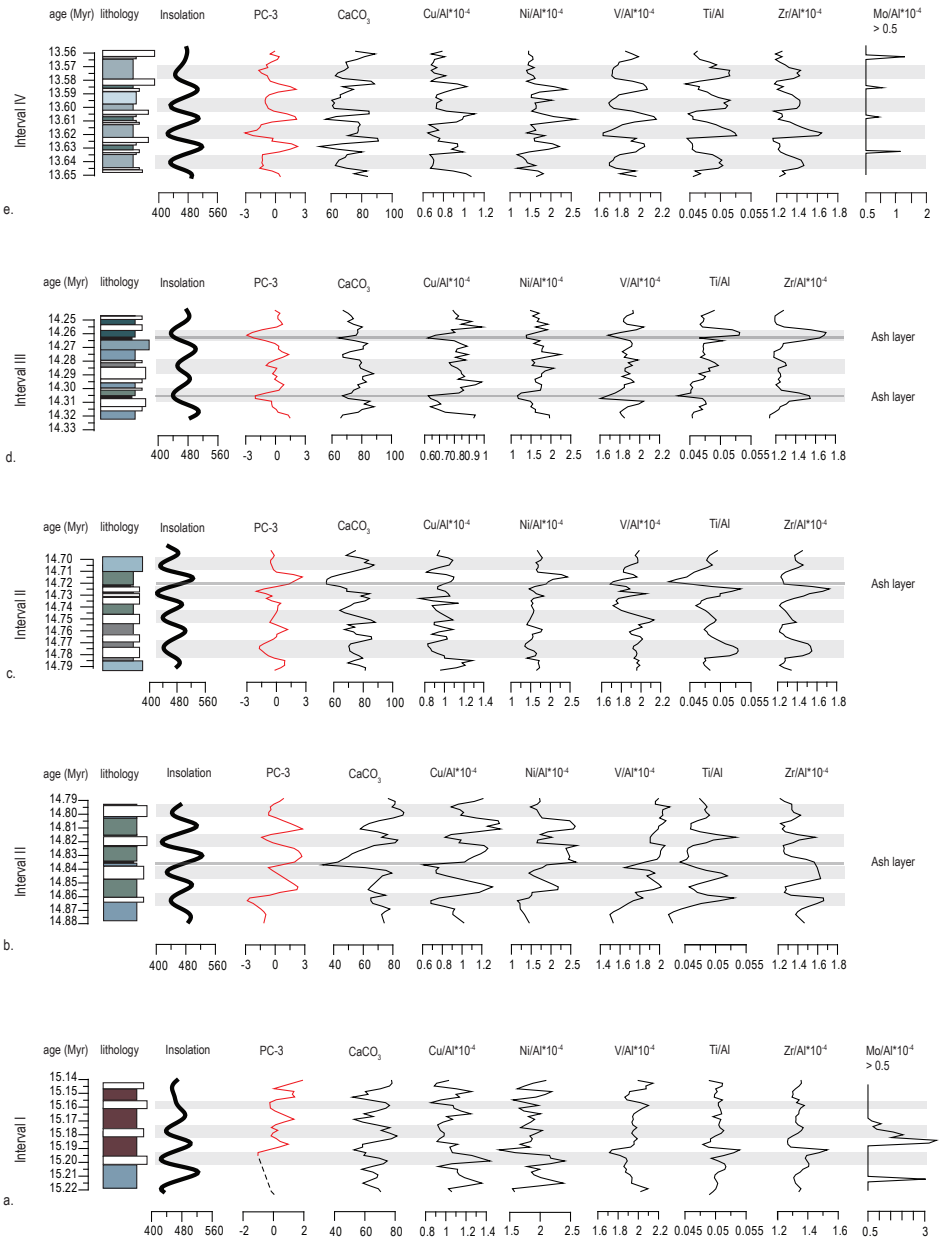

Figure 6. Elemental patterns and PC-3 in relation to insolation and lithology. Light grey shading corresponds to insolation minima. A selection of three to four precession cycles was made for interval I (a), interval II (b and c), interval III (d) and interval IV (e). Only in interval I and IV are molybdenum peaks observed, indicating dysoxic bottom water conditions. Note the small differences in scale.

Climate conditions during this time interval were relatively warm and humid (the Miocene Climatic Optimum) (e.g. Mosbrugger et al., 2005), favoring increased biogeochemical weathering on the continents and an increased input of weathering-derived nutrients into the oceans (Föllmi et al., 2005; John et al., 2003). This may have stimulated productivity and enhanced the deposition and burial of organic rich sediments.

High K* and Mg* ratios in interval I may point to a source area from the northern borderlands of the eastern Mediterranean (Fig. 7). This, presumably fluvial, source was proposed by Wehausen and Brumsack (1998; 2000) to explain Mg* and K* values in site 964 (Pisano Plateau) being higher than the Saharan dust end member (K* = 0.38, Mg* = 0.22; Krom et al., 1999). Nile river influence, characterized by low K* and Mg* ratios, is minimal in the LVBHC section. A decreasing influence of the hypothetical "northern borderland source" towards lower Mg* and K* values can be observed from interval I to IV (Fig. 7).

Interval II

A decrease in sedimentation rates at ~15.06 Ma coincides with a sudden drop in K*, S* and redox sensitive elements like V* (PC-2 and PC-3, Fig. 2a and b). This step coincides with the beginning of a 405 kyr eccentricity minimum at ~15 Ma and may be related to the eccentricity paced onset of the East Antarctic Ice Sheet marking the end of the Miocene Climatic Optimum at ~15 Ma (Shevenell et al., 2008; Tian et al., 2009; Wan et al., 2009; Zachos et al., 2001a).

The brownish marls are replaced by grey or greenish marls and the cycle structure becomes more complex. Figure 6 (b and c) shows details of duplets and quadruplets in which insolation minima correspond to Zr* maxima and Cu*, Ni* and V* minima in the limestones. Conforming to the interpretation of PC-3, this implies well ventilated bottom waters and a relatively high contribution of eolian deposits. By contrast, the marl layers show the opposite pattern and reflect a more reduced environment during insolation maxima.

Ash layers are found in interval II and III. They appear to disturb the regular geochemical patterns as they are characterized by maxima in Zr* and minima in $CaCO_3$, Ti*, V*, K* and other elemental ratios (see supplementary information). The infrequent occurrence of ash-layers in the younger part of the LVBHC section could indicate that volcanic activity ceased, or wind direction changed.

Interval III

Cycle structure in interval III ranges between duplets, triplets and quadruplets and shows a similar elemental distribution to interval II with Cu* and Ni* being elevated during isolation maxima (Fig. 6d). The base of interval III, at ~14.49 Ma, is characterized by a temporary drop in carbonate content, reflected in PC-1. Simultaneously, sedimentation rates increase and elemental/Al records start to show more regular patterns (Fig. 2). The increase in sedimentation rate, associated with the end of the 405 kyr eccentricity minimum around 14.55 Ma, could be related to an increasing influence of eolian input, as can be inferred from the rhythmic occurrence of peaks in Zr*, Ti* and PC-3. Although trade winds as prevailing today (ENE-WSW) were reconstructed for the latest Miocene (Schuster et al., 2006), there is hardly any evidence of deserts being active in the middle Miocene (Kroepelin, 2006; Schuster et al., 2006a, b; Swezey, 2006; 2009), which raises questions about the potential source area of the dust. Considering the transition towards a younger Neogene type of cyclicity in interval IV (next paragraph), a northern African source area would be most likely. Therefore the Ti* and Zr* records may evidence early desertification in the Middle Miocene around the Mediterranean region.

Interval IV

The step from interval III to IV is related to the rapid expansion of the East Antarctic Ice Sheet between 13.92 and 13.78 Ma (Mourik et al., in review; Ch.1). Sedimentation rates increase gradually from this point onwards and the dry phase marls become thicker (Fig. 2). Moreover, the high-amplitude variations in PC-3 suggest increased climate variability during eccentricity maxima after the Middle Miocene Climate Transition (MMCT) (Fig. 4a).

A characteristic quadruplet cycle structure can be observed in interval IV, which is typical for some younger Mediterranean marine successions (e.g. the Serravallian to

Tortonian Monte dei Corvi section; Hilgen et al., 2003). Thick light grey marls alternate with sapropelitic layers developed within a limestone (Fig. 6e). In these sapropelitic layers, enrichments in Cu*, Ni*, V* and Mo* reflect increased productivity and/or dysoxic or anoxic bottom water conditions (e.g. Tribovillard et al., 2006). Such conditions are most likely a combination of decreased ventilation and increased productivity, although the relative importance of these factors for sapropel formation is still debated (De Lange et al., 2008; Emeis et al., 2000; Rohling, 1994; Rohling et al., 2009; Rossignol-Strick et al., 1982).

4.5 Insolation controlled cycle evolution during the MMCT

The insolation controlled dry-wet oscillation is most noticeable in interval IV, which is also the only interval with prominent sapropelitic layers (i.e. clearly visible in the field). In the preceding intervals sapropels are visually absent, but PC-3 variability clearly reflects a similar geochemical pattern for each precession cycle.

Figure 8 shows a simplified scheme of changes in the basic cycle build up as observed in the LVBHC section. Although the elemental composition of Interval I is distinctly different from the younger intervals, the rhythmic occurrence of thin limestone beds suggests that a dominantly precession controlled oscillatory climate system was already operative (Hüsing et al., 2010). However, there are no indications for regular contributions of eolian dust in this interval. With the transition to interval II, marl influx decreases. In this interval, Ti* and Zr* peaks occur, which are usually confined to a limestone or a relatively thin layer within a limestone bed, separated from the next limestone by a marl. This cycle structure results in the observed in-phase relation between Ca* and Ti* and Zr*.

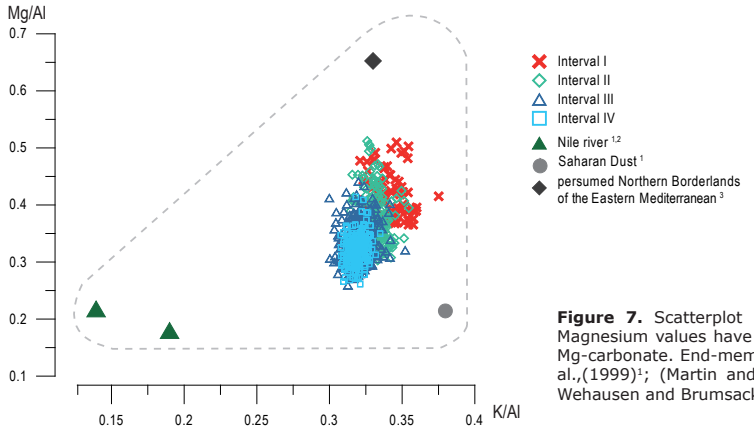

Figure 7. Scatterplot of Mg/Al versus K/Al. Magnesium values have not been corrected for Mg-carbonate. End-member data from Krom et al.,(1999)[1]; (Martin and Meybeck, 1979)[2] and Wehausen and Brumsack (2000)[3].

The cycle thickness increases again in the transition from interval II to III. Although the dry phase marls in interval III are more distinct than in interval II, the structure of the cycles suggests that the increase in cycle thickness is mainly due to the limestones and wet phase marls. The phase relation with Ca* starts to change as soon as the dry phase marls becomes thicker than the wet phase marls. This is mainly observed in interval IV, where the cycle thickness shows a further increase due to the presence of thick dry phase marls. By contrast, the wet phase marls are relatively thin. This structure results in a more in-phase relation between Ca* and Ni* and Cu*.

The evolution of orbitally controlled sedimentary cycles in the LVBHC during the MMCT shows the response of the Mediterranean to global climatic changes from ~15 Ma onwards. The different intervals observed in the lithology are related to changes in sedimentation rate, which have been linked by Hüsing et al. (2010) to the combined effect of the 405 kyr eccentricity cycle superimposed upon a longer-term climatic or tectonic induced trend. The onset of distinct eolian contribution from ~14.5 Ma onwards suggests that aridification commenced prior to the major shift at 13.8 Ma. During

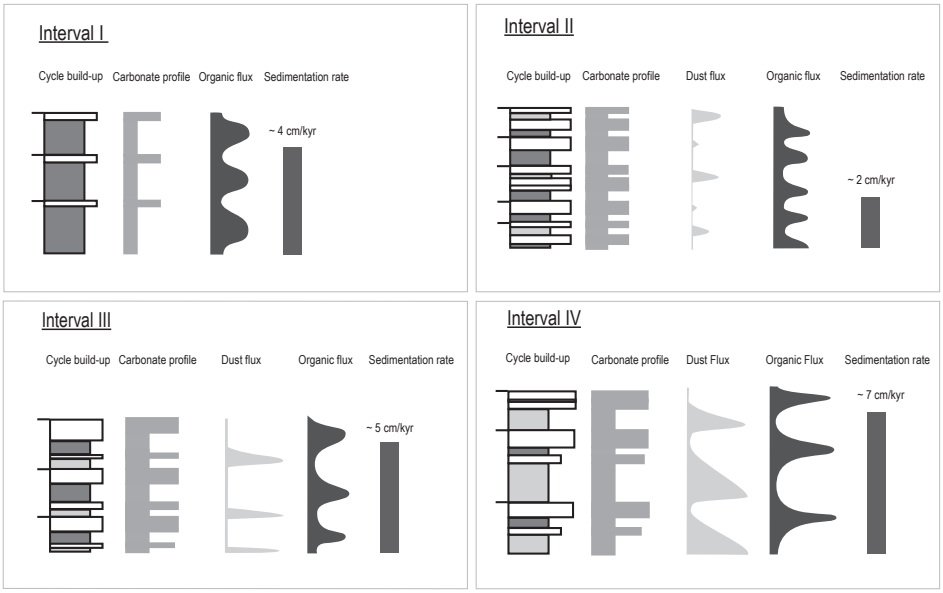

Figure 8. Schematized and hypothetical development of cycle structure, carbonate profile, dust flux and organic flux throughout the LVBHC section. The lines on the left site of the schematic lithological columns indicate the boundaries of the basic cycles. An indication of the associated sedimentation rate for each panel is shown on the right. See text for discussion.

this phase, the basin was still relatively well ventilated. From 13.8 Ma onward, a clear differentiation between predominantly dry seasons during insolation minima and wet conditions during insolation maxima is observed, in which sapropelitic sediments point to decreased bottom water ventilation and relatively high fluxes of organic matter. Sea level lowering as a consequence of ice sheet expansion may have slowed down circulation in the Mediterranean (Rohling and Bryden, 1994). However, this can not explain the increased eolian contribution. Enhanced activity of the African monsoon may therefore be a more likely explanation for the amplified climate variability after the MMCT. Increased stratification as a consequence of enhanced freshwater influx during insolation maxima may alternatively explain the decreased ventilation.

5. Conclusions

Changes in geochemical patterns and cycle structure in the LVBHC composite section suggest that the precession controlled climate oscillation system responded to the global middle Miocene cooling trend. A first step towards dry-wet climate alternations commenced at ~15 Ma, after termination of the Miocene Climatic Optimum. Increased sedimentation rates and prominent enrichments in Ti* and Zr* from ~14.5 Ma onwards suggest eolian dust supply, which might provide evidence of desertification nearby the Mediterranean region as early as the middle Miocene. The major cooling step at ~13.8 Ma resulted in enhanced seasonal contrast, which ultimately triggered sapropel formation during phases of increased freshwater influx and decreased bottom water ventilation.

Acknowledgements
The authors would like to thank João Trabucho Alexandre, Gert de Lange, Ivo Duijnstee, Tom Jilbert and Helen de Waard.

Figure S1 (Supplementary Information) Lithological column of the La Vedova Beach – High Cliff composite (LVBHC) and elemental records of Ca*, Ba*, S*, Ni*, Cu*, K*, Mg*, Fe*, P* and Zr*.

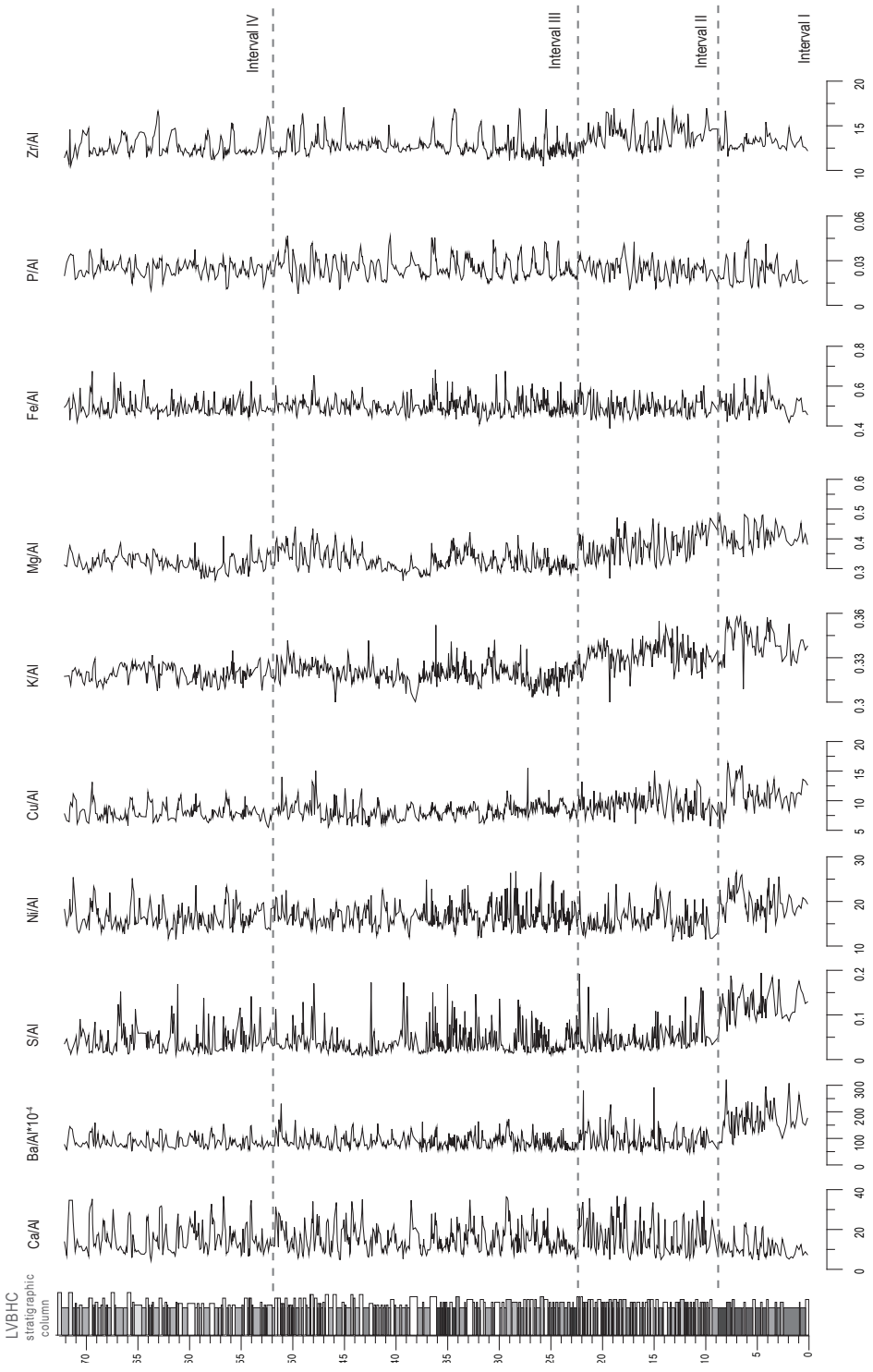

Chapter 3

Improved astronomical age constraints for the Middle Miocene Climate Transition based on high-resolution stable isotope records from the Central Mediterranean (Maltese Islands)

A. A. Mourik, H. A. Abels, F. J. Hilgen, A. Di Stefano and W. J. Zachariasse

Submitted to Paleoceanography

Abstract
Marine outcrops of the Globigerina Limestone and Blue Clay Formations on the Maltese Islands in the Central Mediterranean Sea document the Middle Miocene Climate Transition (MMCT) between ~15 and 13.7 Ma. High-resolution benthic and planktic oxygen isotope records have been constructed for this enigmatic interval in Cenozoic climate evolution and show the Mi3 oxygen event and CM5 and CM6 carbon isotope excursions. Detailed biostratigraphic correlations to the recently astronomically tuned La Vedova section in northern Italy allow revision of the tuning of the Blue Clay Formation, constraining the age of the sediments directly above the formation boundary and Mi-3b event. Biostratigraphic age control and cyclic patterns in the benthic $\delta^{13}C$ record further lead to a new, astronomically tuned age model for the upper member of the Globigerina Limestone Formation approaching the formation boudary and Mi3b from below. Start of sedimentation of the Upper Member of the Globigerina Limestone Formation above the Upper Main Phosphorite Conglomerate Bed is dated at ~14.95 Ma and the oldest Blue Clay sediments directly above the Mi-3b have an age of 13.76 Ma +/- 0.02 Myr. The possibility of a hiatus between 13.95 and 13.76 Ma can not be excluded and could have implications for the GSSP of the Serravallian stage, which is currently defined in this section.

1. Introduction

One of the most enigmatic episodes in Cenozoic climate history is the Middle Miocene Climate Transition (MMCT, ~15-13.7 Ma). This climate transition marks the end of the Miocene Climate Optimum (MCO; ~17 to ~15 Ma), and is characterized by atmospheric and oceanic cooling, East Antarctic Ice Sheet (EAIS) growth, and global carbon cycle variability (Flower and Kennett, 1994; Miller et al., 1991; 1996; Woodruff and Savin, 1989; Wright et al., 1992). The gradual progression of Earth's climate into a colder mode eventually led to the rapid expansion of the EAIS around 13.8 Ma, causing major environmental changes (e.g. Flower and Kennett, 1994; Zachos et al. 2001a).

During the early to middle Miocene, open ocean benthic oxygen isotope records reveal several prominent enrichment events (Miller et al., 1991;1996; Woodruff and Savin, 1991), which reflect concise periods of increased glaciations. The Mi3a and Mi3b or similarly E2 and E3 events respectively defined by Miller et al. (1991; 1996) and Woodruff and Savin (1991), together mark the major shift in $\delta^{18}O$ between ~14.1 and ~13.7 Ma (Abels et al., 2005; Holbourn et al., 2005). The benthic foraminiferal carbon isotope record shows a shift to heavier $\delta^{13}C$ values of the CM6 event coincident with the Mi3b/E3 event (Woodruff and Savin, 1991).

Unfortunately, there are still relatively few high-resolution astronomically-tuned foram specific isotope records available for the middle Miocene (Holbourn et al., 2005; 2007; Tian et al., 2008). Improvement of resolution and age control is crucial, especially for determining the duration of this event and the possible relation to orbital configurations.

A good place to study the paleoenvironmental and climate evolution of the Neogene is the Mediterranean, due to its semi-enclosed land-locked configuration that makes the basin sensitive to astronomically-induced variations in climate (e.g. Rohling et al., 2009). The Middle Miocene Climate Transition is presently known from a few continuous and well-preserved outcrops in Malta and Italy (Abels et al., 2005; Hüsing et al., 2010; Jacobs et al., 1996; John et al., 2003; Mourik et al., in review). Recently, an independent astronomical age model has been constructed for the La Vedova High Cliff section near Ancona, northern Italy, in which the Mi-3b isotope event has been recognized in a bulk carbonate sediment isotope record (Mourik et al., in review; Ch.1). Poor carbonate preservation in this section, however, prevents the construction of high-resolution benthic and planktic carbon and oxygen isotope series along the MMCT in an astronomically-tuned time frame.

Marine sediments exposed along the coast of the Maltese Islands (Central Mediterranean) record the MMCT in an apparently continuous succession and show

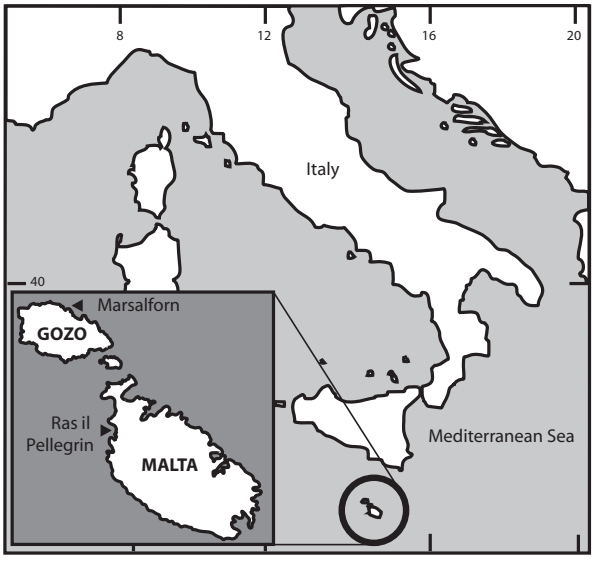

Figure 1. Location map of the Marsalforn section on Gozo and the Ras Il Pellegrin Section on Malta (Maltese Islands, Central Mediterranean).

carbonate preservation suitable for establishing high-resolution isotope records (Jacobs et al., 1996; John et al 2003; Abels et al., 2005). Earlier studies have shown that the transition from the Globigerina Limestone Formation to the Blue Clay Formation coincides with the major middle Miocene isotope step (Mi3b/E3). The Blue Clay Formation was astronomically tuned, dating the formation boundary with the underlying Globigerina Limestone at 13.82 (± 0.03) Ma (Abels et al., 2005). However, the tuning of the lower part of the Blue Clay Formation was subject to uncertainty as it had to be based on counting successive precession-controlled cycles in the Ca/K record down from the oldest reliable astronomically dated tie-point, the Last Common Occurrence (LCO) of *Sphenolithus heteromorphus* at 13.654 Ma. Also, foram-specific isotope records were lacking for the Globigerina Limestone and Blue Clay Formations, hampering evaluation of the bulk carbonate isotope record.

An age model for the Upper Globigerina Limestone Formation (UGL) was constructed by John et al. (2003), based on Sr ages of Jacobs et al. (1996) and matching oxygen and carbon isotope events to open ocean records. However, this age model is not in agreement with new Sr ages for the UGL presented by Fölmii et al. (2008). Using biostratigraphic correlations to the well-tuned La Vedova Beach and La Vedova High Cliff sections, we will attempt to establish a more robust astronomically tuned age model for the Globigerina Limestone Formation and improve the tuning of the lower part of the Blue Clay Formation using additional biostratigraphic tie-points and improved astronomical ages for critical bio-events. The new age model will be used to better understand the MMCT and its regional expression in, and impact on, the Mediterranean.

2. Geological setting

The Maltese islands, composed of the islands Malta, Gozo and Comino (Fig.1), are located on the Malta-Hyblean Plateau in the Central Mediterranean. During the Neogene, sediments were deposited within the Maltese Graben System, a series of Miocene-Quaternary extensional basins that developed on the African foreland of the Sicilian Apennine-Maghrebian fold and thrust belt (Dart et al., 1993; De Visser, 1991).

The Globigerina Limestone Formation is one of five units into which the Neogene lithostratigraphic successions are divided (Felix, 1973). It unconformably overlies the Lower Coralline Limestone Formation of late Oligocene age and is conformably followed by the Blue Clay Formation of Serravallian age. The Globigerina Limestone Formation consists of three members, separated by two phosphorite horizons that mark phases of reduced sedimentation rates and reworking in the form of gravity flows (Föllmi et al., 2008; Pedley and Bennett, 1985; Rehfeld and Janssen, 1995). Only the Upper Member of the Globigerina Limestone Formation (UGL) will be considered in the present study.

The Marsalforn section (MRSF) on Gozo exposed along the coast just east of Marsalforn village was used for detailed logging and sampling of the Upper Globigerina Limestone Formation (UGL) (Fig. 1). This section is easily accessible and less weathered than the outcrops of the UGL in the Ras Il Pellegrin section on the west coast of Malta.

The UGL is of late Langhian age and can be subdivided into three stratal packages. The base of the Upper Member is marked by a phosphate pebble bed, called the Upper Main Phosphorite Conglomerate Bed (UMPC) (Pedley and Bennett, 1985) and is associated with a hiatus with an estimated duration of ~ 2 Myr (Föllmi et al., 2008). The lower and upper packages of the Upper Member consist of yellowish marly limestones, whereas the middle package is a ~5m thick marly clay, referred to as the "clay rich interval" (CRI) by John et al (2003) which we follow here. In the upper part, a phosphatic layer with small phosphate particles has been reported (John et al., 2003). In the outcrop, we did not observe a clear phosphate pebble layer in the Marsalforn and Ras il Pellegrin sections, although dispersed phosphate nodules are present not far below the transition to the Blue Clay Fm at Ras il Pellegrin. A transitional bed (1.12 m thick in the MRSF section and 1.77 m in the RIP section) marks the top of the Globigerina Limestone Formation (Felix, 1973) and is characterized by a decrease in carbonate content from ~70% to 20% (Abels et al., 2005; John et al., 2003).

The Ras Il Pellegrin section (RIP) in the Fomm Ir-Rih bay on the Island of Malta (Fig. 2; see Abels et al. 2005) was sampled for the Blue Clay Formation (BC) and the top

Figure 2. Ras Il Pellegrin section (Malta) seen from the southern shore of the Fomm Ir-Rih Bay showing the Globigerina Limestone Formation (Upper Member) with the clay rich interval and transitional bed, and the Blue Clay Formation with the sapropelitic- and iron nodule layers (SL and INL, respectively).

part of the UGL to generate a small overlap with the Marsalforn section. The GSSP of the Serravallian Stage has recently been ratified in this section at the base of the Blue Clay Formation at the top of the transitional bed (Hilgen et al., 2009). The Blue Clay Fm. consists of ~ 60 m of marly clays with $CaCO_3$-content fluctuating between ~10 and 50%. At the meter scale, sedimentary cycles are present as regular alternations of homogeneous greyish-blue marls and whitish-grey marls, previously linked to precession forcing. At a larger scale, intervals dominated by whitish marls can be recognized which have been related to short and long eccentricity (Abels et al. 2005). Two sapropelitic layers and several levels with chondrite trace fossils point to occasional dysoxic bottom water conditions during deposition of the Blue Clay Fm. (Abels et al., 2005; Bromley, 1990). One sapropelitic layer (SL) occurs between 23.9 and 24.3 m and a brownish, iron-rich layer labeled as "Iron Nodule Layer" (INL) is observed between 28.9 and 29.3 m (Fig. 2). The estimated paleodepth of the BC is around 500 to 600 m, similar to estimates for the UGL. (Bellanca et al., 2002; Bonaduce and Barra, 2002; see also Chapter 4.).

3. Methods

3.1 Calcareous plankton biostratigraphy

3.1.1 Planktic Biostratigraphy

A semi-quantitative analysis of planktic foraminifer assemblages was initially carried out on every other sample and later on all samples around bio-events. Counting is based on the number of a specific taxon in nine fields with a maximum of 20 specimens using a rectangular picking tray of 45 fields. In case of abundant taxa, all specimens in the first field were counted also when they exceeded 30 individuals. The counts, performed at species level, are shown as numbers per field (Fig. 3) to facilitate a direct comparison of the relative abundances of selected biostratigraphic marker taxa. For this purpose, *Paragloborotalia siakensis*, *Globoquadrina dehiscens, Turborotalita* cf. *quinqueloba*, and *Globorotalia peripheroronda* were selected as they show significant changes close to the Langhian/Serravallian boundary (Abels et al., 2005; Di Stefano et al., 2008; Hilgen et al., 2009).

3.1.2 Nannofossil biostratigraphy
A quantitative analysis of calcareous nannofossil assemblages was carried out for the Upper Globigerina Limestone and lower 20 m of the Blue Clay Fm. The analyses were performed with a polarized light microscope, at 1250X magnification, on smear slides prepared following the standard methodology of Bown (1998). A counting of 30 sphenoliths was performed to evaluate the abundance of *S. heteromorphus*, while 50 helicoliths were counted to quantify *Helicosphaera* species. The zonal assignment followed the scheme of Di Stefano et al. (2008) for the Langhian and Serravallian of the Mediterranean area. The quantitative patterns of selected taxa in percentages of the total assemblage are shown in Figure 3.

3.2 Stable Isotope Analysis
Oxygen and carbon isotopes were measured on specimens of the planktic foraminifer *Globigerinoides trilobus* and the benthic foraminifer *Cibicidoides dutemplei*. We assume that the isotope values for *G. trilobus* and *C. dutemplei* are indicative of surface and deep water isotope composition, respectively. Preservation is reasonably good with signs of dissolution in several of the BC and some of the UGL samples. Grain-size sorting is observed in some samples (BC and UGL) pointing to transportation and/or winnowing. Some samples from the UGL have secondary calcite overgrowth.

Measurements were performed on a SIRA-24 of VG (vacuum generators) and a Finnigan MAT 251 mass spectrometer coupled to a Carbo-Kiel Device (Type I), at Utrecht University. In total 738 samples have been measured, with an average sample distance of ~7 cm in the Globigerina Limestone and 9 cm in the Blue Clay Fm. Calcite tests of *G. trilobus* (size fraction 250-300 μm, average 30 per sample) were measured on the SIRA-24, while the less abundant *C. dutemplei* was measured using the Finnigan MAT 251/Kiel Device. Samples of *C. dutemplei* (minimum 6, average 8-10) were crushed and homogenized prior to analysis.

Results were calibrated using NAXOS (in-house standard) and IAEA-CO1 for the SIRA-24 and NAXOS and NBS19 for the Carbo-Kiel Device and are reported on the PeeDee belemnite (PDB) scale. For both devices, the standard external error is less than 0.05‰ and 0.10.‰ for $\delta^{13}C$ and $\delta^{18}O$, respectively. Replicate measurements on 25% of the samples indicate mean reproducibility better than 0.10‰ for $\delta^{13}C_p$, 0.15‰ for $\delta^{13}C_b$, 0.13‰ for $\delta^{18}O_p$ and 0.12‰ for $\delta^{18}O_b$.

3.3 Geochemical analysis
ICP-OES analysis has been performed on 426 samples from the Ras Il Pellegrin section (Malta) and 305 samples from the Marsalforn section (Gozo). Samples were dried and crushed to powder to homogenize. Subsequently, 125 mg of each sample was dissolved in 2.5 ml HF (40%) and 2.5 ml mixing acid (HNO_3 16.25% and $HClO_4$ 45.5%) and heated at 90°C in a closed vial for at least 8 hours. Samples were then evaporated at 160°C and subsequently dissolved in 25 ml HNO_3 (4.5%). The resulting solutions were analyzed for the elements Al, Ba, Ca, Cr, Cu, Fe, K, Mg, Mn, Ni, P, S, Ti, V, Zr by a Perkin Elmer Optima 3000 ICP-OES at Utrecht University. Where needed the results were refined using in-house standards (ise-921 and SO-1). Only Ca and P will be considered here, but a more extended discussion on geochemical elements is given in Chapter 4. Calcium carbonate ($CaCO_3$) content has been calculated from Ca, assuming that the majority of Ca is present in $CaCO_3$. High phosphorous contents may reveal the presence of phosphate nodules or levels (Föllmi et al., 2008; John et al., 2003).

4. Results

4.1 Biostratigraphy
Biostratigraphic results for the lower part of the Blue Clay Fm (BC) and Upper Globigerina Limestone Fm (UGL) are presented in Figure 3. For the BC, all biostratigraphic results have been published earlier in Abels et al. (2005), except for *Turborotalita* cf. *quinqueloba*.

The Acme interval of *Paragloborotalia siakensis* in the MRSF section follows an influx of *Globoquidrina dehiscens* observed at the base of the section. This faunal change is widely recorded in other Mediterranean successions (Di Stefano et al., 2008) and used to constrain the acme base of *P. siakensis*. The base of the acme (AbB) is positioned at

-0.77 m in the MRSF section and the acme end (AbE) at 13.92 m. In the RIP section, the AbE is present in the overlap interval with the MRSF section and positioned at -4.90 m (Fig. 3).

The AE of *T.* cf. *quinqueloba* is located at 19.64 m in the MRSF section and at 2.33 m in the RIP section (Fig. 3). This event forms an important biostratigraphic horizon in the Mediterranean and has recently been astronomically dated 13.751 (± 0.001) Ma at the La Vedova High Cliff section (Mourik et al., in review; Ch. 1).

The nannofossil *Helicosphaera waltrans* is abundant (>10%) in the assemblages of the UGL up till ~10 m where it shows a permanent decline. The Last Common Occurrence (LCO) of *H. waltrans* is difficult to pinpoint exactly as a first decline is observed at -10 m and a second at -12 m. Moreover, abundances of this species are much higher compared to Italian sections and DSDP site 372 (Di Stefano et al., 2008; Fornaciari et al., 1996). A third decrease at -15 m is probably not the LCO, as this event should not be younger than the AbE of P. siakensis (Di Stefano et al., 2008). The First Common Occurrence (FCO) of *Helicosphaera walbersdorfensis*, which for the first time exceeds 10% at 16.68 m, is more reliable for biostratigraphic purposes. The astronomical age of this event in the La Vedova High Cliff section is 14.026 (± 0.003) Ma (Chapter 1; Mourik et al., in review). In terms of calcareous nannofossil biozones, the UGL encompasses a stratigraphic interval that includes the LCO of *H. waltrans* and the FCO of *H. walbersdorfensis* corresponding to the MNN5a and MNN5b subzones of Di Stefano et al. (2008). The boundary between MNN5a/MNN5b is defined by the *H. waltrans* LCO, but the irregular pattern of *H. waltrans* does not allow to accurately position this event. The AbB of *P. siakensis* at the base of the section indicates that only part of the MNN5a subzone is present in the UGL.

4.2 Stable Isotopes

Benthic and planktic stable isotope records of the RIP and MRSF sections are shown in Figure 4. Benthic $\delta^{13}C$ ($\delta^{13}C_b$) values in the UGL of the MRSF section (Fig. 4a) vary between 0.5 and 2‰, with maximum values recorded between 3 to 8 m and around 14 m. Minima are observed between 0 and 2 m, 9 and 10 m and 16 and 17 m. A two-step shift of ~ 1‰ towards more positive values is observed from the base to the top of the Transitional Bed (TB) which can be recognized in the RIP section (Fig. 4b) as well. In the BC (RIP section), values show a similar range as in the UGL, but decrease gradually above ~6 m. The planktic $\delta^{13}C$ ($\delta^{13}C_p$) record fluctuates between 1.5 and 3‰ in both the UGL and BC and has a very similar pattern as $\delta^{13}C_b$. The two-step shift across the Transitional Bed is more prominent in the planktic record and show an increase in $\delta^{13}C$ by almost 1.5‰. In the Blue Clay, fluctuations in the planktic carbon isotope record are larger than in the benthic record and strong depletions recur at regular intervals. An increase in the difference between $\delta^{13}C_b$ and $\delta^{13}C_p$ ($\Delta\delta^{13}C$) is seen above the transition to the Blue Clay Formation.

The benthic oxygen isotope record of the UGL shows a gradual increase from the base to the top of ~0.9‰ with amplitude variability ranging between -1 to 0‰. Variability is low in the Clay Rich Interval between 8 and 10 m (MRSF section, Fig. 4a, b). In both sections, $\delta^{18}O_b$ shows an increase from -0.3‰ below the transitional bed to +0.3‰ in the BC. Values in the BC remain higher than in the UGL and fluctuate between 0 and 0.5‰. In contrast to the $\delta^{13}C$ records, the $\delta^{18}O_p$ record shows a very different pattern than $\delta^{18}O_b$. In the UGL, values remain more or less constant and are -1.5‰ on average. An excursion of ~ 0.75‰ towards lighter values can be observed between 8.5 and 9.5 m in the CRI of the MRSF section. Just after the top of the transitional bed, $\delta^{18}O_p$ shows a similar excursion, which is observed in both sections. Unlike $\delta^{18}O_b$, no step towards heavier values is observed $\delta^{18}O_p$. Instead the record shows an increase in amplitude variability, with values ranging between ~ -2‰ and -1‰.

5. Age Models

5.1 Revised tuning for the Blue Clay Formation

The Blue Clay Fm. has been astronomically tuned by Abels et al (2005). A revision of this age model is necessary for some reasons. Firstly, the astronomical solution used by Abels et al. (2005) is the $La2004_{(1,1)}$ solution of Laskar (2004). Precession-obliquity interference patterns in the proxy records of the La Vedova composite section in Italy

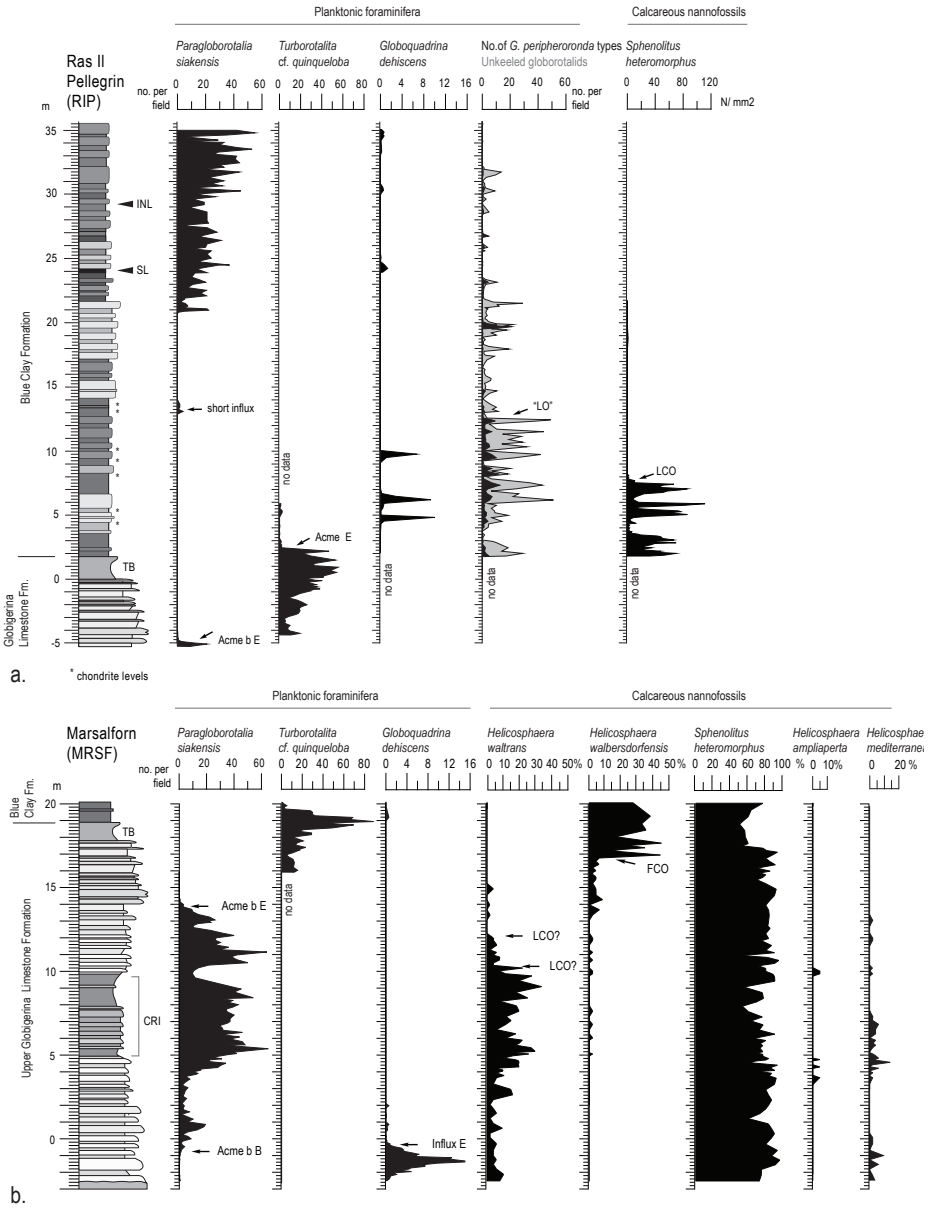

Figure 3.a) Lithological column of the Ras Il Pellegrin section (Fomm Ir-Rih Bay, Malta) showing the top of the Upper Member of the Globigerina Limestone Formation (UGL) with a 1.77m thick transitional bed (TB) and the lower 35 m of the Blue Clay Formation. One sapropelitic layer (SL) occurs between 23.9 and 24.3 m and a brownish, iron-rich layer labeled as "Iron Nodule Layer" (INL) is observed between 28.9 and 29.3 m. Next to the column semiquantitative abundance patterns for the planktic foraminiferal species *Paragloborotalia siakensis, Turborotalita* cf. *quinqueloba*, *Globoquadrina dehiscens*, unkeeled globorotalids (including the number of *G. peripheroronda* types) and for the calcareous nannofossil *Sphenolithus heteromorphus;* b) Lithological column of the Marsalforn section (west of Marsalforn village, Gozo) showing the UGL with a 1.12 m thick transitional bed and the basal part of the Blue Clay Fm. The base of the UGL is marked by a phosphate pebblebed. A ~5m thick clay rich interval (CRI) is observed between 5 and 10 m. Next to the column semiquantitative abundance patterns for the planktic foraminiferal species *P. siakensis, T.* cf. *quinqueloba*, *G. dehiscens*, and for the calcareous nannofossils *Helicosphaera waltrans, Helicosphaera walberdorfensis, Sphenolithus heteromorphus, Helicosphaera ampliaperta* and *Helicosphaera mediterranea.*

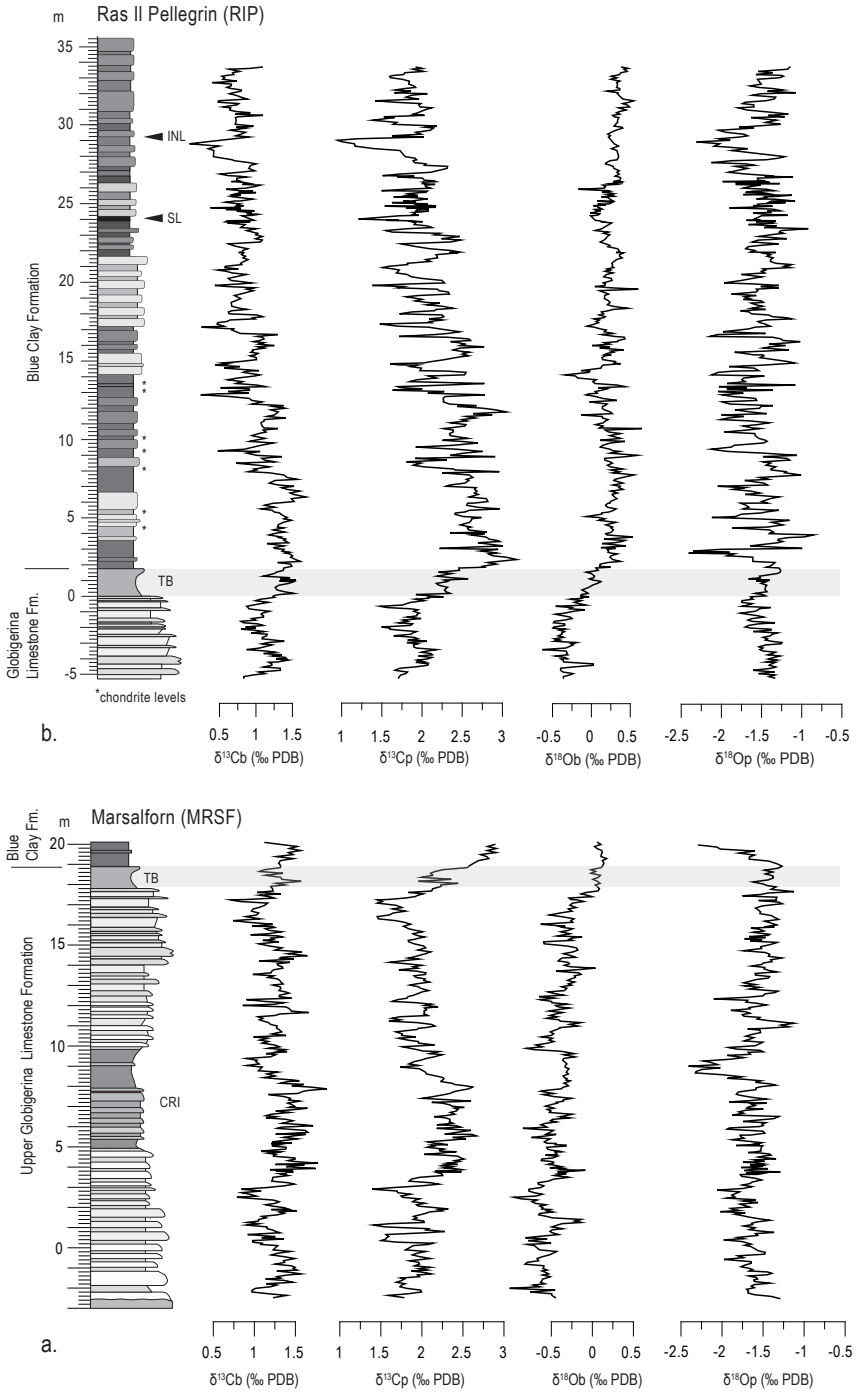

Figure 4. Benthic and planktic $\delta^{13}C$ and $\delta^{18}O$ isotope records for the Marsalforn section (a) and the Ras Il Pellegrin section (b).Grey shading reflects the transitional bed (TB).

(15.3-13.5 Ma) showed that the (1.0,9) solution is preferred over the (1,1) solution for the middle Miocene (Hüsing et al., 2010; Mourik et al., in review). Secondly, the AE of *T.* cf. *quinqueloba* adds a new astronomically-dated calibration point and is important for improving the tuning of the basal part of the Blue Clay Fm, which relied on counting cycles in Ca/K from the LCO of *S. heteromorphus* downwards (Abels et al. 2005). Thirdly, comparison of the Ti/Al record with the astronomically-tuned Ti/Al record of the La Vedova High Cliff section, suggests an opposite phase relation to precession than previously assumed. We slightly revised the tuning of the Ca/K cycles, with cycle 1 of Abels et al. (2005) tuned to the insolation maximum at 13.753 Ma, resulting in a new age for the top of the transitional bed of 13.76 Ma +/- 0.02 Myr. The uncertainty in the astronomical age calibration of the first cycle in the Blue Clay Fm. is less than one precession cycle, assuming that *T.* cf *quinqueloba* AE is a reliable biostratigraphic event for time correlations in the Mediterranean. Details of the revised tuning are presented in the supplementary information.

5.2 Astronomical tuning of the Upper Globigerina Limestone Formation

To construct a reliable age model for the Upper Globigerina Limestone Fm., isotope records were used in combination with biostratigraphic data. Unfortunately, no reliable characteristic remanent magnetisation (ChRM) could be determined using normal demagnetization procedures (Abels et al., 2005), even though very small, 20°C thermal heating steps, starting at 120°C, were applied to reveal any low temperature ChRM component as observed in the Monte dei Corvi section (Hüsing et al., 2007). This approach did not yield sufficiently reliable results and, therefore, no magnetostratigraphy could be established for the Upper Globigerina Limestone Formation.

Redfit spectral analysis, using the REDFIT program by Schultz and Mudelsee (2002), has been performed to reveal cyclicity in the $\delta^{13}C$ and $\delta^{18}O$ isotope records in the depth domain, which can potentially be linked to the astronomical parameters. Significant peaks in the $\delta^{13}C_b$ depth spectrum are present which correspond to cycle thicknesses of ~0.9, 2, and 3.8 m, with confidence levels between 90 and 95% (Fig. 5a). Figure 6a shows the lithological column of the composite section between -21 and +10 m as well as the $CaCO_3$ record and phosphorous content to identify the position of possible condensed intervals. A 0.8-1.4 m filter is used to depict the ~0.9 m $\delta^{13}C_b$ cycles in the depth domain.

To avoid large changes in sedimentation rates, the depth series has been converted into the time domain using an initial age model (IAM) based on astronomical ages of biostratigraphic events, derived from the tuning of the La Vedova Beach and High Cliff sections. The $\delta^{13}C_b$ time-series according to the initial biostratigraphic age model is shown in Figure 6b. The redfit power spectrum of $\delta^{13}C_b$ shows peaks at around 40, 100, and 405 kyr, remarkably similar to periods of obliquity and short and long eccentricity. The filtered components of these spectral peaks (35-45 kyr, 75-110 kyr and 350-450kyr) are shown in Figure 6b. These filters reveal highest amplitude variations in the interval between ~14.7 and 14.3 Ma. Despite the small number of calibration points in the initial biostratigraphic age model, the 405 kyr component nicely follows the 405-kyr eccentricity cycle, linking the carbon isotope maximum between 14.7 and 14.5 Ma to the 405-kyr minimum around 14.6 Ma. The next maximum in the 405-kyr component in $\delta^{13}C_b$ then corresponds to the younger 405-kyr minimum at ~14.2 Ma (Fig. 6b).

The combined influence of eccentricity and obliquity is clearly visible in the data between ~14.7 and 14.3 Ma. In this interval, eccentricity amplitudes are reduced due to minimum eccentricity values related to the 2.4-Myr cycle, thereby enhancing the relative influence of obliquity. This influence is further enhanced by the maximum in the 1.2-Myr obliquity cycle. Similar obliquity and eccentricity related cycle patterns have been observed in the Pacific and were tuned to an ET (eccentricity-tilt) target curve by Holbourn et al. (2005). For the tuning of the Mediterranean $\delta^{13}C_b$ record we constructed a 2ET target curve using normalized obliquity values and 2 times normalized eccentricity values, since the latter appears to be relatively dominant in the $\delta^{13}C_b$ record. The filtered ~40-, ~100- and ~400-kyr components have been added up in order to construct a curve reflecting the combined influence of eccentricity and obliquity in the $\delta^{13}C_b$ time series. Figure 6b shows that this record corresponds very well with the 2ET target curve. Starting from the observed phase relation with the 405-kyr eccentricity cycle, we assume that $\delta^{13}C_b$ maxima correspond to obliquity and eccentricity minima and, hence, to ET minima.

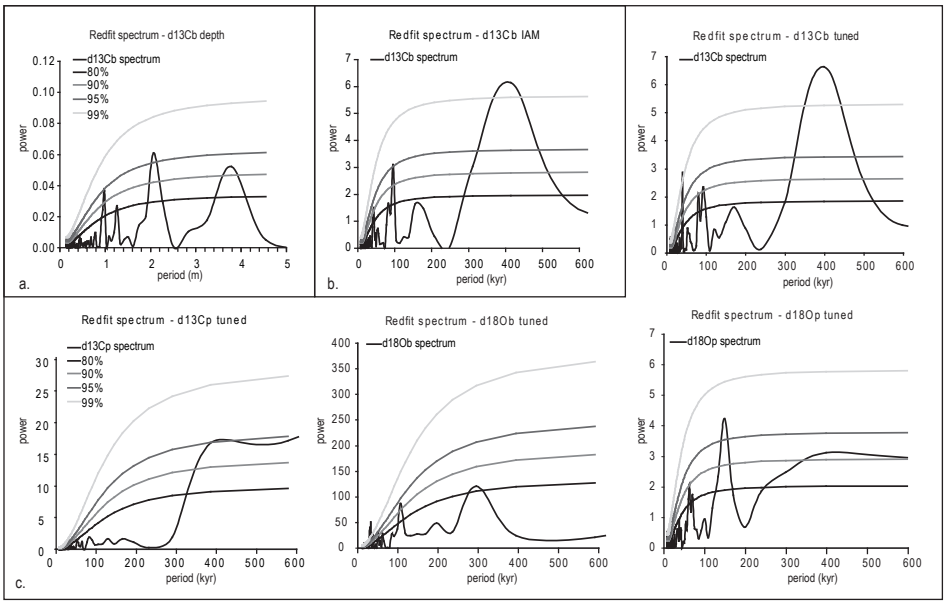

Figure 5. a) Redfit spectral plots of $\delta^{13}C_b$ in depth and in time using the initial age model based on the AbB of *P.siakensis* (14.87 Ma), the AbE of *P. siakensis* (14.23 Ma), the FCO of *H. walbersdorfensis* (14.03 Ma) and the top of the transitional bed (13.76 Ma). b) Redfit spectral plots of the tuned time series for $\delta^{13}C_b$, $\delta^{13}C_p$, $\delta^{18}O_b$ and $\delta^{18}O_p$.

These phase relations are similar to the phase relations that have been found in open ocean records for the same time interval (e.g. Holbourn et al., 2005; 2007). We further assume that no time lags are present as cyclic $\delta^{13}C_b$ variations in open ocean records vary approximately in-phase with $\delta^{18}O$ in the different frequency bands.

The three ~100 kyr $\delta^{13}C_b$ minima in the basal part of the Maltese record, between 14.70 and 14.95 Ma, are linked to the three pronounced maxima in the 2ET curve. However, if the gradual increase in *G. dehiscens* at -19.5 m is correlative to Influx B as observed at La Vedova (Italy) (Hüsing et al., 2010), the base of the section will be older with an age of ~ 15.1 Ma. This alternative option can not be excluded as sedimentation rates in the first few meters on top of the phosphate pebble bed were probably low.

A distinct cyclic pattern in $\delta^{13}C_b$ is observed between ~14.70 and ~14.45 Ma that likely corresponds to the minimum in the 405 kyr eccentricity cycle. Three maxima in the ~100-kyr component in $\delta^{13}C_b$, which are also present in the combined frequency curve, apparently correspond to every second 2ET minimum, thereby suggesting a double obliquity rather than an eccentricity signal. However, eccentricity cycles in this 405-kyr minimum have a period close to 80 kyr instead of 100 kyr. The three maxima in the combined filter are therefore linked to the minima in the target curve (Fig. 6b).

Between 14.45 and 14.15 Ma, the expression of the 100-kyr eccentricity cycle is reduced due to the eccentricity minimum in the 2.4 Myr cycle. Following the tuning of the older interval, the four ~40-kyr cycles in $\delta^{13}C_b$ are tuned to successively younger 2ET minima. From ~14.25 Ma onwards, cycles are difficult to determine in the $\delta^{13}C_b$ record. Moreover, phosphate enrichment between -4 and -2 m may points to a condensed interval (Fig. 6A), which is in line with the low sedimentation rates indicated by the initial age model.

The next higher reliable calibration point is the FCO of *H. walbersdorfensis* which is situated below a marked minimum in $\delta^{13}C_b$. This minimum is also observed in the $\delta^{13}C_p$ record and is tentatively correlated to the eccentricity maximum at ~14.0 Ma. From this point towards the top of the transitional bed, two maxima in $\delta^{13}C_b$ (A and B) are present, which according to the initial age model, should be tuned to the eccentricity minima at 13.95 and 13.85 Ma. However, the low average sedimentation rate and lack of the expression of a $\delta^{13}C_b$ minimum at 13.90 Ma adds some uncertainty to the tuning of this interval as elaborated upon in the supplementary information.

6. Discussion

6.1 Middle Miocene isotope records and age model uncertainties

The presence of phosphate beds in the Globigerina Limestone Formation (Pedley and Bennett, 1985; Rehfeld and Janssen, 1995; Föllmi et al., 2008) and the interruption of predominantly carbonate sedimentation by a clay rich interval in the UGL, reveal a dynamic sedimentation history during the middle Miocene. Despite the few biostratigraphic age calibration points, the distinct pattern in $\delta^{13}C_b$ seems to reflect orbital climate forcing by eccentricity and obliquity well, which allowed us to astronomically tune the record to the 2ET target curve. This resulted in an astronomical age model for the interval encompassing the MMCT that is independent of the age models developed for the same interval in the open ocean. Figures 7a and b show the bulk $\delta^{13}C$ and $\delta^{18}O$ records (Abels et al., 2005), the composite planktic and benthic $\delta^{13}C$ and $\delta^{18}O$ records (this study), and the bulk records of La Vedova High Cliff (Chapter 1; Mourik et al., in review). Furthermore, the benthic $\delta^{13}C$ and $\delta^{18}O$ records from Ceara Rise (Raffi et al. 2006; N.J. Shackleton, unpublished data), DSDP 558A (Flower and Kennett, 1993) and Pacific ODP sites 1237 and 1146 (Holbourn et al., 2005; 2007) are shown. Following the revised tuning of the Blue Clay Formation, the top of the Transitional Bed, which corresponds to the top of the Mi3b isotope event (Fig. 7a), is now dated at 13.758 (+/-0.02). This age is in close agreement with the age of the end of Mi3b as observed in the bulk isotope record of the La Vedova High Cliff section (Fig. 7a).

6.1.1 Onset of the cooling

The Maltese isotope time series show very similar patterns as recorded at equatorial Atlantic and Pacific sites, showing the CM5a, CM5b and CM6 carbon isotope maxima (Woodruff and Savin, 1991; Holbourn et al., 2007), but offsets exist in the timing of these events (Fig. 7b). The relationship between the carbon maxima and 405 kyr cycle of eccentricity is not always obvious. For example, CM5b clearly lags the 405 kyr minimum at 14.2 Ma in ODP Site 1146. The discrepancies can be explained by an error in the tuning of Site 1146, and an alternative tuning for this site is presented in the supplementary information (Fig. S4). This tuning resulted in revised isotope time series that are depicted next to the tuned time series of Holbourn et al. (2005; 2007) in Figure 7 (a, b).

With this revised tuning, the CM-events are more in line with the 405 kyr eccentricity cycle. The onset of CM5a now aligns with our Mediterranean record and for $\delta^{18}O$ there is a better fit with the transition from dominant eccentricity - to dominant obliquity controlled variability, which Holbourn et al. (2007) defined as the onset of the first cooling phase.

6.1.2 The cooling step – Mi-3b

Timing inconsistencies are also encountered in the critical interval encompassing the Mi3(a+b) event and CM6 isotope excursion. Here, discrepancies may arise from uncertainties in the tuning of the Maltese records. The planktic and benthic $\delta^{13}C$ records of Malta show a first increase at 13.96 Ma, at the base of the transitional bed (TB-base) and a second shift at 13.76 Ma, corresponding to the end of the Mi3b event (Fig. 7a). In the bulk record, only a small shift at the TB-base is observed, whereas a more pronounced step occurs at the TB-top. This discrepancy can possibly be explained by a change in bulk sediment composition after the transition to the Blue Clay Fm, due to a higher percentage of ^{13}C-enriched $CaCO_3$ derived from the surface waters. The bulk $\delta^{13}C$ record of La Vedova High Cliff (LVHC) shows the first major $\delta^{13}C$ increase at 13.85 Ma, which is ~100 kyrs later than on Malta. The tuning of LVHC seems correct and is constructed independently from any isotope record (Chapter 1; Mourik et al., in review). Moreover, the record of LVHC seems to be in line with the open ocean records (Fig. 7 a,b). The second step in the LVHC bulk record at 13.76 Ma is in agreement with the second $\delta^{13}C$ increase on Malta. The offset of ~100 kyr in the onset of the CM6 is possibly related to uncertainties in the tuning of the Maltese record in this interval. Figure 8 shows the two alternative tuning options (A and B) that we suggest for the transitional interval (see supplementary information for details).

The first tuning option (A) relates the $\delta^{13}C_b$ minimum at the TB-top to the ET-minimum at 13.85 Ma (see supplementary information), by which the main shift in the $\delta^{13}C$ bulk record of Malta aligns with that observed in the bulk record of La Vedova High Cliff (Fig.

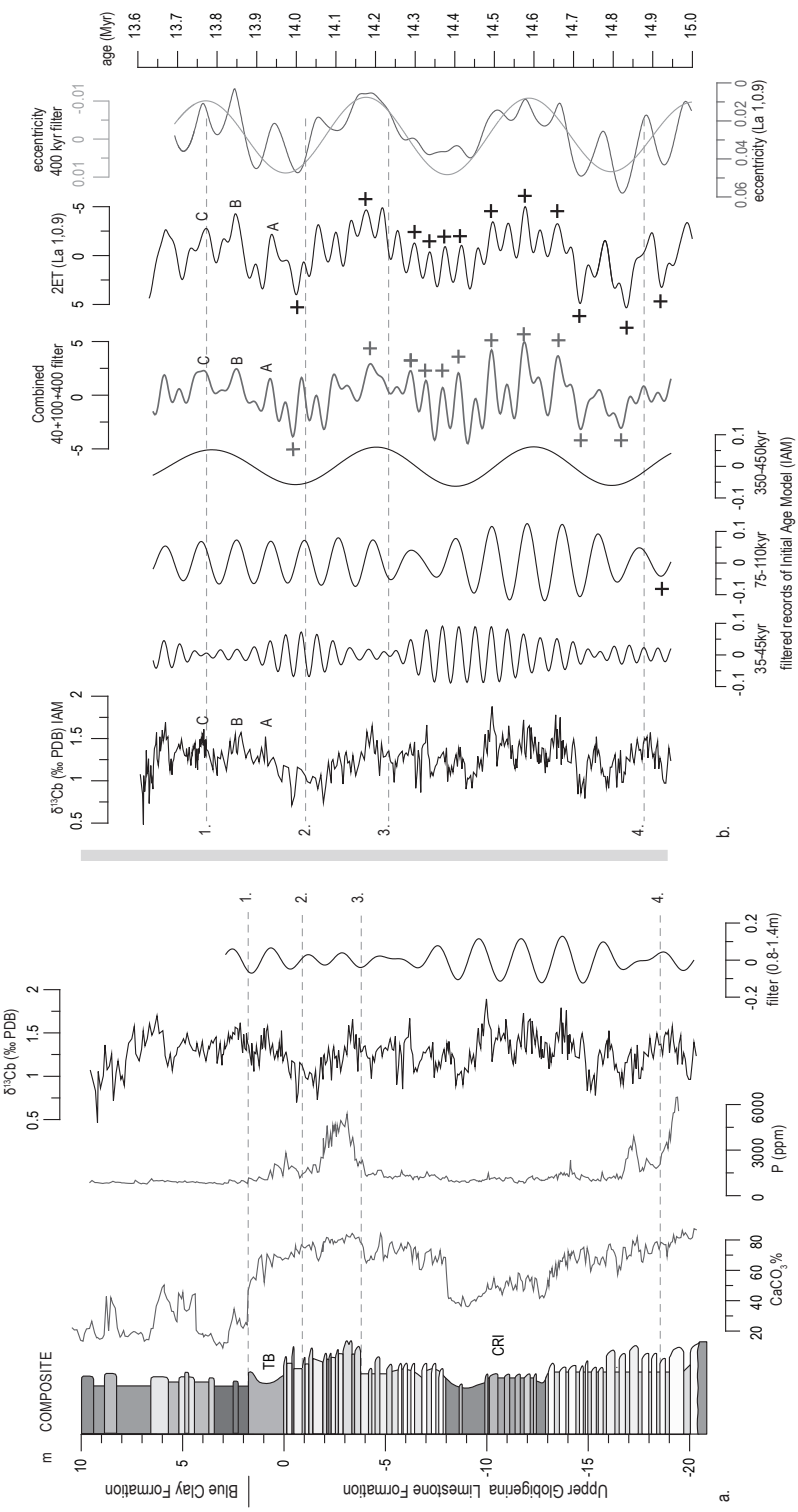

Figure 6.a) Lithological column of the Upper Globigerina Limestone Formation with the positions of the calibration points used for the initial age model: 1 = AbB of *P. siakensis* (14.87 Ma), 2 = AbE of *P. siakensis* (14.23 Ma), 3 = FCO of *H. walbersdorfensis* (14.03 Ma) and 4 = top of the transitional bed (13.76 Ma). Next to the column the records of $CaCO_3$, P (ppm) and $\delta^{13}C_b$ are shown as well as a 0.8 - 1.4 m filter; b). Correlation of the Upper Globigerina Limestone Formation to the 2ET curve using the combined filters resulting from spectral analysis of the $\delta^{13}C_b$ time series based on the initial age model. Calibration points are indicated with a + symbol and A, B, C in the upper part of the UGL. Two alternative tunings for this interval are presented in the supplementary information.

8b). In this option, sedimentation rates are greatly reduced at the base of the transitional bed (TB-base), which could imply that the interval with relatively light $\delta^{18}O$ values, prior to the Mi3b, would in this case be missing (Fig. 7a; 8a). Tuning option B relates the $\delta^{13}C_b$ minimum at the TB-top to the 2ET-minimum at 13.85 Ma (see supplementary information), by which the main shift in the $\delta^{13}C$ bulk record of Malta aligns with that observed in the bulk record of La Vedova High Cliff (Fig. 8b). Also the major bulk oxygen isotope enrichment at the TB-top indicates that tuning option B is more in line with the open ocean records. However, in this option, $\delta^{13}C$ in plankton and benthos shows still a first shift at 13.95 Ma which is not conform the timing of the other records. Unfortunately, the bulk records of LVHC do not provide a clue to the most likely tuning option. Concluding, a condensed interval or hiatus at the TB-base could explain the $\delta^{13}C$ patterns, whereas a condensed interval or hiatus at the TB-top would be more in line with the shift in bulk $\delta^{18}O$. The uncertainties in the tuning of the transitional bed could have implications for the Serravallian GSSP, which has recently been defined at the base of the Blue Clay Formation under the assumption that the transition from the UGL the Blue Clay Fm. coincides with the base of the Mi3b oxygen isotope phase and that this lithological transitions is continuous on Malta (Hilgen et al., 2009).

6.2 Causal connection between Mi3b and orbital configuration

The main Mi3b isotope shift in $\delta^{18}O$ has been related to a specific orbital configuration in which a node in the 1.2-Myr obliquity cycle coincides with a 405-kyr eccentricity minimum (Abels et al., 2005; Holbourn et al., 2005). Such a configuration would result in prolonged periods of low summer isolation due to minimal obliquity and precession amplitudes which would reduce summer melt of snow and ice and allow the growth of an incipient ice sheet. To investigate such a relationship, it is important to document the complete $\delta^{18}O$ shift in a continuous record that is astronomically tuned independently from characteristic patterns in the oxygen isotope series themselves.

The Maltese succession is independently tuned in the Blue Clay Formation approaching the Mi-3b from the top giving an age of 13.76 Ma for the top of the Mi-3b isotope shift. As discussed above, below this point there might be a hiatus or condensed sequence present, most likely at the base or at the top of the Transitional Bed. This is inferred from detailed comparison with the bulk sediment isotope record of La Vedova High Cliff section in Italy and with open ocean records, mainly ODP Site 1146, in which the isotope transitions start at ~13.87 Ma (Fig. 7a, 8a).

The La Vedova High Cliff bulk isotope record indicates a rather gradual transition in which the beginning of the transition is difficult to pinpoint exactly. The record starts to deviate from pre-shift average values around 13.92 Ma (Fig. 7a). The end of the transition occurs at 13.76 Ma. However, it is not certain if the bulk sediment record correctly depicts mean global ocean isotope values.

The ODP Site 1146 record reveals a more rapid transition which consists of two precession or obliquity cycles. Deviation from pre-shift values starts at 13.87 Ma and the end of the transition is dated at 13.84 Ma (Holbourn et al., 2007). However, our alternative astronomical age model suggests uncertainties in the interval preceding and including the isotope transition, and a hiatus of ~100-120 kyr may be present. The most logical place for a hiatus would be at the concurrent and instantaneous shift in $\delta^{13}C$ and $\delta^{18}O$ of the Mi-3b and CM-6 isotope events (see supplementary information).

The critical evaluation of the available stable isotope records and their respective astronomically-tuned age models still suggest a link between the Mi-3b event and long-period obliquity forcing in concurrence with a 405-kyr eccentricity minimum. However, uncertainties still remain in the continuity of the records and in the age models. An important issue here is: when did the shift in $\delta^{18}O$ exactly start, and how rapid was the transition? To better constrain the duration of the shift and its relation to orbital configuration, new, continuous isotopes records are still needed that can be tuned independently down to the precession scale.

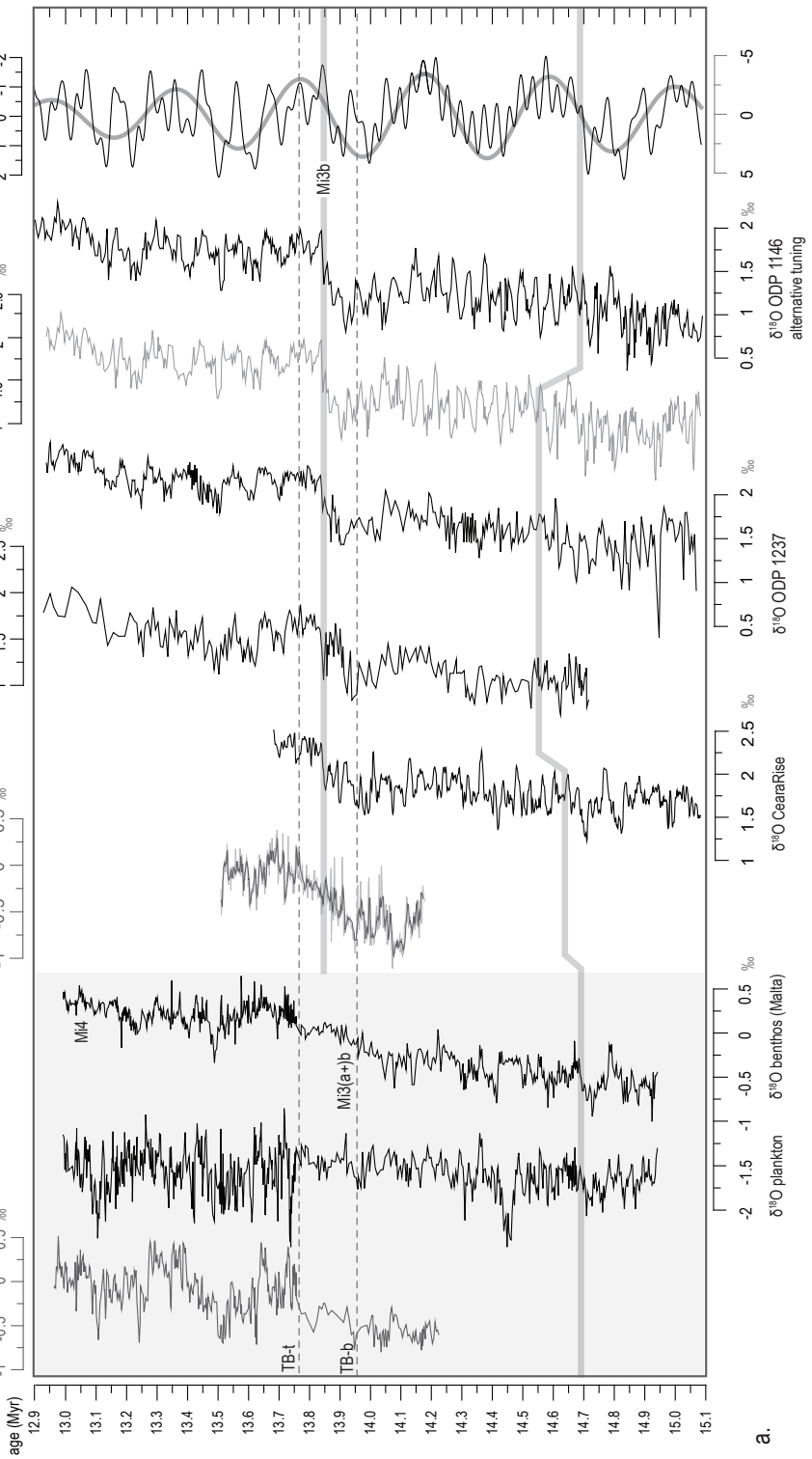
age (Myr)
δ18O bulk (Malta)
δ18O bulk LVHC
δ18O DSDP 588A
δ18O ODP 1146
2ET and 400 kyr filter
δ18O ODP 1146 alternative tuning
δ18O ODP 1237
δ18O CearaRise
δ18O benthos (Malta)
δ18O plankton
MI4
Mi3(a+)b
Mi3b
TB-t
TB-b
‰

a.

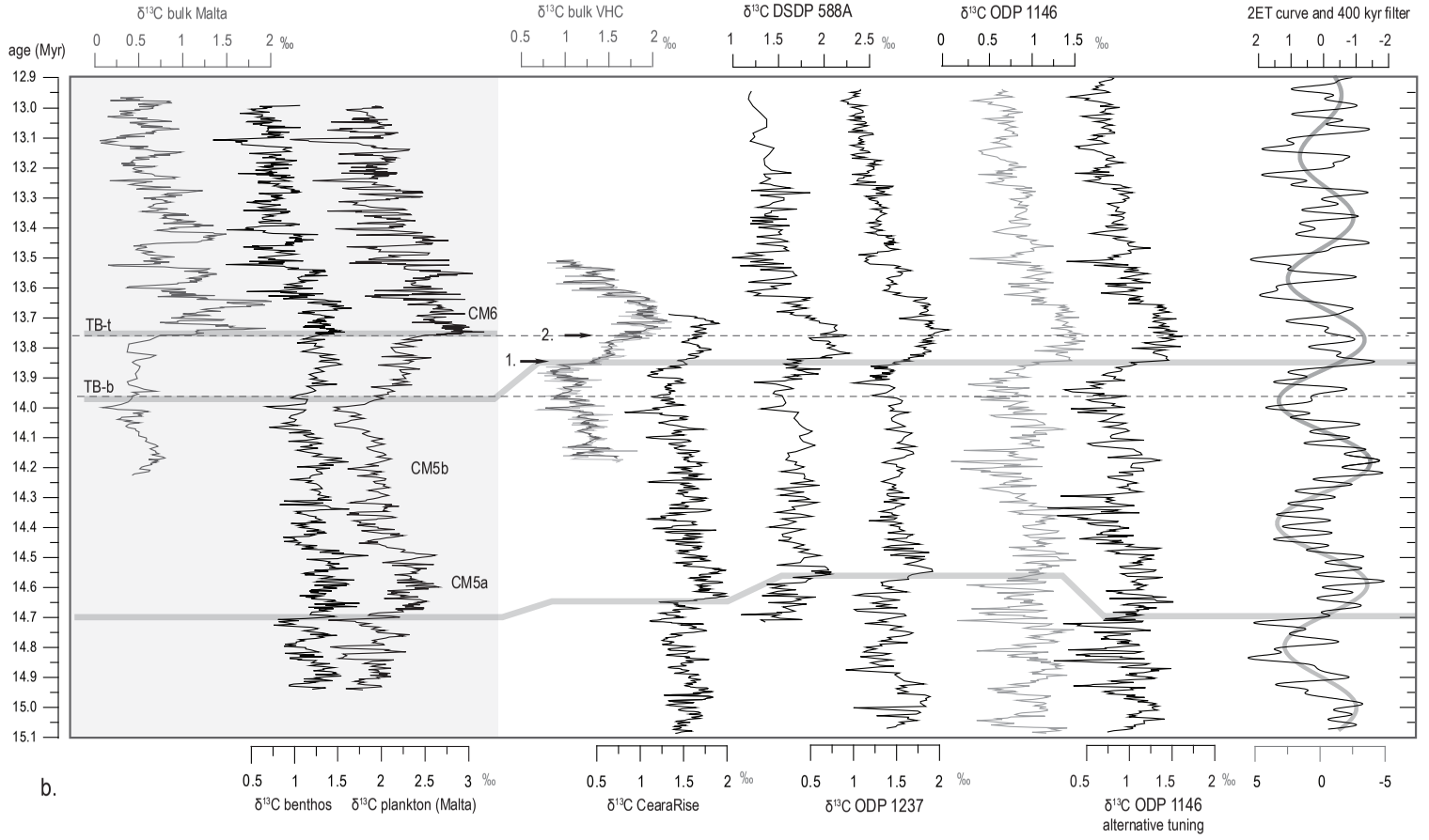

Figure 7 (a, b) Isotope records from the Maltese Islands (bulk, planktic and benthic), La Vedova High Cliff (bulk and 3 point moving average of bulk), and benthic records from Ceara Rise (Raffi et al., 2006; Shackleton, unpublished data), DSDP 558A (Flower and Kennett, 1993) and the Pacific ODP sites 1237 and 1146 (Holbourn et al., 2005; 2007) are shown. The first tuning option, as presented in the main text, is used for the UGL in this figure.

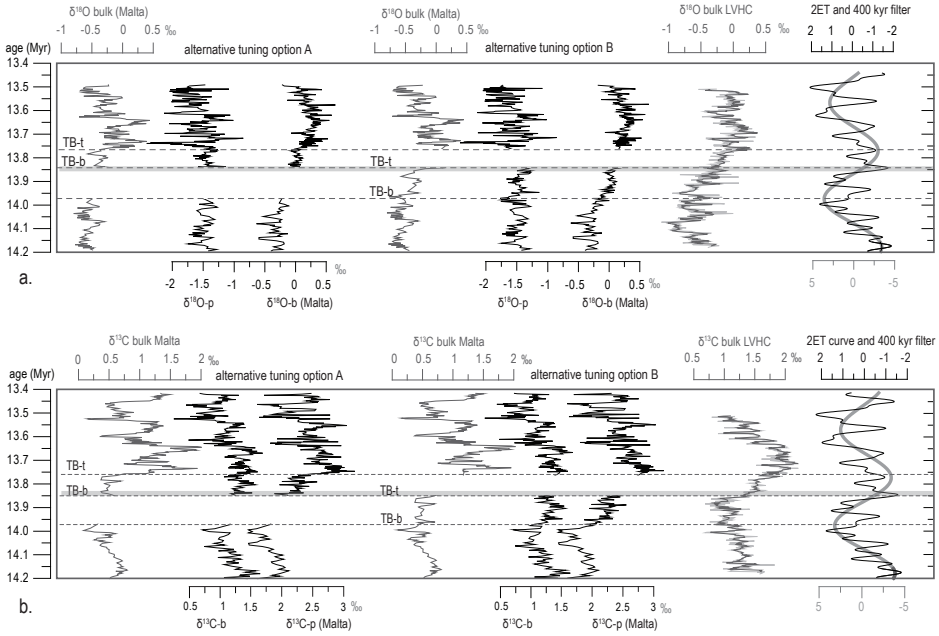

Figure 8 (a, b). Results of the alternative tuning options for the upper part of the UGL. See supplementary information for explanation and text for discussion.

6.3 Paleoenvironmental changes during the MMCT

The benthic oxygen isotope record from the Mediterranean Sea shows a gradual trend towards heavier values between ~14.95 and 13.95 Ma, prior to the Mi3b isotope shift (Miller et al., 1991, 1996). This trend reflects the gradual expansion of Antarctica's cryosphere from the end of the Miocene Climatic Optimum onwards (Shevenell et al., 2004; 2008; Zachos et al., 2001a). In contrast to the poorly defined Mi3a event, the Mi3b isotope shift is well visible in all benthic $\delta^{18}O$ records (Fig. 7a). Prior to the Mi3b, between ~14.0 and 13.9 Ma, open ocean records show a short interval characterized by relatively light benthic $\delta^{18}O$ values which might represent a warm phase. However, this signal seems to be absent in the Mediterranean where a gradual trend towards heavier values can be observed in both bulk and benthic records. As discussed above, this gradual trend could be the consequence of extremely low sedimentation rates in this interval and/or the presence of a hiatus at the TB-base. However, also in the LVHC bulk record the trend in $\delta^{18}O$ is more gradual, which could indicate that this phase of relatively light $\delta^{18}O$, was not recorded in the Mediterranean.

Estimates of the magnitude of Antarctic ice growth and temperature change during the middle Miocene suggest that ~70% of the ~1‰ shift was related to ice volume changes. The ~0.6 ‰ increase in benthic $\delta^{18}O$ between 13.95 and 13.76 Ma on Malta therefore suggest that bottom water temperature in the Mediterranean did not change significantly. The increase in $\delta^{18}O$ at ~13.1 Ma might reflect the Mi4-event (F_1 in DSDP Site 588; Woodruff and Savin, 1991; Westerhold et al., 2005).

In contrast to the benthic record, a cooling trend is not observed in the planktic $\delta^{18}O$ record. Instead, it shows much higher amplitude variability after the climate transition. Increased weathering and run-off have been suggested by John et al., (2003) to account for the increase in sedimentation rates after the climate transition. The establishment of a dry-wet climate oscillation system with seasonally enhanced influx of fresh water and/or changes in net evaporation is a likely cause for the high amplitude variability in $\delta^{18}O_p$ after the MMCT.

The Maltese carbon records show mainly the CM-carbon enrichments related to the Monterey Carbon Excursion (Woodruff and Savin, 1991). Carbon enrichments in the

Miocene have initially been thought to reflect primary productivity phases which promoted the sequestration of carbon in organic-rich sediments (Vincent and Berger, 1985). However, model studies and paleoproductivity reconstructions on Atlantic sites (DSDP 608; ODP 925, 1265) do not show any relationship between marine paleoproductivity and benthic foraminiferal $\delta^{13}C$ excursions (Diester-Haass et al., 2009). Instead, an increase in continental organic carbon burial could have caused $\delta^{13}C$ enrichment in the ocean's carbon pool.

Amplitudes of the carbon maxima observed in the various benthic records are largely consistent for CM5a and b, but differ for CM6. This event is particularly pronounced in the Pacific and South China Sea (Sites 588A, 1237, 1146 and 1171 – see Holbourn et al., 2007), but less clear in the equatorial Atlantic (Site 952) and the Central Mediterranean (Maltese Islands). The apparent absence of CM6 in site 1148 (South China Sea) (Tian et al., 2008; 2009) has been explained by the presence of an older, $\delta^{13}C$ depleted water mass from the deep Pacific. This same mechanism might explain the lack of expression of CM6 in the Atlantic sites and possibly also in the Mediterranean. However, the divergence of planktic and benthic records ($\delta^{18}O$ and $\delta^{13}C$) suggests that weakened circulation, limiting the mixing of $\delta^{13}C$ enriched surface water with deep water masses, is a more likely cause. A change towards a more sluggish circulation is also inferred from studies on benthic foraminifera (e.g. Chapter 4; Bellanca et al., 2002; Gebhardt, 1999) and can be seen as one of the major consequences of the MMCT on the Mediterranean. Finally, the carbon isotope records in the Blue Clay Formation can be correlated to records from the open ocean and continue to show eccentricity control with the recurrence of intervals with high-amplitude precession-related variations. Recurrent depletions in $\delta^{13}C$ have also been recognized in the La Vedova High Cliff section (Chapter 1) and are associated with the sapropelitic layers. Future investigations on the isotope records of the Blue Clay Formation should resolve what part of the signal is globally- and what part is regionally controlled.

7. Conclusions

We established an astronomical-tuned age model for the Upper Globigerina Limestone Formation and improved the tuning of the lower part of the overlying Blue Clay Formation. The Upper Globigerina Limestone Formation, dated between ~14.95 and 13.76 (+/- 0.02) Ma, records the entire Middle Miocene Climate Transition. However, uncertainties in the age model still exist for the upper part of the Globigerina Limestone Fm. where the possible presence of a condensed interval or hiatus can not be excluded.

Benthic and planktic carbon isotope records show 405 kyr maxima in $\delta^{13}C$, associated with the Monterey Carbon Excursion. Comparison with open ocean records suggested that the tuned age model for ODP site 1146 had to be revised, resulting in a much better fit with the astronomical target curve. The global middle Miocene cooling is reflected in the benthic oxygen isotope record, showing a ~0.6‰ increase (Mi3b) between ~13.95 and 13.76 Ma. Increased run-off after the climate transition probably caused a decrease in ventilation thereby inducing a divergence between the planktic and benthic isotope signals.

Acknowledgements
The authors would like to thank Geert Ittmann, Arnold van Dijk and Helen de Waard. For fruitful discussions we thank Ann Holbourn and Tanja Kouwenhoven. Heiko Pälike is acknowledged for providing the unpublished data of Nicholas Shackleton. The Darwin Center for Biogeosciences is acknowledged for financial support.

SUPPLEMENTARY INFORMATION

1. Composite

The base of the Transitional Bed has been used to construct a composite section for the Upper Globigerina Limestone Formation and Blue Clay Formation. Besides lithology, the correlation between the RIP and MRSF section is verified by the position of bio-events and characteristic patterns in the $\delta^{13}C_{p+b}$ isotope records (Fig. S1). In the composite, the lithological column is composed of the Blue Clay Fm and Transitional Bed as logged and sampled on Malta (RIP), and the Upper Globigerina Limestone Fm excluding the Transitional Bed as logged and sampled on Gozo (MRSF). For the isotope records an overlap between -0.5 and +2 m was chosen. Stratigraphic positions of the MRSF samples have been recalculated and adjusted to composite meters.

2. Revised tuning for the Blue Clay Formation

A revised astronomical tuning has been constructed for the Blue Clay Formation, using new astronomical ages from La Vedova High Cliff sections (Mourik et al., in review; Chapter 1) for the LO *S. heteromorphus* of 13.643 ± 0.001 Ma and the Acme End (AE) of *T. cf. quinqueloba* of 13.751 Ma, which was newly recognized on Malta. In the previous astronomical calibration (Figure S2a), tuning towards the base of the Blue Clay was based on precession-cycle counting downwards from the LO *S. heteromorphus.* Precession cycles were recognised from the Ca/K precession filter that in the interval above revealed to contain precession-forced basic cycles. The new calibration point of AE *T. cf. quinqueloba* now indicates that much less precession cycles are present in between these two bioevents and so that sedimentation rates were significantly higher in the lowest portions of the Blue Clay Formation. Therefore, we reinterpret the amount of precession cycles in the particular interval by excluding the cycles 2 and 5, that were defined as vague cycles previously though counted in the tuning (Figure S2b). A new astronomical tuning is then based on correlating cycle number 1 of Abels et al. (2005) now being tuned to the insolation maximum of 13.753 Ma (Fig. S2b). Then, the tuning is made by correlation of the cycles 3, 4, 6, 7, 9 to 17 to subsequent precession cycles. Above from cycle 17 we follow the tuning of Abels et al (2005). In this revised tuning, the two bio-events are in line with their respective ages at Vedova High Cliff section within uncertainty. Also, the extra cycle inferred in the previous tuning between cycles 17 and 18 has disappeared.

Assuming that Ti/Al maxima, related to arid conditions in northern Africa, are in phase between the southern (Malta) and northern (La Vedova + La Vedova High Cliff) Mediterranean sites, the Ti/Al records are used to independently check the BC tuning with respect to the tuning of the La Vedova High Cliff section. The revised tuning in Figure Sb already shows a much better fit of the Ti/Al patterns between Malta and Italy, although the phase relation to insolation is opposite (Fig. S2e). Changing the phase relation by half a precession cycle results in the tuning shown in Figure S2d and, accordingly, Ti/Al patterns are now in much better agreement (Fig. S2f). Moreover, the astronomical ages of the bioevents are even more in line with the astronomical ages derived from the tuning of the La Vedova High Cliff section, i.e. the influx of *P. siakensis* at ~13m is now related to an insolation maximum, and the "LO" of *G. peripheroronda* at 12.8 m is situated close to a minimum. The AE of *T*. cf. *quinqueloba* is dated at 13.748 Ma which is only ~3 kyr younger than the age obtained from La Vedova High Cliff, being 13.751 Ma. Therefore, we regard the latter as the best possible astronomical tuning for the Blue Clay Fm with the present knowledge. Following this tuning, the top of the Transitional Bed is dated 13.758 Ma with an uncertainty of less than a precessional cycle (0.02 Ma) that constitutes a still optional opposite phase relation and uncertainties in cycle recognition in the lowermost Blue Clay.

3. Two alternative tuning options

The transition from the Globigerina Limestone Formation to the Blue Clay Formation is characterized by a major increase in sedimentation rate. However, astronomical time control in this interval can not be gained due to lithofacies change and the age model has to rely on importing astronomical ages for bioevents. Between the LCO of *H. walbersdorfensis* (~1m below the base of the transitional bed) and the top of

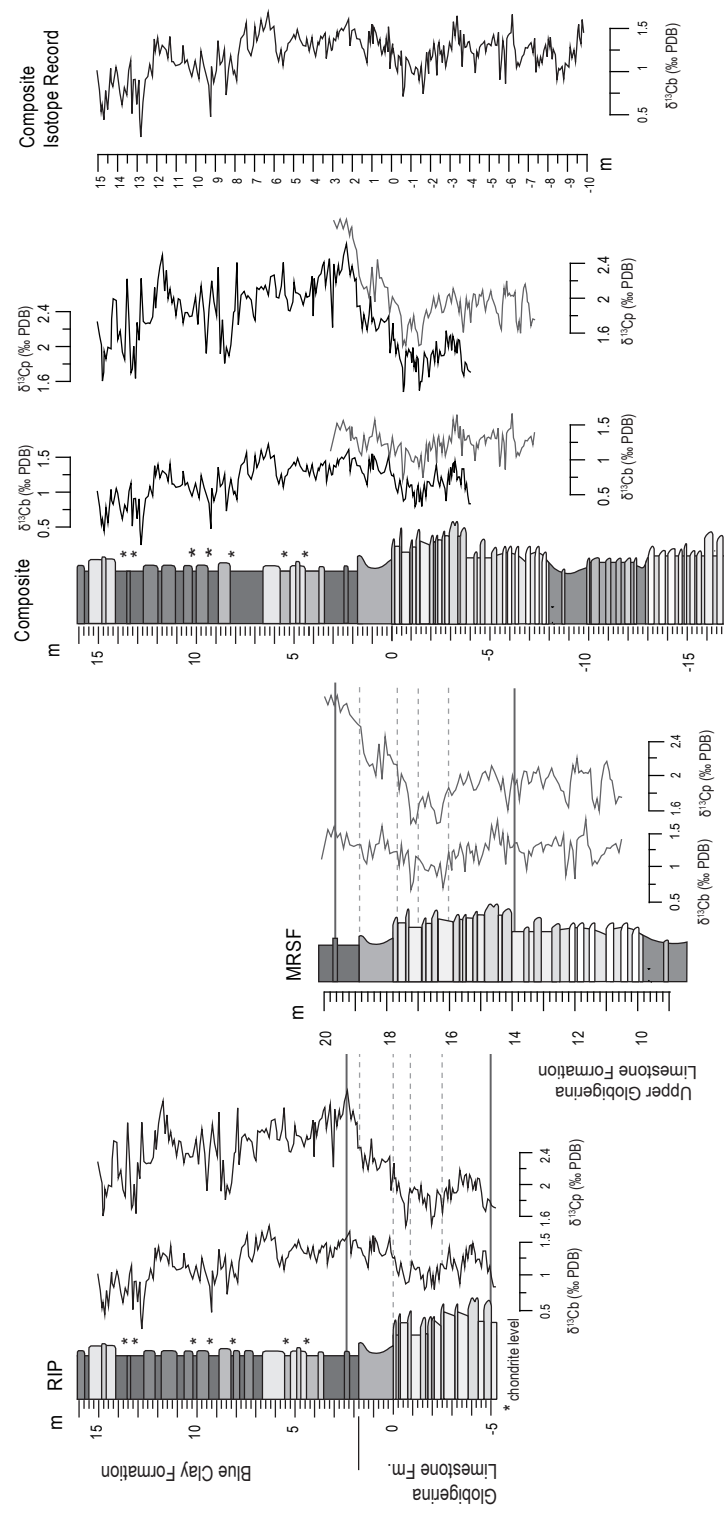

Figure S1. Correlation of the Ras Il Pellegrin section (Fomm Ir-Rih Bay, Malta) and the Marsalfom section (Marsalforn, Gozo) based on *T.* cf. *quinqueloba* AE, *P. siakensis* AbE and planktic $\delta^{13}C$ isotope correlation points.

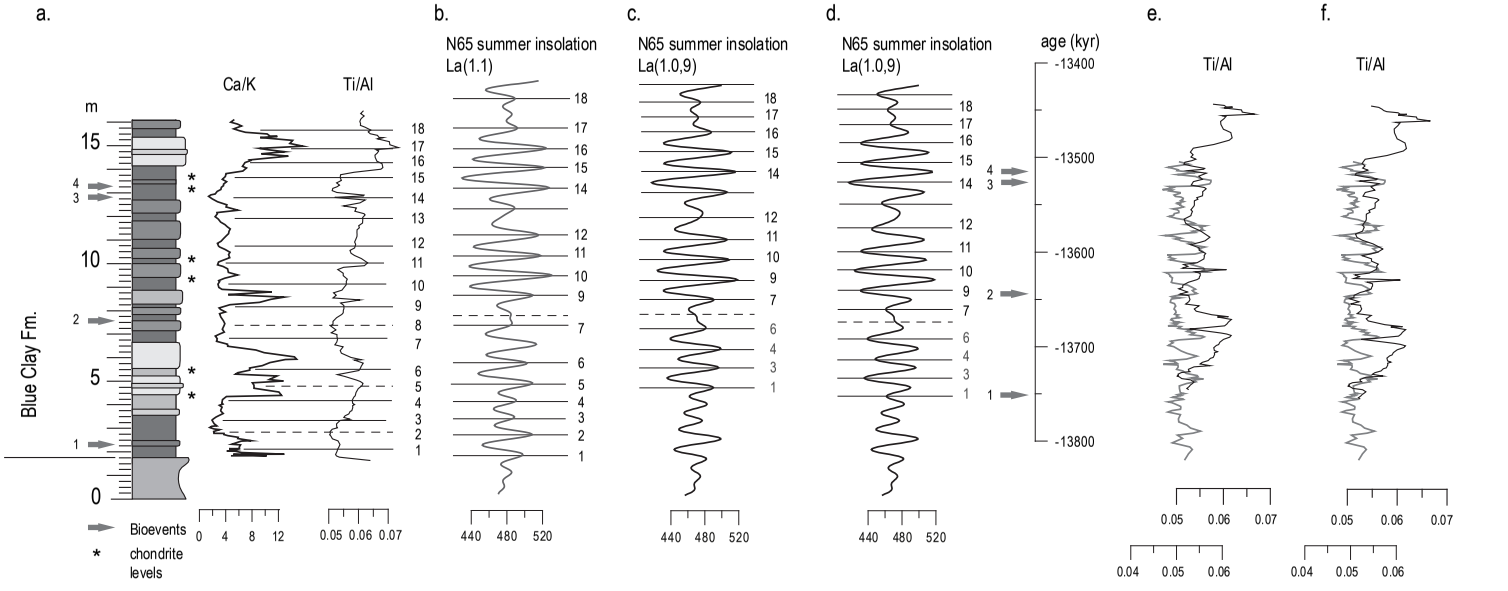

Figure S2. Revised tuning of the basal part of the Blue Clay Formation. Arrows indicate the position of bioevents: 1. = *T.* cf. *quinqueloba* AE, 2. = *S. heteromorphus* LCO, 3. = *G. peripheroronda* LO, 4. = *P. siakensis* short influx; a) The lowermost Blue Clay Formation with Ca/K cycles numbers after Abels et al., 2005; b) 65°N summer insolation of the La2004 (1,0.9) solution with the astronomical correlation made by Abels et al., 2005; c) Astronomical tuning of the lowermost Blue Clay Fm. based on a slightly revised age for the LO *S. heteromorphus* and the age for the newly recognized AbE of *T.* cf. *quinqueloba*. See text for further explanation; d) Astronomical tuning of the lowermost Blue Clay Fm. based on an opposite phase relation of Ca/K to insolation maxima. The resulting Ti/Al patterns of Malta are more in line with La Vedova High Cliff (see panel f); e) Ti/Al records of the astronomical tuning on Malta, according to the tuning in panel c with Ca/K maxima to insolation maxima, in black and of the La Vedova High Cliff section in grey; f) Ti/Al records of the astronomical tuning on Malta, according to the tuning in panel d with Ca/K maxima to insolation minima, in black and of the Vedova High Cliff section in grey.

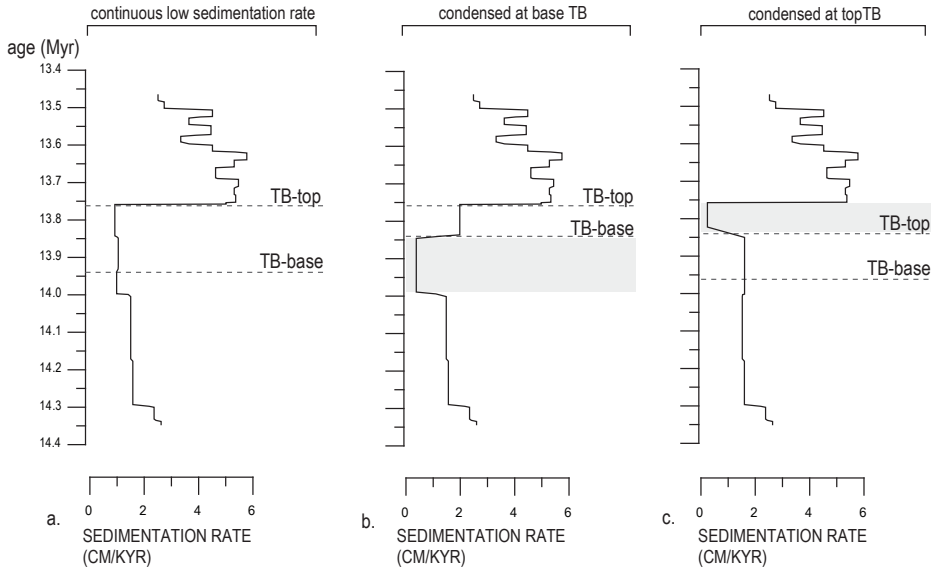

Figure S3. Sedimentation rates across the transition from the Globigerina Limestone Formation to the Blue Clay Formation for the different tuning options; a) Sedimentation rate pattern for the tuning as decribed in the main text; b) Sedimentation rates for tuning option A, with a condensed interval or hiatus at the TB-base; c) Sedimentation rates for tuning option B, with a condensed interval or hiatus at the TB-top.

the transitional bed (13.758 Ma) average sedimentation rate is 1.0 cm/kyr, which is considerably lower than the calculated sedimentation rate of ~5.9 cm/kyr for the basal part of the BC (Fig. S3a). In the tuning based on the initial age model, the minima A and B (Fig. 6b) are linked to the ET minima at ~13.95 and ~13.85 Ma, which follows directly from the assumption of a low but constant sedimentation rate between the base of the transitional bed (TB-base) and the top of the transitional bed (TB-top). However, the decreasing carbonate content in the transitional bed (Fig. 6a) suggests that sedimentation rates rather increased and not decreased with respect to the UGL. In addition, sea level lowering during the rapid EAIS expansion could have caused a hiatus at the TB-top.

A first alternative tuning (A) would be to correlate minimum A (TB-base) to minimum B in the ET target curve (see Fig. 6b), thereby generating a very condensed interval, or hiatus, at the TB-base (Figure S3b). Sedimentation rates will drop to 0.4 cm/kyr between -0.6 and 0 m, then increasing to 1.9 cm/kyr in the transitional bed. The age of the TB-top will remain 13.758 Ma.

In the second alternative (B), minimum C (TB-top) is linked to minimum B in the ET target curve. The first calibration point above the TB-top is cycle 1 at ~2.0 m, which, according to the revised tuning, is linked to the insolation maximum of 13.753Ma. Sedimentation rates across the transitional bed are 1.6 cm/kyr, which is more in line with sedimentation rates in the upper part of the UGL. In the condensed interval at the TB-top, sedimentation rates are 0.2 cm/kyr.

Depending on which scenario will be chosen, the top of the transitional bed, reflecting the most important step in environmental change in the Central Mediterranean, will be at 13.758 Ma, assuming that no hiatus is present at the base of the Blue Clay Fm. The time involved in the transition from the UGL to BC will be 180 kyr if sedimentation was continuous, or 91 kyr in case a hiatus or highly condensed interval is present at the TB-base. Tuning the TB-top to 13.846 Ma, as in the second alternative, the duration of the transitional bed would be 112 kyr.

4. Revised tuning of ODP Site 1146.

Comparison of the astronomically-tuned $\delta^{13}C$ of Malta with the ODP Site 1146 record revealed discrepancies that asked for an evaluation of the tuned age model of ODP site 1146 (Holbourn et al., 2005; 2007). Holbourn et al. (2005; 2007) did not follow the shipboard splice and mainly used hole A while adding two short intervals from hole C to construct a revised splice. These intervals in hole C were selected on the basis of additional isotope data from inferred short overlaps (Holbourn et al. 2007).

The shipboard splice of site 1146 (Shipboard Scientific Party, 2000) is not very convincing in the Middle Miocene as core breaks of the two remaining holes A and C start to coincide and characteristic patterns in magnetic susceptibility, color and natural gamma ray are difficult to recognize in potential overlaps. It seems not possible to enhance the shipboard splice based on these data.

The 400- and 100-kyr eccentricity related cycle patterns can rather easily be identified in the isotope depth records of Holbourn et al. (2005; 2007). Such patterns are clearly visible in both records between 570 and 510 m, and between 490 and 460 m, while they can only be recognized in the $\delta^{13}C$ record between 510 and 490 m (Fig. S4). However, this pattern is markedly interrupted by a strong peak at 530 m in both $\delta^{13}C$ and $\delta^{18}O$, which originates from a short interval of hole C that is incorporated in the revised splice of Holbourn et al. (2007). In our revised composite depth scale, we removed this interval from the splice, because it disturbs the 400-kyr scale related cycle pattern and because a similar peak is not found in other isotope records from the open ocean, such as Ceara Rise (Figure 7). For our tuning, we assumed that the pronounced peak at 538 m indeed corresponds to the most prominent 100-kyr eccentricity maximum at 15.6 Ma. Subsequently, we tuned 100-kyr eccentricity related peaks between 530 and 510 one 100-kyr eccentricity maximum older than in the tuning of Holbourn et al. 2007 (Fig. S4). In fact, this adjustment results in a better fit with the expression of the 400-kyr eccentricity cycle in the isotope records, especially $\delta^{13}C$. The identification of eccentricity related patterns in $\delta^{13}C$ can be continued in the younger interval between 510 and 490 m resulting in the revised tuning proposed in Figure S4.

We assume that the revised astronomical tuning is the best possible with the available data as most eccentricity related patterns are identified. However, ideally, the depth series should be based on a robust and reliable splice to eliminate potential problems at core breaks. The only possible solution to check all core breaks in hole A is to establish isotope records for the whole of hole C.

The revised tuning generates new discrepancies, especially in the number of obliquity-related cycles in the $\delta^{18}O$ time series as compared with obliquity in the interval between 14.6 and 13.85 Ma (Figures 7 and S4). Regarding the good fit with eccentricity and the number of obliquity-related cycles in the lower part of this interval, this discrepancy seems to be confined to the interval between 14.2 and 13.85 Ma. This can be explained by the fact that the $\delta^{18}O$ record in the interval between 14.2 and 13.85 Ma does not reflect obliquity dominance but the combined influence of eccentricity and obliquity, as also suggested by the (2)ET target curves. However, the thickness of the obliquity related cycles in $\delta^{18}O$ between 510 and 495 m remains constant between 495 and 490 m (Figure S4). From this perspective, it is logical to assume that these cycles are related to obliquity as well. The presence of 4.5 to 5 cycles in the interval between 14.15 and 13.85 Ma according to our revised eccentricity-based age model suggests a hiatus of ~100-120 kyr. This would then most likely coincide with the concurrent and instantaneous shift in $\delta^{13}C$ and $\delta^{18}O$ at 490 m. Alternatively the 1146A 52/53 core break at 491.75 m can be responsible for the offset, although it remains difficult to lose about 3 meter of sediment at the core break.

The possible presence of a hiatus at site 1146 may shed new light on the tuning of ODP site 1148 of the same leg in the South China Sea (Tian et al., 2008). They explain the absence of the CM6 carbon event at this site to the influx of deep Pacific waters with a different $\delta^{13}C$ signature rather than to a hiatus. However, within the scope of this paper, we decided not to go into the details of the tuning of this site.

Clearly, a robust tuning of isotope records from the open ocean is necessary to solve the problems with existing age models and explore the potential link between the Mi3b isotope shift and orbital configurations in more detail.

Starting from our revised age model, we carried out a cross-spectral analysis between

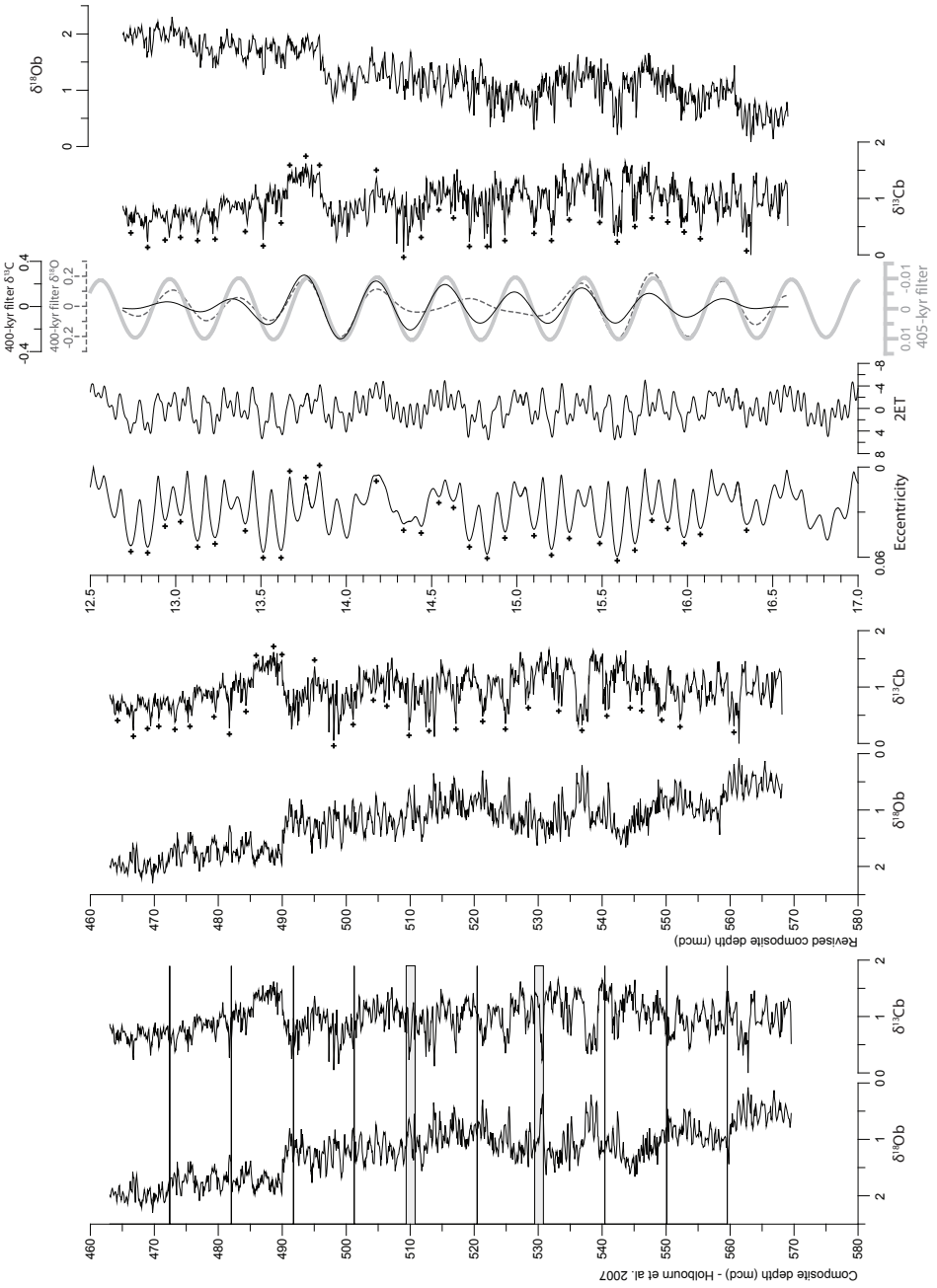

Figure S4. Stable isotope records of ODP Site 1146 showing the original depth series of Holbourn et al. (2007) and the revised depth records and tuning of this paper. Tuning to eccentricity is based entirely on the $\delta^{13}C$ record as it is strongly influenced by eccentricity throughout the record. Selected age calibration points and their correlation to the eccentricity time series are indicated by crosses. The position of the core breaks in hole A and the intervals in the splice of hole C (hatched) have been indicated in the original depth series of Holbourn et al. (2007).

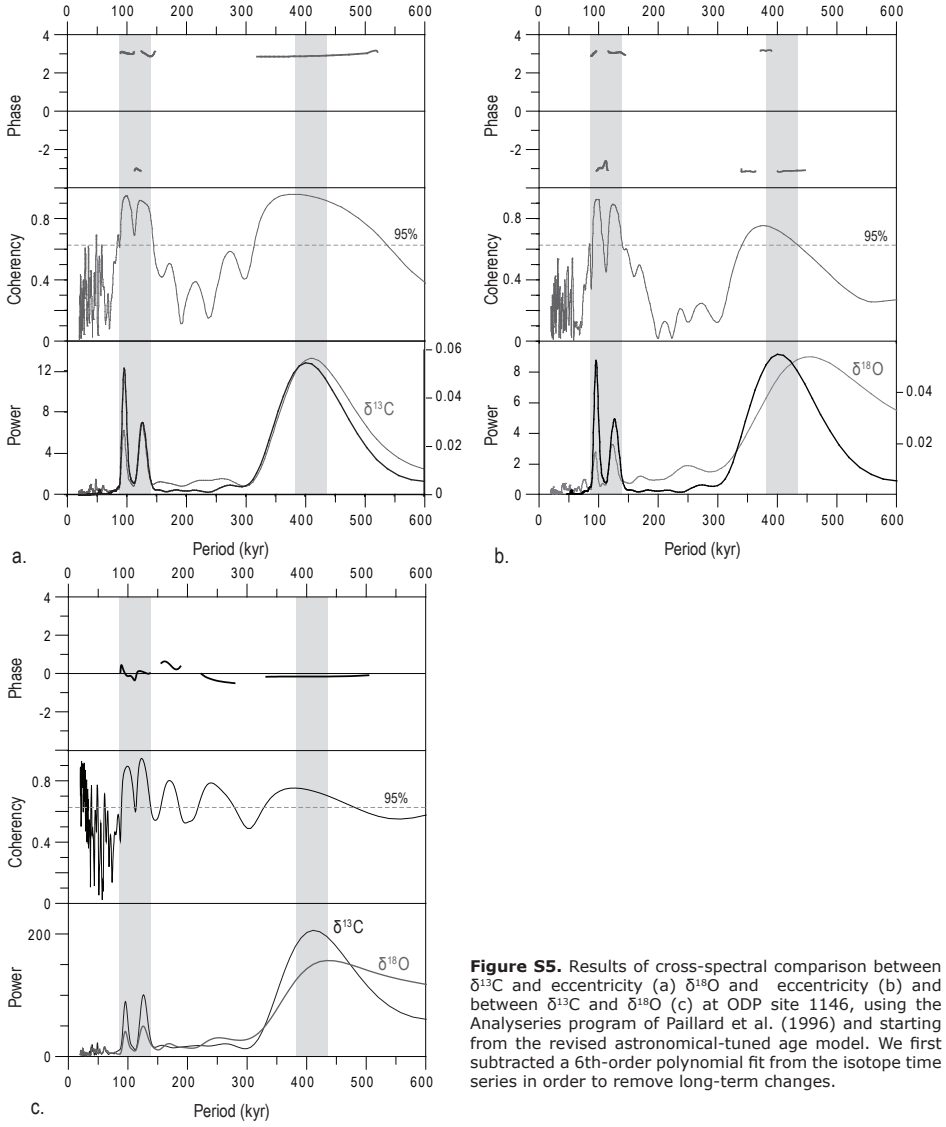

Figure S5. Results of cross-spectral comparison between $\delta^{13}C$ and eccentricity (a) $\delta^{18}O$ and eccentricity (b) and between $\delta^{13}C$ and $\delta^{18}O$ (c) at ODP site 1146, using the Analyseries program of Paillard et al. (1996) and starting from the revised astronomical-tuned age model. We first subtracted a 6th-order polynomial fit from the isotope time series in order to remove long-term changes.

the $\delta^{13}C$ and $\delta^{18}O$ time series and eccentricity, and between $\delta^{13}C$ and $\delta^{18}O$. The results reveal a strong ~400-kyr peak in both $\delta^{13}C$ and $\delta^{18}O$ spectra as well as the expected double 100-kyr peak, which at least partly result from the tuning to eccentricity itself (Fig. S5). Coherency is significant for all peaks in the eccentricity bands at the 95% confidence level. The 100- and 400-kyr cycles in $\delta^{13}C$ and $\delta^{18}O$ are in anti-phase with eccentricity, as isotope maxima correspond to eccentricity minima. The 100-kyr cycles in $\delta^{13}C$ and $\delta^{18}O$ are approximately in-phase with one another, but the ~400-kyr cycle in $\delta^{18}O$ reveals a short lag with respect to $\delta^{13}C$ (Fig. S5). Similar lags have been found elsewhere (e.g. Pälike et al., 2006; Holbourn et al., 2007), although the lag is significantly larger at site 1237 (Holbourn et al., 2007, their Fig. 7). This lag may be explained by the global carbon cycle through a delay in the response of continental weathering to orbital forcing by the 400 kyr eccentricity cycle as compared to the 100-kyr cycle, due to the long timescale associated with weathering (Holbourn et al., 2007).

In contrast, Holbourn et al. (2007) did not find a significant coherency at the 95% level between the 400-kyr cycle in both $\delta^{13}C$ and $\delta^{18}O$ and eccentricity. The improved outcome of the cross-spectral analysis provides an argument in favor of the alternative tuning that we propose for the isotope records of site 1146. Removal of the aberrant peak in these records at 530 m that originates from hole 1146C and retuning the eccentricity related cycle pattern between 530 and 510 m one 100-kyr cycle older and continuing this tuning upwards will have led to an increase in the coherence in the long eccentricity frequency band of the spectrum.

Chapter 4

Benthic foraminiferal response to environmental changes during the Middle Miocene Climate Transition in the Central Mediterranean (Maltese Islands)

A. A. Mourik, J. Sprong, T. J. Kouwenhoven and G. J. van der Zwaan

Submitted to Marine Micropaleontology

Abstract
Benthic foraminifera from a composite marine section of Langhian/Serravallian age sampled at the Maltese Islands (Malta and Gozo; Central Mediterranean) have been studied to gain more insight in the effects of the Middle Miocene Climate Transition (MMCT: ~15-13.7 Ma) on Mediterranean paleoenvironments and circulation patterns. In addition, geochemical element and isotope records have been studied. The transition from the Globigerina Limestone Formation (late Langhian) to the Blue Clay Formation (Serravallian) is related to the Mi3b oxygen isotope event, reflecting the major middle Miocene expansion of the East Antarctic Ice Sheet. Between ~14.95 and 13.9 Ma, the benthic assemblage points to a mesotrophic and well ventilated environment. Minor shifts in the assemblage of the Upper Globigerina Limestone are recorded in the clay-rich interval, possibly related to temporarily increased influx from northern African rivers such as the Nile. At ~13.76 Ma, a rapid increase in clay influx at the base of the Blue Clay Formation causes carbonate content to drop by more than 50%. Increased river runoff is associated with an increase in organic matter availability and lower bottom water oxygen levels to which the benthic assemblage responds with an increase in infaunal taxa, indicating a more eutrophic environment. Ongoing environmental changes, related to restriction in circulation after the MMCT are inferred from the successional increase in infaunal species. The geochemical and isotope records point to monsoonal climate variability at least from the MMCT onwards, which is confirmed by the occurrence of the first sapropelitic sediments and associated benthic taxa at 13.24 Ma.

1. Introduction

The Middle Miocene Climate Transition (MMCT, ~15-13.7 Ma) is one of the major steps in Cenozoic climate evolution. After the warmest interval of the Neogene, the Miocene Climatic Optimum (MCO) (~17-15 Ma), a cooling phase and the rapid expansion of the East Antarctic Ice Sheet (EAIS) at ~13.8 Ma changed global climate considerably (Flower and Kennett, 1994; Shackleton and Kennett, 1975; Woodruff and Savin, 1989; Woodruff and Savin, 1991; Zachos et al., 2001a). Pole-to-equator temperature gradients increased, ocean circulation patterns changed and floral and faunal distributions shifted (e.g. Flower and Kennett, 1994).

Increasing ice volume and ocean cooling during the middle Miocene are particularly evident from benthic oxygen isotope records. The most prominent increase during the middle Miocene: the Mi3b of Miller et al., (1991, 1996) or E2/E3 of Woodruff and Savin (1991), represents the rapid expansion of the East Antarctic Ice Sheet around ~13.8 Ma. Concomitant is the onset of the last carbon isotope maximum (CM6) of the Monterey Carbon Excursion (Woodruff and Savin, 1991).

The termination of the warm MCO and onset of the MMCT have been related to various factors including drawdown of CO_2 by increased silicate weathering (Raymo and Ruddiman, 1992; Wan et al., 2009) and increased carbon burial during the Monterey Carbon Excursion (Diester-Haass et al., 2009; Vincent and Berger, 1985). However, pCO_2 reconstructions for the middle Miocene are not in agreement. Marine geochemical proxies suggest that the pCO_2 has been more or less constant throughout the middle Miocene (Pagani et al., 1999; Pearson and Palmer, 2000). In contrast, recent work on stomatal frequencies suggests a drop in pCO_2 from 400-500 ppmv during the climatic optimum, to 300 ppmv at the time of EAIS expansion (Kürschner et al., 2008).

The restriction and/or closure of the eastern portal of the Tethys Seaway, connecting the proto-Mediterranean to the Indian Ocean, has often been mentioned as another important factor initiating long-term cooling (Woodruff and Savin, 1989; Wright, 1992). However, the exact timing of the closure of the Tethys Seaway is still under debate and estimates range from an early Oligocene to a late middle Miocene closure (Harzhauser et al., 2002; 2007; Hüsing, 2008; Smart et al., 2007). Differentiation between marine faunal provinces and mammal migration waves in the middle Burdigalian (18-19 Ma) (Rögl, 1999; Haurzhauser et al., 2007) suggest that marine connections were impaired well before the onset of the MMCT, although a connection to the Pacific/Indian Ocean during the MMCT can not be entirely excluded.

Nevertheless, the Mediterranean was subject to global climatic changes as evidenced by stable isotope records presented in the preceding chapters. To evaluate the effect of these changes on Mediterranean paleoenvironments, we combine benthic foraminifera

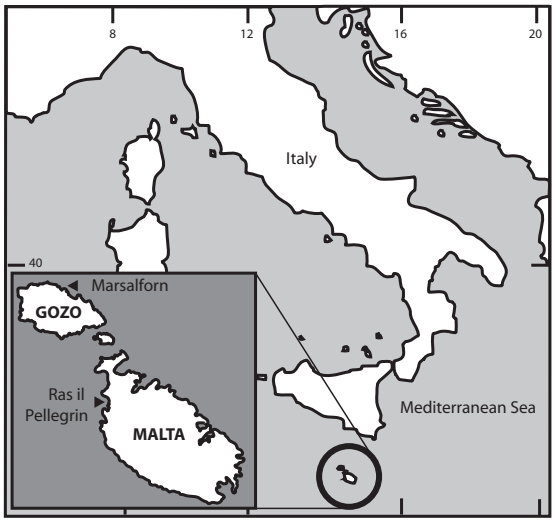

Figure 1. Location map of the Marsalforn section on Gozo and the Ras Il Pellegrin Section on Malta (Maltese Islands, Central Mediterranean).

with geochemical proxy data. Changing paleoenvironments must be reflected by benthic foraminifera, of which distribution in the sediment is predominantly influenced by oxygen and food availability (e.g. Jorissen et al., 1995). The TROX model predicts that oxygen and organic matter supply are the dominant parameters structuring benthic foraminifera assemblages. Oligotrophic, generally well oxygenated environments are predominantly inhabited by epifaunal foraminifera, which usually have a trochospiral test morphology (De Stigter et al., 1998; Rosoff and Corliss, 1992). High organic matter flux will deplete oxygen and oxyphilic taxa will be replaced by taxa adapted to low oxygen levels; many of which are deep infaunal in oxygenated, mesotrophic environments. The TROX model concept of foraminiferal distribution was recently reviewed by (Jorissen et al., 2007), who conclude that organic matter is probably more effective in structuring benthic communities than oxygen, unless oxygen is severely depleted (below 1 mL/L or less; see also Murray, 2001).

This chapter reports on benthic foraminiferal data from a well exposed composite marine section of Langhian/Seravallian age sampled at the Islands Malta and Gozo (Central Mediterranean). In addition, we discuss high-resolution geochemical element (ICP-OES) analysis and stable isotope records. A previous study of Malta sediments by Bellanca et al., (2002) dealt mainly with the Blue Clay Formation, which has been deposited after the major climate step at ~13.8 Ma. Here, we focus on the interval from ~14.95 Ma to ~13.0 Ma, and thereby include the upper Globigerina Limestone Fm. in order to study the effects of the MMCT on the Central Mediterranean paleo-environment. A revised age model for the composite section is presented in Chapter 3.

2. Geological setting

The Maltese Archipelago, located in the Central Mediterranean, consists of the islands Malta, Gozo and Comino (Fig.1) and is situated on the Malta-Hyblean Plateau, extending from the Tunisian shelf to the Ragusa Platform of SE Sicily. The plateau forms part of the African foreland which partially subducts below the southern edge of the European plate (Gardiner et al., 1995; Yellin et al., 1997). The Neogene lithological sequence exposed on the Maltese islands is divided into five Formations: the Lower Coralline Limestone (late Oligocene), Globigerina Limestone (Aquitanian-Langhian), Blue Clay (Serravallian), Greensand (Serravallian-Tortonian), and Upper Coralline Limestone (Tortonian) (Felix, 1973).

To study the MMCT, the interval of interest is the transition from the Globigerina Limestone Formation to the Blue Clay Formation. The Globigerina Limestone Formation consists of three members, separated by two phosphorite horizons that mark phases of reduced sedimentation rates and reworking by gravity flows (Föllmi et al., 2008; Pedley and Bennett, 1985; Rehfeld and Janssen, 1995). The bluish clays of the Blue Clay Formation are easily distinguishable in the field from the underlying Globigerina Limestone Formation. A hiatus between 12.5-10.9 Ma separates the top of the Blue Clay Fm. from the Greensand Fm. (Föllmi et al., 2008),

The composite section spans the time interval from ~14.95 to ~13.0 Ma (Ch.3). The Upper Member of the Globigerina Limestone (UGL: ~14.95 – 13.76 Ma) has been studied, together with the lower 30m of the Blue Clay Formation (BC: for the interval 13.76 -13.08 Ma). The base of the UGL is the upper phosphorite horizon, called the Upper Main Phosphorite Conglomerate Bed (UMPC) (Pedley and Bennett, 1985). The UGL can be subdivided into three stratal packages (Fig. 2). The lower and upper, carbonate rich packages consist of yellowish marly limestones, whereas the middle package is a ~5m thick marly clay, the "clay rich interval" (CRI). In the field the CRI looks very similar to the clays of the Blue Clay Fm; however, in contrast to the latter, the CRI is not related to a glaciation event of similar magnitude (see Chapter 3). The upper package of the UGL contains a condensed interval with a high phosphate content (Ch.3; John et al., 2003). A transitional bed, slightly thicker on Malta (1.77 m) than on Gozo (1.12 m), marks the top of the Globigerina Limestone Formation and is characterized by a decrease in carbonate content from ~70% to 20% (Fig. 2; Ch3; Abels et al., 2005; John et al., 2003). According to Bellanca et al. (2002) and Bonaduce and Barra, (2002), the carbonates of the Globigerina Limestone were deposited in an upper bathyal environment, at an estimated paleodepth of about 500-600m.

Figure 2. Ras Il Pellegrin section (Malta) seen from the southern shore of the Fomm Ir-Rih Bay showing the Globigerina Limestone Formation (Upper Member) with the clay rich interval and transitional bed, and the Blue Clay Formation with the marly intervals I-VI (as distinguished by Abels et al., 2005) and the sapropelitic- and iron nodule layers (SL and INL, respectively).

The Blue Clay Formation consists of ~60 m of marly clays with $CaCO_3$ contents fluctuating between 10 and 60% (Ch. 3; Abels et al., 2005). Distinct sedimentary cycles are visible as homogeneous layers of grayish-blue marls alternating with whitish-grey marls. On a larger scale, intervals dominated by whitish marls can be recognized (see Fig. 2 and Abels et al., 2005). Following Abels et al. (2005), the intervals in the lower 30m of the Blue Clay Fm. (this study), will be labeled I to VI, although we will refer to "marly intervals" (MI), consisting of a grey and a whitish colored part. A sapropelitic layer between 23.9 and 24.3 m, and several levels with chondrite trace fossils point to occasional anoxic or dysoxic bottom water conditions in the Blue Clay Fm. (Abels et al., 2005; Bromley, 1990). Between 28.9 and 29.3 m a brownish iron rich layer, the "iron nodule layer" (INL) is observed. Benthic foraminiferal and ostracode assemblages indicate a similar paleodepth for the Blue Clay as for the Globigerina Limestone Formation (Bellanca et al., 2002; Bonaduce and Barra, 2002).

The transition from the Globigerina Limestone Fm. to the Blue Clay Fm. coincides with the end of the Mi3b isotope event and reflects the rapid expansion of the EAIS during the MMCT (Ch.3; Abels et al., 2005; Miller et al., 1996; Miller et al., 1991). The top of the transitional bed, forming the boundary between the Globigerina Limestone and Blue Clay Formations, has been dated 13.76 Ma (+/- 0.02), although uncertainties in the tuning still exist (see Chapter 3).

3. Methods

Sampling of the selected interval was carried out at two locations to obtain the most complete and expanded composite section possible. The Marsalforn section, exposed on the north coast of Gozo, was sampled for the Upper Globigerina Limestone Fm. (UGL), including the transitional bed. The Ras Il Pellegrin section, exposed along the Fomm Ir-Rih Bay on the west coast of Malta (Fig. 1, 2), was sampled for the Blue Clay Fm. In addition, the upper part of the UGL and the transitional bed were sampled at Malta to create an overlap. The composite section was established by correlating the base of the transitional bed. The samples were collected by coring, with an average sample distance of ~ 7 cm in the Globigerina Limestone and ~9 cm in the Blue Clay Fm.

3.1 Benthic foraminifera

For benthic foraminiferal analysis 113 samples were selected from carbonate rich and carbonate poor layers, reflecting the different lithologies. The transitional bed and the sapropelitic layer between 23.9 and 24.1 m were studied at a higher resolution. The samples were disintegrated in water and washed over sieves with mesh sizes 125 and 595 µm. Using a microsplitter, the samples of the 125-595 µm size fraction were split into sub-samples each yielding ≥200 benthic foraminifera. Specimens were picked, placed on permanent slides, identified to species or generic level, and counted. Relative taxon abundances, expressed as percentage of the total number of benthic foraminifera per sample, were calculated for further analysis. Species diversity (Shannon index) was calculated from simple diversity (S) according to the formula given in Hammer and Harper (2006).

Paleobathymetry was estimated by calculating the P/B ratio, expressed as the fraction of planktic foraminifera in the total foraminiferal fauna (P/(P+B)) and has been applied with a correction for infaunal taxa, following Van der Zwaan et al. (1990) and Van Hinsbergen et al. (2005). The P/B ratios were determined by counting at least 300 specimens from 10 random squares on a picking tray and paleodepth was calculated using the transfer function in Van der Zwaan et al., (1990).

Standard SPSS software was used to run statistical analyses on relative abundance data. The original dataset of 74 variables was reduced by omitting species occurring in frequencies below 4% and ill-defined remainder groups. All costate forms of *Uvigerina semiornata* species were grouped together as *Uvigerina semiornata* sspp. To avoid overrepresentation of species included in the analysis, no new closed sum was calculated. Hierarchical clustering (Pearson correlation, within-group linkage) was performed on the remaining 32 variables. Principal Component Analysis was used to describe the major trends in benthic faunal development. Unrotated factor scores of the first three axes will be considered.

3.2 Geochemical proxies

3.2.1 Geochemical elemental analysis (ICP-OES)

Element (ICP-OES) analysis was performed on 731 samples: 426 samples from the Ras Il Pellegrin section (Malta) and 305 samples from the Marsalforn section (Gozo). Samples were dried, and crushed to powder to homogenize. Subsequently, 125 mg of each sample was dissolved in 2.5 ml HF (40%) and 2.5 ml mixing acid (HNO_3 16.25% and $HClO_4$ 45.5%) and heated at 90°C in a closed vial for at least 8 hours. Samples were then dried by evaporating acids at 160°C and subsequently dissolved in 25 ml HNO_3 (4.5%). The resulting solutions were analyzed on a Perkin Elmer Optima 3000 ICP-OES at Utrecht University. Where needed the results were refined using in-house standards. Calcium carbonate ($CaCO_3$) content has been calculated from Ca, assuming that most of the Ca is present as $CaCO_3$. Selected elements (Ca, Ba, K, Mg, V, and Ti) will be discussed here. Outliers, defined as values exceeding the mean ± three times the standard deviation have been excluded.

3.2.2 Stable isotope analysis

Stable oxygen and carbon isotopes were measured on 738 samples, with an average sample distance of ~10 cm. Measurements on specimens of the planktic foraminifer *Globigerinoides trilobus* and the benthic foraminifer *Cibicidoides dutemplei* were performed at Utrecht University on a SIRA-24 VG (vacuum generators) and a Finnigan MAT 251 mass spectrometer coupled to a Carbo-Kiel Device (Type I). Calcite tests of *G. trilobus* (size fraction 250-300 µm, average 30 per sample) were measured on the SIRA-24, whereas *C. dutemplei* was measured using the Finnigan MAT 251/Kiel Device. Samples of *C. dutemplei* (minimum 6, average 8-10) were crushed and homogenized prior to analysis. The results were calibrated using NAXOS (in-house standard) and EAOA-CO1 for the SIRA-24 and NAXOS and NBS19 for the Carbo-Kiel Device and are reported on the PeeDee belemnite (PDB) scale. The standard external error is for both devices better than 0.05‰ and 0.10.‰ for $\delta^{13}C$ and $\delta^{18}O$, respectively. Replicate measurements on 25% of the samples indicate mean reproducibility better than 0.10‰ for $\delta^{13}C_p$, 0.15‰ for $\delta^{13}C_b$, 0.13‰ for $\delta^{18}O_p$ and 0.12‰ for$\delta^{18}O_b$.

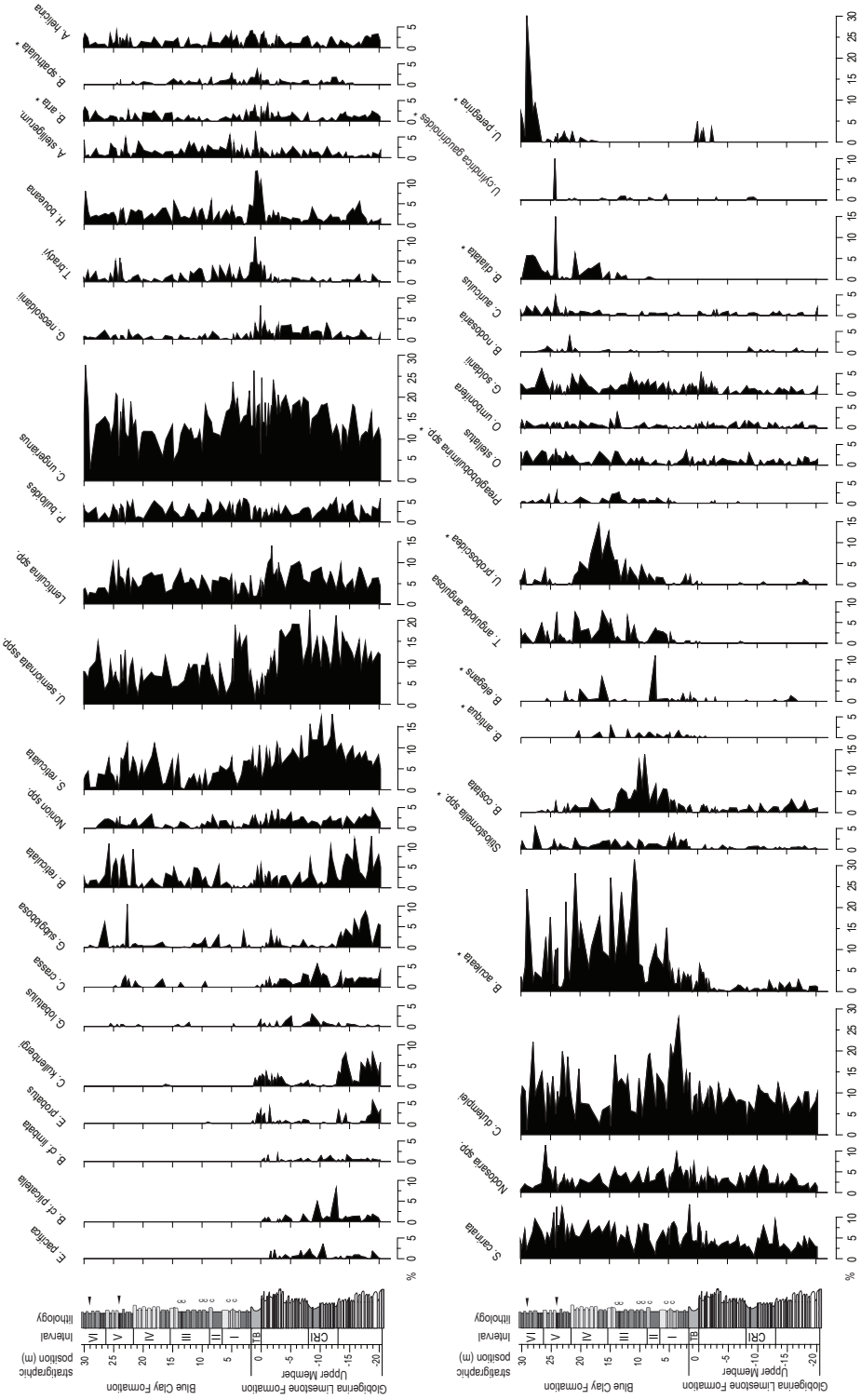
A. helicina
B. spathulata *
B. arta *
A. stelligerum.
H. boueana
T. bradyi
G. neosoldanii
C. ungerianus
P. bulloides
Lenticulina spp.
U. semiornata sspp.
S. reticulata
Nonion spp.
B. reticulata
G. subglobosa
C. crassa
G. lobatulus
C. kullenbergi
E. probatus
B. cf. limbata
B. cf. plicatella
E. pacifica
U. peregrina *
U. cylindrica gaudrinoides *
B. dilatata *
C. auriculus
B. nodosaria
G. soldanii
O. umbonifera
O. stellatus
Preaglobobulimina spp. *
U. proboscidea *
T. angulodа angulosa
B. elegans *
B. antiqua *
B. costata
Stilostomella spp. *
B. aculeata *
C. dutemplei
Nodosaria spp.
S. carinata
%
Blue Clay Formation
Upper Member
Globigerina Limestone Formation
stratigraphic position (m)
Interval
lithology
VI
V
IV
III
II
I
TB
CRI

The bulk, planktic and benthic isotope records are presented in Chapter 3. For the purpose of this study we use the benthic $\delta^{13}C$ and $\delta^{18}O$ records, and the $\Delta\delta^{13}C$ and $\Delta\delta^{18}O$ records derived from subtracting the benthic from the planktic records.

4. Results

4.1 Foraminifera

Preservation of foraminifera is moderate to reasonably good with some effect of post-depositional alteration in many Blue Clay (BC) and in some Upper Globigerina Limestone (UGL) samples. Severe dissolution is observed in samples from a stratigraphic level of ~3 to 3.5 m above the Transitional Bed (TB), and in the phosphate-rich levels. Secondary calcite overgrowth is observed in some carbonate rich UGL samples. Grain size sorting is apparent at several irregularly spaced levels and may point to transportation and/or winnowing.

4.1.1 Relative abundances and diversity

The relative abundances of numerically important taxa (i.e. mentioned in the text) in the UGL and BC Formations are given in Figure 3. Throughout the studied sequence *Cibicidoides ungerianus*, *Cibicidoides dutemplei*, and *Uvigerina semiornata* sspp. are the dominating species. The highest maximum abundances recorded are for *Bulimina aculeata* (31.4%) and for *Uvigerina peregrina* (30.1%).

Substantial changes in the assemblage composition are observed in the transition from the UGL to the BC when a few, though not very common, species disappear: *Bolivina* cf. *limbata, Bolivina* cf. *plicatella, Ehrenbergina pacifica and Cibicidoides kullenbergi.* Other species, like *Globocassidulina subglobosa*, *Bolivina reticulata, Uvigerina semiornata* sspp, *Siphonina reticulata, Bulimina aculeata, Bulimina costata* and *Lenticulina* spp. show a temporary drop in abundance in the transitional bed (Fig. 3). By constrast, *Hanzawaia boueana* and *Trifarina braydi* occur in relatively high numbers in the transitional bed, with maximum abundances of 12.9% and 10.9% respectively.

Throughout the Blue Clay Fm. *B. aculeata*, *B. costata*, *Trifarina angulosa angulosa, Uvigerina proboscidea, Praeglobobulimina* spp., *Bolivina dilatata,* and *U. peregrina* show successive increases in abundance. New species recorded in the BC are *Bolivina antiqua* and *Bolivina dilatata*.

The assemblage of the sapropelitic layer (~24m) is dominated by *B. dilatata* (16%), *B. aculeata* (with a relatively low percentage of 10%) and *U. cylindrica gaudryinoides* (10%). *Praeglobobulimina* spp. are found in low numbers (2.8%) (Fig. 3). Species composition of the iron nodule layer (~29m) is dominated by *B. aculeata* (25%) and *U. peregrina* (31%) (Fig. 4) whereas *U. cylindrica gaudrinoides* and *Praeglobobulimina* spp. are absent. In addition, low abundances of *C. ungerianus* and *C. dutemplei* are observed.

Diversity (Shannon index) in the UGL shows a decreasing trend from 3.2 to 2.8 towards 2 meter below the base of the transitional bed (Fig. 4a). Values increase again to 3.3 in the transitional bed, followed by a drop in the Blue Clay Fm., to 2.4 in the dissolution zone (~3-3.5 m). Throughout MI-II to IV values fluctuate between 2.6 and 3.1, with an exception in the iron nodule layer at ~29m where diversity is 2.4.

4.1.2. Paleobathymetry

The Globigerina Limestone Fm. is characterized by relatively high P/B ratios, fluctuating between 0.68 and 0.87 (Fig. 4a). Using the transfer function of Van der Zwaan et al. (1990), a paleo-water depth between 400 and 800m is estimated. This is in agreement with depth reconstructions based on benthic foraminifera and ostracode distributions by Bellanca et al. (2002) and Bonaduce and Barra (2002). Mean P/B ratios in the Blue Clay Fm. are much lower and, moreover, show large fluctuations between 0.32 and 0.75

←**Figure 3.** Relative species abundance patterns of benthic foraminifera for the Upper Globigerina Limestone Formation and lower part of the Blue Clay Formation of the Maltese Islands (Malta and Gozo, Central Mediterranean). Species marked with a * are considered as (deep) infaunal taxa (Van Hinsbergen et al., 2005) and have been used to correct P/B values. On the left: lithological column of the studied sequence. CRI: Clay Rich Interval; TB: Transitional Bed; c : chondrite levels, SL: sapropelitic layer; INL : "iron nodule layer".

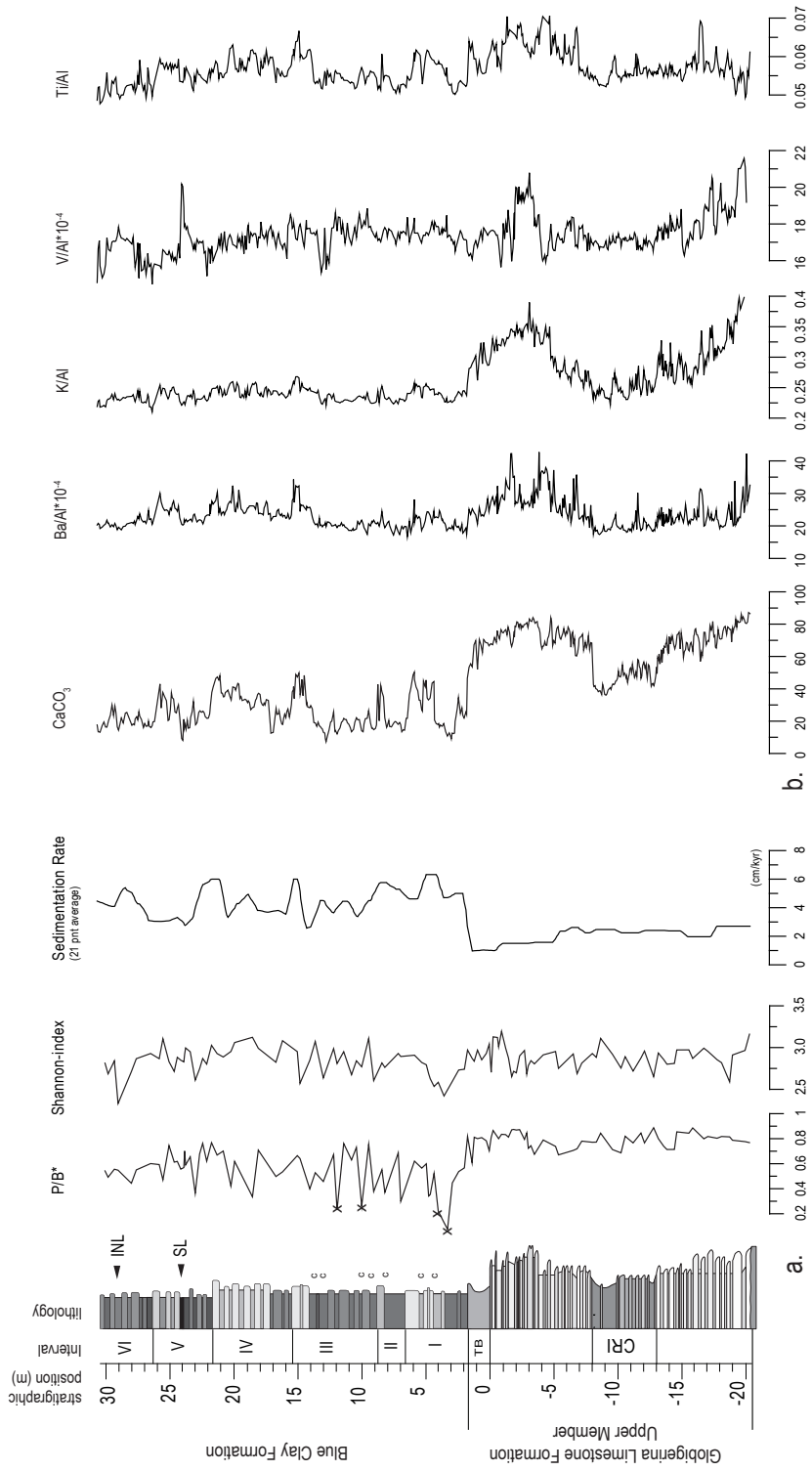

Figure 4. a). Shannon diversity index, P/B ratios (corrected for infaunal elements according to Van Hinsbergen et al. (2005) and sedimentation rates (cm/kyr). Samples marked with 'x' fall below the 2 times standard deviation level and might be biased by dissolution; b) Geochemical records of $CaCO_3$, Ba/Al, V/Al and Ti/Al. CRI: Clay Rich Interval; TB: Transitional Bed; c : chondrite levels, SL: sapropelitic layer; INL : "iron nodule layer".

(Fig. 4a). Applying the transfer function of Van der Zwaan et. al. (1990) the estimated paleodepth in the BC is between 200 and 400 m. Changes in benthic assemblages, e.g. the disappearance of *C. kullenbergi* and the simultaneous decrease in the abundance of *S. reticulata* also suggest a shallower paleoenvironment than the Globigerina Limestone Fm.; however, the distribution of benthic foraminifera in the BC is probably controlled by organic matter flux rather than by water depth (see discussion).

4.1.3 Benthic assemblages

Two main clusters (A and B) result from cluster analysis (Pearson correlation; within-group linkage, Fig. 5, 6a). The two main clusters have been subdivided into five sub-clusters (A-1, A-2, A-3 and B-1 and B-2). In cluster A-3 and B-1 two smaller clusters have been distinguished. The assemblages are named after their most dominant species.

Cluster A-1: *Bolivina reticulata*-assemblage

The *B. reticulata*-assemblage (including *C. kullenbergi*, *Eponides probatus*, *Nonion* spp. and *G. subglobosa*) has highest abundances in the lower part of the UGL reaching up to 25% of the total benthic assemblage. In the Blue Clay Fm. abundances are relatively low.

Cluster A-2: *Uvigerina semiornata* sspp.-assemblage

Most dominant in the UGL is the *Uvigerina semiornata* sspp.-assemblage (30-40% of the total assemblage), which includes among others *S. reticulata* and *Lenticulina* spp. The abundance decreases towards the transitional bed (Fig. 6a).

Cluster A-3: *Cibicidoides ungerianus*-assemblage

The *Cibicidoides ungerianus*-assemblage is most dominant around the transitional bed (up to 40%). Throughout the UGL and BC the cluster makes up ~20% of the total assemblage.

Within cluster A-3 the *H. boueana* sub-assemblage, including *Trifarina braydi, Astrononion stelligerum* and *Gyroidinoides neosoldanii* is causing the dominance of the A-3 cluster in the transitional bed, reaching almost 35% abundance. Throughout the UGL and BC this sub-assemblage makes up ~5-10% of the total benthic foraminifera fauna.

Cluster B-1: *C. dutemplei*-assemblage

The *C. dutemplei*-assemblage, with *C. dutemplei* and *B. aculeata* as most dominant species, is not very abundant in the UGL. A major increase is observed in the Blue Clay Formation which can mainly be attributed to the *B. aculeata* sub-cluster.

Within cluster B-1:The *B. aculeata* sub-assemblage is characteristic for the Blue Clay Fm., with *B. costata, U. proboscidea* and *T. angulosa angulosa* as other dominant species. Maximum relative abundances of >50% are reached in the marly intervals MI-II to IV (8.8 – 21.6 m). Species in this cluster are nearly absent in the UGL.

Cluster B-2: *Uvigerina peregrina*-assemblage

The *Uvigerina peregrina* assemblage (with *B. dilatata*, *U. cylindrica gaudrinoides* and *Cancris auriculus*) is characteristic for MI-V and VI (21.6 – 30.1 m). The assemblage is not very abundant throughout the UGL and BC, except for maximum abundances of >30% which are found in the sapropelitic layer and the iron nodule layer.

4.1.5 Principal Component Analysis

The first three axes of the Principal Component Analysis explain 32.5 %, 14.7% and 9.9% of the total variance, respectively. PC axis 1 has high positive loadings for *B. aculeata, U. proboscidea* and *T. angulosa angulosa* (Table 1). Negatively loading are *U. semiornata* sspp., *C. ungerianus* and *S. reticulata.* PC scores on this axis show a similar pattern as the *B. aculeata*-assemblage, with a first increase in the transitional bed and a major increase in the Blue Clay Fm (Fig. 6b). In the marly intervals MI IV and V, PC scores decrease again, although a maximum is recorded in the iron nodule layer.

PC axis 2 shows positive loadings for *B. reticulata, C. kullenbergi and S. reticulata*, whereas *C. dutemplei* and *Spiroplectammina carinata* are negatively loading. PC scores are more or less constant throughout the UGL but show a decrease towards the transitional bed. In the Blue Clay Fm. PC scores gradually increase again.

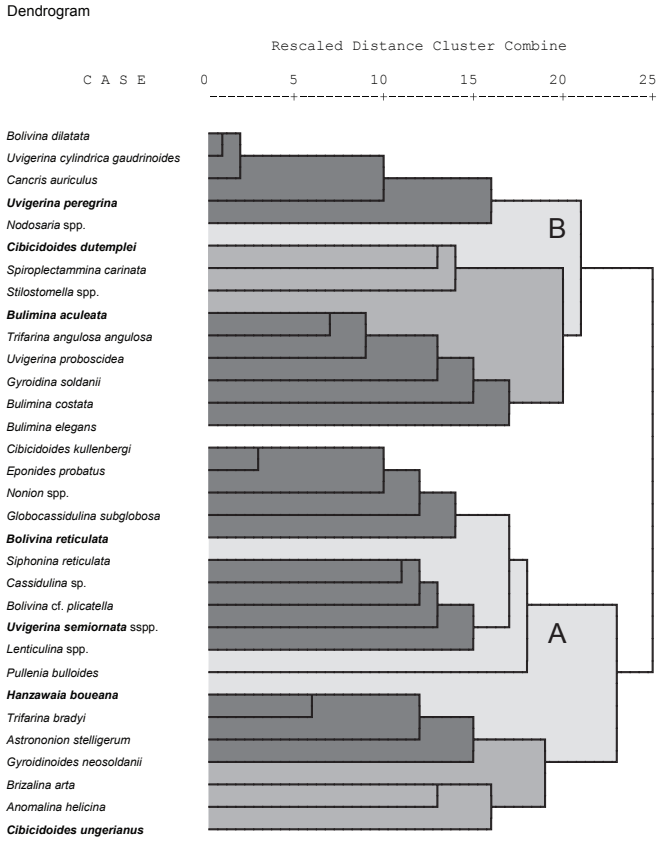

Figure 5. Dendrogram obtained by hierarchical cluster analysis (Pearson correlation, within group linkage). Clustering was based on relative abundances of 32 species of benthic foraminifera with relative abundances >4% in any sample. Two main clusters (A and B, light grey shading) are discerned in which five assemblages (dark grey shading) have been distinguished. The assemblages are named after their most dominant species (in bold).

PC axis 3 is positively loaded by *C. ungerianus*, *H. boueana* and *T. bradyi*, and negatively by *U. semiornata* sspp. and *C. dutemplei*. The pattern of this axis reflects the difference between the last phase of the UGL and the first phase of the Blue Clay Fm. (MI-I, 1.8 – 6.5 m).

4.2 Geochemical proxies

4.2.1 Geochemical element analysis

The calcium carbonate content is relatively high in the Globigerina Limestone Fm. (UGL), fluctuating around 80%, but decreasing in the clay rich interval (CRI) to 40% (Fig. 4b). In the transitional bed, carbonate content decreases from ~70% to ~20%. Calcium carbonate content in the Blue Clay Fm (BC) is relatively low (20%) with maxima of 50% in the whitish marls. At ~3.0 m, 12.8 m and in the sapropelitic layer, the carbonate content is less than 10%.

In order to detect subtle changes in the chemical composition with respect to the detrital sediment fraction, a correction for carbonate dilution was made for the elements K, Ba, V and Ti, using Al as a common divisor. In the UGL, K/Al, Ba/Al, V/Al and Ti/Al show a general decrease from the base towards the CRI, then increasing in the upper part of the UGL in which for all elements the highest values are recorded. Elemental ratios in the BC show enrichments in the whitish marls, and are within the same range as the lower part of the UGL (except for K/Al). A peak in V/Al at ~24m corresponds to

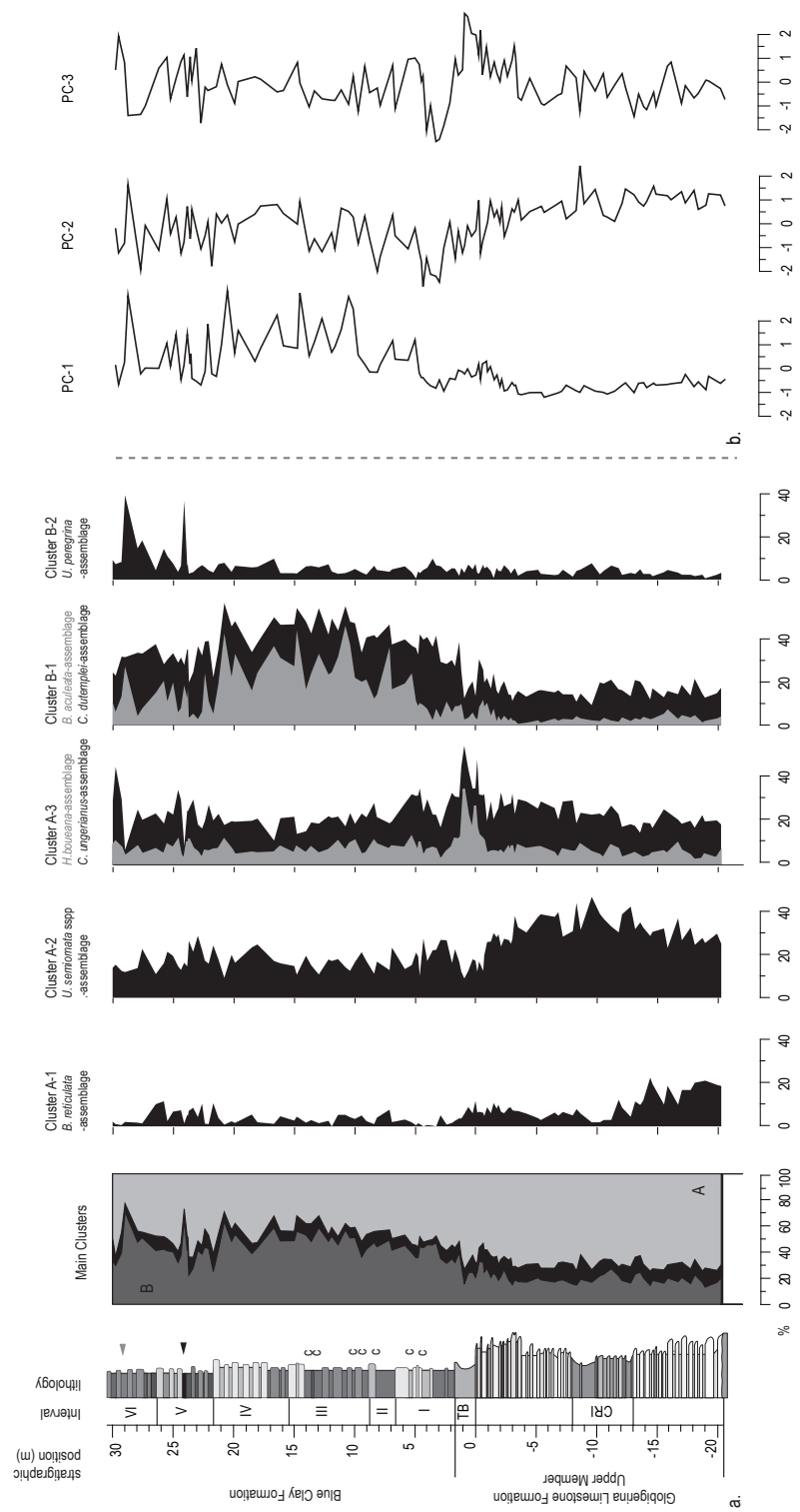

Figure 6. a). Vertical distribution of main clusters (A and B; black area represents rest-group not included in the analysis) and sub- clusters in the Globigerina Limestone Formation and lower part of the Blue Clay Formation. For explanation see text; b) Factor scores obtained from Principal Component Analysis on the 32 variables from the Upper Globigerina Limestone Fm. and lower part of the Blue Clay Fm. CRI: Clay Rich Interval; TB: Transitional Bed; c : chondrite levels, SL: sapropelitic layer; INL : "iron nodule layer".

Table 1. Principal component loadings obtained from PCA on 32 variables from the Globigerina Limestone Fm. and Blue Clay Fm. The most significant variables are reported in bold.

	PC-1	PC-2	PC-3
Anomalina helicina			0.27
Astrononion stelligerum		-0.26	
Bolivina cf. *plicatella*	-0.29	0.38	
Bolivina dilatata	**0.40**		
Bolivina reticulata		**0.46**	
Brizalina arta			0.35
Bulimina aculeata	**0.96**		
Bulimina costata	0.26		
Bulimina elegans			
Cancris auriculus	0.26		
Cassidulina sp.	-0.37	0.39	
Cibicidoides ungerianus	**-0.54**	-0.37	**0.48**
Cibicidoides dutemplei	-0.30	**-0.82**	**-0.41**
Cibicidoides kullenbergi	-0.28	**0.41**	
Eponides probatus		0.24	
Globocassidulina subglobosa		0.31	
Gyroidina soldanii	0.36		0.26
Gyroidinoides neosoldani	-0.22		0.28
Hanzawaia boueana			**0.55**
Lenticulina spp.		0.39	
Nodosaria spp.			
Nonion spp.	-0.38	0.33	
Pullenia bulloides			
Siphonina reticulata	**-0.54**	**0.49**	
Spiroplectammina carinata		**-0.52**	
Stillostomella spp.		-0.39	-0.20
Trifarina angulosa angulosa	**0.59**		
Trifarina bradyi		-0.29	**0.40**
Uvigerina cylindrica gaudrinoides			
Uvigerina peregrina	0.27		
Uvigerina proboscidea	**0.53**		
Uvigerina semiornata sspp.	**-0.57**	0.30	**-0.62**

the sapropelitic layer.

A scatterplot of Mg/Al and K/Al (Fig. 7) reveals high Mg/Al and K/Al values in samples from the lower and upper package of the UGL, plotting between the end members of Nile outflow, Saharan dust and the presumed northern borderlands of the eastern Mediterranean (NBEM) source (see Wehausen and Brumsack, 2000). Highest values are associated with samples from the phosphatic intervals and tend to plot beyond the range of the dust end member. In the clay rich interval and Blue Clay Fm., Mg/Al and K/Al are lower and plot close to Nile outflow values.

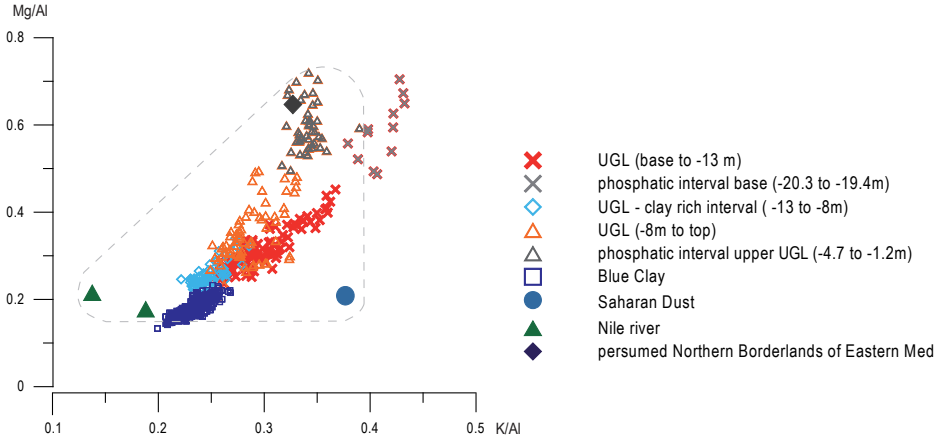

Figure 7. Scatterplot of Mg/Al and K/Al. Nile endmembers from Krom et al., 1999 and Martin and Meybeck, 1979. Saharan Dust endmember from Krom et al., 1999. The "Northern Borderlands of the Eastern Mediterranean" source from Wehausen and Brumsack, 1998; 2000.

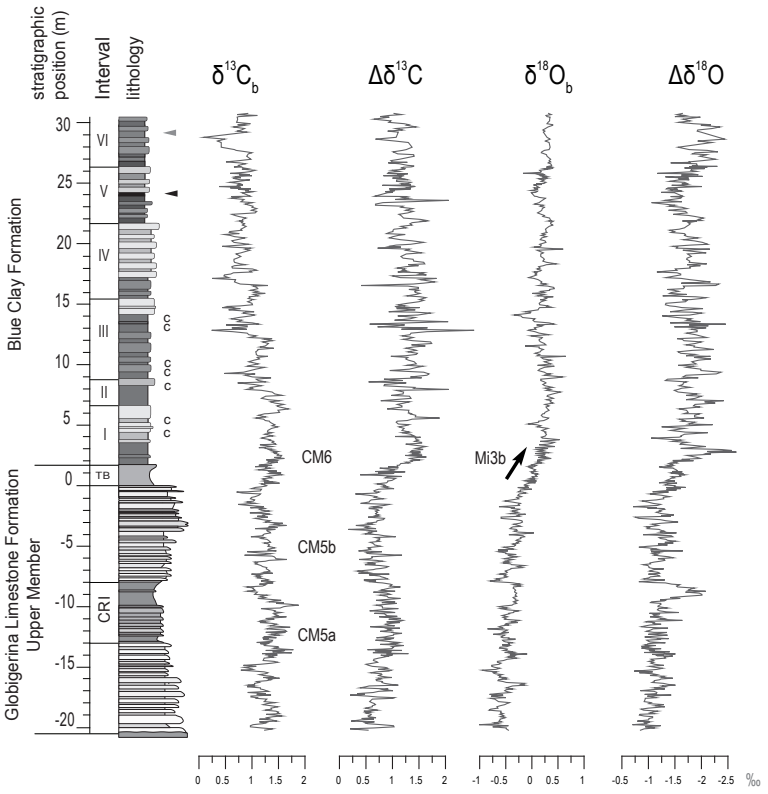

Figure 8. Stable isotope records showing the benthic $\delta^{13}C$, $\Delta\delta^{13}C$, $\delta^{18}O$ and $\Delta\delta^{18}O$ patterns. The MMCT is reflected in the benthic $\delta^{18}O$ record showing a gradual increase towards heavier values in the Globigerina Limestone Formation. In the transition to the Blue Clay Formation a more pronounced shift is observed, which has been related to the Mi3b event (Miller et al., 1991; 1996) representing the expansion of the East Antarctic Ice Sheet at ~13.8 Ma. The carbon isotope record shows the CM5a, CM5b and CM6 carbon maxima (Woodruff and Savin, 1991). CRI: Clay Rich Interval; TB: Transitional Bed; c : chondrite levels, SL: sapropelitic layer; INL : "iron nodule layer".

4.4.2 Stable isotopes

Figure 8 shows the benthic $\delta^{13}C$ and $\delta^{18}O$ isotope records and the $\Delta\delta^{13}C$ and $\Delta\delta^{18}O$. Three benthic $\delta^{13}C$ maxima correspond to the CM5a, CM5b and CM6 events (see Introduction and Chapter 3). Benthic $\delta^{18}O$ shows a gradual increase towards heavier values with a more distinct step across the transitional bed, corresponding to the Mi3b isotope shift.

The $\Delta\delta^{13}C$ and $\Delta\delta^{18}O$ records reveal a gradual increase from the base of the UGL (dated ~14.95 Ma) towards the top of the clay rich interval at -8 m. The excursion in $\Delta\delta^{18}O$ in the top layer of the clay rich interval is related to the planktic $\delta^{18}O$ signal; the $\Delta\delta^{13}C$ record does not show a specific excursion here. A second, more pronounced increase in both records is observed after the transition to the Blue Clay Fm. and coincides with the Mi3b benthic oxygen isotope shift. After the transition to the Blue Clay Fm., $\Delta\delta^{13}C$ and $\Delta\delta^{18}O$ show relatively high-amplitude fluctuations, but no major long term shifts are observed.

5. Discussion

5.1 Paleodepth reconstruction

To reconstruct paleobathymetry of the Maltese composite section P/B ratios are used. Despite well-acknowledged limitations to this method (see Jorissen et al., 2007), careful evaluation can provide an estimate of depositional depth, and depth variations.

The ratio of planktic versus benthic foraminifera was already proposed as a proxy for paleobathymetry by Grimsdale and Van Morkhoven (1955). The percentage of planktic species in a total count of planktic and benthic foraminifera is related to water depth through the export flux, and is a common tool to reconstruct paleobathymetry (Van der Zwaan, 1990; Van Hinsbergen et al., 2005). However, fluctuations in bottom-water oxygen and organic matter (OM) availability may influence the abundance and diversity of benthic foraminifera (e.g. Jorissen et al., 1995, 2007) and thereby alter the percentage of benthic foraminifera. Although a correction for infaunal species can be applied, P/B ratios should be interpreted with caution. Carbonate undersaturation will cause dissolution; most seriously affecting more fragile, often planktic tests. In addition, transportation or winnowing will affect P/B ratios (Van der Zwaan, 1990; Van Hinsbergen et al., 2005) by selective transport of foraminifera.

Preservation of foraminifera in the UGL and BC is not optimal, and indications of dissolution, winnowing and down-slope transport exist at certain levels, especially in the Blue Clay Fm. Throughout the UGL P/B ratios remain more or less constant and a paleodepth is calculated of 400-800m (transfer function in Van der Zwaan et al., 1990). This is conform reconstructions by Bellanca et al.(2002) and Bonaduce and Barra (2002) who estimate a upper bathyal paleodepth on basis of depth indicator (foraminifer and ostracode) species. The disappearance of *C. kullenbergi* and decreasing abundance of *S. reticulata,* reported from relatively deep waters (e.g. Jorissen et al., 2007), suggest a shallowing towards the Blue Clay Fm. which seems to be confirmed by P/B ratios indicating 200-400 m shallowing. However, by applying the transfer function, the high P/B fluctuations in the BC yield unrealistic changes in sea level of more than 100m at precession scale, exceeding by far the estimated sealevel lowering of ~40-50m associated with the MMCT (Fig. 9) (John et al., 2004; Westerhold et al., 2005). Instead, we believe that the P/B ratios are affected by selective dissolution in the BC, which is particularly obvious at ~3m where a P/B ratio of 0.08 is recorded. A drop in benthic diversity and relatively high numbers of the robust species *C. dutemplei* suggest that dissolution has biased the benthic assemblage in this interval (Fig. 3). In addition, abundant organic matter supply to the sea floor may increase the numbers of benthic foraminifera, thereby decreasing the P/B ratio. The maximum P/B ratios in the BC indicate a paleodepth of ~600m which is not much different from the estimated depth for the UGL. The fact that maximum P/B ratios in the BC are slightly lower than in the UGL is more likely the result of a shift in faunal assemblages which is mainly controlled by environmental factors (see section 5.2).

5.2. Changing paleoenvironments

5.2.1 Initial gradual cooling phase of the MMCT (~14.9 - 14.1 Ma; -20 to -2 m)

The benthic oxygen isotope record shows a trend towards more positive values in the upper Globigerina Limestone Formation, corresponding to the first gradual cooling phase of the Middle Miocene Climate Transition. The assemblages that dominate the UGL (*U. semiornata* sspp.-, *B. reticulata*- and *C. ungerianus* –assemblages) are characterized by oxyphylic species (e.g. *C. kullenbergi, C. ungerianus*, *S. reticulata*) as well as infaunal species (e.g. *B. arta*, *B. reticulata, U. semiornata* sspp.), without dominance of species reflecting low oxygen levels or high organic matter flux. Deep infaunal species are lacking. The TROX model (Jorissen et al., 1995) predicts that the environment was fully oxygenated and mesotrophic. Besides a gradual decline in species of the *B. reticulata* assemblage and increase in the *U. semiornata* sspp.- assemblage, the general benthic composition and the first axis of the Principal Component analysis indicate a more or less similar paleoenvironment throughout the UGL with minor shifts related to the CRI. (Fig. 6)

High values in various geochemical elemental ratios either mirror the $CaCO_3$ content, or are related to the intervals with low sedimentation rates and the presence of phosphor. In addition to winnowing processes some elements might be enriched in phosphorites (Tribovillard et al., 2006 and references therein). According to Fölmii et al. (2008) phosphor enrichments in the UGL are mostly allochthonous and associated with transportation.

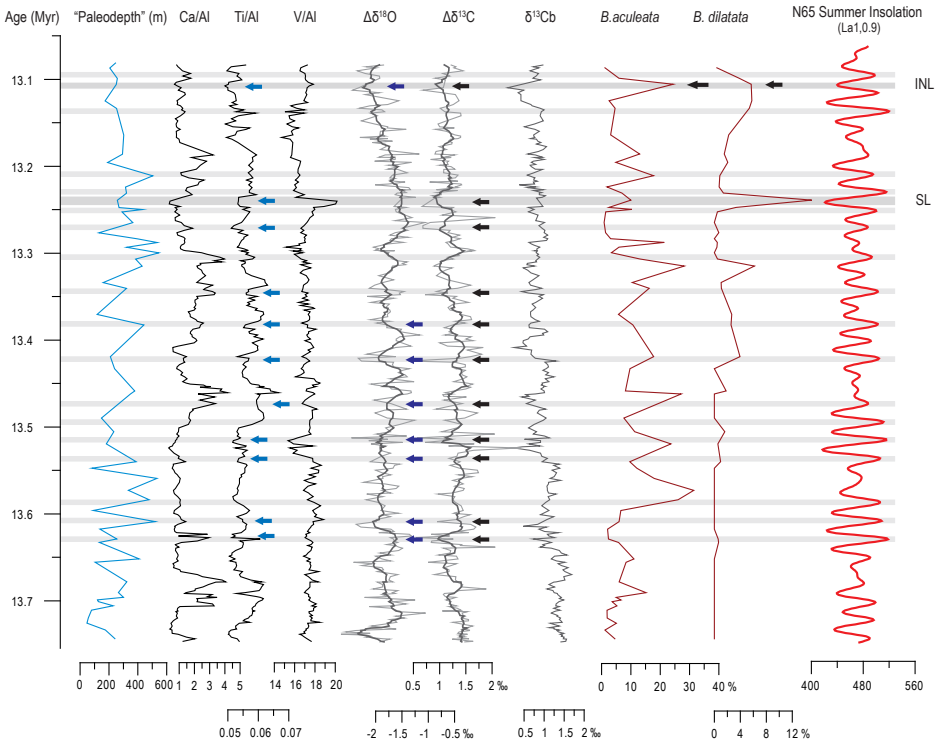

Figure 9. Blue Clay proxy records and their relation to insolation; a) "paleodepth" as inferred from Van der Zwaan et al., 1990. Note that sea-level changes of more than 50 m on precession scale are unlikely and possibly the cause of dissolution (see text for discussion); b) Ca/Al, Ti/Al and V/Al records; c) Isotope records of $\Delta\delta^{18}O$, $\Delta\delta^{13}C$ (with 7 point moving average) and $\delta^{13}C_b$; d) Abundance patterns of *B. aculeata*, and *B. dilatata*; e) Insolation curve (N65 summer) of Laskar 2004 (La1,0.9). Grey shading corresponds to insolation maxima. For discussion see text.

A commonly used proxy in paleoproductivity studies is Ba/Al, although many limitations exist (e.g. Tribovillard et al., 2006). The high Ba/Al values in the UGL are probably not reflecting increased productivity as other proxies like $\delta^{13}C$ or productivity indicator benthic species do not show any indication for this.

The presence of glauconite, a mineral associated with low sedimentation rates and phosphate (e.g. Pedley and Bennett, 1985) could have contributed to the elevated K/Al and Mg/Al ratios (Fig. 4b and 7). Therefore, such simple provenance reconstructions should be reconsidered in case K and Mg could have been enriched by local processes.

The clay rich interval (CRI; 14.6-14.4 Ma; -13 to -8 m) is one of the most remarkable features of the UGL. A gradual decrease in $CaCO_3$ from the base of the UGL onwards suggests that a long term trend should be held responsible. Interestingly, only few species in the benthic fauna seem to respond and show a temporary decrease (*B. reticulata*-assemblage) or increase (*U. semiornata* sspp. – assemblage). Samples from the CRI are relatively low in K/Al and Mg/Al and plot close to average Nile outflow suspended matter, rich in kaolinite and smectite (Fig. 7) (Krom et al., 1999; Martin and Meybeck, 1979; Wehausen and Brumsack, 2000). Kaolinite results from chemical weathering and is typically formed in tropical soils. Its northwards decreasing abundance gradient in marine sediments indicates an African origin (Foucault and Melières, 2000). Considering its proximity to the African continent, the Malta-Hyblean Plateau may well have been under the influence of rivers draining northern Africa such as the Nile. The excursion in $\Delta\delta^{18}O$ at ~14.45 Ma (-9 m) can be attributed to more negative values in planktic $\delta^{18}O$, which is possibly related to increased fresh water influx, associated with the increase in clay deposition. At 14.4 Ma, clay deposition seems to decrease relatively abrupt. What exactly caused the transition to the more condensed and carbonate rich upper part of

the UGL is at present not clear but, tectonic activity in this region can not be excluded. However, the timing of these phases during the middle Miocene is not well constrained (e.g. Pedley and Grasso, 1992). Benthic assemblages still point to a well ventilated mesotrophic environment until at least 14.15 Ma.

5.2.2 The major cooling step of the MMCT (14.1 – 13.7 Ma; -2 to + 4m)

Paleoenviromental changes affect the benthic assemblages again from ~14.1 Ma onwards, causing a decrease in the *U. semiornata* sspp.- and *B. reticulata*- assemblages and an increase in *H. boueana* - and *B. aculeata* – assemblages (Fig. 6, 9). Conditions between ~14.05 and 13.76 Ma were favorable for *H. boueana* and *T. bradyi,* showing remarkable peak abundances in the transitional bed. *Hanzawaia boueana* is a species found associated with low-salinity waters (Eichler et al., 2008). Their temporary high occurrence may be related to the estimated ~40-50 m sea level fall associated with the Mi3b-event (John et al., 2004; Westerhold et al., 2005), although increased fresh water influx seems to commence after the *H. boueana* peak. The relatively well preserved specimens do not seem to be transported.

A significant increase in $\Delta\delta^{13}C$ and $\Delta\delta^{18}O$ reflects greater surface to deep water contrast, related to increased productivity and/or decreased ventilation (in case of $\Delta\delta^{13}C$), and changes in temperature or salinity (in case of $\Delta\delta^{18}O$). The increase in the *B. aculeata* - assemblage, dominated by species favoring an infaunal habitat and high nutrient fluxes (e.g. Jorissen et al., 2007), indicates a change towards a more eutrophic and possibly less well-oxygenated bottom water environment.

At 13.76 Ma, clay influx is rapidly increasing, and sedimentation rates increase from ~1 cm/kyr to more than 5 cm/kyr (Fig. 4a). The high influx of nutrient rich river runoff could have enhanced surface water productivity, causing high organic matter fluxes to the seafloor. Excessive organic matter fluxes could have caused the observed dissolution at ~13.73 Ma, about a meter above the top of the transitional bed; selectively affecting more fragile tests and resulting in the strong decrease in P/B ratios and the relatively high numbers of the robust species *C. dutemplei.* This is also clearly reflected in PC-2 and PC-3 and in the Shannon diversity index (Figs 3, 4a, 6b).

5.2.3 After the MMCT (13.7 to 13.0 Ma; 4 to 30 m)

Most important environmental changes for the benthic community are probably the transition to a more clay rich substrate and an increase in food availability. In addition, oxygen levels will have been more depleted due to enhanced oxygen consumption related to organic matter decay. The heavier $\delta^{13}C$ of planktic foraminifera (see Chapter 3) could be an indication for increased surface productivity which was probably stimulated by nutrient supply from continental runoff (e.g. John et al., 2003). The K/Al versus Mg/Al ratios indicate proximity to outflow of the Nile river (Fig. 7). Increased productivity is, however, not confirmed by Ba/Al, although the relatively low values in the BC might be the result of a change in the sedimentary regime causing different preservation of Ba. Relatively low values in the sapropelitic layer suggest that Ba/Al is not reflecting productivity here.

In contrast to the rather abrupt increase in clay influx from 13.76 Ma onwards, the *B. aculeata*-assemblage and PC-1 suggest a more gradually changing environment, although there may be an effect of time-averaging. The continuous presence of oxyphylic species like *C. dutemplei* and *S. reticulata*, and the rare occurrence of dysoxic indicators like *Praeglobobulimina* spp., *Bulimina elegans* and *Bolivina dilatata* (Fig. 3), suggest that despite increased organic matter flux, oxygen levels were generally sufficiently high to sustain a rather diverse benthic fauna, although the successional increase in infaunal species throughout the Blue Clay Fm. points to an increasing trend in the amount and frequency of organic matter supply, and probably a decreasing trend in ventilation. However, no corresponding long-term trends are observed in the geochemical and isotope records, except for a clear enrichment of V/Al in the sapropelitic layer.

Dysoxic to anoxic conditions with a benthic fauna typically associated with sapropels occur for the first time at ~24 m (13.24 Ma). In detailed studies of Quaternary sapropels S1, S5 and S6 *Bolivina* cf. *dilatata* and *Globobulimina* spp. were found to dominate samples just below the azoic phase; probably due to disappearance of most (all) other species (Jorissen, 1999; Schmiedl et al., 2003). The transition from oxic to azoic sediments is

not recorded in our samples, which may be partly due to time averaging. We suspect that the iron nodule layer is a diagenetically altered sapropel or sapropelitic layer too, where the faunal signal is even more affected by time-averaging, as one sample may contain centuries of accumulated foraminifer tests. It is conceivable that sapropelitic sediments were deposited earlier in the BC succession, but the signal has been erased.

5.3 Monsoon imprint on the Malta-Hyblean Plateau

Figure 9 shows the relation of a selection of proxy records with the insolation curve of Laskar2004 (La1,0.9). After the MMCT, the Blue Clay Formation records a well known paleoclimatic signal for the Mediterranean by the occurrence of sapropelitic sediments. Sapropels have been associated with enhanced freshwater discharge, reduced deepwater ventilation due to diminished excess evaporation and enhanced flux of organic matter sinking from surface waters (for reviews see Cramp and O'Sullivan, 1999; Rohling, 1994; Rohling et al., 2009). Intensified African monsoonal rainfall and enhanced precipitation in the northern Mediterranean are considered to trigger sapropel formation during precession minima, when the Northern Hemisphere receives maximum summer insolation (Rossignol-Strick, 1983;1985). Insolation-driven monsoon variability is often reflected in geochemical parameters and the temporal coincidence between sapropel occurrences and insolation-driven monsoon maxima has become an important tool in building astronomical timescales (e.g. Hilgen, 1991a, b; Lourens et al., 1996; 2004; Hüsing et al., 2007).

No obvious link is observed between the geochemical records of the UGL and orbital parameters, which can possibly be attributed to low sedimentation rates and effects of winnowing and diagenesis. In contrast, the geochemical records in the BC show a relatively good correlation with the N65 summer insolation curve (Fig. 9; Laskar 2004; La(1,0.9)) and suggest monsoonal climate variability. The Ti/Al record, which can be used as an indication of eolian dust input (e.g. Lourens et al., 2001) shows distinct minima, reflecting low dust input during insolation maxima, when fresh water influx is highest. Increased runoff from the African continent might explain the increase in $\Delta\delta^{18}O$ (Fig. 8), caused by relatively light $\delta^{18}O$ in planktic foraminifera (Chapter 3). In addition, Mg/Al and K/Al are low in the Blue Clay Formation (Fig. 7) and may point to a stronger Nile imprint after the climate transition. The benthic $\delta^{13}C$ and $\Delta\delta^{13}C$ records show depleted values during insolation maxima as well. Similar depletions have been observed in the sapropelitic layers at La Vedova High Cliff (Mourik et al., in review; Ch.1) and in Pliocene sapropelitic sediments from Sicily (Gudjonsson and Van der Zwaan, 1986).

The sapropel at 13.24 Ma is associated with a V/Al maximum, pointing to low bottom water oxygen conditions. Although sapropels are generally related to insolation maxima (e.g. Hilgen et al., 1991 a,b) this one seems to coincide with a insolation minimum. This discrepancy is probably the result of the presently used tuning, in which Ca/K minima have been tuned to insolation minima (Chapter 3; Abels et al., 2005). However, when carbonate dissolution has taken place, mistakes are easily made. Therefore, the tuning of the BC has to be verified by using other proxies, like Ti/Al and the foraminiferal isotope records.

The resolution of our benthic foraminifera record is not high enough to distinguish individual precession cycles, however, some species abundance patterns seem to correlate with variability observed in the isotope records, as is the case for *B. aculeata* and *B. dilatata*. Highest abundances coincide with minima in $\delta^{13}C_b$ and $\Delta\delta^{13}C$, thereby indicating a causal link to insolation controlled runoff. A refinement of the age model and the resolution of the benthic foraminiferal records will better depict the relation between assemblage changes and small-scale climate variability.

6. Conclusions

The response of the Mediterranean basin to the Middle Miocene Climate Transition is evidenced by benthic foraminifera and geochemical proxy records. During the first phase of gradual cooling, the Maltese sites were subject to low sedimentation rates with indications for winnowing and transport in the phosphatic rich intervals. The benthic foraminiferal species composition of the Globigerina Limestone Fm. points to a

mesotrophic, well ventilated environment which ultimately changed when sedimentation rates rapidly increased at ~13.76 Ma. Nutrient influx associated with influx of fresh water and fine-grained sediments enhanced productivity, leading to a shift in benthic foraminiferal abundances to taxa associated with more eutrophic environments. A monsoonal imprint after the climate transition is observed in the geochemical- and isotope records, while at the same time the longer-term increase in dysoxic indicator foraminifera suggests an ongoing trend in ventilation restriction which triggered the deposition of sapropels after 13.24 Ma.

Acknowledgements
Frits Hilgen, Hemmo Abels and Rink Kruk are thanked for their help in collecting the material and providing the stratigrafical columns. Geert Ittmann, Arnold van Dijk and Helen de Waard have helped us a lot in preparing the samples and performing geochemical analysis. Ivo Duijnstee has been a "principal component" for the statistical part of this chapter and Karoliina Koho is thanked for fruitful discussions on the ecology of foraminifera. Furthermore we would like to thank Gert-Jan Reichart for his help in the interpretation of the geochemical records. The Darwin Center for Biogeosciences is acknowledged for financial support.

Appendix: Species list of benthic foraminifera

Numerically important taxa in the samples from the Maltese islands are listed in alphabetical order. Identification is based on the following sources: Ellis & Messina, Catalogue of Foraminifera, 1940 -; Van der Zwaan et al., 1986a (papers by Borsetti et al., 1986 and Van der Zwaan et al., 1986b, both for *Uvigerina*); Verhallen, 1991; Jones, 1994; Loeblich and Tappan, 1964, 1988. For some species synonymy is given. For most species additional references to plates are given. Identification at species level was not attempted for single occurrences and species occurring in irregular, but low relative numbers.

Anomalina helicina (Costa): *Nonionina helicina* Costa, 1855, p. 123, Pl. 1, figs. 18a-c; *Anomalina helicina* (Costa), Christodolou, 1960, p. 89, Pl. 8, figs. 5a-c.

Astrononion stelligerum (d'Orbigny): *Nonionina stelligera* d'Orbigny, 1839, p. 128, Pl. 3, figs. 1, 2; *Astrononion stelligerum* (d'Orbigny), Jones, 1994, Pl.109, figs. 3-4.

Bigenerina nodosaria d'Orbigny, 1826, p. 261, Pl. 11, figs. 9-12; Jones, 1994, Pl. 44, figs. 14-18.

Bolivina antiqua d'Orbigny, 1846, p. 240, Pl. 14, figs. 11-13.

Brizalina arta (Macfadyen): *Bolivina arta* Macfadyen, 1930, p. 58, Pl. 4, figs. 21a, b.

Bolivina cf. *plicatella*: cf. *Bolivina plicatella* Cushman, 1930c, p.46, Pl. 8, figs. 10a, b.

Bolivina dilatata Reuss, 1850, p. 381, Pl. 48, figs. 15a, b, c; Cushman, 1937b, p. 78, Pl. 9, figs. 17-20; Verhallen, 1990, p. 117, Pl. 13, figs. 1-10.

Bolivina reticulata Hantken, 1875, p. 65, Pl. 15, figs. 6a, b; Cushman, 1937b, p. 50, Pl. 6, figs. 24-27.

Bolivina cf. *limbata*: cf. *Bolivina limbata* Brady, 1881, pp. 419, 760, pl. 52, figs. 26–28; *Loxostomina limbata* (Brady, 1881): Jones, p. 57, Pl. 52, figs. 26–28.

Bulimina aculeata d'Orbigny, 1826, p. 269, mod. 7; Brady, 1884, p. 406, Pl. 51, fig. 7-9; Fornasini, 1902, p. 153, fig. 4, Jones, p. 55, Pl. 51, figs.7-9.

Bulimina costata d'Orbigny, 1826, p. 269; fig. in Fornasini, 1901, p. 174, Pl. 1; Cushman and Parker, 1938, p.54, Pl. 9, figs. 1, 2; Jorissen, 1988, Pl. 1, fig. 9.

Bulimina elegans: d'Orbigny, 1826, p. 270, mod. no. 9; Brady, 1884, p. 298-9, Pl. 50, figs. 1-4..

Cancris auricula (Fichtel and Moll): *Nautilus auricula* Fichtel and Moll, 1798, p. 108, 110, Pl. 20, figs. a-c (var. a), figs. d-f (var. b); *Cancris auricula* (Fichtel and Moll), Murray, 1971, p. 136, 137, Pl. 57, figs. 1-7.

Cassidulina crassa d'Orbigny, 1839, p. 56, Pl. 7, figs. 18-20; Knudsen 1971, Pl. 7, figs 18, 19.

Cibicidoides dutemplei (d'Orbigny): *Rotalina dutemplei* d'Orbigny, 1846; *Cibicides dutemplei* (d'Orbigny), Batjes, 1958, p. 157, Pl. 8, fig. 9; *Heterolepa dutemplei*, Loeblich and Tappan, 1964, p. C759, Pl. 623, figs. 3a-c.

Cibicidoides kullenbergi (Parker): *Cibicidoides kullenbergi* Parker, 1953, p. 49, Pl. 11, figs. 7, 8; Wright, 1978, p. 713, Pl. 4, figs. 5-7; Schweizer et al., 2009, p. 314, fig. 1i-j, in synonymy with *Cibicidoides mundulus* (Brady, Parker and Jones, 1888), Holbourn and Henderson, 2002, figs. 4.1-9.

Cibicides lobatulus (Walker and Jacob): *Nautilus lobatulus* Walker and Jacob, 1798, in Kanmacher, p. 642, Pl. 14, fig. 36; *Cibicides lobatulus* (Walker and Jacob), Longinelli, 1956, p. 182, Pl. 6, fig. 12; Hageman, 1979, p. 91, Pl. 3, figs. 6a, b, Pl. 4, figs. 1a, b; Holbourn and Henderson, 2002, fig. 3.1-3; *Cibicidoides lobatulus* (Walker and Jacob), Schweizer et al., 2009, p. 315, fig. 1a-h.

Cibicidoides cf. *pachyderma*: cf. *Cibicides pachyderma* (Rhezak): *Truncatulina pachyderma* Rhezak, 1886, p.87, Pl. 1. fig. 5a-c; *Cibicidoides pachyderma* (Rhezak), Schweizer et al., 2009, p. 301. fig. 1p.

Cibicidoides ungerianus (d'Orbigny): *Rotalina ungeriana* d'Orbigny, 1846, p. 157, Pl. 8, figs. 16-18; *Cibicides ungerianus* (d'Orbigny), Marks, 1951, p. 73, Pl. 8, figs. 2a, b; *Cibicidoides ungerianus* (d'Orbigny), Schweizer et al., 2009, p. 315, fig. 1k-l.

Ehrenbergina pacifica Cushman, 1927b, p.5, Pl. 2, fig. 2; Jones, 1994, Pl. 55, figs. 4,6,7.

Eponides probatus Krashennikov, 1958; Loeblich and Tappan, 1988, Pl. 594, 1-13; Jones 1994, Pl. 108, fig. 19. Put in synonymy with *E. repandus* by Szcsechura, 1982; see also Hansen and Revets 1992, p. 168, Pl. 1, figs 7-9.

Globocassidulina subglobosa (Brady): *Cassidulina subglobosa* Brady, 1881, p. 60, fig. in Brady, 1884, p. 430, Pl. 54, fig. 17; Barker, 1960, p. 112, Pl. 54, fig. 17; *Globocassidulina subglobosa* (Brady), Jones, p. 60, Pl. 54, fig. 17; Verhallen, 1990, p. 128, Pl. 14, figs. 3-4.

Gyroidina soldanii d'Orbigny, 1826: *Rotalina soldanii* (d'Orbigny), 1846, p. 155, Pl. 8, figs. 10-12; *Gyroidina soldanii* d'Orbigny, Cushman, 1929a, p. 38, Pl. 8, figs. 3-8; Verhallen, 1990, p. 137, Pl. 18, figs. 2-3; *Gyroidinoides soldanii*: Jones, Pl. 107, figs. 6-7.

Hanzawaia boueana (d'Orbigny): *Truncatulina boueana* d'Orbigny, 1846, p. 169, Pl. 9, figs. 24-26; *Cibicides boueanus* (d'Orbigny), Marks, 1951, p. 72, Pl. 8, fig. 9; *Hanzawaia boueana* (d'Orbigny), Batjes, 1958, p. 154, Pl. 8, fig. 5; Verhallen, 1990, p. 137,, Pl. 15, figs. 3-4.

Lenticulina Lamarck, 1804, Ellis and Messina, 1940 et seq.; Loeblich and Tappan, 1988, p. 405.

Nodosaria Lamarck, 1812, Ellis and Messina, 1940 et seq.; Loeblich and Tappan, 1988, p. 397.

Oridorsalis stellatus (Silvestri): *Truncatulina tenera*? Brady, var. *stellata* Silvestri, 1898, p. 297, Pl. 6, figs. 9a-c; *Oridorsalis stellatus* (Silvestri), Brolsma, 1978, Pl. 3, Fig. 2.

Osangulariella umbonifera (Cushman): *Pulvinulinella umbonifera* Cushman, 1933; *Osangulariella umbonifera* (Cushman), Jones, 1994, Pl. 95, fig 9-10.

Praeglobobulimina Hofker, 1951, Ellis and Messina, 1940 et seq.

Pullenia bulloides (d'Orbigny): *Nonionina bulloides* d'Orbigny, 1846, p. 107, Pl. 5, figs. 9, 10; *Pullenia bulloides* (d'Orbigny), Dieci, 1959, p. 87, Pl. 7, fig. 16; Christodolou, 1960, p. 56, Pl. 2, figs, 11, 12 ; Jones, Pl. 84, figs. 12-13.

Siphonina reticulata (Czjzek): *Rotalina reticulata* Czjzek, 1848, p. 145, Pl. 13, figs. 7-9; *Truncatulina reticulata* (Czjzek), Brady, 1884, p. 669, Pl. 96, figs. 8a-c; *Siphonina bradyana* (Czjzek), Cushman, 1927, p. 11, Pl. 1, figs. 4a-c; *Siphonina reticulata* (Czjzek), Loeblich and Tappan, 1964, p. C591, Pl. 468, fig. 1a, b.

Sphaeroidina bulloides d'Orbigny, 1826, p. 267, mod. 65; d'Orbigny, 1846, p. 284, Pl. 20, figs. 19, 20; Jones, Pl. 84, figs. 1-5.

Uvigerina cylindrica gaudryinoides Lipparini, 1932: *Uvigerina tenuistriata* Reuss var. *gaudryinoides* Lipparini, 1932, p. 65, Pl. 3, figs. 7, 8, *Uvigerina cylindrica gaudryinoides* Lipparini, Thomas, 1980, p. 150-151, Pl.1, figs. 2a-c, Pl. 4, figs. 5, 6, Pl. 5, figs. 2, 4, 7 ; Borsetti et al., 1986, p. 230, Pl. 18, figs. 3-5.

Uvigerina peregrina Cushman, 1923, p. 166, Pl. 42, fig. 7-10; *Uvigerina peregrina peregrina*, Borsetti et al., 1986, p. 224, Pl. 15, figs. 1-2; *Uvigerina peregrina,* Murray, 2003, figs. 6, 10.

Uvigerina proboscidea Schwager, 1866, p. 250, Pl. 7, fig. 96; Borsetti et al., 1986, p. 218, Pl. 12, figs. 1-4

Uvigerina semiornata semiornata: *Uvigerina semiornata* d'Orbigny, 1846, p.189, Pl. 11, figs. 23, 24; *Uvigerina semiornata semiornata,* Van der Zwaan et al., 1986b, p. 200, Pl. 3. figs. 1-4.

Uvigerina rutila Cushman and Todd, 1941, p. 78, Pl. 20, figs. 16-22; Van der Zwaan et al., 1986b, p. 206, Pl. 6. figs. 1-4.

Spiroplectammina carinata: Textularia carinata d'Orbigny 1984; *Spiroplectammina* (*Spiroplectinella*) *carinata* (d' Orbigny); in synonymy with *Textularia pseudocarinata* Cushman, Jones, 1994 Pl. 42, figs. 15-16.

Stilostomella Guppy, 1894, Ellis and Messina, 1940 et seq.

Trifarina bradyi Cushman, 1923, p. 99, Pl. 22, figs. 3-5,9; Jones 1994, Pl. 67, figs. 1-3.

Trifarina angulosa (Williamson): *Uvigerina angulosa* Williamson, 1858, p. 67, Pl. 5, fig. 140; *Trifarina angulosa* (Williamson), Verhallen, 1990, p. 146, Pl. 20, figs.1-8; Jones, 1994. p. 86, Pl.74, figs. 15-16. Wright (1989) separates *T. angulosa angulosa* as a subspecies from *T. angulosa* and *T. angulosa pauperata*.

Chapter 5

Synthesis: Environmental changes in the Mediterranean area across the MMCT – perspectives from the marine and terrestrial realms

Anja Mourik

1. Introduction

Climate is one of the most important factors influencing the distribution of flora and fauna on Earth and changes are often expressed more pronounced in one season, and in one parameter (temperature, humidity). Many organisms tend to be limited to specific thermal ranges and changes in variables such as temperature may influence growth, reproduction, and mortality, and the distribution of species on Earth (Drinkwater et al., 2010).

Climate zones and biomes occur in latitudinal belts, related to temperature and precipitation patterns (Köppen, 1936). Highest solar irradiation is received at the tropics, with only minor day to day and seasonal changes in temperature compared to extra-tropical climates (Seidel et al. 2008). At present, tropical wet climates are related to ascending warm air in the Hadley circulation (Fig. 1.), carrying moisture into the air which promotes rainfall (Seidel et al., 2008). The ascending air causes a low-pressure zone, known as the Intertropical Convergence Zone (ITCZ). This zone is not fixed but migrates in an annual cycle, moving northwards in phase with the development of the Northern Hemisphere summer and southwards in winter (Griffin et al. 2002; Wang, 2009). As a consequence, the subtropical high pressure zone, situated between the polar low and ITCZ, shifts northwards during Northern Hemisphere summer causing dry conditions in the Mediterranean. In winter, when the subtropical high pressure belt is situated off North Africa, the Mediterranean is closer to the influence of the temperate westerlies that dominate over central and northern parts of Europe (Moreno et al., 2005; Rohling et al., 2009).

1.1. Cenozoic cooling

Changes in climate have occurred continuously in the past, but during the last 50 million years an overall cooling trend occurred. Although many complex feedback mechanisms between climate, tectonics, weathering, vegetation, Earth's albedo, and the global carbon cycle are involved (see Hay et al., 2002), the timing of major cooling events in the Cenozoic seems to be controlled by long-period orbital forcing. High-resolution, astronomically tuned deep-sea records show major $\delta^{18}O$ increases at the Eocene/Oligocene boundary, the Oligocene/Miocene boundary and during the middle Miocene (Abels et al., 2005; Coxall et al., 2005; Holbourn et al., 2005; 2007; Pälike et al., 2006; Turco et al., 2001; Zachos et al., 2001a). These cooling steps coincided with long-period nodes in obliquity amplitude, related to the 1.2 Myr cycle, in close harmony with low eccentricity values related to the 405 kyr cycle. In a certain configuration, peak summers are suppressed for a prolonged interval of time, favoring ice sheet growth (see Abels, 2008).

The relation between high atmospheric CO_2 levels and very warm Paleocene and Eocene climates makes the early Cenozoic currently a "hot" topic in Earth Sciences. A general declining trend in temperature and pCO_2 levels from 50 Ma onwards eventually led to the first major cooling step at the beginning of the Oligocene (Miller et al., 1991). After a warm phase in the late Oligocene, climatic cooling continued, being reflected by distinct marine oxygen isotope excursions (Miller et al., 1991; Woodruff and Savin., 1991). However, pCO_2 remained relatively low from the Oligocene onwards (e.g. Pearson and Palmer, 2000; Pagani et al., 2005; Zachos et al., 2008) and the apparent absence of atmospheric CO_2 decline during the Miocene cooling events led to the assumption that climate and global carbon cycling must have been decoupled (e.g. Shevenell et al. 2004; Pagani et al., 2005). However, stomatal indices of fossil leaves indicate a pCO_2 decline from ~ 400-500 ppmv to ~300 ppmv over the MMCT (Kürschner et al., 2008).

Carbon cycle feedback mechanisms must have played an important role since major uplift has taken place during the late Cenozoic thereby increasing erosion and global sedimentation rates (Hay et al., 2002; Potter and Szatmari, 2009; Wan et al., 2009). In addition, $\delta^{13}C$ isotope records have shown a major enrichment during the Miocene Climatic Optimum, with superimposed excursions related to the long eccentricity cycle (Holbourn et al., 2007; Woodruff and Savin, 1991).

The increase in marine $\delta^{13}C$ has previously been related to increased marine productivity as evidenced by thick organic-rich deposits along the circum-Pacifc margin (Vincent and Berger, 1985). However, recent calculations suggest that the amount of organic carbon embedded in the Monterey Formation may not be sufficient to impact on global climate (John et al., 2002; Föllmi et al., 2005) In addition, paleoproductivity reconstructions for the Atlantic Ocean suggest that the $\delta^{13}C$ increase is not related to marine productivity, which is confirmed by model studies (Diester-Haass et al., 2009). Instead, increased organic carbon sequestration would have occurred on the continents.

An important feedback mechanism in the global carbon cycle might be the link between vegetation activity and chemical weathering rates. Model results suggest that soil-weathering rates drop significantly if CO_2 concentrations fall below an ecological threshold of ~150-250 ppmv, thereby dampening CO_2 variability (Pagani et al., 2009). This mechanism could potentially explain why increased weathering rates and tectonic uplift during the Miocene did not cause a significant lowering in pCO_2.

1.2 Closure of the Tethys Seaway

The closure of the Tethys Seaway terminated the exchange of Mediterranean and Indian Ocean waters. Several authors proposed that the disappearance of a warm saline turbulent plume, flowing out from the Mediterranean into the Indian Ocean, could have decreased meridional heat transport to high southern latitudes allowing cooling of Antarctic surface waters and expansion of the EAIS (e.g. Woodruff and Savin, 1989; Flower and Kennett, 1995; Ramsay et al., 1998).

Major reorganization of marine biogeographic realms and faunistic differentiation on both sides of the Tethyan Seaway are already recognizable during the Late Oligocene and early Miocene (Harzhauser 2002; 2007 and references therein). During the middle part of the Burdigalian, between 18 and 19 Ma, the first faunal exchanges between Africa and Eurasia took place across the "*Gomphotherium* Landbridge" (Rögl, 1999; Harzhauser et

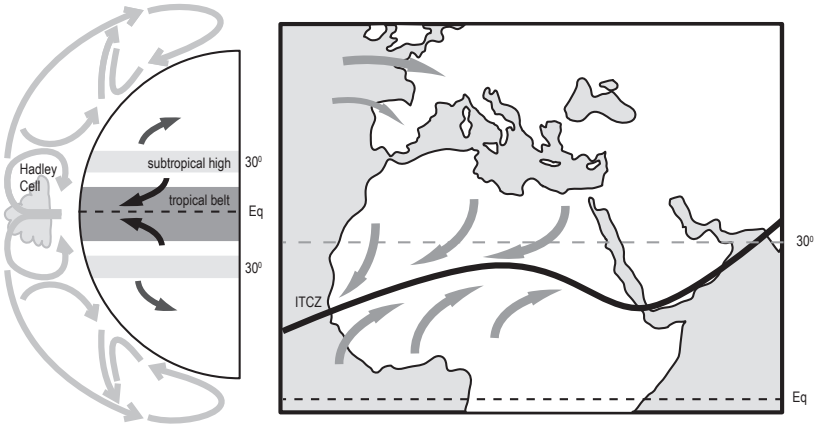

Figure 1. Schematic illustration of the position of the tropical belt, subtropical high and Hadley cell. Ascending air in the Hadley cell, above the Inter Tropical Convergence Zone (ITCZ), causes high rainfall in the tropical belt. The subtropical high is a high pressure zone characterized by low rainfall. On the right: Boreal summer position of the ITCZ between the equator and the Tropic of Cancer. During boreal winter, the ITCZ is positioned on the Southern Hemisphere, causing dryer conditions over northern Africa.

al., 2002; 2007). Elephants and rodents migrated to Eurasia, whereas other rodents, carnivores and primitive giraffoids moved southward (Wessels, 2009).

The absence of mammal migrations during the Langhian, and the expansion of tropical-subtropical marine faunal elements in the Mediterranean, have been tentatively explained by Rögl (1999) as the presence of a renewed open seaway, in relation to a major transgression. However, the existence of this re-opened seaway has so far never been proven. The warm conditions of the Miocene Climatic Optimum could alternatively explain the renewed warm water conditions and perhaps have created a climatological barrier for mammal migration. Moreover, re-opening of an already closed seaway is rather unlikely in an overall converging setting (Hüsing, 2008). These observations suggest that the Tethys Seaway closed well before the onset of the MMCT without evidence for reopening.

2. The Middle Miocene Climate Transition as recorded in the Central Mediterranean sections of Malta and La Vedova

The Central Mediterranean records from La Vedova and Malta, discussed in this thesis have their base at ~15.30 Ma and ~14.95 Ma respectively. Despite the fact that the end of the MCO is not very well defined, the conditions observed at the base of both sections will be most closely related to the MCO. Figure 2 gives an overview of paleo-environmental conditions we observed in the studied intervals and the possible relation to long-period orbital cycles.

2.1 The last phase of the Miocene Climatic Optimum

In the (proto-) Adriatic basin (La Vedova composite, Italy), dysoxic conditions are inferred based on geochemical proxies and the presence of thick brownish marls in the interval between ~15.3 and 15.0 Ma (Ch2). High influx of organic matter was probably related to increased river influx and high sedimentation rates. In contrast, sedimentation was reduced on the Malta-Hyblean Plateau and phosphate hardgrounds and pebble beds evidence a sedimentary regime of erosion with strong bottom currents, sediment reworking and frequent gravity-flow deposition during the last phase of the MCO (Pedley and Bennett., 1985; Rehfeld and Janssen, 1995; Fölmii et al., 2008). The major phases of phosphogenesis correspond to phosporite events outside the Mediterranean realm which have been related to periods of warm global climate and high sea level (Rehfeld

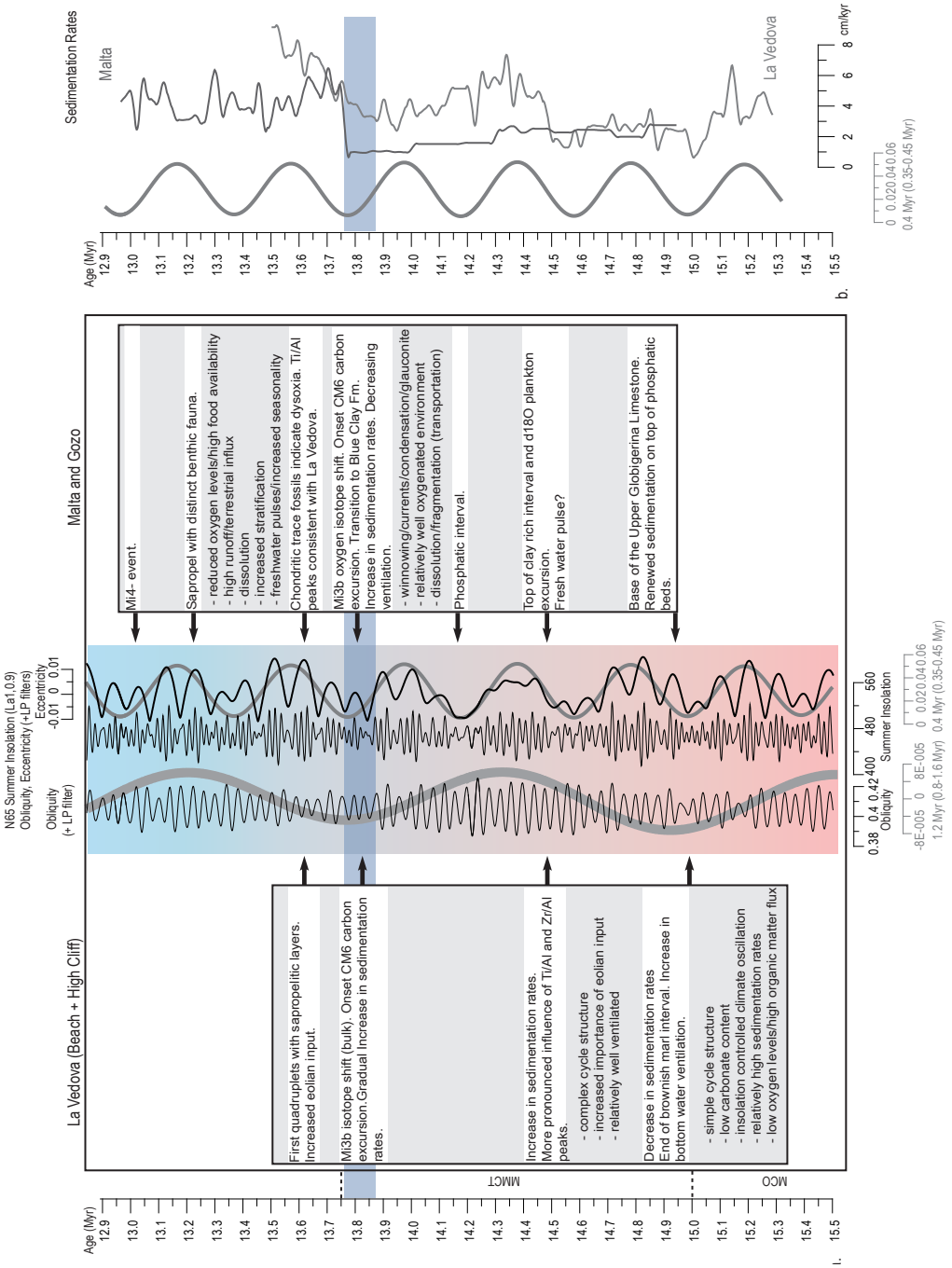

Figure 2. a) Summary of events and trends observed in the proxy records of the La Vedova Beach High Cliff section and on Malta for the interval between ~15.3 and ~13.0 Ma and relation to orbital parameters. Arrows give approximate position, for exact ages see text; b) Sedimentation rates resulting from the astronomical tuned age models of the two studied sections. The lower part of the section on Malta has been tuned in a lower resolution and a hiatus might be present between ~13.95 and 13.76 (Ma) (Chapter 3).

and Janssen 1995; Fölmii et al., 2008). A commonly used scenario to explain the worldwide phosphogenesis events is enhanced chemical weathering on the continents which increased the input of weathering derived phosphate into the oceans, thereby stimulating productivity (Fölmii et al 2008 and references therein).

Although phosphogenesis may be related to global climate conditions, erosional surfaces and hardgrounds developed on the Malta-Hyblean plateau may also be consequences of relative sea level changes associated with tectonic uplift and subsidence, caused by the ongoing convergence between Eurasia and Africa (Pedley and Grasso, 1992; Rehfeld and Janssen, 1995). However, the exact timing of regional tectonic events is not very well constrained.

2.2 The Middle Miocene Climate Transition

A decrease in sedimentation rate and amelioration of bottom water ventilation is observed at 15.0 Ma in the La Vedova succession (Fig. 2a). This step has been related to a 405 kyr minimum in the eccentricity cycle coinciding with a node in the ~1.2 myr obliquity cycle (Chapter 2). Around the same time, at ~15 Ma, sedimentation on the Malta-Hyblean plateau is resumed, although sedimentation rates remain relatively low (Fig. 2b). Whether this step was orbitally controlled or related to a tectonic event is at present not clear.

The $\delta^{13}C_b$ record of Malta shows obliquity and eccentricity control during the interval of the MMCT, but the increase in terrestrial influx on Malta between 14.63 and 14.42 Ma does not seem to be related to a specific orbital configuration. The short $\delta^{18}O_p$ isotope excursion of ~1 ‰ in the "clay rich interval", at 14.45 Ma could possibly reflect increased runoff and freshwater influx. Again, tectonic control can not be excluded here.

Around 14.5 Ma, at the end of the 405 kyr minimum, sedimentation rates in La Vedova increase. The rhythmic occurrence of marls enriched in Ti/Al and Zr/Al suggests more terrestrial influx from an arid region. Based on the presence of characteristic quadruplets in the younger part of the succession, with Ti/Al and Zr/Al rich marls alternating with sapropelitic layers, a dry-wet oscillating climate system can be inferred with a dust source probably located in northern Africa. Although climate reconstructions for northern Africa suggest that open landscapes did not come into existence until ~8 Ma (Sepulchre et al., 2006; Cane and Molnar, 2004), the data suggest that the onset of the aridification of North Africa already started directly after the end of the MCO. Unfortunately, pre-Quarternary paleorecords of African climate are particularly scarce (Wang 2009), which hampers a reliable reconstruction of the northen African climate for the middle Miocene.

At ~14.3 Ma, sedimentation rates on the Malta-Hyblean Plateau drop and a phosphate-rich interval in the 405 kyr minimum of ~14.2 Ma suggests that the environment was again influenced by relatively enhanced bottom current activity. The benthic foraminiferal assemblages from Malta point to a mesotrophic environment with well ventilated bottom water conditions between ~14.95 Ma and ~14.1 Ma. Only minor shifts in the relative abundances of the assemblages occur.

Ice sheet expansion on Antarctica is reflected by a ~0.6-0.7‰ increase in bulk and benthic oxygen isotope records of La Vedova and Malta and coincides with a node in obliquity and a minimum in the 405 kyr cycle of eccentricity. Unlike most open ocean records (e.g. Holbourn et al., 2005; 2007; Tian et al., 2008), a short warm phase preceding the major step seems to be absent in the Mediterranean records which might be attributed to preservation issues, a hiatus, or alternatively, the signal was somehow not recorded in the Mediterranean. During this interval of ice sheet expansion, which has been associated with a 40-50 m sea level fall (John et al., 2004; Westerhold et al., 2005) the benthic foraminifera *Hanzawaia boueana* and *Trifarina bradyi* show remarkable peak abundances on Malta whereas other species disappear from the benthic assemblage (Ch4). The major increase in sedimentation rates at the base of Blue Clay Formation is related to increased runoff which is also reflected by the planktic $\delta^{18}O$ signal (Ch. 3).

2.3 After the Middle Miocene Climate Transition

Insolation controlled climate variability becomes more prominent in the Central Mediterranean after the MMCT, causing precession induced decreases in ventilation during precession minima and summer insolation maxima (i.e. when Earth resides in perihelion during boreal summer) and increased eolian influx during precession maxima

and summer insolation minima. The planktic and bulk oxygen isotope records from La Vedova and Malta point to large fluctuations in temperature and/or fresh water budget. On Malta, the increase in clay influx is accompanied by an increase in $\delta^{13}C_p$, which possibly reflects increased productivity. Periodic supply of nutrient-rich river runoff could have increased productivity thereby favoring high fluxes of organic matter to the seafloor. This may have caused carbonate dissolution, as observed in several faunal samples. The increase in sedimentation rates is moreover accompanied by an increase in the abundance of infaunal benthic foraminifera species on the Malta-Hyblean plateau which responded to an increase in food availability. In addition, ventilation decreased as is inferred from a differentiation between the benthic and planktic isotope records.

A general decrease in ventilation is, however, not observed in La Vedova, where geochemical elements suggest that sufficient oxygen was available most of the time, apart from times that sapropelitic sediments layers were deposited. Molybdenum and Vanadium enrichments in these sapropelitic layers, which occur for the first time in a distinct quadruplet structure after the climate transition, suggest that bottom-water dysoxia could develop periodically during precession minima, when organic matter fluxes were possibly enhanced. At the same time, chondrite trace fossils are found on Malta (Fig. 3). The successive increase in infaunal taxa and the occurrence of the first sapropelitic layer with a distinct faunal assemblage at 13.24 Ma on Malta, suggest that restricted ventilation during high-amplitude precession minima became more severe after the climate transition.

The fact that sedimentary changes observed in Malta and at La Vedova do not always coincide reflects the different environmental settings and the possible influence of local tectonic activity. Nevertheless, an increase in terrestrial influx is related to the Middle Miocene Climate Transition in the Adriatic (La Vedova) and on the Malta-Hyblean Plateau, although the transition seems to have been more gradual in the northern Mediterranean. Well ventilated bottom waters prevailed during most of the transitional phase in both settings, but the massive influx of clay on the Malta-Hyblean Plateau after 13.8 Ma caused a more eutrophic and oxygen depleted environment with an associated increase in stress-tolerant benthic fauna.

3. The MMCT in the Mediterranean from a marine perspective

3.1. Paleoenvironment

The Mediterranean marine environment during the Miocene Climatic Optimum was characterized by warm surface water temperatures and a highly diverse marine fauna (Braga et al. 2007; Kroh, 2007; Bianucci and Landini, 2002). Paleo-temperatures inferred from isotope analysis on bivalve- and pectenid shells from a shelf environment in the Styrian basin (Fig. 4), Austria, indicate warm (subtropical) seawater temperatures (~13-26°C) in the Lower Badenian (early-middle Langhian~16.4 -15 Ma) with pronounced seasonality in temperature (Bojar et al., 2004). Oxygen isotope compositions of fish teeth from the northern Alpine Molasse Basin, the Vienna- and the Pannonian Basins located in the western and central part of the Paratethys, support a sub-tropical to warm temperate climate during the early to middle Miocene, with water temperatures of 14 to 28°C (Koscis et al. 2009). Planktic foraminifer studies indicate warm to warm-temperate conditions for the Paratethys (Carpathian Foredeep) and Mediterranean (northern Italy) (Bicchi et al.,2003) (Fig. 4).

Middle Miocene cooling coincided with a decrease in faunal diversity (Braga and Bassi, 2007; Bianucci and Barra, 2002), a decline in tropical bryozoan taxa (Moisette et al., 2006) and the disappearance of warm-water planktic foraminifera in the late Langhian-early Serravallian (Bicchi et al 2003). Pectenid shells from the Styrian basin (Austria) indicate cooler mean annual temperatures after ~14.2Ma. Moreover, the subtropical fauna disappeared during the early middle Miocene and biogenic limestones were replaced by clastic sediments (Bojar et al., 2004). Benthic foraminiferal assemblages from the Paratethys reveal increased food supply and decreasing oxygen levels on the sea floor after the climate transition. Moreover, the difference between planktic and benthic isotope records points to a strengthened stratification (Baldi et al., 2006).

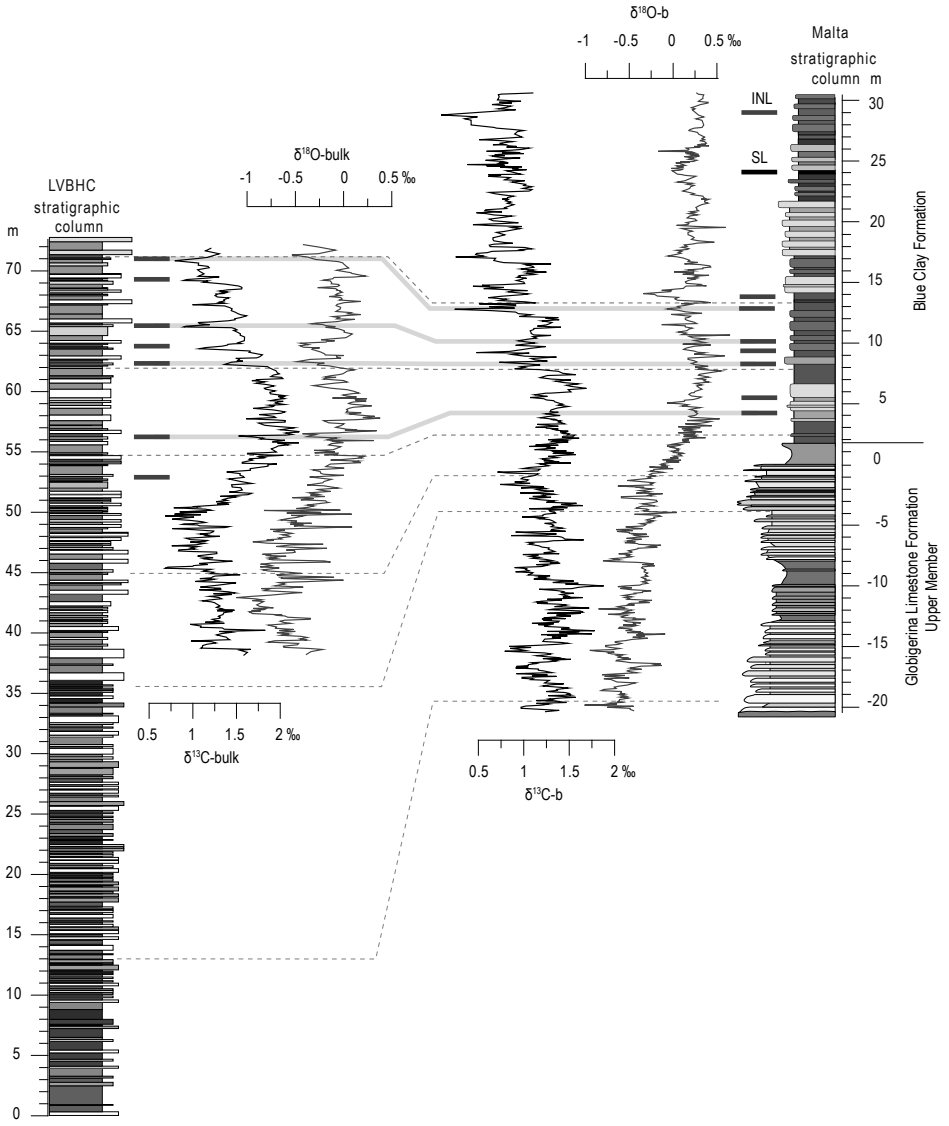

Figure 3. Lithological columns of the La Vedova Beach High Cliff (LVBHC) section and Malta section with bulk isotope records of La Vedova High Cliff and benthic isotope records for Malta. Grey bars next to the LVBHC column represent sapropelitic layers. Light grey bars next to the Malta column show the position of "chondrite levels". A sapropelitic layer (SL) and "iron nodule layer" (INL) are indicated at ~24 m and ~29 m respectively. Dashed lines are biostratigraphic correlation points, light grey shaded lines connect time equivalent sapropelitic- or chondritic layers.

3.2 Paleocirculation

Since the closure of the eastern portal of the Tethys seaway, presumably before the onset of the MMCT, circulation of the Mediterranean must have changed drastically. Model studies predict an estuarine circulation in case the fresh water budget was positive and an anti-estuarine circulation when a negative freshwater budget prevailed (e.g. Karami et al., 2009). The limited amount of well-dated marine early middle Miocene sections hampers proper circulation reconstructions for the time interval of the Miocene Climatic Optimum which currently rely mostly on ostracod studies. In the western and Central Mediterranean psychrospheric ostracods have been interpreted to reflect inflow of cool Atlantic water masses during the Langhian, suggesting an estuarine circulation type (e.g. Gebhardt, 1999; Dall'Antonia et al., 2001). Relative uplift of the Gibraltar Sill and sea-level lowering changed the circulation to an anti-estuarine type at the end of the Langhian (Gebhardt,1999 and references therein). This event supposedly took place during the *O. suturalis* subzone (N9, NN5; between 14.8 and 14.2 Ma), thereby predating the final step in the MMCT. In contrast to the findings of Gebhardt (1999), Dall Antonia et al.(2001) observed a progressive trend from thermospheric to psychrospheric conditions in the Hyblean area towards the late Langhian. Deep inflow of Atlantic bottom water masses is still recognized in Serravallian sediments from the western Mediterranean Balearic basin (DSDP site 372; Benson, 1976), and in Central Mediterranean sediments from the Tremiti islands (paleodepth ~1000m) (Russo et al., 2002).

However, Serravallian ostracod assemblages from the Maltese islands seem to be more in line with the reversal scenario, and suggest a stable thermospheric system and the absence of a psychrospheric environment (Bonaduce and Barra, 2002). This would be in agreement with the interpretation of an intermediate water mass with temperatures of ~12-13˚C flowing over the Malta-Hyblean Plateau (Bellanca et al., 2002).

The deposition of sapropels has been associated with an estuarine circulation type by among others Sarmiento et al. (1988), but there are various reasons to assume that an anti-estuarine circulation is more likely (Rohling, 1994 and references therein). The regular occurrence of sapropels after the MMCT might be in line with an anti-estuarine circulation regime. However, the absence of sapropels before the MMCT does not automatically imply that the circulation was estuarine.

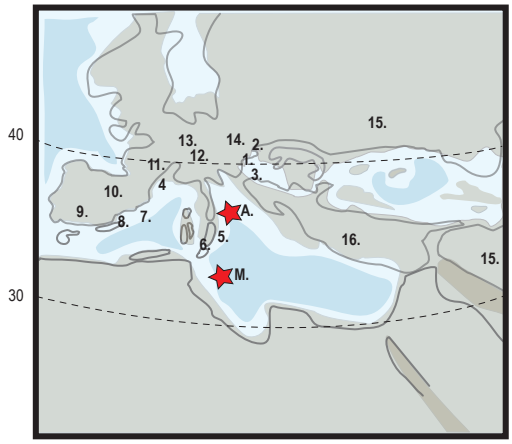

Marine Sites:

A. La Vedova Beach High Cliff (Adriatic)
M. Maltese Islands (Malta & Gozo)

1. Austria: Styrian Basin Austria (Bojar et al., 2004):
2. Northern Alpine Molasse Basin, the Vienna- and the Pannonian Basins (Kocsis et al., 2009)
3. Carpathian (Bicchi et al., 2003)
4. Montferrat (Bicchi et al., 2003
5. Tremiti (Russo et al., 2007)
6. Sicily (Hyblean Plateau) (Dall'Antonia et al., 2001)
7. Balearic (DSDP 372) (Benson, 1976)
8. West Mediterranean (Gebhardt, 1999)

Terrestrial Sites:

9. Southern Spain (Jimenez-Moreno and Suc,2007)
10.Central Spain (Van der Meulen et al., 2005)
11. France (Jimenez-Moreno and Suc,2007)
12. Switserland (Jimenez-Moreno and Suc,2007)
13. Central Europe (o.a. Böhme 2003; Mosbrugger 2005)
14. Panonnian basin (Jimenez-Moreno, 2006)
15. Eastern Europe and Arabia (Böhme, 2004)
16. Anatolia (Akgun et al., 2007)

Figure 4. Paleogeographic map for the middle Miocene Mediterranean modified after Rögl (1999) and Harzhauser and Piller (2007). Numbers refer to localities discussed in the text. Paleolatitude of the area was a few degrees to the south as compared with today (Krijgsman and Tauxe, 2004).

4. The MMCT around the Mediterranean from a terrestrial perspective

During the Miocene Climatic Optimum, the areas of central and southern Europe were characterized by a subtropical to warm-temperate humid climate with evergreen forest vegetation, with a maximum in species richness (Kürschner and Kvacek; 2009; Ivanov et al; 2002; Jimenez-Moreno, 2006; Mosbrugger et al., 2005). A very dry climate is inferred for southern Spain, indicating the presence of steppe environments in the northwestern Mediterranean area (Jimenez-Moreno and Suc, 2007) (Fig. 4). Spanish mammal communities are in line with this and point to open and relatively arid environments (e.g. Van der Meulen et al. 2005; K. Hordijk, pers. comm.). Milder conditions are progressively inferred towards France and Switzerland where pollen assemblages are dominated by taxa with higher water requirements (Jimenez-Moreno and Suc, 2007). The gradient from sub-desertic vegetation in the south to humidity-adapted plant environments in the north has been interpreted as the result of a latitudinal gradient in precipitation with a relatively low latitudinal temperature gradient (Jimenez-Moreno and Suc, 2007). Also for the southern margin of the Pannonian Basin, seasonally drier conditions prevailed (Utescher, 2007). Ectothermic vertebrates analysis reveals warm temperatures but with a seasonality in precipitation with dry periods up to six months (Böhme et al., 2003). Most likely, this dry season fell in the cooler winter months. The absence of snake heads in eastern Europe and Arabia points to arid- to semi-arid conditions with relatively dry summers (Böhme; 2004). Palynoflora studies indicate a subtropical climate for western Anatolia in the Langhian (Akgun et al., 2007).

Climatic cooling in the terrestrial realm is reflected by a decreasing trend in abundance of paleotropic and thermophilous elements (Ivanov et al., 2002). Vegetation in Central Europe became more open and floral diversity declined (Kürschner and Kvacek, 2009). Megaflora studies by Mosbrugger et al. (2005) suggest that cooling was much more pronounced in the Coldest Month Mean (CMM) than in the Warmest Month Mean (WMM), whereas Mean Annual Precipitation (MAP) remained relatively high and constant. A decrease of more than 11°C in the CMM temperature and the possible occurrence of frost periods possibly caused the major regional extinction events of most of the thermophilic vertebrate groups (alligators, chameleons and giant turtles) in Central Europe (Böhme, 2003). The temperature decrease is also evidenced by a progressively southward disappearance of the crocodile Diplocynodon during the middle and earliest late Miocene (Böhme, 2003). Between 14.3 and 13.3 Ma, with a peak at 13.75 Ma, a major turnover in the small-mammal community of the Spanish mainland took place during which species associated with woodlands and the presence of permanent water replaced most of the old (open-country) residents. This faunal change indicates a shift from drier to more humid conditions (Van der Meulen et al. 2005). Humid conditions are reconstructed for Central Europe, although a clear trend to drier conditions towards the east (Pannonian Basin, Balkan area) and the southeast (Turkey) is observed (Utescher et al., 2007). In western and central Anatolia climate was subtropical during the early-late Serravalian (Akgun et al., 2007).

5. Mediterranean climate changes during the MMCT

The terrestrial climate evolution for south-west and central Europe reveals a clear transition from warm-dry (Spain) and warm-humid conditions (central Europe) towards wetter (Spain) and cooler climates (central Europe) after the MMCT. The increase in aridity of, presumably, north Africa, as inferred from the geochemical proxies, could point to a southward displacement of the subtropical high pressure belt, which is usually associated with dry climates (e.g. Griffin, 2002). Figure 5 shows a schematic overview of the climate conditions during the MCO and after the MMCT for the Mediterranean area.

In a study on Pliocene to Pleistocene climate changes on the Iberian Peninsula, Hernandez-Fernandez et. al (2007) linked distinct climatic phases to changes in precipitation regime and latitudinal displacement of zonal climate belts. They suggested that in response to northern hemisphere glaciation, a southward shift of the subtropical

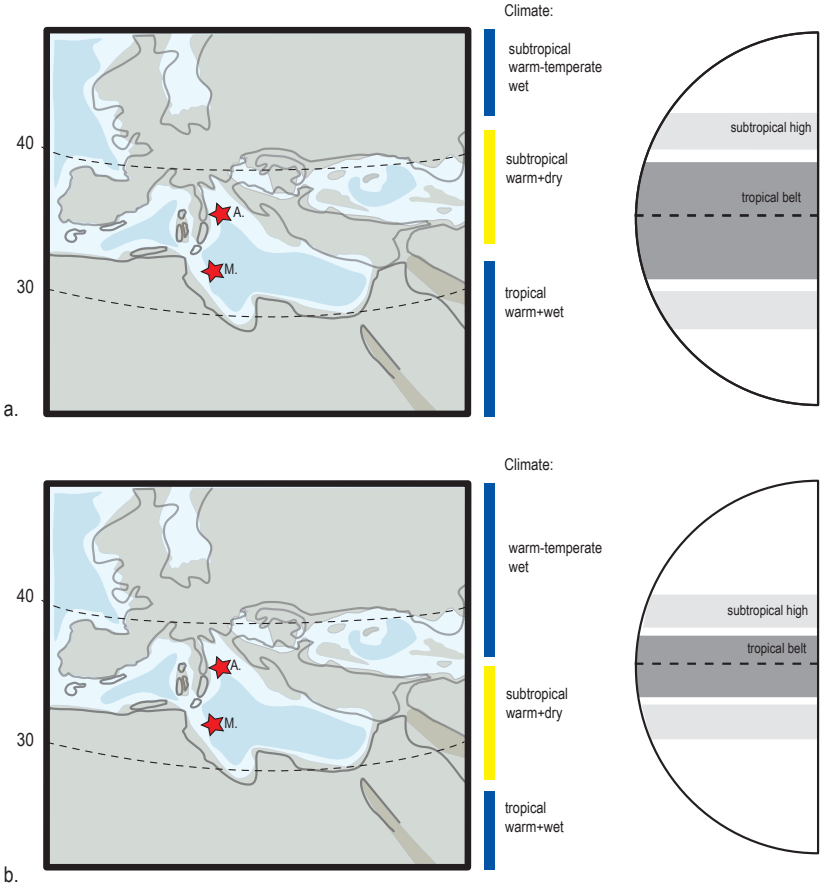

Figure 5. Hypothetical reconstruction of climate zones for the MCO (a) and after the MMCT (b). During the MCO the tropical belt may have been much wider than today. After the MMCT, the tropical belt may have narrowed in response to ice sheet expansion and global cooling. As a consequence, the subtropical high pressure belt shifted southwards. This resulted in the ardification of northern Africa and a more humid climate in Spain (e.g. Van der Meulen et al., 2005). Stars indicate the position of the studied locations (A: La Vedova sections, M: Maltese Islands).

high-pressure belt may have caused a change from a tropical climate with summer rains, to a typical Mediterranean climate with warm and dry summers, and mild and wet winters. At the same time, more arid conditions appeared in northwestern Africa (Leroy and Dupont, 1994; 1997). A similar mechanism may have been responsible for the observed climate changes during the middle Miocene.

Böhme (2004) suggested that a relatively weak thermal gradient on the Northern Hemisphere during the MCO could possibly have located the ITCZ and the subtropical high-pressure zone in a more northerly position than today, causing dry climates in the central and eastern Paratethys region (Fig. 6a). John et al. (2003) envisaged a northward shift of the ITCZ in response to East Antarctic Ice Sheet growth, assuming that the northern hemisphere was ice free and northward winds coming from the Southern Hemisphere must have been stronger than southward winds coming from the Northern Hemisphere. The northward shift in the ITCZ would have caused higher rainfall over northern Africa and hence the observed increased terrestrial influx on the Malta-Hyblean plateau.

One drawback of the latter scenario is that the subtropical high pressure zone is supposed to shift northward as well, which would cause aridification in the northern Mediterranean area after the MMCT. However, vegetation reconstructions show that humidity in central and southern Europe remained relatively high after the climate transition. At the same time, the geochemical records suggest that northern Africa became dryer. Moreover, there is increasing evidence for ice growth on the high northern latitudes after ~13.8 Ma (e.g Moran et al. 2006), which would possibly increase Northern Hemisphere atmospheric circulation as well.

Recent studies suggest that the tropical belt is expanding as a consequence of global warming. This is seen as major concern for the semi-arid regions, since a poleward expansion of the tropics will increase aridity in these regions (Seidel et al., 2008). An opposite process might be envisaged for the MMCT in which the expansion of the icecaps caused a narrowing of the tropical belt and a global redistribution of the climate zones toward a more modern situation (Fig. 5). The increase in terrestrial influx after the MMCT on Malta should therefore not be related to a northward shift of the ITCZ, but to increased erosion which was probably the consequence of a) sea level lowering and b) aridification. The year round humid conditions over northern Africa during the MCO would have sustained a continuous vegetation cover, thereby limiting significant erosion before the MMCT. In addition, enhanced global temperature gradient between the poles and the equator could have accelerated atmospheric circulation and the intensification of the subtropical high-pressure belt (Leroux, 1993; Barreiro et al., 2006), thereby increasing seasonal contrast.

Due to a combination of these factors, a more modern type of climate variability is recorded in the Mediterranean after the MMCT. The precession controlled alternation between sediments enriched in eolian dust and the occurrence of sapropels suggest that the African monsoon system was already operative. This supports the view of Wang (2009) that the monsoon is a common and also important phenomenon in the geological history. In addition, this notion is important for studies on Mediterranean climate change, since monsoon variability might now be traced back into the warm world of the MCO, thereby providing us a further look back into the future.

References

Abdul Aziz, H., Di Stefano, A., Foresi, L. M., Hilgen, F. J., Laccarino, S. M., Kuiper, K. F., Lirer, F., Salvatorini, G., and Turco, E., 2008. Integrated stratigraphy and Ar-40/Ar-39 chronology of early Middle Miocene sediments from DSDP Leg 42A, Site 372 (Western Mediterranean). *Palaeogeography Palaeoclimatology Palaeoecology* **257**, 123-138.

Abels, H. A., 2008. Long-period orbital climate forcing - Cyclostratigraphic studies of Cenozoic continental and marine successions in Europe. *Geologica Ultraiectina* **297**, Utrecht, 178 pp.

Abels, H. A., Hilgen, F. J., Krijgsman, W., Kruk, R. W., Raffi, I., Turco, E., and Zachariasse, W. J., 2005. Long-period orbital control on middle Miocene global cooling: Integrated stratigraphy and astronomical tuning of the Blue Clay Formation on Malta. *Paleoceanography* **20**, PA4012.

Akgun, F., Kayseri, M. S., and Auiraz, M. S., 2007. Palaeoclimatic evolution and vegetational changes during the Late Oligocene-Miocene period in Western and Central Anatolia (Turkey). *Palaeogeography Palaeoclimatology Palaeoecology* **253**, 56-90.

Barreiro, M., Philander, G., Pacanowski, R., and Fedorov, A., 2006. Simulations of warm tropical conditions with application to middle Pliocene atmospheres. *Climate Dynamics* **26**, 349–365.

Bellanca, A., Sgarrella, F., Neri, R., Russo, B., Sprovieri, M., Bonaduce, G., and Rocca, D., 2002. Evolution of the Mediterranean basin during the late Langhian early Serravallian: An integrated paleoceanographic approach. *Rivista Italiana Di Paleontologia E Stratigrafia* **108**, 223-239.

Benson, R. H., 1976. Miocene deep-sea ostracodes of the Iberian Portal and the Balearic Basin. *Marine Micropaleontology* **1**, 249-262.

Bianucci, G. and Landini, W., 2002. Change in diversity, ecological significance and biogeographical relationships of the Mediterranean Miocene toothed whale fauna. *Geobios* **35**, 19-28.

Bicchi, E., Ferrero, E., and Gonera, M., 2003. Palaeoclimatic interpretation based on Middle Miocene planktonic Foraminifera: the Silesia Basin (Paratethys) and Monferrato (Tethys) records. *Palaeogeography Palaeoclimatology Palaeoecology* **196**, 265-303.

Billups, K., Palike, H., Channell, J. E. T., Zachos, J. C., and Shackleton, N. J., 2004. Astronomic calibration of the late Oligocene through early Miocene geomagnetic polarity time scale. *Earth and Planetary Science Letters* **224**, 33-44.

Böhme, M., 2003. The Miocene Climatic Optimum: evidence from ectothermic vertebrates of Central Europe. *Palaeogeography Palaeoclimatology Palaeoecology* **195**, 389-401.

Böhme, M., 2004. Migration history of air-breathing fishes reveals Neogene atmospheric cirulation patterns. *Geology* **32**, 393-396.

Bojar, A. V., Hiden, H., Fenninger, A., and Neubauer, F., 2004. Middle Miocene seasonal temperature changes in the Styrian basin, Austria, as recorded by the isotopic composition of pectinid and brachiopod shells. *Palaeogeography Palaeoclimatology Palaeoecology* **203**, 95-105.

Bonaduce, G. and Barra, D., 2002. The ostracods in the paleoenvironmental interpretation of the late Langhian– early Serravallian Ras il- Pellegrin section (Malta). *Rivista Italiana Di Paleontologia E Stratigrafia* **108**, 211-222.

Bown, P. R., 1998. *Calcareous Nannofossil Biostratigraphy*. Chapman and Hall, Cambridge, p. 16-28.

Braga, J. C. and Bassi, D., 2007. Neogene history of Sporolithon Heydrich (Corallinales, rhodophyta) in the Mediterranean region. *Palaeogeography Palaeoclimatology Palaeoecology* **243**, 189-203.

Bromley, R. G., 1990. Trace Fossils: Biology and Taphonomy, *Special topics in paleontolology, 3*. Unwin Hyman, London, 280 pp.

Brüchert, V. and Pratt, L. M., 1996. Contemporaneous early diagenetic formation of organic and inorganic sulfur in estuarine sediments from St. Andrew Bay, Florida, USA. *Geochimica Et Cosmochimica Acta* **60**, 2325-2332.

Coxall, H. K., Wilson, P. A., Palike, H., Lear, C. H., and Backman, J., 2005. Rapid stepwise onset of Antarctic glaciation and deeper calcite compensation in the Pacific Ocean. *Nature* **433**, 53-57.

Cramp, A. and O'Sullivan, G., 1999. Neogene sapropels in the Mediterranean: a review. *Marine Geology* **153**, 11-28.

Dall'Antonia, B., Di Stefano, A., and Foresi, L. M., 2001. Integrated micropalaeontological study (ostracods and calcareous plankton) of the Langhian western Hyblean successions (Sicily, Italy). *Palaeogeography, Palaeoclimatology, Palaeoecology* **176**, 59-80.

Dart, C. J., Bosence, D. J. W., and McClay, K. R., 1993. Stratigraphy and structure of the Maltese graben system. *Journal of the Geological Society* **150**, 1153-1166.

De Lange, G. J., Thomson, J., Reitz, A., Slomp, C. P., Speranza Principato, M., Erba, E., and Corselli, C., 2008. Synchronous basin-wide formation and redox-controlled preservation of a Mediterranean sapropel. *Nature Geoscience* **1**, 606–610.

De Stigter, H. C., Jorissen, F. J., and Van der Zwaan, G. J., 1998. Bathymetric distribution and microhabitat partitioning of live (Rose Bengal stained) benthic foraminifera along a shelf to bathyal transect in the southern Adriatic Sea. *Journal of Foraminiferal Research* **28**, 40-65.

De Visser, J. P., 1991. Clay mineral stratigraphy of Miocene to recent marine sediments in the Central Mediterranean. Utrecht University, Utrecht, The Netherlands, *Geologica Ultraiectina* **75**, 244 pp.

Di Stefano, A., Foresi, L. M., Lirer, F., Iaccarino, S. M., Turco, E., Amore, F. O., Mazzei, R., Morabito, S., Salvatorini, G., and Abdul Aziz, H., 2008. Calcareous plankton high resolution bio-magnetostratigraphy for the Langhian of the mediterranean area. *Rivista Italiana Di Paleontologia E Stratigrafia* **114**, 51-76.

Diester-Haass, L., Billups, K., Gröcke, D. R., François, L., Lefebvre, V., and Emeis, K. C., 2009. Mid-Miocene paleoproductivity in the Atlantic Ocean and implications for the global carbon cycle. *Paleoceanography* **24**, PA1209 1-19.

Drinkwater, K. F., Beaugrand, G., Kaeriyama, M., Kim, S., Ottersen, G., Perry, R. I., Pörtner, H.-O., Polovina, J. J., and Takasuka, A., 2010. On the processes linking climate to ecosystem changes. *Journal of Marine Systems* **79**, 374-388.

Egli, R., 2004a. Characterization of individual rock magnetic components by analysis of remanence curves, 1. Unmixing natural sediments. *Studia Geophysica Et Geodaetica* **48**, 391-446.

Egli, R., 2004b. Characterization of individual rock magnetic components by analysis of remanence curves. 2. Fundamental properties of coercivity distributions. *Physics and Chemistry of the Earth* **29**, 851-867.

Eichler, P. P. B., Sen Gupta, B. K., Eichler, B. B., Braga, E. S., and Campos, E. J., 2008. Benthic foraminiferal assemblages of the South Brazil: Relationship to water masses and nutrient distributions. *Continental Shelf Research* **28**, 1674-1686.

Ellis, B.F. and Messina, A., 1940 et seq. Catalogue of foraminifera. *American Museum of National History, Micropaleontology Press.*

Ellwood, B. B., Crick, R. E., El Hassani, A., Benoist, S. L., and Young, R. H., 2000. Magnetosusceptibility event and cyclostratigraphy method applied to marine rocks; detrital input versus carbonate productivity. *Geology* **28**, 1135-1138.

Emeis, K. C., Sakamoto, T., Wehausen, R., and Brumsack, H. J., 2000. The sapropel record of the eastern Mediterranean Sea - results of Ocean Drilling Program Leg 160. *Palaeogeography Palaeoclimatology Palaeoecology* **158**, 371-395.

Felix, R., 1973. Oligo-Miocene stratigraphy of Malta and Gozo. *Meded. Landbouwhogesch. Wageningen* **73-20**, 1-103.

Flower, B. P. and Kennett, J. P., 1993. The middle Miocene ocean/climate transition: high-resolution oxygen and carbon isotopic records from Deep Sea Drilling Project Site 588A, Southwest Pacific *Paleoceanography* **8**, 811-843.

Flower, B. P. and Kennett, J. P., 1994. The Middle Miocene Climatic Transition - East Antarctic Ice-Sheet Development, Deep-Ocean Circulation and Global Carbon Cycling. *Palaeogeography Palaeoclimatology Palaeoecology* **108**, 537-555.

Flower, B. P. and Kennett, J. P., 1995. Middle Miocene Deepwater Paleoceanography in the Southwest Pacific: Relations with East Antarctic Ice Sheet Development. *Paleoceanography* **10**, 1095–1112.

Föllmi, K. B., Badertscher, C., de Kaenel, E., Stille, P., John, C. M., Adatte, T., and Steinmann, P., 2005. Phosphogenesis and organic-carbon preservation in the miocene monterey formation at Naples beach, California - The monterey hypothesis revisited. *Geological Society of America Bulletin* **117**, 589-619.

Fornaciari, E., Di Stefano, A., Rio, D., and Negri, A., 1996. Middle Miocene quantitative calcareous nannofossil biostratigraphy in the Mediterranea region. *Marine Micropaleontology* **42**, 37-63.

Foucault, A. and Melieres, F., 2000. Palaeoclimatic cyclicity in central Mediterranean Pliocene sediments: the mineralogical signal. *Palaeogeography Palaeoclimatology Palaeoecology* **158**, 311-323.

Gardiner, W., Grasso, M., and Sedgeley, D., 1995. Plio-Pleistocene fault movement as evidence for mega-block kinematics within the Hyblean-Malta Plateau, central Mediterranean. *Journal of Geodynamics* **19**, 35-51.

Gebhardt, H., 1999. Middle to Upper Miocene benthonic foraminiferal palaeoecology of the Tap Marls (Alicante Province, SE Spain) and its palaeoceanographic implications. *Palaeogeography Palaeoclimatology Palaeoecology* **145**, 141-156.
Gladstone, R., Flecker, R., Valdes, P., Lunt, D., and Markwick, P., 2007. The Mediterranean hydrologic budget from a Late Miocene global climate simulation. *Palaeogeography, Palaeoclimatology, Palaeoecology* **251**, 254-267.
Griffin, D. L., 2002. Aridity and humidity: two aspects of the late Miocene climate of North Africa and the Mediterranean. *Palaeogeography, Palaeoclimatology, Palaeoecology* **182**, 65-91.
Grimsdale, T. F. and Van Morkhoven, F. P. C. M., 1955. The ratio between pelagic and benthonic foraminifera as a means of estimating depth of deposition of sedimentary rocks. *Proceedings of 4th World Petroleum Congress* **Section I**, 473–491.
Grimsdale, T. F. and Van Morkhoven, F. P. C. M., 1955. The ratio between pelagic and benthonic foraminifera
Hammer, O. and Harper, D., 2006. *Paleontological data analysis.* Blackwell Publishing, Oxford, UK, 351p.
Haq, B. U., Hardenbol, J., and Vail, P. R., 1987. Chronology of fluctuating sea levels since the Triassic. *Science* **235**, 1156-1167.
Harzhauser, M. and Piller, W. E., 2007. Benchmark data of a changing sea - Palaeogeography, palaeobiogeography and events in the Central Paratethys during the Miocene. *Palaeogeography Palaeoclimatology Palaeoecology* **253**, 8-31.
Harzhauser, M., Kroh, A., Mandic, O., Piller, W. E., Göhlich, U., Reuter, M., and Berning, B., 2007. Biogeographic responses to geodynamics: A key study all around the Oligo–Miocene Tethyan Seaway. *Zoologischer Anzeiger* **246**, 241-256.
Harzhauser, M., Piller, W. E., and Steininger, F. F., 2002. Circum-Mediterranean Oligo-Miocene biogeographic evolution - the gastropods' point of view. *Palaeogeography Palaeoclimatology Palaeoecology* **183**, 103-133.
Hay, W. W., 1996. Tectonics and climate. *Geologische Rundschau* **85**, 409-437.
Hay, W. W., 1998. Detrital sediment fluxes from continents to oceans. *Chemical Geology* **145**, 287-323.
Hay, W. W., Soeding, E., DeConto, R. M., and Wold, C. N., 2002. The Late Cenozoic uplift - climate change paradox. *International Journal of Earth Sciences* **91**, 746-774.
Hernández Fernández, M., Álvarez Sierra, M. Á., and Peláez-Campomanes, P., 2007. Bioclimatic analysis of rodent palaeofaunas reveals severe climatic changes in Southwestern Europe during the Plio-Pleistocene. *Palaeogeography, Palaeoclimatology, Palaeoecology* **251**, 500-526.
Heslop, D., McIntosh, G., and Dekkers, M. J., 2004. Using time- and temperature-dependent Preisach models to investigate the limitations of modelling isothermal remanent magnetization acquisition curves with cumulative log Gaussian functions. *Geophysical Journal International* **157**, 55-63.
Hilgen, F. J., 1991a. Astronomical Calibration of Gauss to Matuyama Sapropels in the Mediterranean and Implication for the Geomagnetic Polarity Time Scale. *Earth and Planetary Science Letters* **104**, 226-244.
Hilgen, F. J., 1991b. Extension of the Astronomically Calibrated (Polarity) Time Scale to the Miocene Pliocene Boundary. *Earth and Planetary Science Letters* **107**, 349-368.
Hilgen, F. J., Abels, H. A., Iaccarino, S., Krijgsman, W., Raffi, I., Sprovieri, R., Turco, E., and Zachariasse, W. J., 2009. The Global Stratotype Section and Point (GSSP) of the Serravallian Stage (Middle Miocene). *Episodes* **32**, 152-166.
Hilgen, F. J., Aziz, H. A., Krijgsman, W., Raffi, I., and Turco, E., 2003. Integrated stratigraphy and astronomical tuning of the Serravallian and lower Tortonian at Monte dei Corvi (Middle-Upper Miocene, northern Italy). *Palaeogeography Palaeoclimatology Palaeoecology* **199**, 229-264.
Hilgen, F. J., Krijgsman, W., Langereis, C. G., Lourens, L. J., Santarelli, A., and Zachariasse, W. J., 1995. Extending the astronomical (polarity) time scale into the Miocene. *Earth and Planetary Science Letters* **136**, 495-510.
Hilgen, F. J., Krijgsman, W., Raffi, I., Turco, E., and Zachariasse, W. J., 2000. Integrated stratigraphy and astronomical calibration of the Serravallian/Tortonian boundary section at Monte Gibliscemi (Sicily, Italy). *Marine Micropaleontology* **38**, 181-211.
Holbourn, A., Kuhnt, W., Schulz, M., and Erlenkeuser, H., 2005. Impacts of orbital forcing and atmospheric carbon dioxide on Miocene ice-sheet expansion. *Nature* **438**, 483-487.
Holbourn, A., Kuhnt, W., Schulz, M., Flores, J. A., and Andersen, N., 2007. Orbitally-paced climate evolution during the middle Miocene "Monterey" carbon-isotope excursion. *Earth and Planetary Science Letters* **261**, 534-550.

Hsü, K. J. and Bernoulli, D., 1978. Genesis of the Tethys and the Mediterranean. *Initial Reports DSDP,* **42**, 943-949.
Hüsing, 2008. Astrochronology of the Mediterranean Miocene - Linking paleoenvironmental changes to gateway dynamics. *Geologica Ultraiectina* **295**, Utrecht, 171p.
Hüsing, S. K., Dekkers, M. J., Franke, C., and Krijgsman, W., 2009. The Tortonian reference section at Monte dei Corvi (Italy): evidence for early remanence acquisition in greigite-bearing sediments. *Geophys. J. Int.* doi: 10.1111/j.1365-246X.2009.04301.x.
Hüsing, S. K., F.J., H., Abdul Aziz, H., and Krijgsman, W., 2007. Completing the Neogene geological time scale between 8.5 and 12.5 Ma. *Earth and Planetary Science Letters* **253**, 340-358.
Hüsing, S. K., Hilgen, F. J., Kuiper, K. F., Krijgsman, W., Turco, E., Cascella, A., and Wilson, D., 2010. Astrochronology of the Mediterranean Langhian bewteen 15.29 and 14.17 Ma *Earth and Planetary Science Letters*, **290**, 3-4, 254-269.
Hüsing, S. K., Kuiper, K. F., Link, W., Hilgen, F. J., and Krijgsman, W., 2009. The upper Tortonian-lower Messinian at Monte dei Corvi (Northern Apennines, Italy): Completing a Mediterranean reference section for the Tortonian Stage. *Earth and Planetary Science Letters* **282**, 140-157.
Ivanov, D., Ashraf, A. R., Mosbrugger, V., and Palamarev, E., 2002. Palynological evidence for Miocene climate change in the Forecarpathian Basin (Central Paratethys, NW Bulgaria. *Palaeogeography Palaeoclimatology Palaeoecology* **178**, 19-37.
Jacobs, E., Weissert, H., Shields, G., and Stille, P., 1996. The monterey event in the Mediterranean: A record from shelf sediments of Malta. *Paleoceanography* **11**, 717-728.
Jickells, T. D., An, Z. S., Andersen, K. K., Baker, A. R., Bergametti, G., Brooks, N., Cao, J. J., Boyd, P. W., Duce, R. A., Hunter, K. A., Kawahata, H., Kubilay, N., laRoche, J., Liss, P. S., Mahowald, N., Prospero, J. M., Ridgwell, A. J., Tegen, I., and Torres, R., 2005. Global iron connections between desert dust, ocean biogeochemistry, and climate. *Science* **308**, 67-71.
Jimenez-Moreno, G. and Suc, J. P., 2007. Middle Miocene latitudinal climatic gradient in Western Europe: Evidence from pollen records. *Palaeogeography Palaeoclimatology Palaeoecology* **253**, 208-225.
Jimenez-Moreno, G., 2006. Progressive substitution of a subtropical forest for a temperate one during the middle Miocene climate cooling in Central Europe according to palynological data from cores Tengelic-2 and Hidas-53 (Pannonian Basin, Hungary). *Review of Palaeobotany and Palynology* **142**, 1-14.
John, C. M., Follmi, K. B., De Kaenel, E., Adatte, T., Steinmann, P., and Badertscher, C., 2002. Carbonaceous and phosphate-rich sediments of the Miocene Monterey Formation at El Capitan State Beach, California, USA. *Journal of Sedimentary Research* **72**, 252-267.
John, C. M., Karner, G. D., and Mutti, M., 2004. δ18O and Marion Plateau backstripping: Combining two approaches to constrain late middle Miocene eustatic amplitude. *Geology* **32**, 829-832.
John, C. M., Mutti, M., and Adatte, T., 2003. Mixed carbonate-siliciclastic record on the North African margin (Malta) - coupling of weathering processes and mid Miocene climate. *Geological Society of America Bulletin* **115**, 217-229.
Jones, R.W., 1994. The Challenger Foraminifera, Oxford University Press, London (1994), 149pp.
Jorissen, F. J., 1999. Benthic foraminiferal successions across Late Quaternary Mediterranean sapropels. *Marine Geology* **153**, 91-101.
Jorissen, F. J., deStigter, H. C., and Widmark, J. G. V., 1995. A conceptual model explaining benthic foraminiferal microhabitats. *Marine Micropaleontology* **26**, 3-15.
Jorissen, F. J., Fontanier, C., and Thomas, E., 2007. Paleoceanographical Proxies Based on Deep-Sea Benthic Foraminiferal Assemblage Characteristics. In: Hillaire-Marcel, C. and De Vernal, A. (Eds.), *Proxies in late Cenozoic paleoceanography*, 843 pp.
Karami, M. P., Meijer, P. T., Dijkstra, H. A., and Wortel, M. J. R., 2009. An oceanic box model of the Miocene Mediterranean Sea with emphasis on the effects of closure of the eastern gateway. *Paleoceanography* **24**, PA4203: 1-15.
Kender, S., Peck, V. L., Jones, R. W., and Kaminski, M. A., 2009. Middle Miocene oxygen minimum zone expansion offshore West Africa; evidence for global cooling precursor events. *Geology* **37**, 699-702.
Kidd, R. B., Cita, M. B., and Ryan, W. B. F., 1978. Stratigraphy of eastern Mediterranean sapropel sequences recovered during DSDP Leg 42A and their paleoenvironmental significance, *Initial Reports of the Deep Sea Drilling Project Leg 42, Part 1*. Texas A & M University, p421-443.

Kocsis, L., Vennemann, T. W., Hegner, E., Fontignie, D., and Tutken, T., 2009. Constraints on Miocene oceanography and climate in the Western and Central Paratethys: O-, Sr-, and Nd-isotope compositions of marine fish and mammal remains. *Palaeogeography Palaeoclimatology Palaeoecology* **271**, 117-129.

Köppen, W., 1936. Das geographische System der Klimate. In: Köppen, W. and Geiger, G. (Eds.), *Handbuch der Klimatologie*. Vol. 1, part C, pp.1-44. Gebrüder Borntraeger, Berlin.

Krijgsman, W. and Tauxe, L., 2004. Shallow bias in Mediterranean paleomagnetic directions caused by inclination error. *Earth and Planetary Science Letters* **222**, 685-695.

Kroepelin, S., 2006. Revisiting the age of the Sahara desert. *Science* **312**, 1138-1138.

Kroh, A., 2007. Climate changes in the Early to Middle Miocene of the Central Paratethys and the origin of its echinoderm fauna. *Palaeogeography, Palaeoclimatology, Palaeoecology* **253**, 169-207.

Krom, M. D., Cliff, R. A., Eijsink, L. M., Herut, B., and Chester, R., 1999. The characterisation of Saharan dusts and Nile particulate matter in surface sediments from the Levantine basin using Sr isotopes. *Marine Geology* **155**, 319-330.

Kruiver, P. P., Dekkers, M. J., and Heslop, D., 2001. Quantification of magnetic coercivity components by the analysis of acquisition curves of isothermal remanent magnetisation. *Earth Planet. Sc. Lett.* **189**, 269-276.

Kürschner, W. M. and Kvacek, Z., 2009. Oligocene-Miocen CO2 fluctuations, climatic and palaeofloristic trends inferred from fossil plant assemblages in central Europe. *Bulletin of Geosciences* **84**, 189-202.

Kürschner, W. M., Kvacek, Z., and Dilcher, D. L., 2008. The impact of Miocene atmospheric carbon dioxide fluctuations on climate and the evolution of terrestrial ecosystems. *Proceedings of the National Academy of Sciences of the United States of America* **105**, 449-453.

Laskar, J., Joutel, F., and Boudin, F., 1993. Orbital, Precessional, and Insolation Quantities for the Earth from -20 Myr to +10 Myr. *Astronomy and Astrophysics* **270**, 522-533.

Laskar, J., Robutel, P., Joutel, F., Gastineau, M., Correia, A. C. M., and Levrard, B., 2004. A long-term numerical solution for the insolation quantities of the Earth. *Astronomy & Astrophysics* **428**, 261-285.

Leroux, M., 1993. The Mobile Polar High: a new concept explaining present mechanisms of meridional air-mass and energy exchanges and global propagation of palaeoclimatic changes. *Global and Planetary Change* **7**, 69-93.

Leroy, S. A. G. and Dupont, L. M., 1997. Marine palynology of the ODP site 658 (N-W Africa) and its contribution to the stratigraphy of Late Pliocene. *Geobios* **30**, 351-359.

Leroy, S. and Dupont, L., 1994. Development of vegetation and continental aridity in northwestern Africa during the Late Pliocene: the pollen record of ODP site 658. *Palaeogeography, Palaeoclimatology, Palaeoecology* **109**, 295-316.

Loeblich, A.R. and Tappan, H. 1964. Sarcodina, chiefly "Thecamoebians" and Foraminiferida. In Treatise on invertebrate paleontology (Moore RC, ed.). Lawrence: Geological Society of America and University of Kansas Press, Part C, Protista 2, 2: 511-900.

Loeblich, A.R. and Tappan, H. 1988. Foraminiferal genera and their classification. Van Nostrand Reinhold Company, New York, 2 vol., 970 p. plus 212 p. + 847 pls

Lourens, L. J., Antonarakou, A., Hilgen, F. J., VanHoof, A. A. M., VergnaudGrazzini, C., and Zachariasse, W. J., 1996. Evaluation of the Plio-Pleistocene astronomical timescale. *Paleoceanography* **11**, 391-413.

Lourens, L. J., Hilgen, F. J., Laskar, J., Shackleton, N., and Wilson, D., 2004. The Neogene period. In: Gradstein, F. M., Ogg, J. G., and Smith, A. G. (Eds.), *A Geologic Time Scale 2004;*. Cambridge University Press.p. 405-440.

Lourens, L. J., Hilgen, F. J., Raffi, I., and VergnaudGrazzini, C., 1996. Early Pleistocene chronology of the Vrica section (Calabria, Italy). *Paleoceanography* **11**, 797-812.

Lourens, L. J., Wehausen, R., and Brumsack, H. J., 2001. Geological constraints on tidal dissipation and dynamical ellipticity of the Earth over the past three million years. *Nature* **409**, 1029-1033.

Mader, D., Cleaveland, L., Bice, D. M., Montanari, A., and Koeberl, C., 2004. High-resolution cyclostratigraphic analysis of multiple climate proxies from a short Langhian pelagic succession in the Conero Riviera, Ancona (Italy). *Palaeogeography Palaeoclimatology Palaeoecology* **211**, 325-344.

Martin, J.-M. and Meybeck, M., 1979. Elemental mass-balance of material carried by major world rivers. *Marine Chemistry* **7**, 173-206.

Middelburg, J. J., Vlug, T., Jaco, F., and van der Nat, W. A., 1993. Organic matter mineralization in marine systems. *Global and Planetary Change* **8**, 47-58.

Miller, K. G., Fairbanks, R. G., and Mountain, G. S., 1987. Tertiary oxygen isotope synthesis, sea level history, and continental margin erosion *Paleoceanography* **2**, 1-19.
Miller, K. G., Mountain, G. S., and and Members of the Shipboard Party, 1996. Drilling and dating New Jersey Oligocene-Miocene sequences: Ice volume, global sea level, and Exxon records. *Science* **271**, 1092-1095.
Miller, K. G., Mountain, G. S., Browning, J. V., Kominz, M., Sugarman, P. J., Christie-Blick, N., Katz, M. E., and Wright, J. D., 1998. Cenozoic global sea level, sequences, and the New Jersey transect: Results from coastal plain and continental slope drilling. *Reviews of Geophysics* **36**, 569-601.
Miller, K. G., Wright, J. D., and Fairbanks, R. G., 1991. Unlocking the Ice House - Oligocene-Miocene Oxygen Isotopes, Eustasy, and Margin Erosion. *Journal of Geophysical Research-Solid Earth and Planets* **96**, 6829-6848.
Montanari, A., Beaudoin, B., Chan, L. S., Coccioni, R., Deino, A., DePaolo, D. J., Emmanuel, L., Fornaciari, E., Kruge, M., Lundblad, S., Mozzato, C., Portier, E., Renard, M., Rio, D., Sandroni, P., and Stankiewicz, A., 1997. Integrated stratigraphy of the Middle to Upper Miocene pelagic sequence of the Conero Riviera (Marche Region, Italy). In: Montanari, A., Odin, G. S., and Coccioni, R. Eds.), *Miocene Stratigraphy: An Integrated Approach. Developments in Paleontology and Stratigraphy*. Vol. 15., Elsevier, Amsterdam, p. 409-450.
Moran, K., Backman, J., Brinkhuis, H., Clemens, S. C., Cronin, T., Dickens, G. R., Eynaud, F., Gattacceca, J., Jakobsson, M., Jordan, R. W., Kaminski, M., King, J., Koc, N., Krylov, A., Martinez, N., Matthiessen, J., McInroy, D., Moore, T. C., Onodera, J., O'Regan, M., Palike, H., Rea, B., Rio, D., Sakamoto, T., Smith, D. C., Stein, R., St John, K., Suto, I., Suzuki, N., Takahashi, K., Watanabe, M., Yamamoto, M., Farrell, J., Frank, M., Kubik, P., Jokat, W., and Kristoffersen, Y., 2006. The Cenozoic palaeoenvironment of the Arctic Ocean. *Nature* **441**, 601-605.
Moreno, A., Cacho, I., Canals, M., Grimalt, J. O., Sánchez-Goñi, M. F., Shackleton, N., and Sierro, F. J., 2005. Links between marine and atmospheric processes oscillating on a millennial time-scale. A multi-proxy study of the last 50,000 yr from the Alboran Sea (Western Mediterranean Sea). *Quaternary Science Reviews* **24**, 1623-1636.
Mosbrugger, V., Utescher, T., and Dilcher, D. L., 2005. Cenozoic continental climatic evolution of Central Europe. *Proceedings of the National Academy of Sciences of the United States of America* **102**, 14964-14969.
Mourik, A. A., Bijkerk, J. F., Cascella, A., Hilgen, F. J., Hüsing, S. K., Lourens, L. J., and Turco, E., in review. Astronomical tuning of the La Vedova High Cliff Section (Ancona, Italy) – Implications of the Middle Miocene Climate Transition for Mediterranean sapropel formation. *EPSL*.
Müller, P. J. and Suess, E., 1979. Productivity, sedimentation rate, and sedimentary organic matter in the oceans--I. Organic carbon preservation. *Deep Sea Research Part A. Oceanographic Research Papers* **26**, 1347-1362.
Murray, J. W., 2001. The niche of benthic foraminifera, critical thresholds and proxies. *Marine Micropaleontology* **41**, 1-7.
Nijenhuis, I. A. and de Lange, G. J., 2000. Geochemical constraints on Pliocene sapropel formation in the eastern Mediterranean. *Marine Geology* **163**, 41-63.
Nijenhuis, I. A., Schenau, S. J., VanderWeijden, C. H., Hilgen, F. J., Lourens, L. J., and Zachariasse, W. J., 1996. On the origin of upper Miocene sapropelites: A case study from the Faneromeni section, Crete (Greece). *Paleoceanography* **11**, 633-645.
Nijenhuis, I., Wehausen, R., and De Lange, G. J., 1998. The trace element budget of the eastern Mediterranean during Pliocene sapropel formation. In: Robertson, A. H. F., Emeis, K.-C., Richter, C., and Camerlenghi, A. (Eds.), *Proceedings of the Ocean Drilling Program, Scientific Results*. Vol. 160, p. 199-206.
Okay, A. I., Zattin, M., and Cavazza, W., 2010. Apatite fission-track data for the Miocene Arabia-Eurasia collision. *Geology* **38**, 35-38.
Pagani, M., Arthur, M. A., and Freeman, K. H., 1999. Miocene evolution of atmospheric carbon dioxide. *Paleoceanography* **14**, 273-292.
Pagani, M., Caldeira, K., Berner, R., and Beerling, D. J., 2009. The role of terrestrial plants in limiting atmospheric CO2 decline over the past 24 million years. *Nature* **460**, 85-89.
Paillard, D., Labeyrie, L., and Yiou, P., 1996. Macintosh program performs timeseries analysis. *Transactions of the American Geophysics Union (EOS)* **77**, 379.
Pälike, H., Frazier, J., and Zachos, J. C., 2006. Extended orbitally forced palaeoclimatic records from the equatorial Atlantic Ceara Rise. *Quaternary Science Reviews* **25**, 3138–3149.

Pearson, P. N. and Palmer, M. R., 2000. Atmospheric carbon dioxide concentrations over the past 60 million years. *Nature* **406**, 695-699.
Pedley, H. M. and Bennett, S. M., 1985. Phosphorites, hardgrounds and syndepositional solution subsidence; a palaeoenvironmental model from the Miocene of the Maltese Islands. *Sedimentary Geology* **45**, 1-34.
Pedley, H. M. and Grasso, M., 1992. Miocene syntectonic sedimentation along the western margins of the Hyblean-Malta platform: A guide to plate margin processes in the central Mediterranean. *Journal of Geodynamics* **15**, 19-37. Potter, P. E. and Szatmari, P., 2009. Global Miocene tectonics and the modern world. *Earth-Science Reviews* **96**, 279-295.
Poulton, S. W. and Raiswell, R., 2002. The low-temperature geochemical cycle of iron: From continental fluxes to marine sediment deposition. *American Journal of Science* **302**, 774-805.
Raffi, I., Backman, J., Fornaciari, E., Pälike, H., Rio, D., Lourens, L., and Hilgen, F., 2006. A review of calcareous nannofossil astrobiochronology encompassing the past 25 million years. *Quaternary Science Reviews* **25**, 3113–3137.
Ramsay, A. T. S., Smart, C. W., and Zachos, J. C., 1998. A model of early to middle Miocene deep ocean circulation for the Atlantic and Indian Oceans. In: Cramp, A., MacLeod, C. J., Lee, S. V., and Jones, E. J. W. (Eds.), *Geological Evolution of Ocean Basins: Results From the Ocean Drilling Program*. Geological Society of London Special Publication, **131**, p. 55-70.
Raymo, M. E. and Ruddiman, W. F., 1992. Tectonic Forcing of Late Cenozoic Climate. *Nature* **359**, 117-122.
Rehfeld, U. and Janssen, A. W., 1995. Development of Phosphatized Hardgrounds in the Miocene Globigerina Limestone of the Maltese Archipelago, Including a Description of Gamopleura-Melitensis Sp-Nov (Gastropoda, Euthecosomata). *Facies* **33**, 91-106.
Roberts, A. P., 1995. Magnetic properties of sedimentary greigite (Fe_3S_4). *Earth and Planetary Science Letters,* **134**, 227-236.
Rögl, F., 1999. Mediterranean and Paratethys. Facts and hypotheses of an Oligocene to Miocene paleogeography (short overview). *Geologica Carpathica* **50**, 339-349.
Rohling, E. J. and Bryden, H. L., 1994. Estimating past changes in the Eastern Mediterranean freshwater budget, using reconstructions of sea level and hydrography. *Proceedings of the Koninklijke Nederlandse Akademie van Wetenschappen* **97**, 201-217.
Rohling, E. J., 1994. Review and new aspects concerning the formation of eastern Mediterranean sapropels. *Marine Geology* **122**, 1-28.
Rohling, E. J., Abu-Zied, R. H., Casford, J. S. L., Hayes, A., and Hoogakker, B. A. A., 2009. The Marine Environment: Present and Past. In: Woodward, J. C. (Ed.), *The Physical Geography of the Mediterranean*. Oxford University Press, Oxford, 592pp.
Rosoff, D. B. and Corliss, B. H., 1992. An Analysis of Recent Deep-Sea Benthic Foraminiferal Morphotypes from the Norwegian and Greenland Seas. *Palaeogeography Palaeoclimatology Palaeoecology* **91**, 13-20.
Rossignol-Strick, M., 1983. African monsoons, an immediate climate response to orbital insolation. *Nature* **304**, 46-49.
Rossignol-Strick, M., 1985. Mediterranean Quaternary sapropels, and immediate response of the African monsoon to variation of insolation. *Palaeogeography Palaeoclimatology Palaeoecology* **49**, 237-263.
Rossignol-Strick, M., Nesteroff, W., Olive, P., and C., V.-G., 1982. After the deluge; Mediterranean stagnation and sapropel formation. *Nature* **295**, 105-110.
Ruddiman, W.F., 2000. Earth's Climate: Past and Future. W.H. Freeman, New York (2000), 465 pp.
Russo, B., Curcio, E., and Iaccarino, S., 2007. Paleoecology and paleoceanography of a Langhian succession (Tremiti Islands, southern Adriatic Sea, Italy) based on benthic foraminifera. . *Bollettino della Societa Paleontologica Italiana* **46**, 107-124.
Sarmiento, J. L., Herbert, T., and Toggweiler, J. R., 1988. Mediterranean nutrient balance and episodes of anoxia. *Global Biogeochemical Cycles* **2**, 427–444.
Schenau, S. J., Antonarakou, A., Hilgen, F. J., Lourens, L. J., Nijenhuis, I. A., van der Weijden, C. H., and Zachariasse, W. J., 1999. Organic-rich layers in the Metochia section (Gavdos, Greece): evidence for a single mechanism of sapropel formation during the past 10 My. *Marine Geology* **153**, 117-135.
Schmiedl, G., Mitschele, A., Beck, S., Emeis, K. C., Hemleben, C., Schulz, H., Sperling, M., and Weldeab, S., 2003. Benthic foraminiferal record of ecosystem variability in the eastern Mediterranean Sea during times of sapropel S-5 and S-6 deposition. *Palaeogeography Palaeoclimatology Palaeoecology* **190**, 139-164.

Schnetger, B., Brumsack, H. J., Schale, H., Hinrichs, J., and Dittert, L., 2000. Geochemical characteristics of deep-sea sediments from the Arabian Sea: a high-resolution study. *Deep Sea Research Part II: Topical Studies in Oceanography* **47**, 2735-2768.

Schulz, M. and Mudelsee, M., 2002. REDFIT: estimating red-noise spectra directly from unevenly spaced paleoclimatic time series. *Computers & Geosciences* **28**, 421-426.

Schuster, M., Duringer, P., Ghienne, J. F., Vignaud, P., Mackaye, H. T., Likius, A., and Brunet, M., 2006a. The age of the Sahara Desert. *Science* **311**, 821-821.

Seidel, D. J., Fu, Q., Randel, W. J., and Reichler, T. J., 2008. Widening of the tropical belt in a changing climate. *Nature Geoscience* **1**, 21-24.

Shackleton, N. J. and Kennett, J. P., 1975. Paleotemperature History of the Cenozoic and the Initiation of Antarctic Glaciation: Oxygen and Carbon Isotope Analyses in DSDP Sites 277, 279 and 281. *Init. Rep. Deep Sea Drilling Project* **29**, 801-807.

Shevenell, A. E. and Kennett, J. P., 2004. Paleoceanographic Change During the Middle Miocene Climate Revolutoin: An Antarctic Stable Isotope Perspective. In: Kennett, J. P. and Warnke, D. A. Eds.), *The Cenozoic Southern Ocean: Tectonics, Sedimentation and Climate Change Between Australia and Antarctica. Geophysical Monograph Series.* American Geophysical Union, Washington, p. 235-251.

Shevenell, A. E., Kennett, J. P., and Lea, D. W., 2004. Middle Miocene Southern Ocean cooling and Antarctic cryosphere expansion. *Science* **305**, 1766-1770.

Shevenell, A. E., Kennett, J. P., and Lea, D. W., 2008. Middle Miocene ice sheet dynamics, deep-sea temperatures, and carbon cycling: A Southern Ocean perspective. *Geochemistry Geophysics Geosystems* **9**, -Q02006, doi:10.1029/2007GC001736.

Shipboard Scientific Party, 2000. Site 1146. *In* Wang, P., Prell, W.L., Blum, P., et al., *Proc. ODP, Init. Repts.,* 184, 1-101.

Smart, C. W., Thomas, E., and Ramsay, A. T. S., 2007. Middle-late Miocene benthic Foraminifera in a western equatorial Indian Ocean depth transect; paleoceanographic implications. *Palaeogeography Palaeoclimatology Palaeoecology* **247**, 402-420.

Sprovieri, R., Bonomo, S., Caruso, A., Di Stefano, A., Di Stefano, E., Foresi, L. M., Iaccarino, S. M., Lirer, F., Mazzei, R., and Salvatorini, G., 2002. An integrated calcareous plankton biostratigraphic scheme and biochronology for the Mediterranean Middle Miocene. *Rivista Italiana Di Paleontologia E Stratigrafia* **108**, 337-353.

Swezey, C. S., 2006. Revisiting the age of the Sahara desert. *Science* **312**, 1138-1139.

Swezey, C. S., 2009. Cenozoic stratigraphy of the Sahara, Northern Africa. *Journal of African Earth Sciences* **53**, 89-121.

Tian, J., Zhao, Q. H., Wang, P. X., Li, Q. Y., and Cheng, X. R., 2008. Astronomically modulated Neogene sediment records from the South China Sea. *Paleoceanography* **23**, -PA3210, doi:10.1029/2007PA001552.

Tian, J., Shevenell, A., Wang, P., Zhao, Q., Li, Q., and Cheng, X., 2009. Reorganization of Pacific Deep Waters linked to middle Miocene Antarctic cryosphere expansion: A perspective from the South China Sea. *Palaeogeography, Palaeoclimatology, Palaeoecology* **284**, 375-382.

Tribovillard, N., Algeo, T. J., Lyons, T., and Riboulleau, A., 2006. Trace metals as paleoredox and paleoproductivity proxies: An update. *Chemical Geology* **232**, 12-32.

Tuenter, E., Weber, S. L., Hilgen, F. J., and Lourens, L. J., 2003. The response of the African summer monsoon to remote and local forcing due to precession and obliquity. *Global and Planetary Change* **36**, 219-235.

Turco, E., Hilgen, F. J., Lourens, L. J., Shackleton, N. J., and Zachariasse, W. J., 2001. Punctuated evolution of global climate cooling during the late Middle to early Late Miocene: High-resolution planktonic foraminiferal and oxygen isotope records from the Mediterranean. *Paleoceanography* **16**, 405-423.

Utescher, T., Djordjevic-Milutinovic, D., Bruch, A., and Mosbrugger, V., 2007. Palaeoclimate and vegetation change in Serbia during the last 30 Ma. *Palaeogeography Palaeoclimatology Palaeoecology* **253**, 141-152.

Van der Meulen, A. J. and Daams, R., 1992. Evolution of early-middle miocene rodent faunas in relation to long-term palaeoenvironmental changes. *Palaeogeography, Palaeoclimatology, Palaeoecology* **93**, 227-253.

Van der Zwaan, G. J. and Gudjonsson, L., 1986. Middle Miocene-Pliocene stable isotope stratigraphy and paleoceanography of the Mediterranean. *Marine Micropaleontology* **10**, 71-90.

Van der Zwaan, G.J., Jorissen, F.J., Verhallen, P.J.J.M. and Von Daniels, C.H., 1986, Atlantic-European Oligocene to Recent Uvigerina: taxonomy, paleoecology and paleobiography. Utrecht Micropaleontological Bulletins **35**, 240 pp.

Van der Zwaan, G. J., Jorissen, F.J., De Stigter, H.C., 1990. The depth dependency of planktonic/benthic foraminiferal ratios: Constraints and applications. *Marine Geology* **95**, 1-16.

Van Hinsbergen, D. J. J., Kouwenhoven, T. J., and Van der Zwaan, G. J., 2005. Paleobathymetry in the backstripping procedure: Correction for oxygenation effects on depth estimates. *Palaeogeography Palaeoclimatology Palaeoecology* **221**, 245-265.

Vasiliev, I., Franke, C., Meeldijk, J. D., Dekkers, M. J., Langereis, C. G., and Krijgsman, W., 2008. Putative greigite magnetofossils from the Pliocene epoch. *Nature Geoscience* **1**, 782-786.

Verhallen, P.J.J.M., 1991, Late Pliocene to Early Pleistocene Mediterranean mud-dwelling foraminifera: influence on a changing environment on community structure and evolution. Utrecht Micropaleontological Bulletin **40**, 219 pp.

Vincent, E. and Berger, W. H., 1985. Carbon dioxide and polar cooling in the Miocene: the Monterey hypothesis. In: Sundquist, E. T. and Broecker, W. S. (Eds.)*The Carbon Cycle and Atmospheric CO2: Natural Variations Archean to Present, Geophysical Monograph Series* **32**, p. 455-468.

Wan, S., Kürschner, W. M., Clift, P. D., Li, A., and Li, T., 2009. Extreme weathering/erosion during the Miocene Climatic Optimum: Evidence from sediment record in the South China Sea. *Geophysical Research Letters* **36**, L19706 1-5.

Wang, P. X., 2009. Global monsoon in a geological perspective. *Chinese Science Bulletin* **54**, 1113-1136.

Wehausen, R. and Brumsack, H. J., 1998. The formation of Pliocene Mediterranean sapropels: constraints from high-resolution major and minor element studies. In: Robertson, A. H. F., Emeis, K.-C., Richter, C., and Camerlenghi, A. (Eds.), *Proceedings of the Ocean Drilling Program, Scientific Results* **160**, p. 207-217.

Wehausen, R. and Brumsack, H. J., 1999. Cyclic variations in the chemical composition of eastern Mediterranean Pliocene sediments: a key for understanding sapropel formation. *Marine Geology* **153**, 161-176.

Wehausen, R. and Brumsack, H. J., 2000. Chemical cycles in Pliocene sapropel-bearing and sapropel-barren eastern Mediterranean sediments. *Palaeogeography Palaeoclimatology Palaeoecology* **158**, 325-352.

Wessels, W., 2009. Miocene rodent evolution and migration; Muroidea from Pakistan, Turkey and Northern Africa. In: Wessels, W. (Ed.), *Miocene rodents, faunal exchange and migrations routes between Eurasia and Africa*. Geologica Ultraiectina **307,** Utrecht, 290 pp.

Westerhold, T., Bickert, T., and Rohl, U., 2005. Middle to late Miocene oxygen isotope stratigraphy of ODP site 1085 (SE Atlantic): new constrains on miocene climate variability and sea-level fluctuations. *Palaeogeography Palaeoclimatology Palaeoecology* **217**, 205-222.

Woodruff, F. and Savin, S. M., 1989. Miocene deepwater oceanography. *Paleoceanography* **4**, 87-140.

Woodruff, F. and Savin, S. M., 1991. Mid-Miocene isotope stratigraphy in the deep sea : high-resolution correlations, paleoclimatic cycles, and sediment preservation. *Paleoceanography* **6**, 755-806.

Wright, J. D., Miller, K.G. and Fairbanks, R.G., 1992. Early and middle Miocene stable isotopes: implications for deepwater circulation and climate. *Paleoceanography* **7**, 357-389.

Yellin, D. A., Grasso, M., Ben, A. Z., and Tibor, G., 1997. The subsidence history of the northern Hyblean Plateau margin, southeastern Sicily. *Tectonophysics* **282**, 277-289.

Zachos, J., Pagani, M., Sloan, L., Thomas, E., and Billups, K., 2001a. Trends, rhythms, and aberrations in global climate 65 Ma to present. *Science* **292**, 686-693.

Zachos, J. C., Shackleton, N. J., Revenaugh, J. S., Palike, H., and Flower, B. P., 2001b. Climate response to orbital forcing across the Oligocene-Miocene boundary. *Science* **292**, 274-278.

Introductie en Samenvatting

1. Introductie

Het begrijpen van het complexe systeem Aarde, waarin landschappen continu transformeren, een ongelofelijke variabiliteit aan levensvormen heerst, en het klimaat voortdurend verandert, is van groot belang om de toekomst van de Aarde te voorspellen. De toenemende broeikas omstandigheden waar we vandaag de dag mee geconfronteerd worden zijn een belangrijk onderwerp van discussie voor onze dicht bevolkte wereld. Klimaatmodellen zijn essentieel om de toekomst te voorspellen, maar hun robuustheid hangt onder andere af van wat we leren van klimaatveranderingen uit het verleden. Het is daarom van groot belang om de klimaatverschuivingen uit het verleden te bestuderen en vooral ook om te kijken hoeveel tijd er betrokken was in deze transities. Daarnaast is het van belang om meer kennis te vergaren over terugkoppelingsmechanismen, die de processen mogelijk kunnen vertragen of juist versnellen.

Klimaatveranderingen in het verleden zijn ontdekt door studies naar, onder andere, fossielen planten en dieren, fossiele bodems, meerafzettingen en zeebodem sedimenten. Sinds het begin van het "Deep Sea Drilling Programme" (DSDP) in 1968, later gevolgd door het "Ocean Drilling Programme" (ODP) en tegenwoordig het "International Ocean Drilling Programme" (IODP), is veel onderzoek gedaan aan Mesozoische en Cenozoische sedimenten uit de Atlantische Oceaan, de Pacific, Indische Oceaan en de Middellandse Zee.

Belangrijke hulpmiddelen in klimaatreconstructies uit diepzee sedimenten zijn foraminiferen: eencellige organismen die vaak een schaaltje van calcium carbonaat om zich heen bouwen. De meeste soorten foraminiferen leven op de zeebodem en staan bekend als benthische foraminiferen. Planktonische foraminiferen hebben een pelagische levenswijze en bewonen de oppervlakkige watermassa's.

De chemische compositie van de schaaltjes van foraminiferen wordt veelvuldig gebruikt in paleo-studies omdat ze informatie bevatten over de zeewater temperatuur, ijsvolume, saliniteit, productiviteit, de koolstof cyclus en oceanische circulatie patronen (Raymo en Ruddiman, 1992; Ruddiman, 2000). Daarnaast worden foraminiferen bestudeerd vanwege hun ecologische voorkeuren. De fossiele assemblages kunnen het paleo-mileu waarin ze leefden reflecteren.

Tijdens het Cenozoicum, dat 65 miljoen jaar geleden (Ma) begon, hebben drie belangrijke afkoelingsfases plaatsgevonden die de wereld van een broeikas- naar de "ijskast"-staat van vandaag hebben gebracht. De meest belangrijke afkoelingen waren tijdens de Eoceen/Oligoceen transitie, tijdens het midden Mioceen en tijdens het midden Plioceen (Shackleton en Kennett, 1975; Miller et al., 1987; Lear et al., 2000; Zachos et al., 2001a). Grote continentale ijskappen begonnen zich vanaf ~34 Ma geleden te ontwikkelen op Antarctica, terwijl de belangrijkste glaciaties op het Noordelijk Halfrond vooral tijdens het latere Neogeen plaatsvonden (Zachos et al., 2001a; 2008). Gletsjers en kleinere geïsoleerde ijskappen kwamen waarschijnlijk al eerder op het Noordelijk Halfrond voor en waren aanwezig gedurende groot deel van het Cenozoicum, met name als de orbitale configuraties gunstig waren (DeConto et al., 2008).

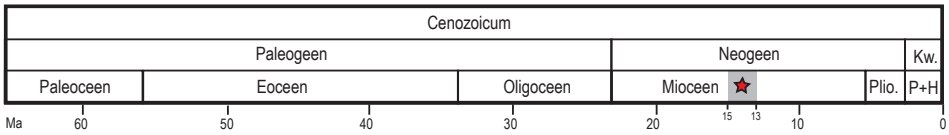

1.1 De Midden Miocene Klimaattransistie

De focus van dit proefschrift is de Midden Miocene Klimaattransitie (MMKT). Deze transitie markeert het einde van het Mioceen Klimaat Optimum (MKO), de warmste fase van het Neogeen. Een sterke uitbreiding van de Oost Antarctische IJskap zorgde voor een overgang naar een koeler klimaat en er vonden veranderingen in oceanische circulatiepatronen plaats (bijv. Kennett, 1975; Miller et al., 1987; Flower en Kennett, 1994; Zachos et al., 2001a; Shevenell en Kennett, 2004). Een gedetailleerde samenvatting over de Midden Miocene Klimaattransitie wordt gegeven in Flower en Kennett (1994).

Het tijdskader dat de MMCT omvat verschilt tussen auteurs en kan ergens tussen ~17-11 Ma liggen, afhankelijk van of de focus op alle zuurstofisotopen verrijkingen gedurende het midden Mioceen ligt, of alleen op de voornaamste verschuiving rond ~13.8 Ma (Miller et al., 1991; 1996; Woodruff en Savin, 1991; Flower en Kennett, 1994; Shevenell en Kennett, 2004). Op dit moment is het nog niet geheel duidelijk wanneer het Mioceen Klimaat Optimum ten einde kwam. Ondanks het feit dat het eind van het MKO niet goed gedefinieerd is wordt in dit proefschrift ~15 Ma aangehouden als de laatste representatieve warme fase. De Midden Miocene Klimaattransitie zal daarom worden gedefinieerd als de fase tussen het einde van het Mioceen Klimaat Optimum (~15 Ma) en het einde van de snelle afkoelingsstap rond ~13.7 Ma.

Belangrijke factoren in lange termijn trends in klimaatverandering zijn variaties in atmosferisch CO_2 verbonden met de koolstofcyclus, het openen en sluiten van oceanische passages, en het omhoogkomen van bergketens (bijv. Hay et al., 2002). De MMKT wordt geassocieerd met al deze factoren maar op de dag van vandaag bestaat er nog geen duidelijke consensus over de oorzaak.

Zoals bij andere Cenozoische klimaatverschuivingen lijkt de timing van de belangrijke afkoelingsstap bepaald te zijn door lang-periodieke orbitaal forcering (Abels et al., 2005; Holbourn et al., 2005; 2007). Minima in de amplitude variatie van de scheefstand van de aardas ("obliquiteit") en minima in de ellipsvormigheid van de baan van de aarde om de zon ("excentriciteit"), hetgeen de amplitude van de klimatologische precessie (de rotatie beweging van de aardas ten op zichte van de ellipsvormige baan) moduleert, blijken maxima in de zomerinstraling te onderdrukken gedurende een lange tijd waardoor de groei van ijs gestimuleerd wordt. Echter, orbitaal forcering op zich zelf kan niet de lange termijn afkoeling verklaren die vanaf het MKO doorzet.

Een langdurige positieve excursie in koolstof isotopen records tussen ~17 en 13.5 Ma - de "Monterey Excursie" van Vincent en Berger, (1995) – is een prominent verschijnsel in de oceanische stabiele isotopen records (Woodruff en Savin, 1991). Gelijktijding met de depositie van grote hoeveelheden organisch rijk sediment langs de circum-Pacifische marges, gaf dit ondersteuning aan de hypothese dat door de toename in het begraven van organisch koolstof CO_2 uit de atmosfeer werd onttrokken waardoor het broeikaseffect verminderd werd (Vincent en Berger, 1985; Woodruff en Savin, 1991; Flower en Kennett, 1994).

Een andere afvoer voor CO_2 op geologische tijdschaal is toenemende verwering van silica. In het begin werd de afkoeling in het midden Mioceen onder andere gerelateerd aan de groei – en verwering- van het Tibetaans Plateau (bijv. Raymo en Ruddiman, 1992), alhoewel recent werk van Wan et al. (2009) suggereert dat de warme en vochtige omstandigheden tijdens het MKO een wereldwijde toename in erosie veroorzaakten. Huidige hypothesen stellen dat de toename van $\delta^{13}C$ in het marine bereik vooral werd veroorzaakt door een toename van koolstof opslag op de continenten, hetgeen in overeenstemming is met de depositie van ligniet in die tijd (Diester-Haass et al., 2009).

Veranderingen in de oceanische circulatiepatronen zijn ook vaak genoemd als een belangrijke factor in lange termijn afkoeling van de Antarctische regio. Verschillende auteurs hebben verondersteld dat de sluiting van de Tethys zeestraat, die de Atlantische

en Indische Oceaan door de proto-Middellandse Zee verbond, een afname in meridionaal warmte transport naar de zuidelijke breedtegraden teweeg bracht, waardoor het Antarctisch oppervlakte water kon afkoelen en de Oost Antarctische IJskap kon uitbreiden (bijv. Woodruff en Savin, 1989; Flower en Kennett, 1995; Ramsay et al., 1998). Echter, een direct verband tussen de Midden Miocene Klimaattransitie en de sluiting van de Tethys zeestraat is tot nu toe nooit bewezen (bijv. Hüsing, 2008; Smart et al., 2007). Vele pogingen zijn ondernomen om de sluiting nauwkeuriger te dateren maar de afwezigheid van goed dateerbare sedimenten en de complexe processen die betrokken waren bij de collisie tussen de Eurasische en Afro-Arabische platen compliceren de reconstructie van de sluiting. Wanneer de Tethys zeestraat precies sloot is dus nog steeds onduidelijk en schattingen variëren tussen laat Oligoceen en laat midden Mioceen. Zoogdier migraties vanaf ~18 Ma (bijv. Rögl, 1999; Wessels, 2009) suggereren dat de zeestraat zo goed als dicht was voordat de MMKT begon.

1.2 De Midden Miocene Klimaattransitie in het Middellandse Zeegebied

De klimatologische geschiedenis van de half afgesloten Middellandse Zee begint na de disconnectie met de Indische Oceaan, meest waarschijnlijk al voor het begin van het Mioceen Klimaat Optimum. Wateruitwisseling vond alleen met de Atlantische Oceaan plaats en afhankelijk van het zoetwater budget een anti-estuarine of een estuarine circulatie ontwikkelde (bijv. Karami et al., 2009). Doordat de Middellandse Zee nu bijna geheel door land omsloten was verlaagde de buffercapaciteit van het bekken, waardoor het gevoeliger werd voor klimaatverandering (Gladstone et al., 2007; Rohling et al, 2009; Karami et al., 2009). Bovendien ligt het Middellandse Zeegebied geografisch gezien op de grens tussen het subtropische/moessonale regime van Afrika en de gematigde westen winden van Europa waardoor het bekken beïnvloed wordt door veranderingen in beide systemen (Rohling et al., 2009). Dit maakt het Middellandse Zeegebeid tot een uitstekende plek om klimaatveranderingen uit het verleden te bestuderen.

Het frequent voorkomen van donkere organisch-rijke lagen ("sapropelen") in sedimenten van de Middellandse Zee wordt gerelateerd aan verhoogde moesson activiteit en toevoer van vochtige lucht met westenwinden tijdens periodes van maximale zomerinstraling gerelateerd aan variaties in excentriciteit, obliquiteit en precessie (Rossignol-Strick, 1983; 1985; Hilgen et al., 1991a, b; Hilgen et al., 1995; Lourens et al., 1996). De depositie van sapropelen reflecteert meestal een toename in marine productiviteit en een restrictie in de ventilatie, veroorzaakt door verhoogde zoetwater toevoer naar de Middellandse Zee (voor reviews zie Rohling et al., 1994; Cramp en O'Sullivan, 1999; Rohling et al., 2009).

Ritmische sedimentaire afwisselingen in marine successies hebben de potentie om astronomisch gedateerd te worden, waarbij de ouderdommen van belangrijke veranderingen in het milieu nauwkeuriger kunnen worden bepaald. Ondanks uitgebreide studies aan laat Neogene sedimentaire sequenties (bijv. Hilgen et al., 2000; Wehausen en Brumsack, 2000; Turco et al., 2001; Hüsing et al., 2009), weinig werk heeft zich gericht op het midden Mioceen van de Middellandse Zee. Dit is deels het gevolg van DSDP regelgeving waarbij het niet was toegestaan om door Messinische zoutlagen te boren. Ontsluitingen van marine sedimenten op het land zijn daarom de enige plek om de vroege geschiedenis van de half afgesloten Middellandse Zee te onderzoeken.

Sedimenten van de Adriatische kust nabij Ancona (Italië) en van de Maltese Eilanden (Malta en Gozo) zijn onderwerp van dit proefschrift omdat ze de Midden Miocene Klimaattransitie in de Middellandse Zee omvatten. Dit proefschrift heeft als doel om de wereldwijde klimaatverandering te relateren aan de geobserveerde veranderingen in het milieu van de Middellandse Zee en daarnaast om de ouderdomsmodellen voor dit interval te verbeteren.

2. Samenvatting

Aanvankelijk begon dit onderzoek met de secties van Malta en Gozo, maar de constructie van een astronomisch gekalibreerd ouderdomsmodel voor het oudere deel van de sectie werd gecompliceerd door de afwezigheid van goede magnetostratigrafie en een niet zo duidelijke cyclostratigrafie. Met de recente constructie van een astronomisch gekalibreerd ouderdomsmodel voor de La Vedova Beach sectie in Italië (Hüsing et al., 2010) en een opwaartse uitbreiding van de sectie hoog in de kliffen werd het mogelijk om het interval van de MMKT in Italië astronomisch te dateren. Met deze nieuwe gegevens werd als doel gesteld de dateringsproblemen op Malta op te lossen.

Hoofdstuk 1 begint daarom met de constructie van een astronomisch gekalibreerd ouderdomsmodel voor de nieuwe La Vedova High Cliff sectie. Deze sectie is een van de weinige Middellandse Zee-secties die het kritische tijdsinterval van de MMKT omvat. Voor het interval tussen 14.2 en 13.5 Ma wordt in dit hoofdstuk een robust astronomisch gekalibreerd ouderdomsmodel gemaakt, met behulp van geochemische elementen data en tijd-series analyse. Bulk carbonaat isotopen records laten een verschuiving in $\delta^{18}O$ zien tussen ~13.92 en 13.78 Ma hetgeen gecorreleerd kan worden aan de Mi3b-stap in zuurstof isotopen. Het begin van de $\delta^{13}C$ CM6 koolstof isotopen excursie is nu gedateerd op ~13.86 Ma. De resultaten bevestigen dat deze stappen samenvallen met een ~405 duizend jaar minimum in excentriciteit en een knoop in de amplitudes van obliquiteit gerelateerd aan de ~1.2 miljoen jaar cyclus. Vanaf 13.8 Ma beginnen specifieke quadrupletten te vormen waarin sapropelitische sedimenten kunnen worden geobserveerd. Dit suggereert een causaal verband tussen de voornaamste midden Miocene afkoelingsstap en sedimentatie en circulatie in de Middellandse Zee.

Door de La Vedova Beach en La Vedova High Cliff secties te combineren kan een compositie sectie worden bestudeerd voor het interval tussen ~15.3 en 13.5 Ma. In **Hoofdstuk 2** is een hoge resolutie geochemische dataset gebruikt om lange termijn ontwikkelingen van de sedimentaire cycli te bestuderen. Laag zuurstof gehalte in het bodem water kan worden afgeleid voor het interval van de laatste fase van het Mioceen Klimaat Optimum waar hoge sedimentatie snelheden worden gerelateerd aan hoge rivier afwatering en organische input. Regelmatige verrijking in Ti/Al en Zr/Al suggereert dat de aanvoer van eolische stof significanter werd vanaf ~14.5 Ma, hetgeen op verdroging van noordelijk Afrika in het midden Mioceen kan duiden. Nat-droog oscillaties worden duidelijker na de voornaamste wereldwijde afkoelings stap rond 13.8 Ma, wanneer mergels met hoog Ti/Al en Zr/Al toenemen in dikte. Het voorkomen van sapropelitische lagen in een cyclus met een karakteristieke quadruplet structuur wijzen op periodieke afname in ventilatie van het bodemwater. De toegenomen differentiatie tussen sedimentaire fases die aan voornamelijk droge en voornamelijk natte condities zijn gerelateerd suggereert dat het seizoenaal contrast toenam na de MMKT. Vooral hogere zoetwater toevoer tijdens maxima in zomerinstraling kan een voorwaarde zijn geweest voor het vormen van sapropelitische sedimenten na 13.8 Ma.

In **Hoofdstuk 3** wordt een astronomisch gekalibreerd ouderdomsmodel voor het bovenste deel van de Globigerina Limestone Formatie (Maltese Eilanden) gepresenteerd, gebaseerd op hoge resolutie isotopen records. Daarnaast wordt het ouderdomsmodel voor het onderste deel van de Blue Clay Formatie herzien met behulp van nieuwe ouderdommen voor biostratigrafische niveaus verkregen uit Hoofdstuk 1. Het bovenste deel Globigerina Limestone is nu gedateerd tussen ~14.95 en 13.76 Ma (± 0.02), alhoewel de mogelijkheid van een hiaat tussen 13.95 en 13.76 niet volledig kan worden uitgesloten. Dit kan mogelijk gevolgen hebben voor de GSSP ("Global Stratotype Section and Point") van het Serravallian die tegenwoordig gedefinieerd is in deze sectie. Benthische en planktonische koolstof isotopen records tonen ~405 duizend jaar maxima in $\delta^{13}C$, geassocieerd met de Monterey Koolstof Excursie. De wereldwijde midden Miocene afkoeling is te zien in de benthische zuurstof isotopen record, waar een verzwaring van ~0.6‰ plaatsvindt (Mi3b) tussen ~13.95 en 13.76 Ma. Een toename in afwatering na de klimaattransitie heeft waarschijnlijk gezorgd voor een afname in de ventilatie waardoor de planktonische en benthische isotopen records een divergentie tonen.

In **Hoofdstuk 4** worden assemblages van benthische foraminiferen van de Maltese Eilanden bestudeerd om meer inzicht te verkrijgen in de effecten van de Midden Miocene Klimaattransitie op het Mediterrane paleo-milieu. Daarnaast zijn geochemische- en isotopen records gebruikt om veranderingen in het milieu op te sporen . Tussen ~14.95 en 13.9, wijzen de benthische assemblages op een mesotroof en goed geventileerd milieu. De sterke toename van klei aanvoer aan de basis van de Blue Clay Formatie (~13.76 Ma) zorgde voor een afname in het carbonaat gehalte met meer dan 50%. Verhoogde rivier afwatering heeft voor een toename in voedsel beschikbaarheid gezorgd en een lager zuurstofgehalte van het bodemwater. Hierop reageerde de benthische assemblage door een toename van infaunale taxa. Een successieve toename van infaunale soorten en het voorkomen van de eerste sapropelitische sedimenten op 13.24 Ma suggereert dat de veranderingen in het milieu, met name de restrictie in ventilatie, bleven doorgaan na de MMKT.

Hoofdstuk 5 is een synthese gebaseerd op de resultaten van Hoofdstuk 1-4. Daarnaast wordt een impressie gegeven van de klimaat- en milieu veranderingen in en rond het Middellandse Zeegebied voor, gedurende en na de MMKT. Wanneer de secties uit het Centrale Middellandse Zeegebied worden vergeleken dan nam de terrestrische input toe in samenhang met de MMKT. Dit gebeurde zowel in de Adriatische Zee (La Vedova) als op het Malta-Hyblean Plateau (Maltese Eilanden). Precessie gestuurde afwisseling van sedimenten aangerijkt in eolisch stof en het voorkomen van sapropelitische sedimenten suggereert dat het Afrikaanse moesson systeem operatief was in het midden Mioceen. Klimaatgordels zijn waarschijnlijk ingekrompen door het uitbreiden van de Oost Antarctische IJskap waardoor meer moderne klimaat condities zich in het Middellandse Zeegebied hebben kunnen ontwikkelen.

Acknowledgements

Four and a half years ago I decided to make a journey to the bottom of the Mediterranean Sea. The reason to do this was my interest in the life and environment of the past. On a sunny day in September I stepped into a submarine and sank down to below the photic zone, where life flourishes in darkness. My first stop was at the Maltese Islands where I emerged to view the old seafloor which was now exposed along the coastline. After taking some samples there, I submerged again to the forgotten darkness.

I was trying to picture how the Mediterranean looked like 14 million years ago. What influences did climate have on the habitat of the bugs I was studying? How rapid did climate change? And which part of the observations had been caused by other things than climate? I got stuck in the puzzle of determining the age of the Maltese sediments and decided to go to Italy. I arrived there in May 2008. Again, I had to climb up the cliffs, but what a terrific view! Getting there, however, was one of the most challenging things of my entire journey. But I survived.

Back in the submarine a second period of analysis and data interpretation started. "This puzzle is like a sudoko of the highest degree!", a friend once said to me. Yeah, I know... Nevertheless, I decided to write a little story on the results of my journey. And if you're interested in how the Mediterranean looked like 14 Million years ago, you might have actually read it.

Anyhow, even though the journey was a bit lonesome some days, I have had lot's of fun as well thanks to all my friendly colleagues, friends and family. Because I am very grateful to all these species I've collected some memories, as you will see on the next page. If you think some species are missing, it might be that they slipped through the sieve. However, I would like to thank everybody who has supported me!

Acknowledgement assemblage

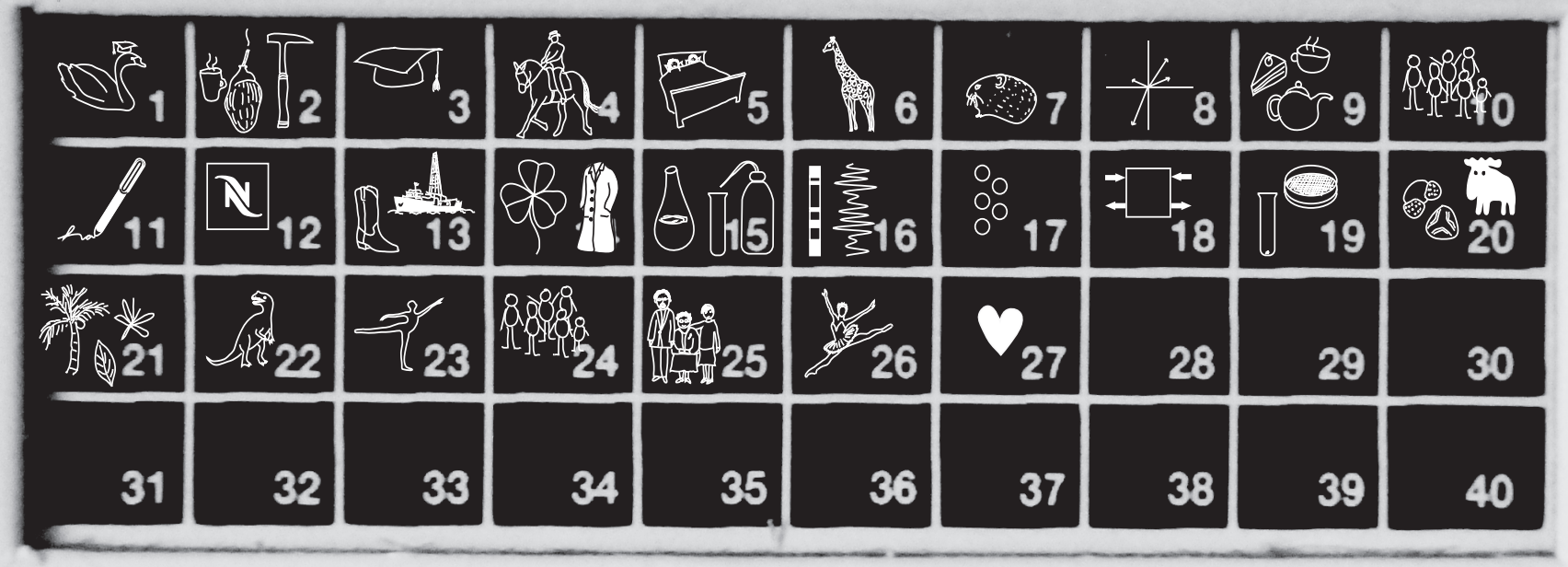

Species of the Acknowledgement Assemblage

1. Group: **Promotoridae**
Species: *B. Van der Zwaan*
Proxy for: Moral support, even at a distance (Unnik building). Making decisions: "Welke noten hebben we te kraken?". Thanks for everything Bert!

2. Group: **Co-promotoridae**
Species: *F. Hilgen* and *T. Kouwenhoven*
Proxy for: Cyclostratigraphy (*Frits*) and Paleo-ecology of benthic foraminifera (*Tanja). F. Hilgen* is frequently found in Spain or Italy, whereas *T. Kouwenhoven* can be associated with coffee and cigarette breaks. Dank voor de gezellige jaren!

3. Group: **Professoridae** (cf. reading committee members)
Species: *D. Kroon*, *A. Lotter*, *J. Middelburg*, *A. Holbourn*, *W. Kuhnt*, *C. Lear*.
Proxy for: Critical evaluation of this PhD thesis. Most species in this group are marine, but some have a preference for the terrestrial realm. Thanks to all of you!

4. Group: **Strat-Pal-idae**
Species: *Karoliina Koho*
Proxy for: 1) Sharing: office, coffee, cookies, dropjes, information on foraminifera, information on horses; 2) Lot's of fun. Thanks for the great time! Olet paras, ja minä kaipaan sinua (for mistakes blame google translate).

5. Species*: Lucy Stap*; *L. Afman*; Paranimph
Proxy for: Having a good time, especially at conferences ;) Lucy ik ga je missen hoor!

6. Species: *Hemmo Abels*
Proxy for: This very tall species can often be found in Spain, China, Wyoming and in Fort Hoofdijk. *H. Abels* occupies a similar scientific niche as *F. Hilgen* but lives in the same room as *K. Hordijk*. Muchas gracias for all your enerGIE!

7. Species: *K. Hordijk, W. Wessels, A. van der Meulen*
Proxy for: small mammals of the Miocene. Thanks for the nice cooperation!

8. Species: *I. Duijnstee*
Proxy for: statistics and foraminifera. Although now party living in the US, "I V O" has his roots in the Netherlands (and therefore likes a lot of cheese). Bedankt voor al je hulp!

9. Species: *M. Wolthers* and *M. Brouwer*
Proxy for: long conversations (often about kids) during long tea breaks. Thanks for the good time and I suggest we organise another high-tea soon!

10. Species: *M. Ziegler, C. Zeeden, L. Lourens, J. W. Zachariasse, M. Schweitzer, S. Langezaal, S. Ernst, L. de Nooijer; K. Kuijper, J. Reumer* and the rest of strat-pal
Proxy for: a stratigraphic and paleontologic family. Dank voor alle gezelligheid!

11. Group: **Co-authoridae**
Species: *J. Bijkerk, E. Turco, A. Cascella, A. Di Stefano, J. Sprong*
Proxy for: providing an important contribution to this thesis. Thanks to *J. Bijkerk* I survived Vedova High Cliff. Tanks to *Elena* I survived Italy ;) Thank you all for your cooperation!

12. Group: **Sedimentologidae**
Species: *João Trabucho Alexandre*
Proxy for: black shales and black coffee. This small species originating from Portugal is a good story teller and guarantees lot's of fun. Thanks for the good time! Also thanks to your sedi-colleagues!

13. Group: **Geochemistidae**
Species: *G. J. Reichart* and *G. de Lange*
Proxy for: marine geochemistry. *G. J. Reichart* can be recognized by cowboy boots (not to be confused with *H. Brinkhuis*). He usually sneaks into the office in search for dropjes. Although he looks a little bit like Elvis, he is not genetically related. *G. de Lange* is commonly found on a research vessel or behind a pile of papers. Thanks for all your help with the elemental stuff!

14. Species: *Shauna Ní Fhlaithearta* and *Adriana Dueñas-Bohórquez*
Proxy for: *Shauna* is a typical Irish species although sometimes by mistake interpreted as German. She likes good coffee and might ask for a cookie if her energy levels drop. *Adriana* is a small species originating from Colombia. She is often very actively running around in the building or outside. Thanks for all the good time girls!

15. Species: *Tom, Elisabeth, Cornelia, Peter, Julia, Eveline, Jos, Jose, Iana, Vasso*
Proxy for: geochemistry, running, partying… Thanks for all the fun!

16. Group: **Paleomagnetidae**
Species: *Silja Hüsing*
Proxy for: A good scientist, a traveller, a dancer. Like many other species in Utrecht, *Silja* has a preference for the warm environment of the Mediterranean. If it's too hot there, she might be found in New Zealand. Thanks for the nice time together and for sharing the Adriatic Coast (maybe we should go there together one day…).

17. Species: *Maud, Martijn, Arjan, Wout, Cor* and others
Proxy for: Although hiding in the darkness of Fort Hoofdijk, Paleomagnetidae should be associated with fieldwork, drilling holes and having great borrels. Ook jullie heel erg bedankt!

18. Group: **Tectonophysidae**
Species*: P. Meijer, P. Karami, B. Alhammoud*
Proxy for: Mediterranean circulation models. Thanks for the nice discussions!

19. Group: **Technicidae**
Species: *G. Ittmann, H. de Waard, A. van Dijk, J. Drenth, O. Stiekema*
Proxy for: hard working species, almost exclusively found in the lab. Thanks for all the sieving and measuring!

20. Group: **Pal-and-Pal-idae**
Species: *N. Bonis; Nina Rosa; Pollenina*
Proxy for: a good friend, lunch walks in the botanical gardens, baking cookies, samen lachen samen huilen. Heeeel veel dank voor de leuke jaren samen op de universiteit!

21. Species: *Micha, Maarten, Judith, Frederike, Emmy, Emi, aAp, Henk*; and the rest of the south- and west corridors
Proxy for: the best "neighbours" and lots of fun (and science…). Thanks for learning me all about non-biting midges, T/J and the hot climate of the Eocene.

22. Group: **Biogeologidae**
Species: *Anne, Faruk, Herman, Wouter, Tjitske* and *Barbara*
Thanks for all your support during the last 4 years!

23. Group: **Dans Centrum Utrecht-idae**
Species: *Arienne, Sarah, Soosan, Minke, Linda*
Thanks for keeping me flexible all the time and Linda dank je wel voor de gezellige wandelingetjes tussendoor!

24. Group: **Miscellaneous**
Species: Friends and Family of Demis
Bedankt voor alle gezelligheid afgelopen jaren!

25. Group: **Familidea**
Species: *Papa, Mama, Oma* (en de opa's en oma die van boven meekeken)
Ook jullie heel erg bedankt voor alle steun!

26. Species: Dr.-to-be *Marjon; M. J. Mourik*; *Sjonnie*; *Jontje*; Paranimph
This very elegant species is my favourite! She's a good dancer and a very good scientist (already!). In addition, she guarantees lots of fun. She's the best little sister in the world! Jontje, heel erg bedankt voor alles!

27. Group: **the following species can not be placed into a group**
Species: *Demis*
Van jou is er maar één, en jij bent de liefste! Bedankt voor de zonnebloemen tijdens de regenzomer.

Curriculum Vitae

Anja Ariëtta Mourik was born on September 22, 1981 in Haarlem, and grew up in Heemstede, the Netherlands. She discovered the wonders of nature at a young age when she was going out to the field with her father who worked at the Amsterdamse Waterleiding Duinen as an ecologist. The collection of fossils and stones that were hidden in a secret cabinet in her fathers office fed her imagination of the world in the past. Although initially she wanted to become a biologist, she went to study Physical Geography at Utrecht University after she graduated at College Hageveld in Heemstede in 1999. In January 2001 she changed study direction and started to follow the Master Biogeology.

During her Master, she did two research projects. One was focused on the morphometry and ecology of the burrowing shrimp *Protocalianassa faujasi* from the late Cretaceous, under supervision of R.H.B. Fraaije from the Oertijdmuseum in Boxtel, the Netherlands. For her graduation project she went to the Soutpansberge in South-Africa where she spent three months at Lajuma Research and Education Center to study the limiting factors of tree recruitment at the boundary of termite-mound bush clumps. This project was supervised by Dr. ir. F. van Langevelde and Dr. ir. I.M.A. Heitkönig from the Resource Ecology Group, Wageningen University.

With her growing interest in the effects of climate change on ecosystems she started a PhD on the Middle Miocene Climate Transition at the stratigraphy and paleontology group (Utrecht University) in September 2005. Under supervision of Dr. F. J. Hilgen and Dr. T. J. Kouwenhoven she studied the effects of global cooling on the Mediterranean. This project was financed by the Darwin Center for Biogeosciences and the University of Utrecht. The results are presented in this thesis.

In September 2010 she is planning to go back to Lajuma in South-Africa to help students with their projects and to do a voluntary research on the effects of climate change on the ecosystems of the Soutpansberge.

Photographs from left to rigth: During fieldwork on Malta (2005); The highest level of the La Vedova High Cliff section (2008); View from the High Cliff; Fieldwork on the High Cliff; Frits Hilgen, Jochem Bijkerk and Anja Mourik survived the High Cliff. Photos by H. Abels, J. Bijkerk and A. Mourik.